Design and synthesis of three dimensional covalent organic frameworks with new topologies

Xue Wang

Department of Chemistry and Materials Innovation Factory,
University of Liverpool

Thesis submitted in accordance with the requirements of the University of Liverpool for the degree of Doctor of Philosophy

July 2022

Supervisor: Prof. Andrew I. Cooper

Abstract

Covalent organic frameworks (COFs) are a class of crystalline porous material. The crystallinity in COFs endows them with improved performance for specific applications, such as higher surface area and higher photocatalytic efficiency, compared to their amorphous counterparts. Since their first report in 2005 by Yaghi and co-workers, 2D COFs have been explored widely. 3D COFs, on the other hand, have been much less explored but have received increasing attention in the last 5 years. Compared with the closely packed 2D COFs, 3D COFs have advantages in enhanced overall framework rigidity, multiple types of cavities and pore channels, and higher surface areas for catalysis due to lower density.

Although 3D COFs have great potential, the realization of structural diversity is harder from a synthetic perspective. There are generally two possible routes for the preparation of 3D COFs: one is from organic polyhedral type multi-linking building blocks, while the other is by controlling the spatial arrangement of planar building units. The first strategy requires the synthesis of specifically shaped organic molecules, which can be challenging and adds complexity to this route. While the alternative spatial arrangement control of planar building units alleviates synthetic complexity, the success of this second strategy relies on accurate dihedral angle set up between each planar unit. This thesis will focus on the latter strategy for targeting 3D COFs with new topologies.

One reliable method to construct 3D COFs of certain topology from planar building units is to apply rigid polyhedral type linkages. Specifically, in our case, we applied a tetrahedral-shaped spiroborate linkages to successfully reticulate two neighbouring square cobalt coordinated phthalocyanine (PcCo) units into perfect perpendicular orientation and produce 3D SPB-COFs of **nbo** topology. Among these SPB-COFs, SPB-COF-DBA showed very high crystallinity and its crystal lattice was clearly visualized using high-resolution transmission electron microscopy (HRTEM) images.

Another method we used to target 3D COFs with **nbo** topology was inspired by previous work on MOFs, specifically MOF-601. Here, we synthesized two 2,2’ and 2,2’,6,6’ methyl substituted biphenyl diboronic acid linkers and attempted COF synthesis through boronate ester linkages. Using this approach, we expected to realize a larger pore size compared with the former ionic spiroborate linkage (5.5 nm *vs.* 3.7 nm). However, we unexpectedly isolated spiroborate-linked COFs. We then characterised this reaction system using related characterizations and investigated model compounds to understand the reaction mechanism that leads to spiroborate formation.

Acknowledgement

Now is a deep, silent summer night in Liverpool, ideal moment for looking back these four years of my PhD adventures. Liverpool is a beautiful city and I have spent a happy time here. These four years leave me a lot of memorable moments that I would always cherish.

First and foremost, I would like to express my sincerest gratitude to my supervisor, Prof. Andrew I. Cooper, for giving me the opportunity to do research work in this top-class laboratory. He has inspired me during my four-year PhD study from either research aspect or his personality. He is an open-minded and creative researcher and has led several pioneering research projects like 'mobile robotic chemist' and 'crystal structure prediction', he is doing 'future science' and it has been my honour to be in this team. As a supervisor, he has always been supportive, patient and encouraging. The email from him titled as "Progress" on 23rd June 2021 to all our group members had been really encouraging during the hard Lockdown period, and I will keep this letter forever. I wish I can grow into a person like him in the future. Thanks also goes to the Leverhulme Research Centre for funding my PhD study.

I would like to gratefully thank Dr. Linjiang Chen, who expands my research backgrounds to computation chemistry, which opened my eye to view chemistry from atomic level and this has been the fundamental of all my PhD works included in this thesis. Thank him for co-supervising me, for being a good listener and for all the inspiring discussions. He has been a role-model for me. Thanks must also go to Dr. John Ward for co-supervising my PhD research and for his help and guidance.

I have been lucky to spend these four years with a lot of very nice persons and this is the biggest fortune I received during my four-year PhD. Firstly, thank Dr. Ming Liu, Dr. Xiaoyan Wang, Dr. Yang Bai, Dr Hui Gao for their daily encouragement and supports, which brings me energy to carry on when I feel down from the failed experiments and when I doubt myself. Thank Zhongfu Pang and Dr. Zhiwei Fu, who generously led me to the research fields of COFs and provides me lots of assistance. Thank my brilliant colleagues, Yongjie Xu, Qiang Zhu, Donglin He, Aiting Kai, Wei Zhao, I have learnt a lot from everyone, and it is my honour to work with them. Thank Dr. Marc Little, Dr. Mounib Bahri, Dr. Kewei Wang, Dr. Zhifang Jia, Dr. Weiwei Zhang, Dr. Veronica Del Angel, Dr. Tom Fellowes, Dr. Hongjun Niu, Dr. Lunjie Liu, Dr. Hongmei Chen, Dr. Haofan Yang, Xiang Zhou, Dr. Ai He, Dr. Samantha Y. Chong for their contribution to my projects and supporting me. Special thanks to Rob Clowes and the MIF technical support team for training and fixing all

the instruments. Special thanks to Dr. Xiaofeng Wu, who has always been supportive to we Chinese students.

Finally, I want to thank and dedicate this thesis to my grandparents, for educating me, supporting me and loving me, always. Thank my aunts for guiding me since I was a child and treating me equally as friends. Thank my parents and my brother for their support, love and accompany all these years. Thank my boyfriend Jiayin Song, who accepts all my unhappiness and returns me with patience, encouragement, and love, I can’t make this PhD without him staying by my side. I would also like to thank myself, for not giving up and being strong.

List of publications

1. Z. Fu, X. Wang, A.M. Gardner, **X. Wang**, S.Y. Chong, G. Neri, A.J. Cowan, L. Liu, X. Li, A. Vogel, R. Clowes, M. Bilton, L. Chen, R.S. Sprick, & A.I. Cooper. A stable covalent organic framework for photocatalytic carbon dioxide reduction. Chem. Sci., 2020, 11, 2, 543-550.
2. X. Wang, Z. Fu, L. Zheng, C. Zhao, **X. Wang**, S.Y. Chong, F. McBride, R. Raval, M. Bilton, L. Liu, X. Wu, L. Chen, R.S. Sprick, & A.I. Cooper. Covalent Organic Framework Nanosheets Embedding Single Cobalt Sites for Photocatalytic Reduction of Carbon Dioxide. Chem. Mater., 2020, 32, 21, 9107−9114.
3. K. Wang, Z. Jia, Y. Bai, **X. Wang**, S.E. Hodgkiss, L. Chen, S.Y. Chong, X. Wang, H. Yang, Y. Xu, F. Feng, J.W. Ward, & A.I. Cooper. Synthesis of Stable Thiazole-Linked Covalent Organic Frameworks via a Multicomponent Reaction. J. Am. Chem. Soc., 2020, 142, 25, 11131−11138.
4. Q. Zhu, **X. Wang**, R. Clowes, P. Cui, L. Chen, M.A. Little, & A.I. Cooper. 3D Cage COFs: A Dynamic Three-Dimensional Covalent Organic Framework with High-Connectivity Organic Cage Nodes. J. Am. Chem. Soc., 2020, 142, 39, 16842−16848.
5. H. Gao, Q. Zhu, A.R. Neale, M. Bahri, **X. Wang**, H. Yang, L. Liu, R. Clowes, N.D. Browning, R.S. Sprick, M.A. Little, L.J. Hardwick, & A.I. Cooper. Integrated Covalent Organic Framework/Carbon Nanotube Composite as Li-Ion Positive Electrode with Ultra-High Rate Performance. Adv. Energy Mater., 2021, 11, 39, 2101880.
6. **X. Wang**, M. Bahri, Z. Fu, M.A. Little, L. Liu, H. Niu, N.D. Browning, S.Y. Chong, L. Chen, J.W. Ward, & A.I. Cooper. A Cubic 3D Covalent Organic Framework with nbo Topology. J. Am. Chem. Soc., 2021, 143, 37, 15011−15016.

Table of Contents

Chapter 1

Introduction

1.1 Introduction to Covalent Organic Frameworks (COFs)

It had long been argued that the crystallization of 2-dimensional (2D) or 3-dimensional (3D) periodic frameworks from entirely covalent bonds would be very difficult or even impossible due to the foreseeable crystallization problems caused by the strong covalent bonds. The benchmark study that achieved the crystallization of covalent organic frameworks (COFs) was first reported by the Yaghi research group in 2005.[1] In this work, 2D boronate ester and boroxine-linked COFs with hexagonal pores were synthesized and the powder X-ray diffraction (PXRD) showed multiple strong diffraction peaks, corroborating their crystalline structures. Benefitting from their crystalline nature, this work presented the very pioneering methodology of using PXRD comparison between the experimental pattern and the patterns simulated based on the COF models proposed as a way to solve the crystal structures of COFs obtained. This exemplar method for solving COF structures has been applied as the most efficient strategy for novel COF structure discovery until now, and greatly propagated the COF structure diversity development for both 2D and 3D COFs.[2,3]

Since the report of the first COFs mentioned above, researchers have showed strong interest and devoted a lot of effort to exploring the applications of COFs. Currently, COFs have been reported for applications including sorption and separations,[4,5] electrochemical applications,[6] catalytic applications,[7] solar-driven fuels production,[8] and biomedical applications.[9] We can anticipate that COFs will be applied more widely in various applications in the future. As the performance of materials relies on their chemical components and structures, effort has also been made to explore novel 2D and 3D COFs structures.

From the structure perspective, one notable attribute of COFs is, like MOFs, that they can be designed in a bottom-up manner from molecular building units based-on reticular chemistry principles.[10] Reticular chemistry of COFs deals with linking discrete organic molecular building units into extended structures adopting expected topologies by strong covalent bonds.[11] This principle has guided the discovery of most COF structures reported. Early studies of COF structures mainly focused on 2D COFs[2,12] and an accelerating exploration of 3D COF structures has started in recent 5 years.[3,13] According to the reticular chemistry principle, to target 3D COFs of certain topologies, suitable linkages need to be selected to reticulate organic building units, which have the same geometry as the deconstructed geometric units from the topology, into the desired 3D alignment.[14] The following part will provide a detailed introduction to these subjects.

1.2 COF linkages

Since the report of the first 2D COF structures from Yaghi research group in 2005,[1] which applied the reversible boroxine linkage (COF-1) and boronate ester (also called 'boronic ester') linkage (COF-5) for COF synthesis (**Figure 1.1**), several other linkages had been developed for COF synthesis including imine,[15] *β*-ketoenamine,[16] polyimide,[17] hydrazone,[18] azine,[19] spiroborate,[20] triazine,[21] dioxin,[22] phenazine,[23] sp^2 carbon-conjugated linkage,[24] *etc*. Among the linkages reported, some are formed from reversible condensation reactions, while others are from irreversible reactions or condensation reactions which include both reversible and irreversible steps. Differences among them will be discussed in the following text in detail.

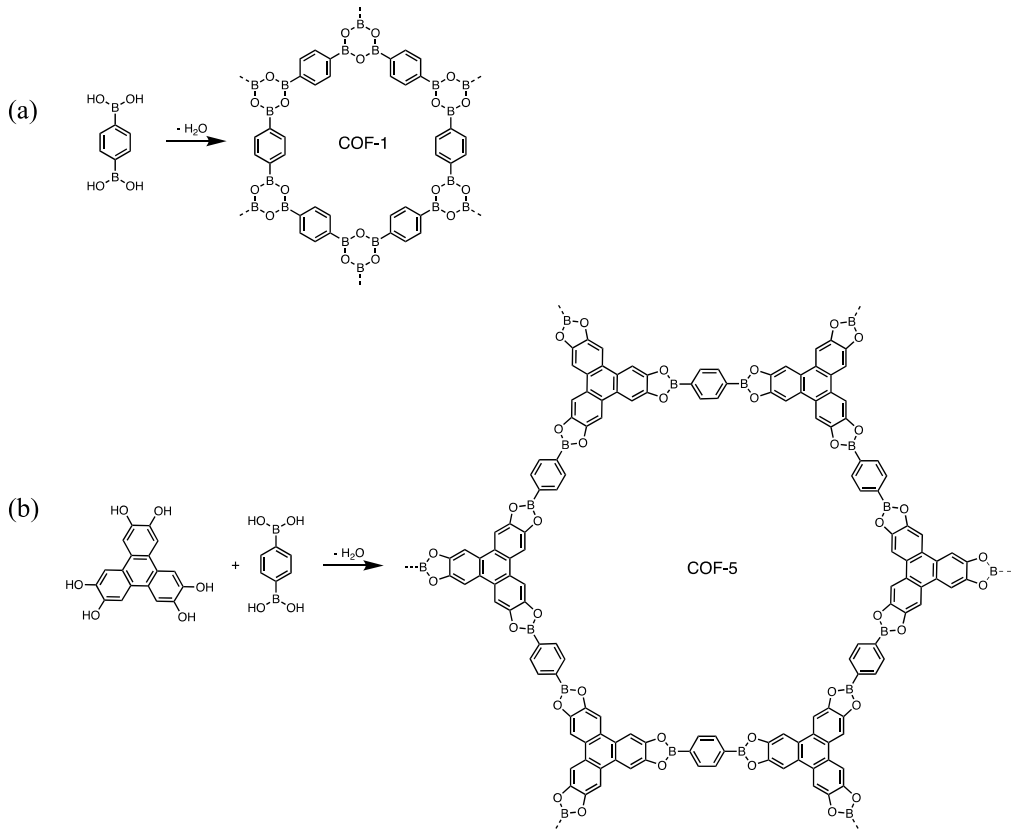

Figure 1.1. Scheme for the synthesis of **COF-1** and **COF-5** and their structure representation.[1]

1.2.1 COFs synthesised by reversible condensation reactions - under mild conditions

In the early studies of COF synthesis, researchers mainly focused on reversible self- or co-condensation reactions. It is believed that the reversible linkage formation permits error correction and rearrangement of the network by cleavage and reformation of connections within the lattice thus allowing for crystalline frameworks. This linkage reversibility is believed critical for obtaining

a crystalline framework, especially in the cases where COFs are constructed entirely from strong covalent bonds.[25]

Examples of COFs formed from linkages of good reversibility include boroxine, boronate ester, spiroborate, imine, hydrazone and azine (**Figure 1.2**). COFs from these linkages exhibits high crystallinity, with multiple diffraction peaks in the experimental PXRD pattern, which can fit with the simulated patterns. For example, in the work of COF-1 and COF-5, which were synthesized from boroxine and boronate ester linkages, respectively, all showed 14 well-resolved diffraction peaks in experimental PXRD that can well fit the simulated pattern based on the COF models of staggered packing mode (COF-1) and eclipsed packing mode (COF-5).[1] The later reported COFs synthesized from reversible spiroborate linkages also showed very good crystallinity as can be evidenced by the multiple diffraction peaks by experimental PXRD.[20,26] One limitation of these boron-based linkages is their poor stability. COFs from these linkages suffer from partial or full hydrolysis in an environment where H_2O or acid exists.[27] Though highly crystalline, this bond fragility has hindered the real-world applications of these boron-linked COFs.

Similarly, COFs from reversible imine condensation[15] and its hydrazone[18] and azine[19] derivatives, all show good crystallinity. Since the report of the first imine-based 3D COF-300 with five-fold interpenetrated **dia** topology,[15] the Schiff-base imine linkage has become the most extensively used linkage for COF synthesis. The reversibility of the imine linkage is achieved by employing acid as the catalyst. Imine-COFs showed improved chemical stability compared with COFs of boron-based linkages mentioned above. Imine-COFs are stable under H_2O and neutral pH environment, however, still undergo partial structure decomposition upon exposure to strong acids (12 M HCl at 100 °C for 1 day) and strong bases (14 M NaOH at 100 °C for 1 day), as can be evidenced by the PXRD, FT-IR and mass comparison before and after treatment.[28] Though hydrazone-linked COFs were reported to have good chemical stability in common solvents, like H_2O, tetrahydrofuran (THF), EtOH, hexane and *N*,*N*-dimethylformamide (DMF) at room temperature for 24 h,[29] a recent study has shown several examples of hydrazone-linked COF structures reconstructed into imine-COFs under H_2O at 160 °C, demonstrating the hydrazone-linked COFs are not that stable.[30] Chemical stability of azine-linked COFs was far from satisfying also, either in common solvents like THF, hexane, DMF and $CHCl_3$ or in acid (pH =1.0) and base solutions (pH =14.0).[31]

For the above-mentioned COFs, high linkage reversibility can be realized under relatively mild reaction conditions (generally prepared from solvothermal synthesis conditions at 120 °C for 3 days). While such easily accessible high reversibility under mild conditions contributed to the formation of highly crystalline COFs, it also means the reverse linkage cleavage can happen easily.

Generally, crystallinity and stability are inversely related to each other, as increased reversibility leads to higher crystallinity and lower stability, and *vice versa*.[32] To escape from this dilemma and aim to improve the chemical stability of COFs, we can either synthesize COFs from linkages that only have reversibility under harsh conditions or by introducing linkages that formed from a combination of reversible and irreversible steps.

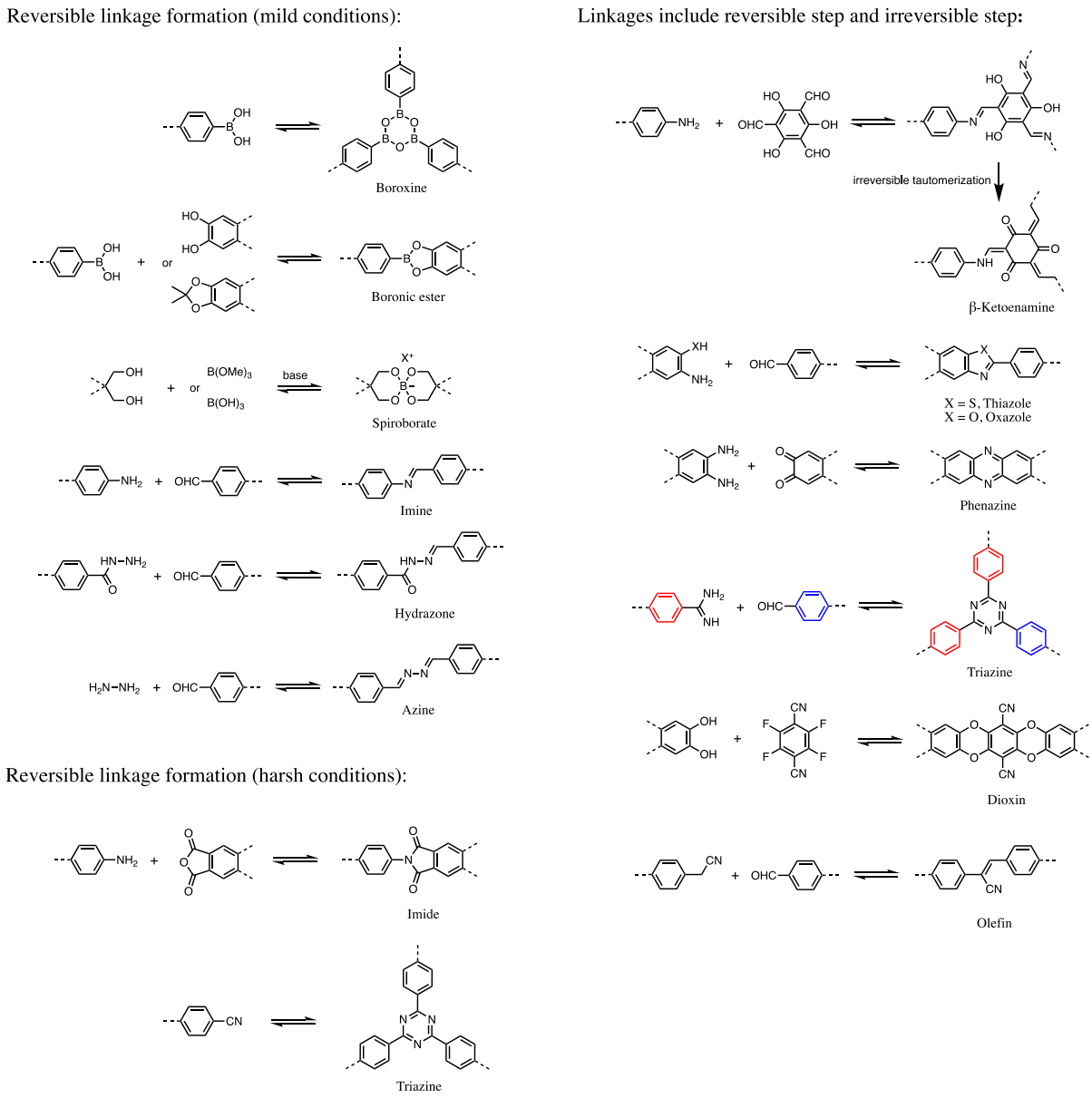

Figure 1.2. Widely used condensation reactions for the formation of COFs.

1.2.2 COFs synthesised by reversible condensation reactions – under harsh conditions

Stability improvement of COFs can be realized by synthesizing COFs with the help of reactions that are only reversible under harsher conditions, such as significantly higher reaction temperatures. Two typical examples of stable COFs prepared from harsh conditions include imide-linked COFs

and covalent triazine frameworks (CTFs) prepared from the trimerization of aromatic dicyanide units (**Figure 1.2**).

Polyimide (PI) polymers synthesized from imidization reactions are known for their high thermal and chemical stability. For example, a PI polymer can fully retain its porosity after soaking the as-synthesized samples in H_2O or in 0.1 M HCl for 24 h.[33] PI polymers shows excellent mechanical robustness, processability, and structural diversity and are used in a wide range of commercial applications.[34] However, early reports of these PI polymers were all amorphous and showed low BET surface area which limited their applications. Imide-based COFs were firstly reported by Fang *et al*. in 2014.[17] In this work, three polyimide-based COFs, namely PI-COF-1, PI-COF-2 and PI-COF-3 were synthesized from the co-condensation reactions between pyromellitic dianhydride and aromatic triamines under solvothermal conditions at 200 ~ 250 °C for 5 ~7 days, with 1-methyl-2-pyrrolidone (NMP) and mesitylene as solvents and isoquinoline as the catalyst. Among these three COFs, PI-COF-3 showed a very large pore size of 5.3 nm and a Brunauer-Emmett- Teller (BET) surface area of 2346 m^2 g^{-1}, which is much higher than the previously reported amorphous porous polyimide polymers.[33] All three PI-COFs exhibited very high thermal stability, with decomposition temperature above 530 °C. This work also emphasized that the solvents ratio (related to monomers solubility), suitable isoquinoline catalyst (related to reaction rate) and appropriate polymerization temperature (high temperature to promote the imide ring-closing reactions) all played a crucial role to realize reversibility of this imidization reaction. PI-COFs exhibited excellent chemical stability upon immersing samples in 0.5 M $KHCO_3$, 12 M HCl, NMP, THF, H_2O, ethanol and DMF at ambient temperature for 20 days, as can be evidenced by PXRD comparison of the treated samples with as-synthesized ones.[35] This good stability has allowed PI-COFs to be used in various applications including electrocatalytic CO_2 reduction[35] and energy storage.[36]

Crystalline covalent triazine frameworks (CTFs) were first reported by Kuhn *et al*. in 2008.[21] In this work, CTF-1 with moderate crystallinity was synthesized from the dynamic dicyanobenzene trimerization under ionothermal condition in molten $ZnCl_2$ at 400 ºC. One note that need to be mentioned is, dicyanobenzene is temperature-stable and starts to decompose at temperatures far above 400 °C. In this work, the author attributed the moderate crystallinity of CTF-1 to the $ZnCl_2$ which, as an ionic melt, does not perform as well as organic solvents but has beneficial strong Lewis acid–base interactions for the trimerization reaction, allowing the reaction to be sufficiently reversible under the reaction conditions applied. Drawbacks of CTFs synthesized from ionothermal conditions is 5 wt% $ZnCl_2$ residues left which was unable to be fully removed after extensively washed by diluted HCl (aq.) at ambient temperature for 15 h. Also, the authors observed that some

nitrile monomers were unable to withstand such harsh reaction conditions and partial carbonization of materials occured.[37] High purity CTFs were reported in 2012 from a room temperature microwave-assisted synthesis with trifluoromethanesulfonic acid as the catalyst. This method gave CTFs as free-flowing, fluorescent powders, though the crystallinity was not as high as CTFs prepared from ionothermal conditions, indicating higher reversibility of nitrile trimerization reactions at elevated temperatures.[38] Owning to their highly robust and fully conjugated structures, CTFs exhibited high thermal and chemical stability, which makes them appealing in various applications including energy storage,[39] photocatalysis[40] and heterogeneous catalysis.[41]

1.2.3 COFs synthesised by condensation reactions including both reversible and irreversible steps

Another strategy for obtaining COFs of high stability is to apply linkages which are formed from a combination of reversible and irreversible steps. Using this method, COFs were synthesised in moderate crystallinity and high stability under mild reaction conditions. Examples of such linkages include *β*-ketoenamine, thiazole, oxazole, phenazine, triazine (from polycondensation reactions), dioxin and sp^2 carbon-conjugated (**Figure 1.2**).

Two *β*-ketoenamine linked COFs, TpPa-1 and TpPa-2, were reported in 2012 by Kandambeth *et al*.[16] The formation of *β*-ketoenamine linkage includes the reversible enol-imine formation and the following irreversible enol-keto tautomerization step. The irreversible nature of the tautomerism does not affect the crystallinity of the COF since the transformation involves tautomerisation while keeping the atomic positions almost the same, while at the same time, improving the chemical stability of COF TpPa-1 and TpPa-2 due to the absence of imine bonds in the final framework. Both TpPa-1 and TpPa-2 showed excellent stability in 9 M HCl, 9 M NaOH and in boiling water, upon immersion in these solutions for 7 days, evidenced by PXRD, FT-IR and BET surface area comparison before and after treatment. Owing to the highly crystalline and stable COFs based on *β*-ketoenamine linkage, these COFs have been widely used in various applications including energy storage[42,43] and photocatalysis.[44]

COFs with thiazole and oxazole linkages could be prepared either through one-pot multicomponent synthesis[45] or through post-synthetic modifications.[46] In both cases, the reversible imine formation and cyclization ensure the framework crystallinity, while the irreversible oxidative step strengthens linkage chemical stability. For example, the thiazole-linked COFs exhibited excellent chemical stability in boiling water, strong acid (12.5 M HCl), strong bases (12 M KOH and 1 M CH_3ONa) and reducing agents (1 M $NaBH_4$) for 2 days at ambient temperature.[45] Similarly, the preparation

of phenazine-linked COFs includes two consecutive imine condensations, where the second step is irreversible due to the stabilization of the product by aromaticity. The phenazine-linked CS-COF showed good stability in 1 M HCl and 1 M NaOH for 1 day at ambient temperature and the delocalized π-clouds in CS-COF make it potential for electronics-related applications.[47] Based on the developments of CTFs, they can now be prepared from the co-polymerization between aldehydes and amidines under relatively mild conditions (120 °C, no strong acids) which involve reversible Schiff-base formation followed by an irreversible Michael addition. CTFs synthesized from this method are high stability and have good crystallinity, simultaneously.[48,49]

Dioxin-linked COFs were first reported by Zhang *et al*. in 2018.[22] The formation of this dioxin linkage includes a reversible nucleophilic attack step and an irreversible ring-closure step. Dioxin-linked COFs showed excellent chemical stability under harsh environments including 12 M HCl, 40 wt% HF, 18 M H_2SO_4, 14 M NaOH, 5 M CH_3ONa in MeOH, 0.1 M $K_2Cr_2O_7$ in concentrated H_2SO_4 and 2.4 M $LiAlH_4$ in THF and various types of organic solvents. This is to date, the most stable COFs ever reported.[50] Olefin-linked COFs prepared from Knoevenagel polycondensation were reported in 2016 and 2017.[24,51] Knoevenagel co-condensation includes reversible methylene deprotonation step and the following irreversible C-C bond formation and dehydration step. These olefin-linked COFs showed good chemical stability and have been used for photocatalytic CO_2 reductions.[52]

1.3 Introduction to RCSR and topology

Metal-organic frameworks (MOFs) have emerged as an extensive class of crystalline materials with ultrahigh porosity (up to 90 % free volume) and enormous internal surface areas, extending beyond 6000 m^2 g^{-1}.[53] Although early study of metal organic coordination framework structures dates back to 1959,[54] it was the report of MOF-5, in 1999, and the subsequent highly systematic study of MOFs by Yaghi and co-workers that have opened a new era of crystalline porous frameworks.[55] These two decades have witnessed explosive growth and advances in this field. MOFs have now been used in various applications including gas sorption and separation, catalysis and sensors.[56,57,58]

New MOF structures can be realized from either connecting metal clusters (also called, secondary building units) and organic linkers of new geometries or from isoreticular expansion by simply replacing the linker with new linkers of the same geometry but different lengths and functionalities. With this expansion method, MOFs can be obtained with new chemical composition, functionality, and pore sizes but with the same underlying framework structure (topology). A typical example of such isoreticular structure expansion is the successful preparation of several MOF-5 derivatives in 2002.[55] The accessibility of various inorganic metal clusters and organic linkers together with the expansion strategy have propagated the explosive growth of a number of new MOF structures.

Based on these studies, an increasing need then arose for a universal system of nomenclature, classification, identification, and retrieval of these topological structures. Yaghi and co-workers then developed a system of symbols for the identification of three periodic nets of interest, and this system is now in wide use - the Reticular Chemistry Structure Resource (RCSR) database of symbols for crystal nets (**Figure 1.3**).[59] At the time of writing, this database includes information on 2940 3D topologies, which contains searchable topology symbols, keywords, and attributes. RCSR also contains systematic nomenclature and structure information for 0-dimensional (0D) polyhedrons and 2D layered structures. Since my PhD project is concerned with the design and synthesis of 3D COFs, here I will introduce this resource with 3D nets as an example.

Figure 1.3. Home page of RCSR.[59] (http://rcsr.anu.edu.au;)

1.3.1 Nomenclature of topology

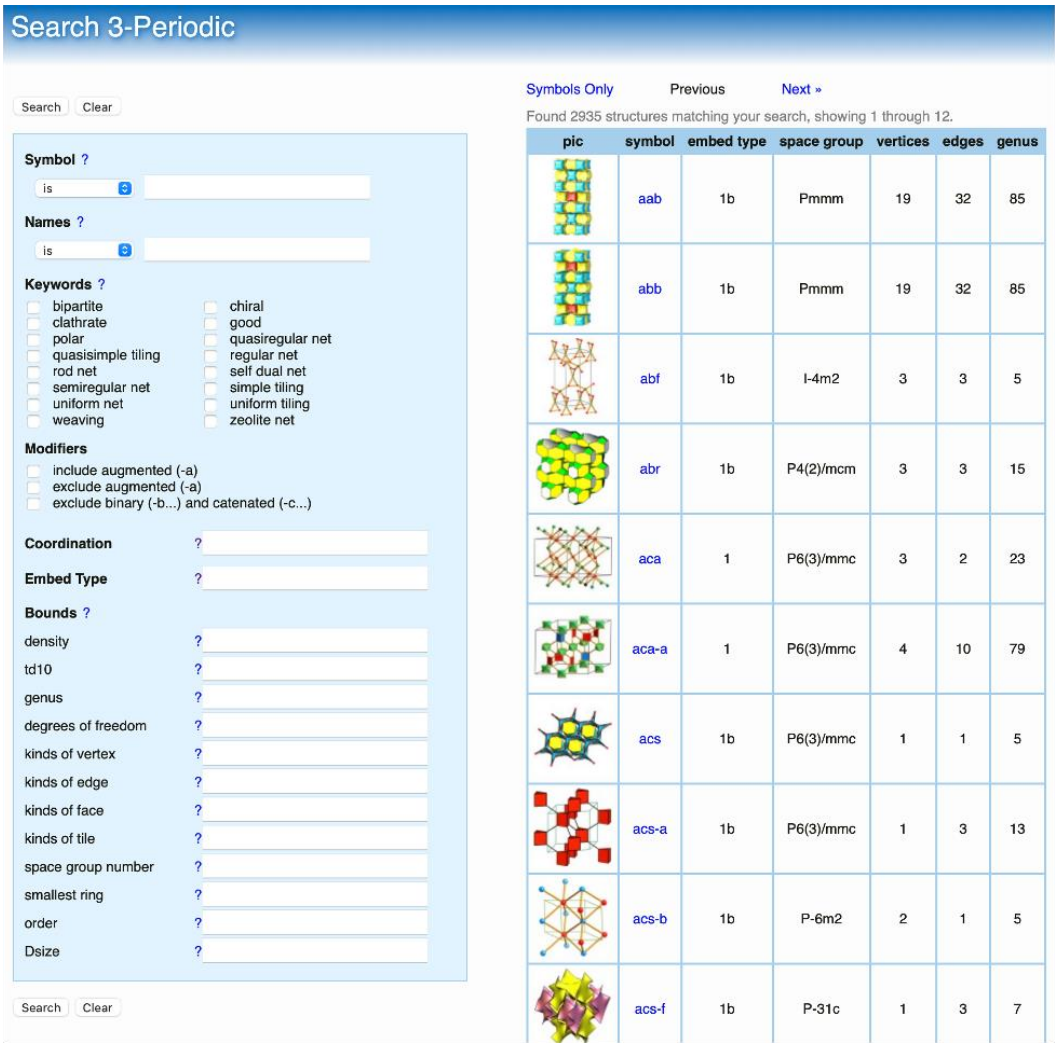

pic	symbol	embed type	space group	vertices	edges	genus
	aab	1b	Pmmm	19	32	85
	abb	1b	Pmmm	19	32	85
	abf	1b	I-4m2	3	3	5
	abr	1b	P4(2)/mcm	3	3	15
	aca	1	P6(3)/mmc	3	2	23
	aca-a	1	P6(3)/mmc	4	10	79
	acs	1b	P6(3)/mmc	1	1	5
	acs-a	1b	P6(3)/mmc	1	3	13
	acs-b	1b	P-6m2	2	1	5
	acs-f	1b	P-31c	1	3	7

Figure 1.4. One representative page of 3D-periodic nets represented by three-letter symbols in RCSR.[59] (http://rcsr.anu.edu.au)

In RCSR, each unique 3D-periodic structure is represented by a periodic net graph and named by a three-letter symbol to describe the underlying topology of the structure (**Figure 1.4**). The occurrence of these topology symbols includes the abbreviation of the corresponding zeolite framework type, like **sod**, which is an important four-connected net in crystal chemistry; or abbreviated from other corresponding inorganic crystal structures, like **dia** from diamond crystals, **qtz** from quartz crystals, *etc*.[59]

Some topologies in RCSR are derived from simple nets, like the augmented nets, which are denoted with a suffix of "**-a**". For example, **acs-a** is derived by replacing each vertex in **acs** topology with its corresponding polyhedrons, which in this case, is a trigonal prism. Augmented nets are commonly used for drawing periodic graphs to facilitate framework structure visualization since it

shows the geometry of building blocks that constructed the frameworks. Besides, it is very helpful in guiding researchers to targeted design and synthesis of frameworks with certain topologies. Another type of important derived net is denoted with the suffix "**-cn**", where "**c**" means catenation, "**n**" means there are n separate interpenetrating nets. Usually, "**-c2**" can be abbreviated as "**-c**" to represent 2-fold interpenetration of the original nets, while "**-cn**" (n > 2) corresponds to the n-fold interpenetration of the original nets. As for the meaning of other suffixes including "**-b**", "**-e**" and "**-x**", can refer to the reference cited here.[59]

1.3.2 Information included in RCSR for each topology

dia

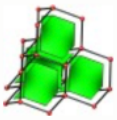

RCSR reference: http://rcsr.net/nets/dia

names: diamond, sqc6, 4/6/c1
key words: regular net, uniform net, self dual net, quasisimple tiling, good
references: Acta Cryst. A59, 22-27 (2003), Acta Cryst. A60, 517-520 (2004)

embed type	space group	volume	density	genus	td10	deg freedom
1a	Fd-3m	12.3168	0.6495	3	981	1

a	b	c	alpha	beta	gamma
2.3094	2.3094	2.3094	90.0	90.0	90.0

vertices: 1

vertex	cn	x	y	z	symbolic	Wyckoff	symmetry	order
V1	4	0.1250	0.1250	0.1250	1/8, 1/8, 1/8	8 a	-43m	24

vertex	cs_1	cs_2	cs_3	cs_4	cs_5	cs_6	cs_7	cs_8	cs_9	cs_{10}	cum_{10}	vertex symbol
V1	4	12	24	42	64	92	124	162	204	252	981	6(2).6(2).6(2).6(2).6(2).6(2)

edges: 1

edge	x	y	z	symbolic	Wyckoff	symmetry
E1	0.0000	0.0000	0.0000	0, 0, 0	16 c	-3m

tiling:

tiling	dual	vertices	edges	faces	tiles	D-symbol
[6^4]	dia	1	1	1	1	2

Find occurrences...

Figure 1.5. Information included of the **dia** topology page from the RCSR database.[59] (http://rcsr.anu.edu.au)

Here, the common **dia** topology was used for a brief introduction of the information that RCSR includes for each net. As is shown in **Figure 1.5**, firstly, there is a periodic graph representing the structure of the topology (easier structure visualization is available at https://www.mofplus.org).[60] The name of the topology and the corresponding reference are listed. Below in the table are the crystal structure information of the topology in its highest symmetry embedding (or called maximum-symmetry embedding),[61,62,59] including the space group, density, volume, and lattice parameters of the crystal. Atomic coordinates and symmetry information of the vertex and edge are provided also. Combining the numbers of kinds of vertex (*p*), edge (*q*), face (*r*), and tile (*s*) gives the transitivity [*pqrs*], which measures the "regularity" of the topology. Topologies with transitivity [1111] and with a regular polyhedron vertex are called regular nets, there are in total five regular 3D nets in RCSR, including **srs**, **nbo**, **dia**, **pcu** and **bcu**.[61] The "find occurrence…" link at the bottom of the page will lead you to the Cambridge Structural Database (CSD) (http://www.cdc.cam.ac.uk/) if the occurrence of the topology is a known material.

The term topology has been widely used for the description of infinite, extended crystalline solid-state materials like MOFs, ZIFs and COFs. The introduction of this concept of topology allows us to simplify structures by only considering the connections between constituents rather than their chemical nature, thus significantly reducing the complexity of a given structure description. One most prominent achievement of applying this descriptor is that it allows reverse design or targeted synthesis of certain framework structures, which transferred this "trivial synthesis" field into a more "rational designed" era.[14] This rational design from molecular building blocks into periodic frameworks lead to the emergence of a discipline called reticular chemistry.[59]

1.4 Reticular synthesis of COFs

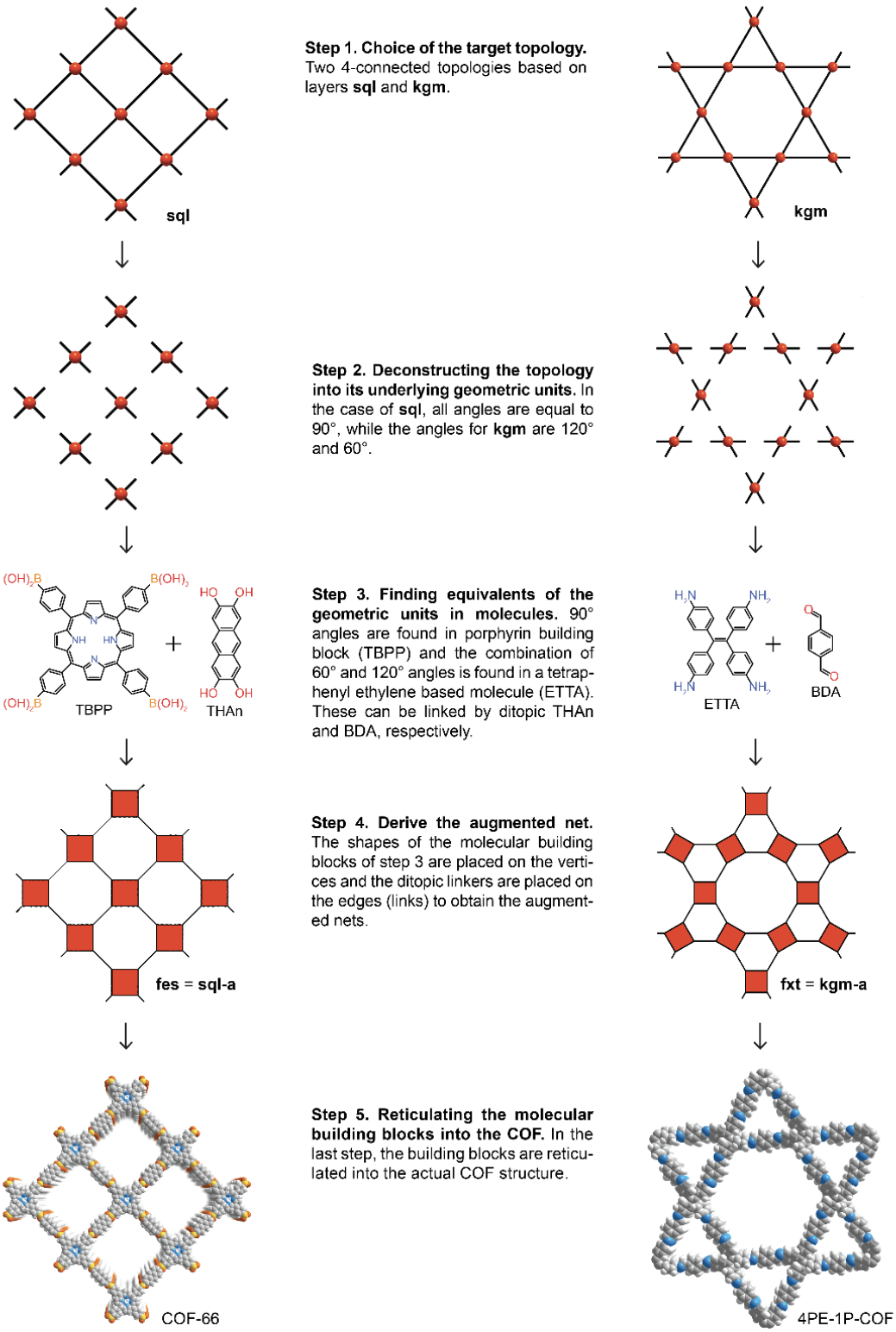

Figure 1.6. General approach for the reticular synthesis of COFs. color code: H, white; B, orange; C, gray; O, red.[14]

MOFs and COFs can be designed in a bottom-up manner from molecular building blocks applying reticular chemistry principles. Reticular chemistry allows us to target COFs of a specific topology. General approach for the reticular synthesis of COFs includes five steps (**Figure 1.6**): (1) Choose the topology want to target; (2) Deconstruct the topology into its underlying geometric units; (3) Find organic building units that have the same geometry and symmetry as the geometric units deconstructed from the last step, sometimes an organic linear linker is necessary depending on the linkage selected; (4) Derive the corresponding augmented net; (5) Reticulate the organic building blocks into COFs under certain reaction conditions. This reticular synthesis (or reticular chemistry) principle applies to both 2D and 3D COF cases.[14]

One typical example of reticular chemistry-guided COF design is the successful preparation of 2D imine COF-346, where a complex multinary **tth** topology (2 edges) was realized by precisely selecting building blocks that meet the essential geometry and metric requirements for **tth** topology.[63] As is shown in **Figure 1.7**, following the reticular chemistry principle, upon deconstructing the 2D **tth** topology we can see it is composed of three vertices with 3, 4 and 6 connection sites, abbreviated as 3-c node, 4-c node and 6-c node, respectively. The next step is to choose organic building blocks that satisfy the geometric requirements of the three vertices. Following the interior angle of polygon rule (interior angles is $(n - 2) \times 180°$, n = number of sides) together with considering the symmetry of each vertex, angles between each functional group in the 3-c node should be 120°; for the 6-c node, this angle is 60°; the 4-c node should have two different angles of 60° and 120°, respectively (**Figure 1.8**). Based on this, the author chose trigonal 1,3,5-tris(p-formylphenyl)benzene as the 3-c node, hexagonal hexaminophenyl benzene as the 6-c node and tetragonal tetrakis(4-aminophenyl) ethane as the 4-c node, all these building units well satisfies the geometric requirements for **tth** topology. Eventually, upon joining these building units together through dynamic imine bonds, a complex multinary 2D COF-346 with underlying **tth** topology was successfully synthesized by following the reticular chemistry principle.

One thing needs to be noted here is that for complex topological systems which have more than one node (with connection site > = 3), the organic building blocks selected need to satisfy not only the geometry requirement (symmetry and angles), but also need to make sure their size (or length) can also fit the geometric requirements of the topology. For example, in this example of COF-346 (**Figure 1.8**), while 1,3,6,8-tetrakis(4-aminophenyl)-pyrene can satisfy the angle requirement as tetrakis(4-aminophenyl) ethane, its length (size) does not allow to form a closed quadrilateral ring with the other two nodes selected, thus it is not suitable to be selected as the 4-c node in this case.

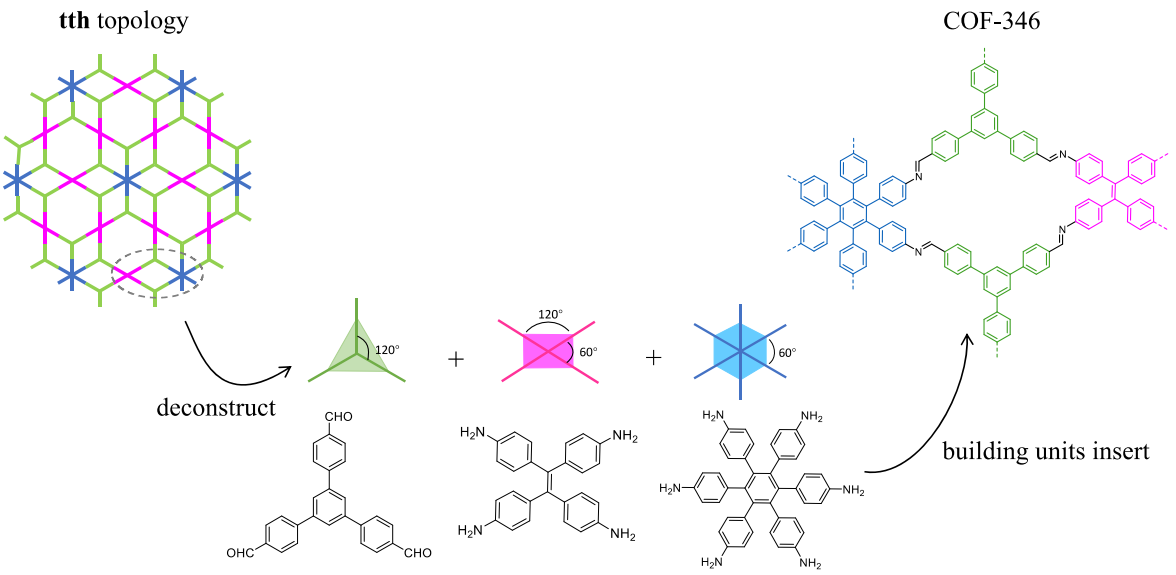

Figure 1.7. A typical example of successful COF preparation following the reticular chemistry principle - a multinary COF-**346** with **tth** topology.[63]

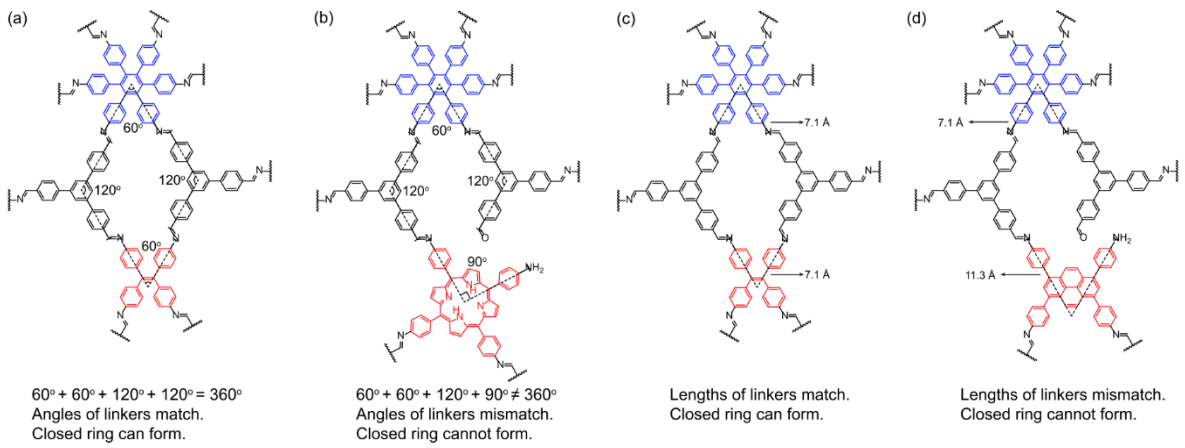

Figure 1.8. (a, b) Sum of the angles of linkers are required to be 360° to form a strain-free closed-ring quadrilateral structure. (c, d) Hexatopic and tetratopic linkers are required to have the same length to form a strain-free closed-ring quadrilateral structure.[63]

This reticular chemistry principle applies to both 2D and 3D COFs cases. In the following text, I will give a brief introduction to the 3D COF structures reported to illustrate the important role that reticular chemistry plays in guiding the design and synthesis of 3D COFs. To clarify, I will call all the organic building blocks with more than 2 connection sites as nodes and building blocks with 2 connection sites as linkers. The term ‘topology’ is of the same meaning as ‘net’.

1.4.1 3D COF structures reported

There are two general approaches to construct 3D COFs. One is from polyhedral type multi-linking nodes. The other one is from all planar building units but with the connectivity or alignment between them finely controlled.

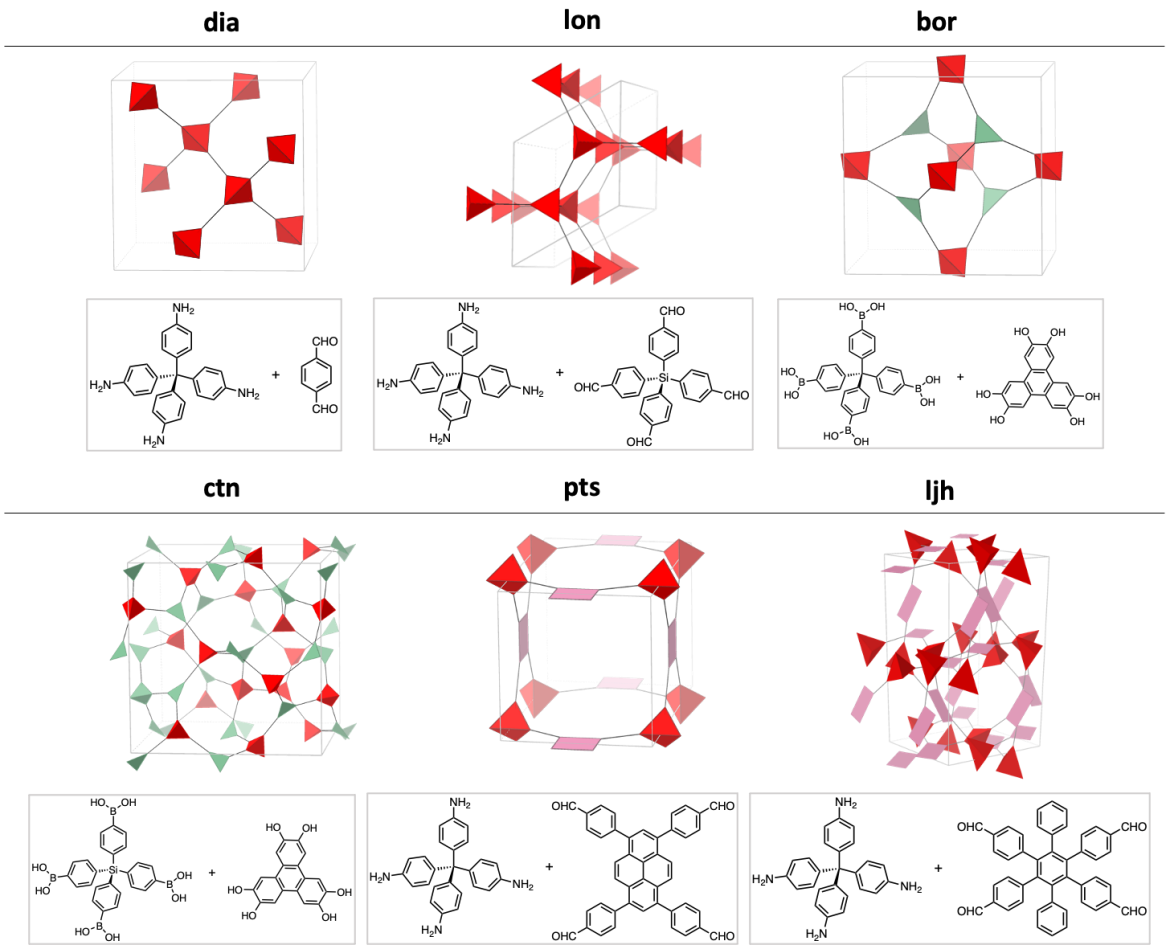

Figure 1.9. COFs structures reported that were built from tetrahedra nodes. All topologies are shown as their corresponding augmented net. The gray lines indicate the unit cells.

Currently, most of the 3D COFs structures reported are based on the first method. For example, COFs of **dia**,[15] **lon**,[64] **bor**,[65] **ctn**,[65] **pts**[66] and **ljh**[67] were all built from organic building blocks of tetrahedra geometry. Organic building blocks of tetrahedra geometry includes: tetraphenylmethane, tetraphenylsilane, adamantane,[68] spirobifluorene,[69] copper(I)-bisphenanthroline core,[70] 3,3',5,5'-tetraphenyl-bimesitylene[71] and their derivatives. As is shown in **Figure 1.9**, COFs of **dia** topology were constructed from tetrahedra building units and a linear linker, while COFs of **lon** topology (LZU-111) were formed by co-condensation reaction between methane-based tetraamine and silane-based tetraaldehyde. Theoretically, these two topologies are hard to distinguish by PXRD,

in fact, here, the crystal structure of LZU-111 was solved by single crystal X-ray diffraction (SCXRD).[64] COFs of **bor** or **ctn** topology were prepared from building blocks of tetrahedral and triangle geometry, COFs with these two topologies can be distinguished from PXRD. Reactions between organic tetrahedral nodes and rectangular nodes gave 3D COFs of **pts** topology. The 3D-TPB-COF-Ph, which was also synthesized from tetrahedral and rectangular nodes showed an unprecedented self-penetrated **ljh** topology, which the COF structure was solved with the help of the continuous rotation electron diffraction (cRED) technique.[67]

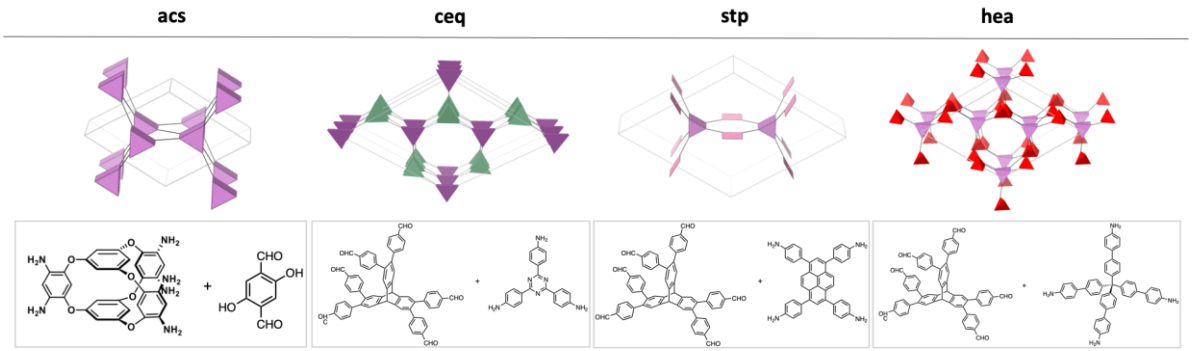

Figure 1.10. COFs structures reported that were built from nodes with trigonal prism geometry. All topologies are shown as their corresponding augmented net. The gray lines indicate the unit cells.

COFs with **acs**,[72] **ceq**,[73] **stp**[74] and **hea**[75] topologies were constructed from building blocks with trigonal prism geometry (**Figure 1.10**). Trigonal prism-shaped organic building blocks are mostly triptycene and its derivatives. For example, COFs of **ceq**,[73] **stp**[74] and **hea**[75] topologies are all built from the condensation reactions between triptycene molecules with organic building blocks with triangle, rectangular and tetrahedral geometry, respectively. One breakthrough study is, that for the synthesis of COFs with **acs** topology, high-connectivity organic cage molecules were introduced as the building blocks for the construction of 3D COFs for the first time, and the resulting frameworks exhibited dynamic behaviours toward the adsorb/removal of DMF molecules. This work demonstrated a new potential approach for expanding the structure complexity of 3D COFs by applying multi-linking organic cage molecules as the building blocks.[72]

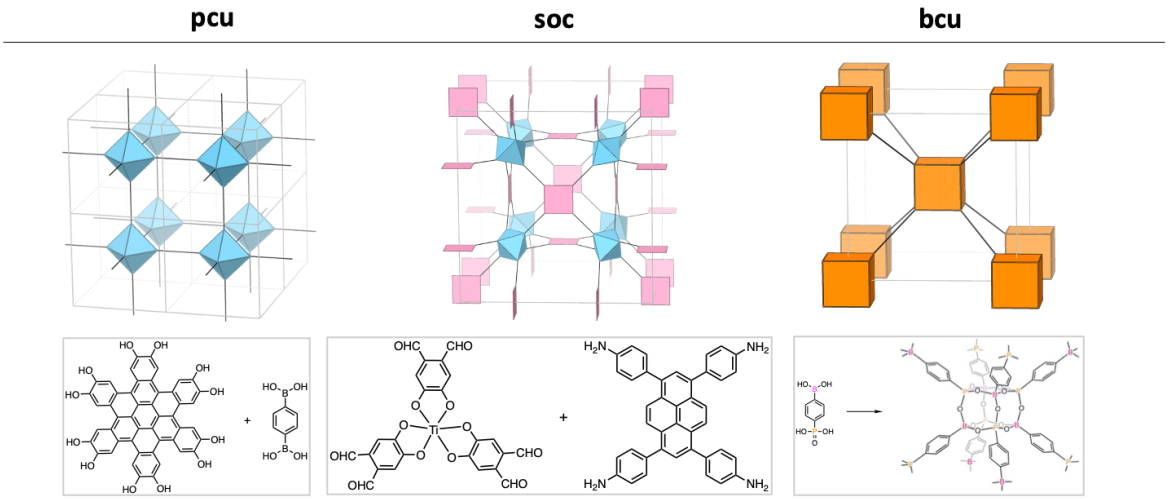

Figure 1.11. COFs structures reported that were built from nodes with octahedra or cubic geometry. All topologies are shown as their corresponding augmented net. The grey lines indicate the unit cells.

COFs with **pcu**[76] and **soc**[77] topologies were constructed from the condensation reactions between the octahedral-shaped organic molecules and a linear linker or a rectangular organic unit, respectively (**Figure 1.11**). In the example of **pcu** topology, 2,3,6,7,10,11,14,15,18,19,22,23-dodecahydroxy-cata-hexaben-zocoronene plays the role of the octahedral building block, this polycyclic aromatic hydrocarbon monomer distorted with a triangular antiprismatic (D_{3d}) structure, which comes from the steric congestion between hydrogens on the peripheral rings and eventually leads to the catechol residues on the outer rim above and below the coronene plane.[76] COFs of **soc** topology were constructed from an anionic 6-c octahedral Ti^{IV} complex $Na_2Ti(2,3\text{-DHTA})_3$, the obtained Ti-COF-1 presents high charge mobility and had been studied as a promising catalyst for Meerwein addition reactions.[77] COFs of **bcu** topology was constructed from cubic building blocks.[78] In this case reported in 2020, a cubane-like borophosphonate cubic node was formed in-situ by applying simple linear BPA linkers, which self-condensed into cubic motifs during the reactions (**Figure 1.11**). The versatility of this chemistry was further exploited by cleaving the cubes in the polycubane COFs, leading to structures with rod units of infinite valency. The feasibility and efficiency of this in-situ polyhedral node formation is inspiring and this is a promising method to enhance the COFs structure complexity in future.

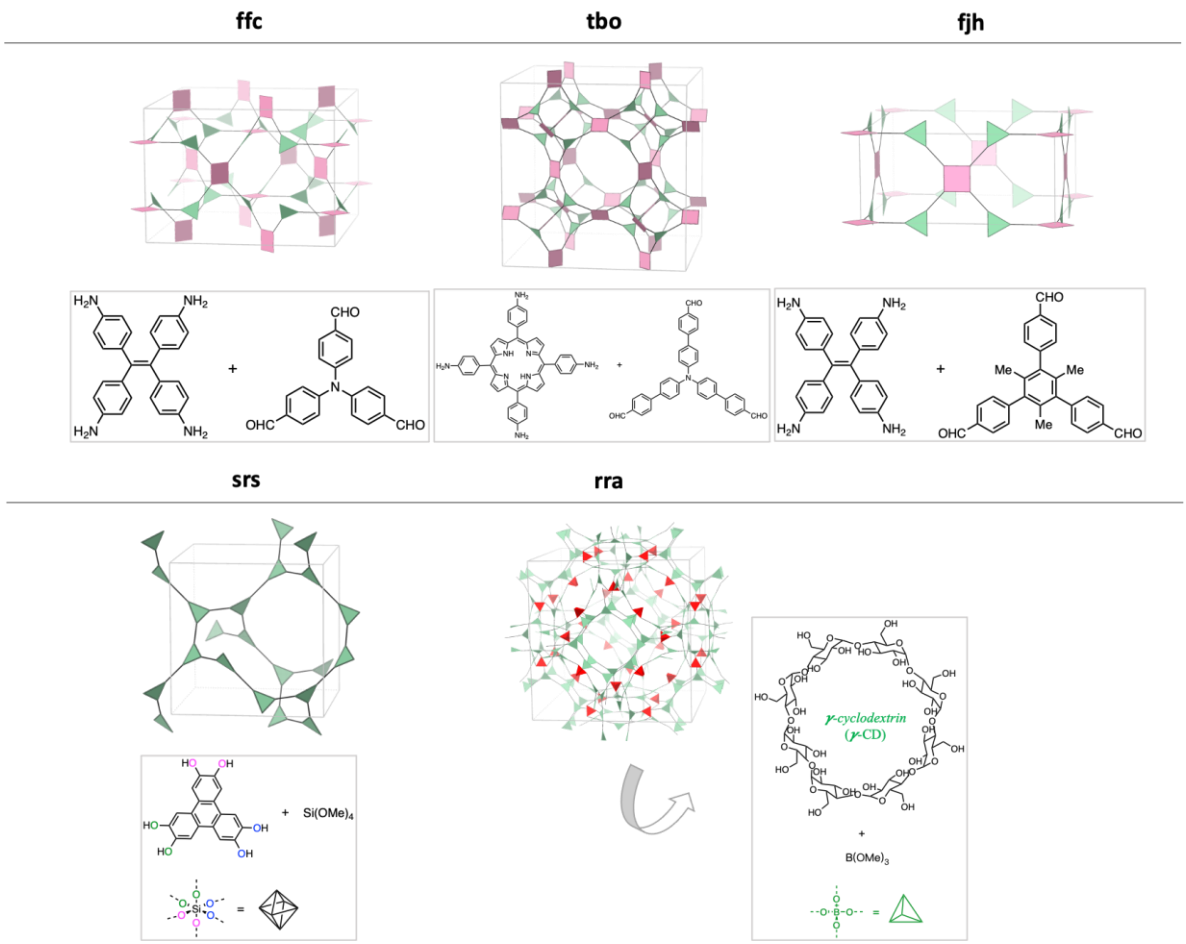

Figure 1.12. COFs structures reported that were built from all planar building blocks. All topologies are shown as their corresponding augmented net. The grey lines indicate the unit cells.

Another method to construct 3D COFs is to reticulate planar (or near planar) organic building blocks into 3D spatial arrangements by controlling the connectivity and alignment among them. For example, 3D COFs of **ffc**,[2] **tbo**[79] and **fjh**[80] all apply this strategy and these three topologies all constructed from the condensation reactions between a 4-c rectangular and a triangle organic unit (**Figure 1.12**). The difference between these three topologies is the spatial arrangements of the 4-c and 3-c organic nodes, which in all these three cases, were decided by the rotation of imine bonds. This rotatable imine bonds also account for the 3D frameworks structures formation in these examples. One drawback of accessing 3D COFs depending on the rotatable imine bonds to reticulate planar nodes into 3D spatial arrangement is its unpredictability, which makes this method not ideal for targeting COFs of specific topologies. While in the case of the 3D COFs with **srs**[81] and **rra**[26] topologies, rigid polyhedral-shaped linkages, which were formed from the hybridization of atoms, were used for reticulating planar (or near planar) organic building units into 3D spatial arrangement. The 3D anionic silicate SiCOF-5 of **srs** (**srs**-c) topology was synthesized by reticulating dianionic hexacoordinate $[SiO_6]^{2-}$ nodes with triangular triphenylene building blocks.

In this example, the author demonstrated that the gradual generation of the silicon source during the course of the reaction is the key factor in controlling the nucleation and growth rate of SiCOF-5.[81] COF of 3D **rra** topology was constructed by reticulating γ-cyclodextrin unit into 3D arrangement through a tetrahedra-shaped spiroborate linkage, which was formed from the sp^3 hybridization of boron.[26]

In summary, two general methods are available for constructing 3D COFs, one is from polyhedral organic nodes, the other is from all planar building blocks by tuning the connectivity. In the first case, the polyhedral can come from the intrinsic geometry of organic molecules that are induced either by the hybridization state of the atom, or from the influence of steric hindrance. Or organic polyhedral molecules can be inserted either through prior design (like organic cages) or by in-situ formation. The advantage of this method is the rigid polyhedral building blocks and the very limited flexibility of the linear linkers greatly convenient the targeted COF preparation. This will simplify structural characterisation, as COF structure determination still heavily relies on PXRD comparisons between experimental and simulated patterns. The disadvantage of this method is the synthetic complexity of these polyhedral building blocks is still challenging. For the latter method, the advantage is clear - the readily available planar building units greatly shorten the precursors' preparation procedure, while the disadvantage of this method mostly come from the unpredictability of the building block arrangement during reactions, unless adopting rigid linkages.

Besides, the reticular chemistry principle not only serving to help targeting COFs of certain specific topology, but also provides us with a way to predict possible frameworks achieved for certain building block pairs.

1.4.2 Topological preference – general rules

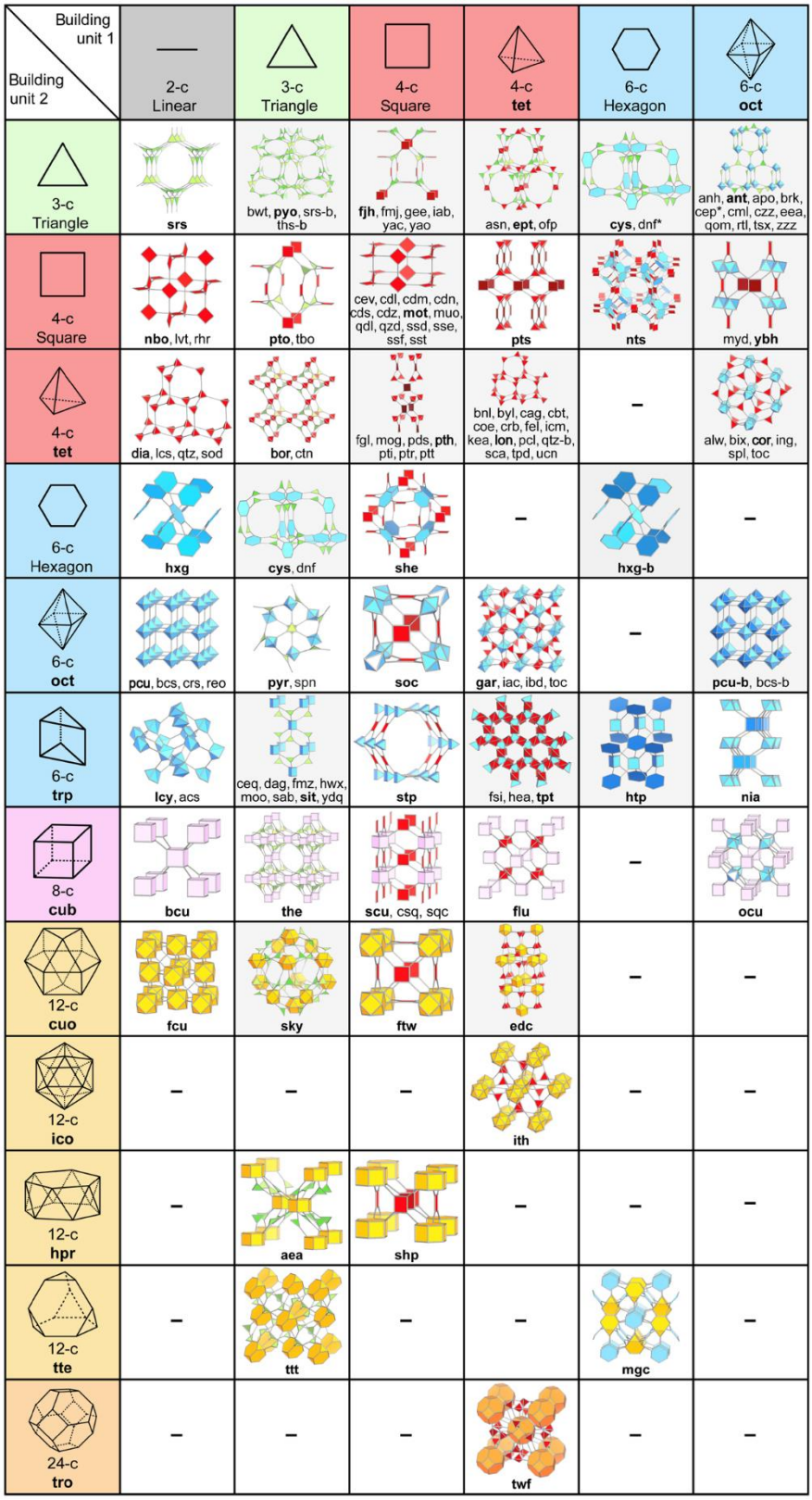

Figure 1.13. The reticular table. A table of possible bipartite nets representing binary frameworks made by reticular chemistry. All topologies are shown as their corresponding augmented net.[10]

Although the proposal of the reticular chemistry principle did turn serendipitous novel framework structure discovery into a more rational design era, uncertainty still exists. Theoretically, either in MOFs or COFs realm, the same building block pairs can possibly be reticulated into frameworks of different underlying topologies, and this situation can be more commonly encountered in 3D cases. **Figure 1.13** shows a reticular table listing some possible uninodal or binodal topologies for building block pairs with specific geometries.[10] In these cases, benefitting from numerous MOF structures reported and researchers' intensive investigation of these structures, several general rules have been proposed to help decide which topology is more likely to form.

The first rule is the minimal edge-transitive principle. According to this rule, for certain building blocks pairs, the edge-transitive nets (also referred as 'default' nets, No. edge = 1, this information is available in RCSR for each net, as is shown in **Figure 1.5**) are most likely to form. One typical example to illustrate this rule is the five regular nets with the transitivity of [1111], including **srs**, **nbo**, **dia**, **pcu** and **bcu**, which are reported to have the highest possibility to form when building blocks of suitable corresponding geometry are chosen. Despite the existence of an almost infinite number of possible nets, investigation on a large number of MOF structures revealed that only a handful of topologies are frequently observed in the MOF crystals. The five regular nets occurred with the highest frequency followed by edge-transitive nets and those with minimum edges.[82] Based on this rule, the minimal edge-transitive nets (with one or two kinds of edge) can be regarded as the most ideal blueprints for the rational design and construction of COFs,[83] as can be supported by the 3D COFs structures reported until now, summarized in **Table 1.1**. All the default nets for corresponding building block pairs are marked in bold in **Figure 1.13** for clarification.

The other frequently applied rule for topological preference ranking is topology density (topology density = $N_{\text{vertice per unit cell}}$/ $V_{\text{unit cell}}$). Dense materials are more favoured to form when two nets have the same transitivity or the same number of edges.[10] One example to illustrate this rule is the **bor** and **ctn** topology. Frameworks of **bor** and **ctn** topology are all constructed from a combination of tetrahedral and trigonal building units and these two nets are all edge-transitive, so we cannot decide the more favoured structure from the last rule, but, since **ctn** (density = 0.5513) topology have higher topology density than **bor** (density = 0.4763), a theoretical study had revealed that COFs of **ctn** topology exhibited higher stability compared to COFs of **bor** topology.[84] However, for real studies, these two structures should all be considered for a more accurate result, this also applies to the first rule discussed above.

Table 1.1. The table summarized some crystal information of all the reported 3D COFs structures.

3D COFs reported	topology underlying	No. edge	transitivity [*pqrs*]	maximum symmetry embedding	topological density
COF-300	**dia**	1	[1111]	Fd-3m (No. 227)	0.6495
LZU-111	**lon**	2	[1222]	P6(3)/mmc (No. 194)	0.6494
COF-108	**bor**	1	[2122]	P-43m (No. 215)	0.4763
COF-102	**ctn**	1	[2112]	I-43d (No. 220)	0.5513
3D-(Cu)Por-COF	**pts**	1	[2132]	P4(2)/mmc (No. 131)	0.6495
3D-TPB-COF-Ph	**ljh**	-	-	-	-
CD-COFs	**rra**	3	[3344]	Im-3m (No. 229)	0.3247
3D-CageCOF-1	**acs**	1	[1122]	P6(3)/mmc (No. 194)	1.0000
3D-ceq-COF	**ceq**	2	[32--]	P-62m (No. 189)	0.7277
JUC-564	**stp**	1	[2133]	P6/mmm (No. 191)	0.6250
3D-hea-COFs	**hea**	2	[2233]	R32 (No. 155)	0.8089
Marta-COF-3	**pcu**	1	[1111]	Pm-3m (No. 221)	1.0000
Ti-COF-1	**soc**	1	[2122]	Im-3m (No. 229)	0.8839
BP-COFs	**bcu**	1	[1111]	Im-3m (No. 229)	1.2990
SiCOF-5	**srs**	1	[1111]	I4(1)32 (No. 214)	0.3536
3D-ETTA-TFPA	**ffc**	2	[32--]	P4/mmm (No. 123)	0.4226
(**tbo**-) COF-1 (2)	**tbo**	1	[2123]	Fm-3m (No. 225)	0.4763
COF-790	**fjh**	2	[3243]	I4/mcm (No. 140)	0.6187

One point to note is that the above-mentioned reticular principle shows higher accuracy only when the following prerequisites are satisfied since the key idea of this reticular chemistry principle is to insert building blocks with prefabricated geometries into the framework: 1. the geometry of the polyhedral node can be remained during the reaction, for targeting certain topology, building units with minimal flexibility are better choices. 2. All the precursors are chemically stable and will not transform into other structures during reactions.

The principle of the reticular table in **Figure 1.13** plays a pivotal role in helping us solving COF structures with a combined use of computational structure modelling. However, this principle has its limitations. For example, firstly, as rigid building units are better candidates for targeting certain topologies, if we limit our choices to these rigid building units, we might miss some interesting

phenomena like dynamic behaviours in COFs.[72] Another point is that the reticular synthesis of COFs limits structures to already known topologies. Sometimes, COFs with novel unprecedented topologies can be realised and, in this case, the structure cannot be solved by the general strategy of a combination of the reticular chemistry principle and structure modelling. Other direct characterization techniques such as single crystal X-ray diffraction (SCXRD) and three-dimensional electron diffraction (3DED), should be considered.

1.5 COF structure determination technique

1.5.1 Single crystal X-ray diffraction

Unlike its MOFs counterpart, where the growth of single crystalline frameworks occurs during the solvothermal synthesis procedure, the first report of single crystalline covalent organic networks was in 2013,[85] six years after the report of the first COF structures.[1] In this work, large single crystals (with sizes between 50 ~ 370 μm) of three covalent nitroso polymer networks NPN-1, NPN-2 and NPN-3 were realized from the reversible self-addition polymerizations of three monomers with tetrahedrally oriented nitroso groups. The structure of the three covalent organic networks was characterized by single crystal X-ray diffraction (SXRD). However, in this example, though the formed azodioxides linkage can be broken and reformed reversibly under relatively mild conditions, it is not a typical linkage that is widely applied in the COF field.

Ma *et al.* reported a breakthrough study in 2018,[64] whereby a general procedure for the growth single crystals of the most reported imine-based 3D COF was achieved. In this work, upon the addition of a mono-functional aniline modulator of different equivalents, single crystals of COF-300, COF-303, LZU-79 and a new COF LZU-111 were obtained with crystal sizes between 15 ~ 100 μm (**Figure 1.14-1.15**). Aniline serves as an inhibitor to nucleation, and thus alters the crystallization process. The high quality of these COF crystals allowed unambiguous solution of their crystal structures and uncovered some characteristics that were impossible to determine without single crystals. For example, crystal structure of COF-300 was solved and showed a seven-fold interpenetrated **dia** topology (**dia**-c7), rather than the former reported **dia**-c5 topology. Besides, single crystal structure of the newly prepared chiral COF LZU-111 was solved with an underlying topology of three-fold interpenetrated **lon** topology (**lon**-b-c3), which was rarely reported even in MOFs. Without the single crystal structure, the structure of LZU-111 could be easily attributed to **dia** topology and thus give us an inaccurate result if simply relying on powder XRD data. Following this work, Ma *et al.* later reported a single crystal structure of a non-interpenetrated 3D imine COF with **pts** topology following the same aniline modulating procedure.[86] During my PhD, a single crystal structure of a spiroborate-based, mechanically entwined helical covalent polymer was reported. Although not a COF, this is also an example of a single crystal structure of a polymer which was fully connected with covalent bonds.[87]

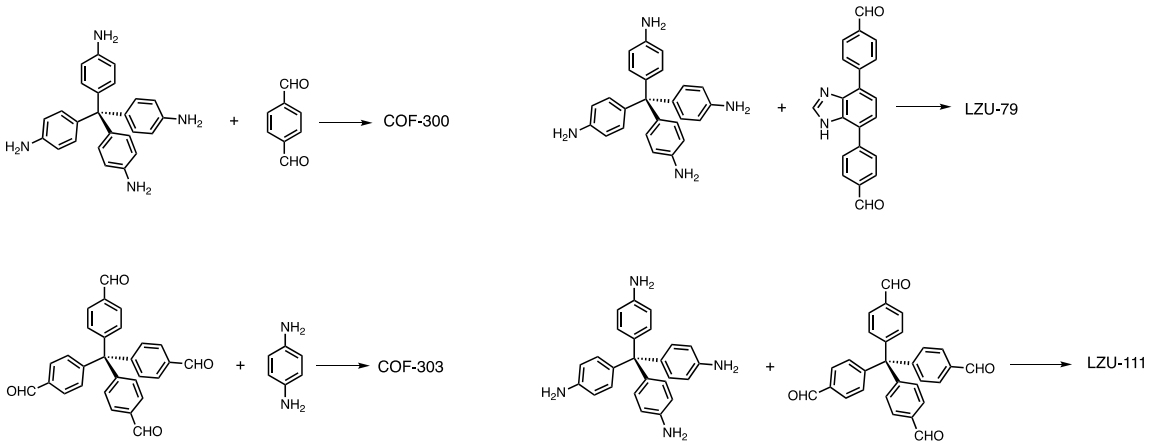

Figure 1.14. Reaction scheme for **COF-300**, **COF-303**, **LZU-79** and **LZU-111**.[64]

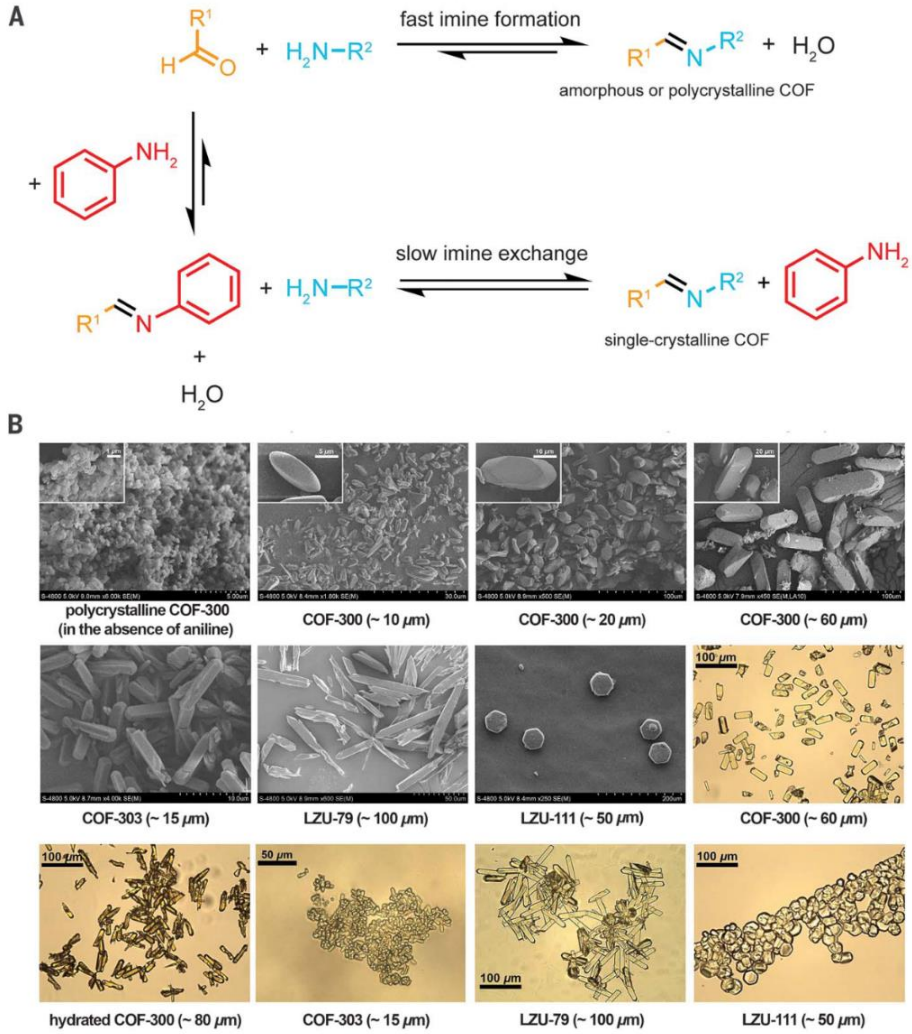

Figure 1.15. Crystal growth of large imine-based COFs modulated by aniline. (A) Imine bond formation mechanism with or without aniline modulator. (B) Scanning electron microscopy (SEM) and optical microscopy images of single-crystalline COFs. The SEM image of polycrystalline COF-300 without the addition of aniline is shown for comparison.[64]

One prominent advantage of SCXRD for structure determination is that it cannot only unambiguously decipher the structural features of COF crystals with atomic precision, but also helps to uncover a lot of characteristics that are impossible to determine precisely without a crystal, such as the degree of interpenetration, arrangement of guest molecules inside frameworks, linker disorder, and uncommon topology, *etc*.[87] Single-crystal X-ray diffraction (SXRD) remains the gold standard for accuracy in crystal structure determination.

1.5.2 Three-dimensional electron diffraction

While SCXRD remains the most widely used technique for crystal structure determination, the kinetics and thermodynamics involved in the synthesis of COFs are mostly unfavourable for growing sufficiently large crystals (> 5 μm) for SCXRD. Moreover, in some cases, even larger COF single crystals with sizes up to 50 μm were obtained, the low framework electron density induced by the light elements (C, H, N) constituted fully organic building blocks together with a non-interpenetrated framework structure will ultimately lead to poor diffraction quality and not enough to decide all the unit cell parameters and space groups of the crystals, let alone the accurate determination of atomic coordinates.[86] Alternatively, benefiting from the strong Coulomb interaction between electrons and matter, electrons generate diffraction patterns with much higher signal-to-noise ratios compared to X-rays, three-dimensional electron diffraction (3DED) thus allows the periodic porous framework structures determination of nano and submicron-sized crystals.[88]

Besides, recent breakthroughs in 3DED methods like continuous rotation electron diffraction (cRED) had greatly aided the wide spreading use of 3DED for the structure solution of inorganic-organic hybrids or fully organic nanocrystals, like MOFs,[89] COFs[67] and HOFs.[90] These materials are very prone to beam damage compared to inorganic crystals from conventional ED techniques, thus significantly limiting the data resolution and quality. While in cRED, the effective angular step in continuous rotation methods is determined by the detector exposure time and the goniometer rotation speed. Data acquisition can be performed at a high goniometer rotation speed to minimize the total electron dose applied to the crystal, and beam damage can therefore be minimized. The general procedure for structure analysis using 3DED is, tilting a crystal around the goniometer axis, acquiring a series of ED patterns, reconstructing the 3D reciprocal lattice, and extracting intensities of the observed reflections. The acquired 3DED data can then be used as SCXRD-like data for structural analysis.[88]

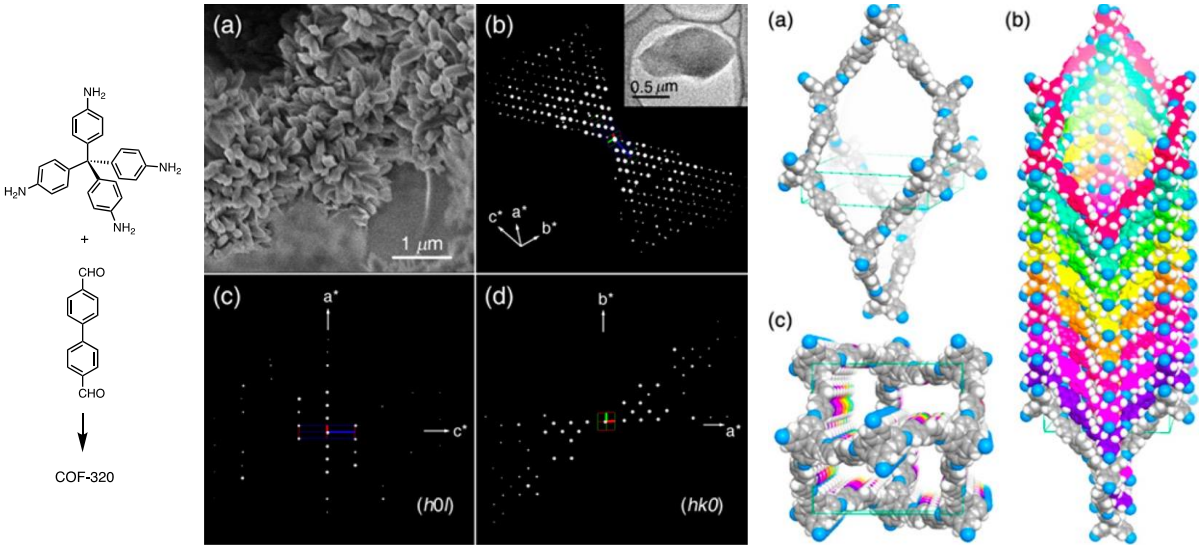

Figure 1.16. Single-crystal structure analysis of **COF-320** using the RED technique. Left: the reaction scheme of **COF-320**. Middle: Morphology and electron diffraction of **COF-320**. Right: Single-crystal structure of **COF-320** determined from RED data at 89 K.[91]

The first example of applying the 3D rotation electron diffraction (RED) method for COF structure determination was reported in 2013.[91] COF-320 was synthesized from the imine condensation between tetra-(4-anilyl)methane and 4,4′-biphenyldialdehyde in 1,4-dioxane at 120 °C. Scanning electron microscopy (SEM) imaging of the as-synthesized COF-320 (**Figure 1.16**) shows aggregated rice-shaped crystals with a maximum size < 1 μm. Single crystal COF-320 was prepared for TEM and 3D RED measurement by the ultrasonic oscillation of the as-synthesized sample in THF. 3D RED data of the COF-320 single crystals (**Figure 1.16**) were collected on a JEOL JEM2100 TEM by combing small beam tilt and large goniometer tilt steps using the RED−data collection software. RED data sets were collected at both 298 and 89 K. Diffraction patterns collected at 89 K were of higher quality compared to the data collected at 298 K possibly due to reduced beam damage of COFs under lower temperature, with 570 unique reflections with resolution up to 1.5 Å were obtained. The unit cell parameters (a = 30.17 Å, c = 7.28 Å, V = 6628 Å^3), space group of crystals (I4̄2d, No.122) and atom coordinates (expect hydrogen atom) were determined by the 3D RED data. The solved crystal structure of COF-320 showed a 9-fold interpenetrated **dia** topology. Lower quality diffraction patterns collected at 298 K only allowed to allocate the central carbon atom of the tetrahedral building blocks, with unit cell parameters (a = 27.93 Å, b = 31.31 Å, c = 7.89 Å, V = 6899 Å^3) and space group of COF-320 crystals (Imma, No.74). Eventually, based on the unit cell, space group, and atom coordinates determined from RED data collected at 298 K, a COF model was built using Materials Studio 5.0 software package, by comparing the two crystal structures at 89 K and 298 K, the distortion of the framework at 298

K was attributed to the positional relation between the two nitrogen atoms on the biphenylbisimine fractions (the distance between them changed from 11.3 to 11.9 Å), altering the size of 1D rectangular channels from 13.5 Å × 6.2 Å (89 K) to 11.5 Å × 11.5 Å (298 K). This 3DED method was then applied in several works for assisting the COFs structure solution.[92,93,94]

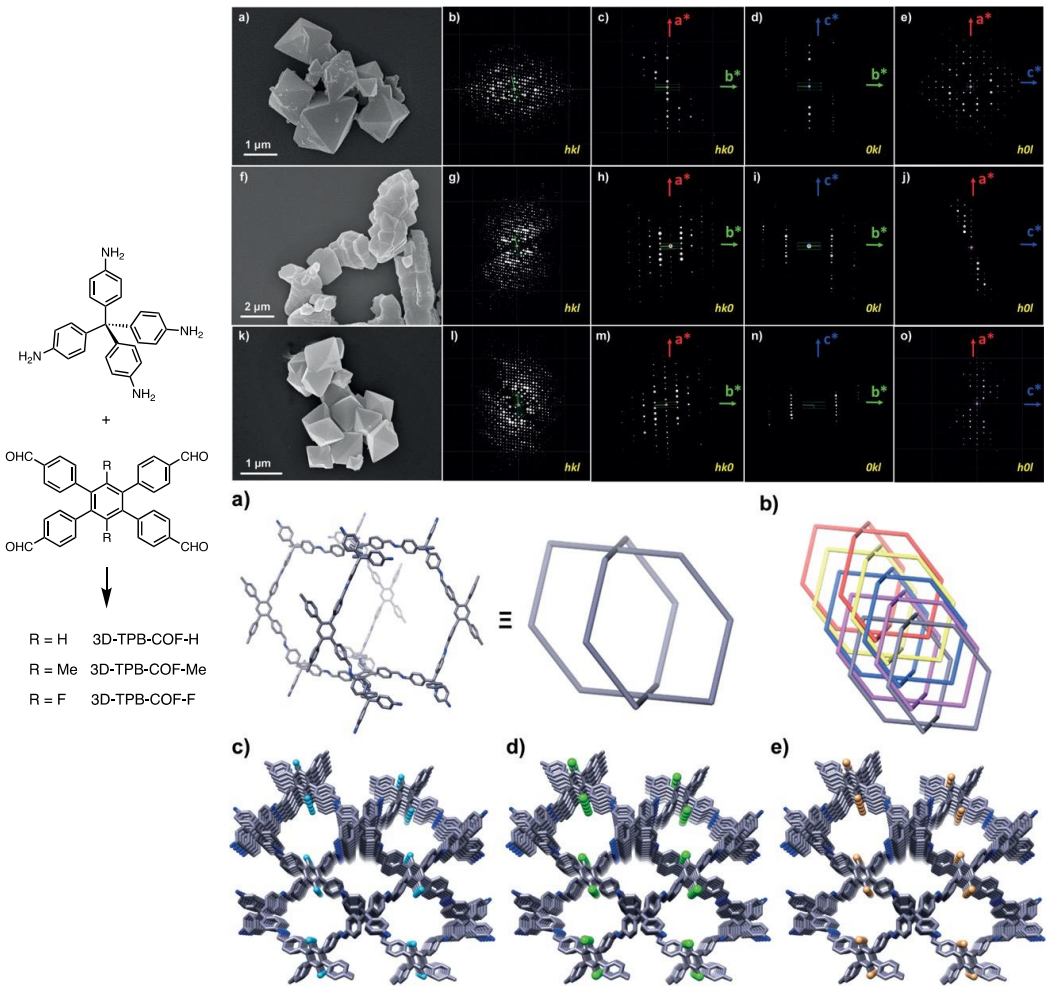

Figure 1.17. The three **3D-TPB-COFs** structure analyses using the cRED method. Left: the reaction scheme of the three **3D-TPB-COFs**. Top: Morphology and electron diffraction of the three **3D-TPB-COFs**. Bottom: Single-crystal structure of the three **3D-TPB-COFs** determined from cRED data.[95]

In 2019, Gao *et al.* synthesized three 3D COFs from the imine condensation reaction between tetra(paminophenyl)methane and 1,2,4,5-tetraphenylbenzene, with -H, -Me and -F substituted on the 3,6 positions of 1,2,4,5-tetraphenylbenzene, which yielded three COFs, denoted as 3D-TPB-COF-H, 3D-TPB-COF-Me and 3D-TPB-COF-F, respectively (**Figure 1.17**).[95] SEM images of these 3D-TPB-COFs showed homogeneous octahedral-like morphology with an average crystal size between 1 ~ 2 µm, still too small for SCXRD measurement. They then tried 3D cRED method for diffractions collection. cRED data of all 3DTPB-COFs single crystals were collected on a JEM2100 TEM at 99 K by continuously rotating the goniometer and the data obtained was then

processed, with intensities extracted using XDS data procession software, resulting in 3DED data with resolutions of 1.0, 0.9, and 1.0 Å for 3D-TPB-COF-H, 3D-TPB-COF-Me and 3D-TPB-COF-F, respectively. Such high resolution allowed them to accurately locate all the non-hydrogen atoms and be able to distinguish the -H, -Me and -F groups in three COFs by using cRED, respectively, since the average length of C-H, C=C, C-F and C-C bond are 0.96, 1.38, 1.37, and 1.53 Å. Based on the cRED results, 3D reciprocal lattices of the 3DTPB-COFs were reconstructed and finally, all the three 3DTPB-COFs were determined to have five-fold interpenetrated **pts** topology. A later work reported in 2020 by Xu *et al.* also successfully solved the single crystal structure of a one-dimensional metallo-COFs (mCOF-Ag) by single-crystal electron diffraction (SCED) technique, with a high resolution of ~ 0.95 Å.[96] More detailed introduction on the use of 3DED for MOFs and COFs measurement can be found in the two literature references here.[88,97]

All the successful examples of the atomic determination of COFs structures either include heavy metals in the backbone of the frameworks (the 1D mCOF-Ag) or fully organic backbones but with high levels of interpenetration (the three 3D-TPB-COF, 5-fold interpenetrated **pts** topology). These two elements enabled high overall framework electron density and this, contributed to the high electron diffraction resolution and ultimately led to the accurate structure solution. One thing I want to add here is, except for X-ray and electron diffraction, neutrons offer unique possibilities due to the radically different trend of their scattering cross sections and do not strongly decrease with lower atomic numbers - thus allowing light and heavy elements to contribute similarly to diffraction patterns. With such attributes, neutron diffraction had been employed on polycrystalline MOFs to study host-guest interactions involving H_2, CH_4, and CO_2. For this reason, we can imagine its great potential in COF characterisation in the future. One thing we need to overcome is, due to the scarcity of neutron sources, the minimum size requirement for crystals to do neutron diffraction is 0.5 mm. At this size range, we can already perform SCXRD measurement.[98] We expect the development of this technique in the future could assist the structure determination of nano-sized crystals.

Currently, researchers still strive for further developments of 3DED techniques.[99] Looking to the future, we can expect more automatic sample measurement and data processing in 3DED, and researchers working on COFs can easily solve the structure of their materials using 3DED without spending months trying to grow larger crystals to satisfy the requirements for SCXRD measurement. The structure-property relationships in COFs can then be uncovered and propagate the more rational discovery of the best material for specific performance.

1.5.3 Powder X-ray diffraction

COFs are commonly obtained as polycrystalline, microcrystalline, or inter-grown aggregates, which cannot satisfy the requirement for operating either SCXRD or 3DED measurements. While it cannot lead so directly to an unambiguous structure, powder X-ray diffraction (PXRD) is currently still the most widely applied characterization for COF structure determination, either in an *ab initio* structure determination manner or used in combination with computational structure modelling.

1.5.3.1 *Ab initio* structure determination from PXRD

A typical example of a porous framework structure solution using *ab initio* method from PXRD was reported in a Zr-MOF, UiO-66.[100] The structure of UiO-66 was solved by direct methods implemented in the program EXPO[101] using high-quality PXRD data collected with synchrotron radiation, following the general procedure of (1) indexing of the PXRD pattern, (2) integration of intensity, (3) structure solution, and (4) refining the structure by Rietveld refinement.[102] The same method had also been applied for unveiling the guest-dependent dynamics of COF-300. In this example, the H_2O induced framework contraction (~ 6% in unit cell volume) and THF led framework expansion (~ 50%) behaviours of COF-300 were unambiguously explored, through synchrotron in-house powder X-ray diffraction (PXRD) and Rietveld refinements, with the minimum 7 resolved diffraction peaks in PXRD.[103]

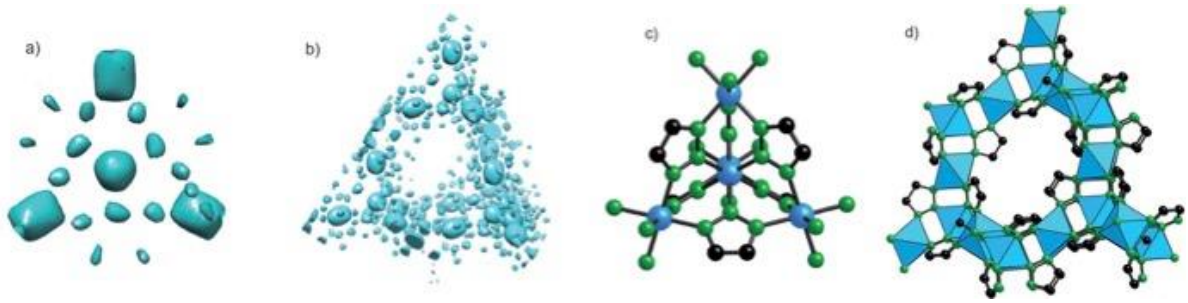

Figure 1.18. Electron density maps were generated by applying the charge-flipping method to PXRD data, clearly showing the position of the metal atoms and the triazole ring (a). The full unit cell is shown in (b). The crystal structure was refined accordingly. The tetrahedral SBU is shown in (c). The polyhedral representation of the framework is shown in (d). Metal atoms are represented as blue spheres (c) or polyhedra (d), nitrogen and carbon atoms are green and black spheres, respectively. Hydrogen atoms are omitted for clarity.[104]

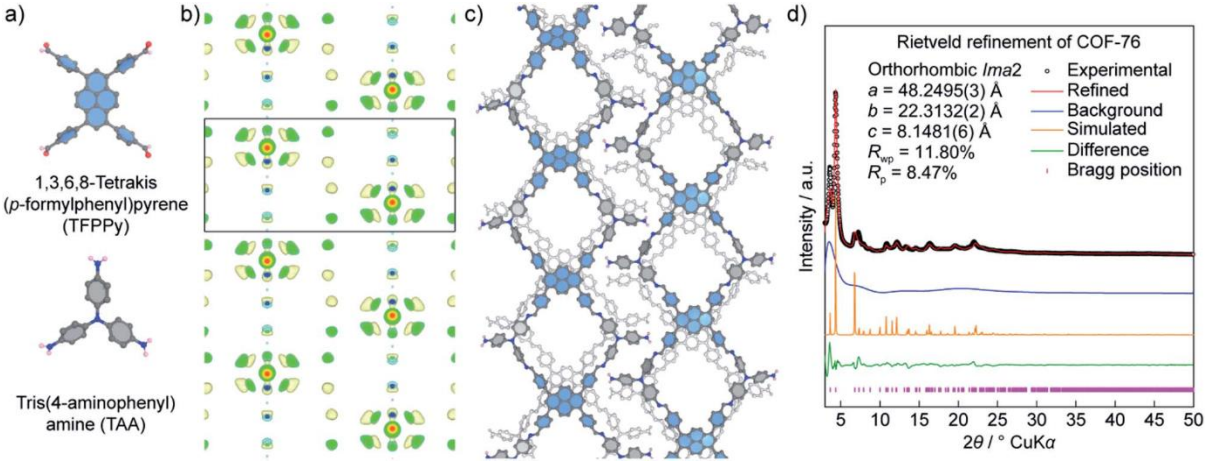

Figure 1.19. Structural analysis of COF-76 adopting a ribbon-like topology. (a) Chemical structures of square-planar 1,3,6,8-tetrakis(p-formylphenyl) pyrene (TFPPy) and triangular tris(4-aminophenyl)amine (TAA) units used to form COF-76. (b) Electron density map analysis of COF-76 generated by the charge-flipping method displays the fragments of TFPPy arranged in the form of ribbons. (c) Crystal structure of COF-76 showing a ribbon-based topology. (d) Rietveld refinement of COF-76 demonstrates a good agreement between the experimental and simulated PXRD pattern.[11]

Except for the above-mentioned direct method, the charge-flipping method is another strategy for framework structure determination from PXRD. The procedure to obtain the initial solution in this method is similar to that of single crystal diffraction data, although includes modifications such as histogram matching with chemical composition.[102] Advances made in 2011 showed that the solution obtained with the application of the charge-flipping method to powder diffraction data can be greatly improved, allowing the obtained electron density maps to be interpreted, unveiling the structure of microporous zeolites.[105] This allowed the structure solution of porous frameworks with only the use of powder diffraction data. Currently, this charge-flipping method had assisted the structure solution of a family of metal-triazolates (MET 1-6, a branch of MOFs)[104] (**Figure 1.18)** and helped the structure solution of COF-432 of **mtf** topology[106] and a ribbon COF-76 (**Figure 1.19**),[107] which the structure cannot be solved by common methods. This method is a good compensation for crystal structure solution while suitable crystal size for doing ED and SXRD analyses cannot be obtained, though problems of low crystallinity, diffraction peak overlapping, and lack of heavy metal issues exist in COFs.

1.5.3.2 PXRD and structure modelling approach to solve COFs structure

Currently, COF structure elucidation still mostly relies on a combination of computational structure modelling and powder X-ray diffraction analysis. This routine method had been played a crucial role in COFs structure solving since the report of the first COF structures in 2005.[1]

Benefiting from the reticular chemistry principle and the crystalline nature of COFs, computational structure modelling can be used. A general approach for COF structure modelling includes (1) placing the organic building blocks to the positions of nodes and edges in the selected net topology, (2) geometry optimization of the COF model built, (3) PXRD pattern calculation of the simulated model. The final step is to compare the experimental and simulated PXRD pattern, well-fitted pattern indicating the same framework structure.

For a result with higher accuracy, theoretically, for certain building blocks, COF models based on all possible topologies that can be found in RCSR should be built for PXRD comparison. This time and effort-consuming work can now be automated through custom code packages, which allows the generation of hypothetical structures in large quantities, and also, propagated the progress of hypothetical COFs for screening studies. Although in principle, an almost infinite number of possible nets exist for certain building block combinations, following the above-mentioned topological preference rule, the number of possible topologies can usually be limited to very small numbers, thus rendering this computation modelling assisted COFs structure to solve a realistic method, especially in 3D cases. Detailed introduction to the related computation modelling can be found in **Section 1.6** of the introduction part in this thesis.

The limitation of this method is it only applies to known topologies. If a COF is synthesized with a new framework structure which was not recorded in RCSR or *TOPOS*, like the above-mentioned one-dimensional ribbon COF-76[107] and a 3D COF reported recently with underlying **ljh**[67]topology, in such cases, either SCXRD, 3DED or the above-mentioned *ab initio* structure determination from PXRD should be looked.

1.5.4 Microscopy

Scanning Electron Microscopy (SEM) is widely used in MOFs/COFs fields for size, morphology, and surface elemental composition investigations. An SEM demagnifies an electron beam that is produced by a source into a probe which scans across the surface of a sample in a raster fashion. The interaction between the sample and the electron probe produces various types of emissions, which are captured by different detectors placed in appropriate positions. While morphological contrast is obtained by collecting all the secondary electrons (SEs - with energies smaller than 50 eV), compositional information is obtained by collecting the backscattered electrons (BSEs - with energies larger than 50 eV), since the atomic number at the sample surface influence BSEs more compared with SEs. Further compositional information is obtained through the detection of characteristic X-rays using an X-ray detector, also known as energy-dispersive X-ray analysis

(EDX).[108] As for the COFs sample preparation for SEM measurement, we can either put the ground dry powder samples on the conductive carbon adhesive tapes or disperse powders in ethanol/acetone and drop onto a silicon wafer, followed by the sample sputtering step with chromium/gold/carbon, for improving the conductivity of organic materials. In COFs, SEM is mostly used for providing morphology information of COF microcrystals. For example, if COF microcrystals with uniform morphology and sizes larger than 200 nm can be distinguished from SEM, we can then think applying 3DED or, if larger crystals, SCXRD measurement, for COFs structure solution.[95] SEM can also be used for unveiling the elemental components of COFs by EDS, however, since EDS analysis is limited to sample surface, for quantitative elemental analysis of bulk materials, inductively coupled plasma-optical emission spectroscopy (ICP-OES) or mass spectrometry (ICP-MS) and elemental analysis are more suited.

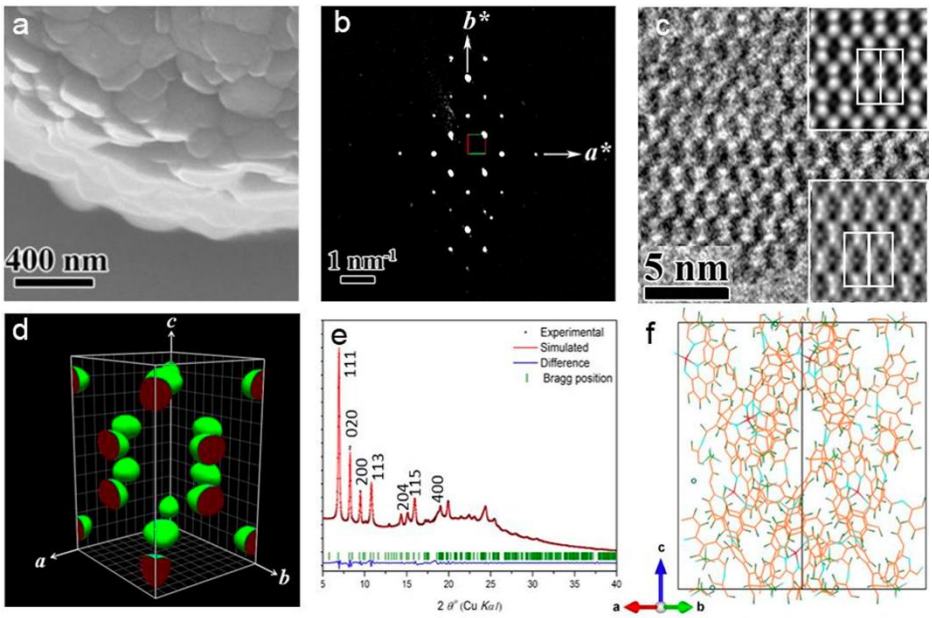

Figure 1.20. a) SEM image, b) projection of 3D EDT data along c*, c) HRTEM image taken along [110], d) reconstructed 3D electrostatic potential map, e) PXRD pattern with Pawley refinement results and f) final crystal structure solution of COF-505.[109]

Transmission Electron Microscopy (TEM) is one of the most effective techniques for the analysis of crystalline porous frameworks like MOFs/COFs as it can provide the morphology and atomically resolved crystallographic information of the sample. TEM imaging system works as follows: electron beams generated from electron guns were focused by metal apertures and electromagnetic lens, which allowed only electrons within a small range of energy could pass through, forming a well-defined energy electron beam. The transmitted electrons are applied to the specimen, which is placed onto the TEM grid (e.g., holey carbon films on 200 mesh copper grids) equipped with a mechanical arm for controlling the position and holding the specimen. The thickness of a TEM

specimen usually should be within 100 nm to allow electrons to pass through. The transmitted electrons are refocused and then magnified by an electromagnetic lens system and are projected on a phosphor screen to convert the electron image information to a visible form.[110] The TEM samples preparation of MOFs/COFs is similar to that of SEM samples. Since dense and bulk samples (> 100 nm) are hard for electrons to penetrate and give images without resolved structures, it would be better if samples could be prepared with very small particles. However, in cases where damage might be caused by intensive grinding, samples can be deposited on the TEM grid by simple mechanical contact, for instance, by rubbing the grid gently on some powder lying on a cleaned glass slide. As for TEM measurement, one notable attribute of MOFs/COFs is their high beam sensitivity, which often led to samples amorphization within a few seconds of illumination. Applying higher electron voltages is a strategy to decrease the damage rate at the expense of reduced detection efficiency and therefore collected information, while operating at a lower electron dose (e-beam current and irradiation time) had been reported as the most crucial factor to minimize the electron damage and get good, resolved TEM images for these porous solids. Examples of TEM-assisted COF structure solving, like COF-505 (**Figure 1.20**). The combinational use of TEM and 3DED had been a powerful tool for COFs structure solutions and we can anticipate more widespread use in the future as these porous solids are still experiencing prosperous development.

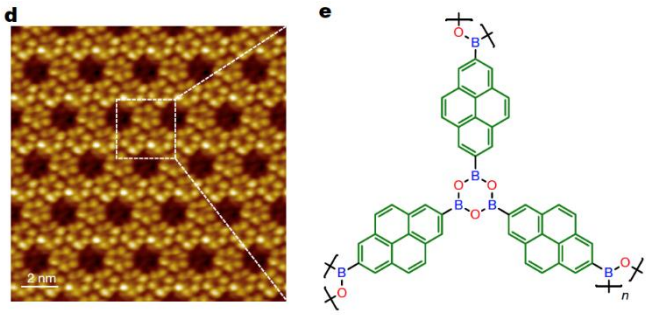

Figure 1.21. d. High-resolution STM image of the honeycomb cluster. The white dotted square points out the unit three-armed pattern of 2D polymers with the chemical structure shown in e. e. Chemical structure of the 2DP.[111]

Scanning Tunnelling Microscopy (STM) is another technique that allows direct visualization of atomic level resolved crystalline frameworks. STM is based on the exponential dependence of the quantum tunnelling current, the obtained STM images are three-dimensional, recording the variation in the tip height when scanning in the plane of the sample. However, with an ultrahigh resolution, in COFs field, STM is more often applied for in-situ monitoring the reaction for the 2D COFs crystallization mechanism uncovering, like a nice exemplar work reported recently (**Figure 1.21**).[111]

1.5.5 Gas sorption

One paramount feature of MOFs/COFs is their permanent porosity (materials showed permanent porosity if their porous structure is stable upon guest molecules removal). The permanent porosity of MOFs/COFs is commonly measured by nitrogen gas adsorption experiments (at 77 K relative pressures between 0~1), which is the standard practice for porosity evaluation. Based on the gas adsorption isotherm, surface area, pore size distribution, and pore volume can be obtained, the accuracy of these results relies on the theoretical models applied. For the surface area calculations of MOFs/COFs, Brunauer−Emmett−Teller (BET) method is the most widely applied. One limitation of this BET method is, for structures of microporous, data from low-pressure range ($P/P_0 < 0.1$) in which the term $V(1 - P/P_0)$ continuously increases with P/P_0, rather than the classical range ($P/P_0 = 0.05−0.3$), should be used in the BET equation. A correlation coefficient greater than 0.995 and a positive C value are the gold standards for the multipoint BET method.[57] The accuracy of the pore size distribution (PSD) is strongly influenced by the model selected and the non-local density functional theory (NL-DFT) is currently believed the most suited model for the description of the microporous of MOFs and COFs. Argon and CO_2 are also applied for the porosity measurement sometimes, considering that Argon does not have a quadrupole moment as N_2 and the smaller kinetic diameter of CO_2 compared to N_2 (330 pm *vs.* 364 pm).[112,113]

Small-angle X-ray scattering (SAXS) is an alternative strategy for uncovering the porosity of microporous (< 2 nm) and mesoporous materials (2 ~ 50 nm). This method is reported to show higher accuracy for the porosity measurement of microporous materials compared to the traditional nitrogen or other gases sorption isotherms since the latter suffers from the effect of closed porosity and diffusion hindrance in microporous materials, and its reliance on analytical models might lead to inaccurate results due to the porosity complexity. Such a method had been applied for disclosing the porosity of MOF-5, in this work, they also operated an in-situ SAXS/WAXS experiment demonstrate the effect of temperature on the concurrent evolutions of pore structure and crystal phase during the removal of solvent upon heating.[114]

Mercury intrusion porosimetry (MIP) is another method for porosity characterizations of mesoporous (2 ~ 50 nm) and microporous (> 50 nm) materials. Mercury has the advantage of not wetting most substances and not penetrating pores by capillary action. The MIP method uses pressure to force mercury into the pores, where the volume of mercury that enters, the pores is related to the pore volume, and the pressure needed is related to the pore size.[115] This method had been applied for studying the pressure-induced mechanical behaviours of a flexible MOF materials, MIL-53.[116,117]

1.6 Computational methods

All COF models in this thesis are built by zeo++ code[118,119] and the BIOVIA Materials Studio software (ver. 8.0, Accelrys Software Inc.), the choice of topology follows the reticular chemistry principle. COF models based on all possible topologies will be built for accurate results.

General procedure for COFs structural construction using zeo++ code includes: (1) interpreting the topology information (vertices, edges, and crystal space group); (2) aligning the building blocks. Analyse the connectivity and symmetry information of building blocks and allocate each building block to the corresponding vertex/edge positions in the interpreted net; (3) assemble building blocks into periodic frameworks according to certain algorithms written in the code, framework structure exhibits the lowest deviation (deviation is defined as the maximum distance between pairs of connectivity markers in adjacent building blocks) will be returned as output. For more details of this method could refer to the reference cited here.[119] To clarify this procedure, here, I use a reported 2D COF with **sql** topology as an example (**Figure 1.22**).[120]

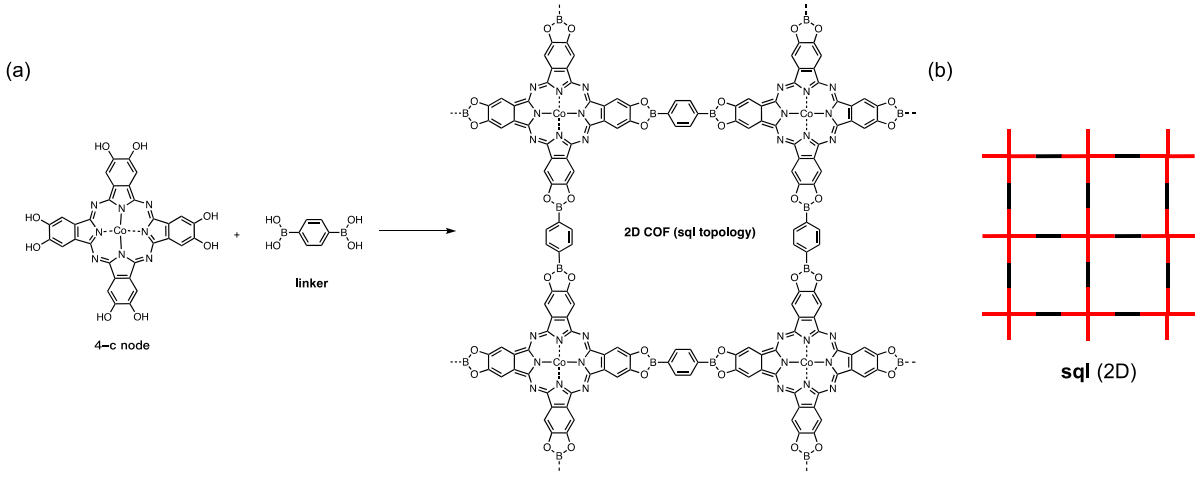

Figure 1.22. (a) Reaction scheme for the synthesis of a 2D COF of **sql** topology, from a 4-c node and a linear linker.[120] (b) Graph of the 2D **sql** topology. The red square corresponds to the 4-c node and the black line represents the linear linker.

As is shown **Figure 1.22a**, the reaction between a square 4-c node and a linear linker is supposed to give a 2D COF of **sql** topology (**Figure 1.22b**), according to RCSR.[59] To construct this COF model, the corresponding topology information and building blocks need to be provided to zeo++. Topology information can be downloaded from RCSR in a format (.cgd) compatible with zeo++. In this example here, the "sql.cgd" file. As for the building blocks preparation, the most important thing is to manually define the dummy atom "Q" as the connection sites on building blocks. This dummy "Q" atom sites works to: (1) help the code to distinguish between vertex and linker (if

exists), according to their number of connection sites and underlying symmetry; (2) act as the overlay position to connect building blocks. Generally, there are multiple ways to define the dummy "Q" sites on building blocks to build a specific COF structure. For example, in **Figure 1.23**, we proposed three methods to define the dummy "Q" sites on building blocks for the 2D COF construction in **Figure 1.22a**. As the dummy "Q" atom is not a real-exist atom and acts only as the position for structure overlay, when it is defined in a position that overlapped an original atom in the building block, the original atom needs to be remained on one of the building blocks, as is shown in **Figure 1.23a-b**. Alternatively, it can also be defined at a position where there is no original atom exists, like the example in **Figure 1.23c**, where the dummy "Q" atom is defined at the centre of the benzene linker. In this case, one important thing is to avoid atom duplicates in the final framework structure, which will lead to structure optimization failure in the following geometry optimization step. For example, here in **Figure 1.23c**, we need to remove all the carbons that are marked in green on the building block. Building blocks preparation for 3D COFs construction follows the same principle as for 2D COFs. After we provide topology information and the corresponding building units, zeo++ will assemble these building units into periodic frameworks and return us the lowest deviated structure as the output.

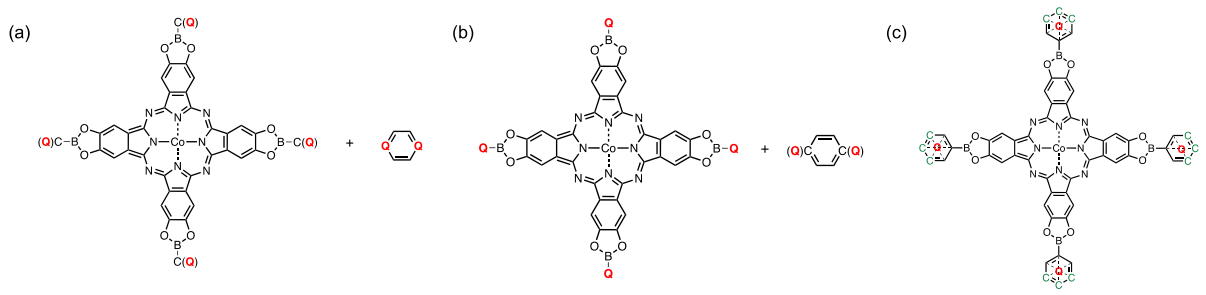

Figure 1.23. Three ways to define the dummy "Q" site for the 2D COF (**Figure 1.22a)** construction using zeo++ code.[119] Dummy "Q" sites defined in a position overlapped an original atom (in this example, carbon), with the original carbon remained (a) in the 4-c node; (b) in the linear linker. (c) Dummy "Q" sites defined at the centre of benzene linker.

If not specified, the geometry optimization of the output COF models from the last step is usually performed using the Forcite module of Materials Studio, specifically, using Dreiding (for fully organic frameworks) or Universal forcefield (while metals are incorporated into the frameworks) in conjunction with the QEq charge equilibration method.[121] Geometry optimization allows the structure model to relax to realize energetic minimization, through reducing the magnitude of calculated forces smaller than defined convergence tolerances. After geometry optimization, bond lengths and angles will be checked (compare with the related single crystal structures recorded in the Cambridge Structural Database, CSD) to confirm the obtained optimized model is reasonable.

PXRD simulations of the optimized COF models is performed in Mercury, a software package issued by the Cambridge Structural Database (CSD).

This computational method can only be used for constructing COFs with a defined net topology known in RCSR.

1.7 Project aim

The design and synthesis of 3D COFs were mainly focused on multi-linking polyhedral organic nodes construction; however, the synthetic complexity of these building blocks hindered their fast development compared to their MOFs counterparts. An alternative strategy to obtain versatile 3D COF structure libraries is to control the alignment of planar (or near planar) building units, which had been used for constructing 3D COFs of **ffc**[2] **tbo**[79] and **fjh**[80] topology. In these examples, the 3D spatial arrangements of the planar precursors were all based on the rotation of imine bonds during synthesis, which is difficult to predict, thus limiting applications to target 3D COFs of certain topologies. The aim of my PhD is the targeted design and synthesis of 3D COFs of novel, unreported topologies, based on planar building units.

In Chapter 2, I will develop a strategy to prepare 3D COFs of **nbo** topology. Following the reticular chemistry principle. Two elements are required to target **nbo** topology: (1) organic building blocks of square planar geometry, (2) a method or linkage to achieve the perpendicular orientation of the two neighbouring square units. In this work, I plan to find a short linkage which can satisfy the perpendicular orientation required and avoid the formation of an interpenetrated structure. This strategy will be used to maintain porosity and simplify the structure characterisation. Full characterization will be achieved using a combination of gas sorption, FT-IR and solid-state NMR spectra, and transmission electron microscopy (TEM).

In Chapter 3, I will investigate a second strategy to prepare 3D COFs of **nbo** topology following the same principle applied for targeting the first 3D **nbo** MOF, MOF-601.[122] With this new strategy, we expect to obtain a 3D COF with large pores, and hopefully, this large pore will endow these new COFs with some good performance in either gas adsorptions or separations. Full characterization will be achieved using a combination of gas sorption, FT-IR and solid-state NMR spectra.

1.8 Reference

(1) Ockwig, N. W.; Co, A. P.; Keeffe, M. O.; Matzger, A. J.; Yaghi, O. M. Porous , Crystalline , Covalent Organic Frameworks. *Science* **2005**, *310* (5751), 1166–1171.

(2) Lan, Y.; Han, X.; Tong, M.; Huang, H.; Yang, Q.; Liu, D.; Zhao, X.; Zhong, C. Materials Genomics Methods for High-Throughput Construction of COFs and Targeted Synthesis. *Nat. Commun.* **2018**, *9*, 5274.

(3) Gui, B.; Lin, G.; Ding, H.; Gao, C.; Mal, A.; Wang, C. Three-Dimensional Covalent Organic Frameworks: From Topology Design to Applications. *Acc. Chem. Res.* **2020**, *53* (10), 2225–2234.

(4) Yuan, S.; Li, X.; Zhu, J.; Zhang, G.; Van Puyvelde, P.; Van Der Bruggen, B. Covalent Organic Frameworks for Membrane Separation. *Chem. Soc. Rev.* **2019**, *48* (10), 2665–2681.

(5) Gendy, E. A.; Ifthikar, J.; Ali, J.; Oyekunle, D. T.; Elkhlifia, Z.; Shahib, I. I.; Khodair, A. I.; Chen, Z. Removal of Heavy Metals by Covalent Organic Frameworks (COFs): A Review on Its Mechanism and Adsorption Properties. *J. Environ. Chem. Eng.* **2021**, *9* (4), 105687.

(6) Zhao, X.; Pachfule, P.; Thomas, A. Covalent Organic Frameworks (COFs) for Electrochemical Applications. *Chem. Soc. Rev.* **2021**, *50* (12), 6871–6913.

(7) Sharma, R. K.; Yadav, P.; Yadav, M.; Gupta, R.; Rana, P.; Srivastava, A.; Zbořil, R.; Varma, R. S.; Antonietti, M.; Gawande, M. B. Recent Development of Covalent Organic Frameworks (COFs): Synthesis and Catalytic (Organic-Electro-Photo) Applications. *Mater. Horizons* **2020**, *7* (2), 411–454.

(8) Xia, C.; Kirlikovali, K. O.; Nguyen, T. H. C.; Nguyen, X. C.; Tran, Q. B.; Duong, M. K.; Nguyen Dinh, M. T.; Nguyen, D. L. T.; Singh, P.; Raizada, P.; Nguyen, V. H.; Kim, S. Y.; Singh, L.; Nguyen, C. C.; Shokouhimehr, M.; Le, Q. Van. The Emerging Covalent Organic Frameworks (COFs) for Solar-Driven Fuels Production. *Coord. Chem. Rev.* **2021**, *446*, 214117.

(9) Guan, Q.; Zhou, L. Le; Li, W. Y.; Li, Y. A.; Dong, Y. Bin. Covalent Organic Frameworks (COFs) for Cancer Therapeutics. *Chem. - A Eur. J.* **2020**, *26* (25), 5583–5591.

(10) Kalmutzki, M. J.; Hanikel, N.; Yaghi, O. M. Secondary Building Units as the Turning Point in the Development of the Reticular Chemistry of MOFs. *Sci. Adv.* **2018**, *4* (10), eaat9180.

(11) Nguyen, H. L. Reticular Design and Crystal Structure Determination of Covalent Organic Frameworks. *Chem. Sci.* **2021**, *12* (25), 8632–8647.

(12) Zhao, X.; Liang, R. R.; Jiang, S. Y.; Ru-Han, A. Two-Dimensional Covalent Organic Frameworks with Hierarchical Porosity. *Chem. Soc. Rev.* **2020**, *49* (12), 3920–3951.

(13) Guan, X.; Chen, F.; Fang, Q.; Qiu, S. Design and Applications of Three Dimensional Covalent Organic Frameworks. *Chem. Soc. Rev.* **2020**, *49* (5), 1357–1384.

(14) Yaghi, O.M., Kalmutzki, M.J. and Diercks, C. S. Reticular Design of Covalent Organic Frameworks. *Introduction to Reticular Chemistry*. May 6, 2019, pp 225–243.

(15) Uribe-Romo, F. J.; Hunt, J. R.; Furukawa, H.; Klöck, C.; O'Keeffe, M.; Yaghi, O. M. A Crystalline Imine-Linked 3-D Porous Covalent Organic Framework. *J. Am. Chem. Soc.* **2009**, *131* (13), 4570–4571.

(16) Kandambeth, S.; Mallick, A.; Lukose, B.; Mane, M. V.; Heine, T.; Banerjee, R. Construction of Crystalline 2D Covalent Organic Frameworks with Remarkable Chemical (Acid/Base) Stability via a Combined Reversible and Irreversible Route. *J. Am. Chem. Soc.* **2012**, *134* (48), 19524–19527.

(17) Fang, Q.; Zhuang, Z.; Gu, S.; Kaspar, R. B.; Zheng, J.; Wang, J.; Qiu, S.; Yan, Y. Designed Synthesis of Large-Pore Crystalline Polyimide Covalent Organic Frameworks. *Nat. Commun.* **2014**, *5*, 4503.

(18) Uribe-Romo, F. J.; Doonan, C. J.; Furukawa, H.; Oisaki, K.; Yaghi, O. M. Crystalline Covalent Organic Frameworks with Hydrazone Linkages. *J. Am. Chem. Soc.* **2011**, *133* (30), 11478–11481.

(19) Dalapati, S.; Jin, S.; Gao, J.; Xu, Y.; Nagai, A.; Jiang, D. An Azine-Linked Covalent Organic Framework. *J. Am. Chem. Soc.* **2013**, *135* (46), 17310–17313.

(20) Du, Y.; Yang, H.; Whiteley, J. M.; Wan, S.; Jin, Y.; Lee, S. H.; Zhang, W. Ionic Covalent Organic Frameworks with Spiroborate Linkage. *Angew. Chemie - Int. Ed.* **2016**, *55* (5), 1737–1741.

(21) Kuhn, P.; Antonietti, M.; Thomas, A. Porous, Covalent Triazine-Based Frameworks Prepared by

Ionothermal Synthesis. *Angew. Chemie-International Ed.* **2008**, *47* (18), 3450–3453.

(22) Zhang, B.; Wei, M.; Mao, H.; Pei, X.; Alshmimri, S. A.; Reimer, J. A.; Yaghi, O. M. Crystalline Dioxin-Linked Covalent Organic Frameworks from Irreversible Reactions. *J. Am. Chem. Soc.* **2018**, *140* (40), 12715–12719.

(23) Vitaku, E.; Gannett, C. N.; Carpenter, K. L.; Shen, L.; Abruña, H. D.; Dichtel, W. R. Phenazine-Based Covalent Organic Framework Cathode Materials with High Energy and Power Densities. *J. Am. Chem. Soc.* **2020**, *142* (1), 16–20.

(24) Zhuang, X.; Zhao, W.; Zhang, F.; Cao, Y.; Liu, F.; Bi, S.; Feng, X. A Two-Dimensional Conjugated Polymer Framework with Fully Sp2-Bonded Carbon Skeleton. *Polym. Chem.* **2016**, *7* (25), 4176–4181.

(25) Lohse, M. S.; Bein, T. Covalent Organic Frameworks: Structures, Synthesis, and Applications. *Adv. Funct. Mater.* **2018**, *28* (33), 1705553.

(26) Zhang, Y.; Duan, J.; Ma, D.; Li, P.; Li, S.; Li, H.; Zhou, J.; Ma, X.; Feng, X.; Wang, B. Three-Dimensional Anionic Cyclodextrin-Based Covalent Organic Frameworks. *Angew. Chemie - Int. Ed.* **2017**, *56* (51), 16313–16317.

(27) Li, H.; Li, H.; Dai, Q.; Li, H.; Brédas, J. L. Hydrolytic Stability of Boronate Ester-Linked Covalent Organic Frameworks. *Adv. Theory Simulations* **2018**, *1* (2), 1700015.

(28) Li, X.; Zhang, C.; Cai, S.; Lei, X.; Altoe, V.; Hong, F.; Urban, J. J.; Ciston, J.; Chan, E. M.; Liu, Y. Facile Transformation of Imine Covalent Organic Frameworks into Ultrastable Crystalline Porous Aromatic Frameworks. *Nat. Commun.* **2018**, *9*, 2998.

(29) Chen, G.; Lan, H. H.; Cai, S. L.; Sun, B.; Li, X. Le; He, Z. H.; Zheng, S. R.; Fan, J.; Liu, Y.; Zhang, W. G. Stable Hydrazone-Linked Covalent Organic Frameworks Containing O,N,O′-Chelating Sites for Fe(III) Detection in Water. *ACS Appl. Mater. Interfaces* **2019**, *11* (13), 12830–12837.

(30) Zhang, W.; Chen, L.; Dai, S.; Zhao, C.; Ma, C.; Wei, L.; Zhu, M.; Chong, S. Y.; Yang, H.; Liu, L.; Bai, Y.; Yu, M.; Xu, Y.; Zhu, X.-W.; Zhu, Q.; An, S.; Sprick, R. S.; Little, M. A.; Wu, X.; Jiang, S.; Wu, Y.; Zhang, Y.-B.; Tian, H.; Zhu, W.-H.; Cooper, A. I. Reconstructed Covalent Organic Frameworks. *Nature* **2022**, *604* (7904), 72–79.

(31) Li, Z.; Zhi, Y.; Feng, X.; Ding, X.; Zou, Y.; Liu, X.; Mu, Y. An Azine-Linked Covalent Organic Framework: Synthesis, Characterization and Efficient Gas Storage. *Chem. - A Eur. J.* **2015**, *21* (34), 12079–12084.

(32) Haase, F.; Lotsch, B. V. Solving the COF Trilemma: Towards Crystalline, Stable and Functional Covalent Organic Frameworks. *Chem. Soc. Rev.* **2020**, *49* (23), 8469–8500.

(33) Farha, O. K.; Spokoyny, A. M.; Hauser, B. G.; Bae, Y. S.; Brown, S. E.; Snurr, R. Q.; Mirkin, C. A.; Hupp, J. T. Synthesis, Properties, and Gas Separation Studies of a Robust Diimide-Based Microporous Organic Polymer. *Chem. Mater.* **2009**, *21* (14), 3033–3035.

(34) Liaw, D. J.; Wang, K. L.; Huang, Y. C.; Lee, K. R.; Lai, J. Y.; Ha, C. S. Advanced Polyimide Materials: Syntheses, Physical Properties and Applications. *Prog. Polym. Sci.* **2012**, *37* (7), 907–974.

(35) Han, B.; Ding, X.; Yu, B.; Wu, H.; Zhou, W.; Liu, W.; Wei, C.; Chen, B.; Qi, D.; Wang, H.; Wang, K.; Chen, Y.; Chen, B.; Jiang, J. Two-Dimensional Covalent Organic Frameworks with Cobalt(II)-Phthalocyanine Sites for Efficient Electrocatalytic Carbon Dioxide Reduction. *J. Am. Chem. Soc.* **2021**, *143* (18), 7104–7113.

(36) Duan, H.; Li, K.; Xie, M.; Chen, J. M.; Zhou, H. G.; Wu, X.; Ning, G. H.; Cooper, A. I.; Li, D. Scalable Synthesis of Ultrathin Polyimide Covalent Organic Framework Nanosheets for High-Performance Lithium-Sulfur Batteries. *J. Am. Chem. Soc.* **2021**, *143* (46), 19446–19453.

(37) Zhang, W.; Li, C.; Yuan, Y. P.; Qiu, L. G.; Xie, A. J.; Shen, Y. H.; Zhu, J. F. Highly Energy- and Time-Efficient Synthesis of Porous Triazine-Based Framework: Microwave-Enhanced Ionothermal Polymerization and Hydrogen Uptake. *J. Mater. Chem.* **2010**, *20* (31), 6413–6415.

(38) Ren, S.; Bojdys, M. J.; Dawson, R.; Laybourn, A.; Khimyak, Y. Z.; Adams, D. J.; Cooper, A. I. Porous, Fluorescent, Covalent Triazine-Based Frameworks via Room-Temperature and Microwave-Assisted Synthesis. *Adv. Mater.* **2012**, *24* (17), 2357–2361.

(39) Liu, J.; Lyu, P.; Zhang, Y.; Nachtigall, P.; Xu, Y. New Layered Triazine Framework/Exfoliated 2D Polymer with Superior Sodium-Storage Properties. *Adv. Mater.* **2018**, *30* (11), 1705401.

(40) Xie, J.; Shevlin, S. A.; Ruan, Q.; Moniz, S. J. A.; Liu, Y.; Liu, X.; Li, Y.; Lau, C. C.; Guo, Z. X.; Tang, J. Efficient Visible Light-Driven Water Oxidation and Proton Reduction by an Ordered Covalent Triazine-Based Framework. *Energy Environ. Sci.* **2018**, *11* (6), 1617–1624.

(41) Palkovits, R.; Antonietti, M.; Kuhn, P.; Thomas, A.; Schuth, F. Solid Catalysts for the Selective Low-Temperature Oxidation of Methane to Methanol. *Angew. Chemie-International Ed.* **2009**, *48* (37), 6909–6912.

(42) EL-Mahdy, A. F. M.; Hung, Y. H.; Mansoure, T. H.; Yu, H. H.; Hsu, Y. S.; Wu, K. C. W.; Kuo, S. W. Synthesis of [3 + 3] β-Ketoenamine-Tethered Covalent Organic Frameworks (COFs) for High-Performance Supercapacitance and CO2 Storage. *J. Taiwan Inst. Chem. Eng.* **2019**, *103*, 199–208.

(43) Gao, H.; Zhu, Q.; Neale, A. R.; Bahri, M.; Wang, X.; Yang, H.; Liu, L.; Clowes, R.; Browning, N. D.; Sprick, R. S.; Little, M. A.; Hardwick, L. J.; Cooper, A. I. Integrated Covalent Organic Framework/Carbon Nanotube Composite as Li-Ion Positive Electrode with Ultra-High Rate Performance. *Adv. Energy Mater.* **2021**, *11* (39), 2101880.

(44) Wang, X.; Chen, L.; Chong, S. Y.; Little, M. A.; Wu, Y.; Zhu, W. H.; Clowes, R.; Yan, Y.; Zwijnenburg, M. A.; Sprick, R. S.; Cooper, A. I. Sulfone-Containing Covalent Organic Frameworks for Photocatalytic Hydrogen Evolution from Water. *Nat. Chem.* **2018**, *10* (12), 1180–1189.

(45) Wang, K.; Jia, Z.; Bai, Y.; Wang, X.; Hodgkiss, S. E.; Chen, L.; Chong, S. Y.; Wang, X.; Yang, H.; Xu, Y.; Feng, F.; Ward, J. W.; Cooper, A. I. Synthesis of Stable Thiazole-Linked Covalent Organic Frameworks via a Multicomponent Reaction. *J. Am. Chem. Soc.* **2020**, *142* (25), 11131–11138.

(46) Waller, P. J.; Alfaraj, Y. S.; Diercks, C. S.; Jarenwattananon, N. N.; Yaghi, O. M. Conversion of Imine to Oxazole and Thiazole Linkages in Covalent Organic Frameworks. *J. Am. Chem. Soc.* **2018**, *140* (29), 9099–9103.

(47) Guo, J.; Xu, Y.; Jin, S.; Chen, L.; Kaji, T.; Honsho, Y.; Addicoat, M. A.; Kim, J.; Saeki, A.; Ihee, H.; Seki, S.; Irle, S.; Hiramoto, M.; Gao, J.; Jiang, D. Conjugated Organic Framework with Three-Dimensionally Ordered Stable Structure and Delocalized π Clouds. *Nat. Commun.* **2013**, *4*, 2736.

(48) Wang, K.; Yang, L. M.; Wang, X.; Guo, L.; Cheng, G.; Zhang, C.; Jin, S.; Tan, B.; Cooper, A. Covalent Triazine Frameworks via a Low-Temperature Polycondensation Approach. *Angew. Chemie - Int. Ed.* **2017**, *56* (45), 14149–14153.

(49) Guo, L.; Wang, X.; Zhan, Z.; Zhao, Y.; Chen, L.; Liu, T.; Tan, B.; Jin, S. Crystallization of Covalent Triazine Frameworks via a Heterogeneous Nucleation Approach for Efficient Photocatalytic Applications. *Chem. Mater.* **2021**, *33* (6), 1994–2003.

(50) Guan, X.; Li, H.; Ma, Y.; Xue, M.; Fang, Q.; Yan, Y.; Valtchev, V.; Qiu, S. Chemically Stable Polyarylether-Based Covalent Organic Frameworks. *Nat. Chem.* **2019**, *11* (6), 587–594.

(51) Jin, E.; Asada, M.; Xu, Q.; Dalapati, S.; Addicoat, M. A.; Brady, M. A.; Xu, H.; Nakamura, T.; Heine, T.; Chen, Q.; Jiang, D. Two-Dimensional sp2 Carbon – Conjugated Covalent Organic Frameworks. *Science* **2017**, *357* (6352), 673–676.

(52) Fu, Z.; Wang, X.; Gardner, A. M.; Wang, X.; Chong, S. Y.; Neri, G.; Cowan, A. J.; Liu, L.; Li, X.; Vogel, A.; Clowes, R.; Bilton, M.; Chen, L.; Sprick, R. S.; Cooper, A. I. A Stable Covalent Organic Framework for Photocatalytic Carbon Dioxide Reduction. *Chem. Sci.* **2020**, *11* (2), 543–550.

(53) Grünker, R.; Bon, V.; Müller, P.; Stoeck, U.; Krause, S.; Mueller, U.; Senkovska, I.; Kaskel, S. A New Metal-Organic Framework with Ultra-High Surface Area. *Chem. Commun.* **2014**, *50* (26), 3450–3452.

(54) Kinoshita, Y.; Matsubara, I.; Higuchi, T.; Saito, Y. The Crystal Structure of Bis(Adiponitrilo)Copper(I) Nitrate. *Bull. Chem. Soc. Jpn.* **1959**, *32* (11), 1221–1226.

(55) Hailian Li, Mohamed Eddaoudi, M. O. & O. M. Y. Design and Synthesis of an Exceptionally Stable and Highly Porous Metal-organic Framework. *Nature* **1999**, *402*, 276–279.

(56) Hong-Cai Zhou, Jeffrey R. Long, and O. M. Y. Introduction to Metal − Organic Frameworks. *Chem. Rev.* **2012**, *112* (2), 673–674.

(57) Gropp, C.; Canossa, S.; Wuttke, S.; Gándara, F.; Li, Q.; Gagliardi, L.; Yaghi, O. M. Standard Practices of Reticular Chemistry. *ACS Cent. Sci.* **2020**, *6* (8), 1255–1273.

(58) Safaei, M.; Foroughi, M. M.; Ebrahimpoor, N.; Jahani, S.; Omidi, A.; Khatami, M. A Review on Metal-Organic Frameworks: Synthesis and Applications. *TrAC - Trends Anal. Chem.* **2019**, *118*, 401–425.

(59) Keeffe, M. O.; Peskov, M. a; Ramsden, S. J.; Yaghi, O. M. (RCSR) Database of , and Symbols for , Crystal. *Acc. Chem. Res.* **2008**, *41* (12), 1782–1789.

(60) Keupp, J.; Schmid, R. Molecular Dynamics Simulations of the "Breathing" Phase Transformation of MOF Nanocrystallites. *Adv. Theory Simulations* **2019**, *2* (11), 1900117.

(61) Delgado-Friedrichs, O.; O'Keeffe, M.; Yaghi, O. M. Taxonomy of Periodic Nets and the Design of Materials. *Phys. Chem. Chem. Phys.* **2007**, *9* (9), 1035–1043.

(62) Delgado-Friedrichs, O.; Foster, M. D.; O'Keeffe, M.; Proserpio, D. M.; Treacy, M. M. J.; Yaghi, O. M. What Do We Know about Three-Periodic Nets? *J. Solid State Chem.* **2005**, *178* (8), 2533–2554.

(63) Zhang, B.; Mao, H.; Matheu, R.; Reimer, J. A.; Alshmimri, S. A.; Alshihri, S.; Yaghi, O. M. Reticular Synthesis of Multinary Covalent Organic Frameworks. *J. Am. Chem. Soc.* **2019**, *141* (29), 11420–11424.

(64) Ma, T.; Kapustin, E. A.; Yin, S. X.; Liang, L.; Zhou, Z.; Niu, J.; Li, L.; Wang, Y.; Su, J.; Li, J.; Wang, X.; Wang, D.; Wang, W.; Sun, J.; Yaghi, O. M. Single-Crystal X-Ray Diffraction Structures of Covalent Organic Frameworks. *Science.* **2018**, *361* (6397), 48–52.

(65) El-Kaderi, H. M.; Hunt, J. R.; José L. Mendoza-Cortés, A. P. C.; Taylor, R. E.; O'Keeffe, M.; Yaghi, O. M. Designed Synthesis of 3D Covalent Organic Frameworks. *Science.* **2007**, *316* (5882), 268–273.

(66) Lin, G.; Ding, H.; Chen, R.; Peng, Z.; Wang, B.; Wang, C. 3D Porphyrin-Based Covalent Organic Frameworks. *J. Am. Chem. Soc.* **2017**, *139* (25), 8705–8709.

(67) Xie, Y.; Li, J.; Lin, C.; Gui, B.; Ji, C.; Yuan, D.; Sun, J.; Wang, C. Tuning the Topology of Three-Dimensional Covalent Organic Frameworks via Steric Control: From Pts to Unprecedented Ljh. *J. Am. Chem. Soc.* **2021**, *143* (19), 7279–7284.

(68) Fang, Q.; Wang, J.; Gu, S.; Kaspar, R. B.; Zhuang, Z.; Zheng, J.; Guo, H.; Qiu, S.; Yan, Y. 3D Porous Crystalline Polyimide Covalent Organic Frameworks for Drug Delivery. *J. Am. Chem. Soc.* **2015**, *137* (26), 8352–8355.

(69) Liu, Y.; Wu, C.; Sun, Q.; Hu, F.; Pan, Q.; Sun, J.; Jin, Y.; Li, Z.; Zhang, W.; Zhao, Y. Spirobifluorene-Based Three-Dimensional Covalent Organic Frameworks with Rigid Topological Channels as Efficient Heterogeneous Catalyst. *CCS Chem.* **2021**, *3* (4), 2418–2427.

(70) Liu, Y.; Ma, Y.; Zhao, Y.; Sun, X.; Gándara, F.; Furukawa, H.; Liu, Z.; Zhu, H.; Zhu, C.; Suenaga, K.; Oleynikov, P.; Alshammari, A. S.; Zhang, X.; Terasaki, O.; Yaghi, O. M. Weaving of Organic Threads into a Crystalline Covalent Organic Framework. *Science.* **2016**, *351* (6271), 365–369.

(71) Gao, C.; Li, J.; Yin, S.; Sun, J.; Wang, C. Twist Building Blocks from Planar to Tetrahedral for the Synthesis of Covalent Organic Frameworks. *J. Am. Chem. Soc.* **2020**, *142* (8), 3718–3723.

(72) Zhu, Q.; Wang, X.; Clowes, R.; Cui, P.; Chen, L.; Little, M. A.; Cooper, A. I. 3D Cage Cofs: A Dynamic Three-Dimensional Covalent Organic Framework with High-Connectivity Organic Cage Nodes. *J. Am. Chem. Soc.* **2020**, *142* (39), 16842–16848.

(73) Li, Z.; Sheng, L.; Wang, H.; Wang, X.; Li, M.; Xu, Y.; Cui, H.; Zhang, H.; Liang, H.; Xu, H.; He, X. Three-Dimensional Covalent Organic Framework with Ceq Topology. *J. Am. Chem. Soc.* **2021**, *143* (1), 92–96.

(74) Li, H.; Ding, J.; Guan, X.; Chen, F.; Li, C.; Zhu, L.; Xue, M.; Yuan, D.; Valtchev, V.; Yan, Y.; Qiu, S.; Fang, Q. Three-Dimensional Large-Pore Covalent Organic Framework with Stp Topology. *J. Am. Chem. Soc.* **2020**, *142* (31), 13334–13338.

(75) Li, Z.; Sheng, L.; Hsueh, C.; Wang, X.; Cui, H.; Gao, H.; Wu, Y.; Wang, J.; Tang, Y.; Xu, H.; He, X. Three-Dimensional Covalent Organic Frameworks with Hea Topology. *Chem. Mater.* **2021**, *33* (24), 9618–9623.

(76) Martínez-Abadía, M.; Strutyński, K.; Lerma-Berlanga, B.; Stoppiello, C. T.; Khlobystov, A. N.; Martí-Gastaldo, C.; Saeki, A.; Melle-Franco, M.; Mateo-Alonso, A. π-Interpenetrated 3D Covalent Organic Frameworks from Distorted Polycyclic Aromatic Hydrocarbons. *Angew. Chemie - Int. Ed.* **2021**, *60* (18), 9941–9946.

(77) Lu, H. S.; Han, W. K.; Yan, X.; Chen, C. J.; Niu, T.; Gu, Z. G. A 3D Anionic Metal Covalent Organic Framework with Soc Topology Built from an Octahedral TiIV Complex for Photocatalytic Reactions. *Angew. Chemie - Int. Ed.* **2021**, *60* (33), 17881–17886.

(78) Gropp, C.; Ma, T.; Hanikel, N.; Yaghi, O. M. Design of Higher Valency in Covalent Organic Frameworks. *Science.* **2020**, *370* (6515), eabd6406.

(79) Kang, X.; Han, X.; Yuan, C.; Cheng, C.; Liu, Y.; Cui, Y. Reticular Synthesis of Tbo Topology Covalent Organic Frameworks. *J. Am. Chem. Soc.* **2020**, *142* (38), 16346–16356.

(80) Nguyen, H. L.; Gropp, C.; Ma, Y.; Zhu, C.; Yaghi, O. M. 3D Covalent Organic Frameworks Selectively Crystallized through Conformational Design. *J. Am. Chem. Soc.* **2020**, *142* (48), 20335–20339.

(81) Yahiaoui, O.; Fitch, A. N.; Hoffmann, F.; Fröba, M.; Thomas, A.; Roeser, J. 3D Anionic Silicate Covalent Organic Framework with Srs Topology. *J. Am. Chem. Soc.* **2018**, *140* (16), 5330–5333.

(82) Ockwig, N. W.; Delgado-Friedrichs, O.; O'Keeffe, M.; Yaghi, O. M. Reticular Chemistry: Occurrence and Taxonomy of Nets and Grammar for the Design of Frameworks. *Acc. Chem. Res.* **2005**, *38* (3), 176–182.

(83) Chen, Z.; Jiang, H.; O'Keeffe, M.; Eddaoudi, M. Minimal Edge-Transitive Nets for the Design and Construction of Metal-Organic Frameworks. *Faraday Discuss.* **2017**, *201*, 127–143.

(84) Bureekaew, S.; Schmid, R. Hypothetical 3D-Periodic Covalent Organic Frameworks: Exploring the Possibilities by a First Principles Derived Force Field. *CrystEngComm* **2013**, *15* (8), 1551–1562.

(85) Beaudoin, D.; Maris, T.; Wuest, J. D. Constructing Monocrystalline Covalent Organic Networks by Polymerization. *Nat. Chem.* **2013**, *5* (10), 830–834.

(86) Liang, L.; Qiu, Y.; Wang, W. D.; Han, J.; Luo, Y.; Yu, W.; Yin, G. L.; Wang, Z. P.; Zhang, L.; Ni, J.; Niu, J.; Sun, J.; Ma, T.; Wang, W. Non-Interpenetrated Single-Crystal Covalent Organic Frameworks. *Angew. Chemie - Int. Ed.* **2020**, *59* (41), 17991–17995.

(87) Hu, Y.; Teat, S. J.; Gong, W.; Zhou, Z.; Jin, Y.; Chen, H.; Wu, J.; Cui, Y.; Jiang, T.; Cheng, X.; Zhang, W. Single Crystals of Mechanically Entwined Helical Covalent Polymers. *Nat. Chem.* **2021**, *13* (7), 660–665.

(88) Huang, Z.; Grape, E. S.; Li, J.; Inge, A. K.; Zou, X. 3D Electron Diffraction as an Important Technique for Structure Elucidation of Metal-Organic Frameworks and Covalent Organic Frameworks. *Coord. Chem. Rev.* **2021**, *427*, 213583.

(89) Wang, B.; Rhauderwiek, T.; Inge, A. K.; Xu, H.; Yang, T.; Huang, Z.; Stock, N.; Zou, X. A Porous Cobalt Tetraphosphonate Metal–Organic Framework: Accurate Structure and Guest Molecule Location Determined by Continuous-Rotation Electron Diffraction. *Chem. - A Eur. J.* **2018**, *24* (66), 17429–17433.

(90) Cui, P.; Svensson Grape, E.; Spackman, P. R.; Wu, Y.; Clowes, R.; Day, G. M.; Inge, A. K.; Little, M. A.; Cooper, A. I. An Expandable Hydrogen-Bonded Organic Framework Characterized by Three-Dimensional Electron Diffraction. *J. Am. Chem. Soc.* **2020**, *142* (29), 12743–12750.

(91) Zhang, Y. B.; Su, J.; Furukawa, H.; Yun, Y.; Gándara, F.; Duong, A.; Zou, X.; Yaghi, O. M. Single-Crystal Structure of a Covalent Organic Framework. *J. Am. Chem. Soc.* **2013**, *135* (44), 16336–16339.

(92) Ding, H.; Li, J.; Xie, G.; Lin, G.; Chen, R.; Peng, Z.; Yang, C.; Wang, B.; Sun, J.; Wang, C. An AIEgen-Based 3D Covalent Organic Framework for White Light-Emitting Diodes. *Nat. Commun.* **2018**, *9*, 5234.

(93) Liu, X.; Li, J.; Gui, B.; Lin, G.; Fu, Q.; Yin, S.; Liu, X.; Sun, J.; Wang, C. A Crystalline Three-Dimensional Covalent Organic Framework with Flexible Building Blocks. *J. Am. Chem. Soc.* **2021**, *143* (4), 2123–2129.

(94) Jin, F.; Nguyen, H. L.; Zhong, Z.; Han, X.; Zhu, C.; Pei, X.; Ma, Y.; Yaghi, O. M. Entanglement of Square Nets in Covalent Organic Frameworks. *J. Am. Chem. Soc.* **2022**, *144* (4), 1539–1544.

(95) Gao, C.; Li, J.; Yin, S.; Lin, G.; Ma, T.; Meng, Y.; Sun, J.; Wang, C. Isostructural Three-Dimensional Covalent Organic Frameworks. *Angew. Chemie - Int. Ed.* **2019**, *58* (29), 9770–9775.

(96) Xu, H. Sen; Luo, Y.; Li, X.; See, P. Z.; Chen, Z.; Ma, T.; Liang, L.; Leng, K.; Abdelwahab, I.; Wang, L.; Li, R.; Shi, X.; Zhou, Y.; Lu, X. F.; Zhao, X.; Liu, C.; Sun, J.; Loh, K. P. Single Crystal of a One-Dimensional Metallo-Covalent Organic Framework. *Nat. Commun.* **2020**, *11*, 1434.

(97) Sun, T.; Lei, W.; Ma, Y.; Zhang, Y. B. Unravelling Crystal Structures of Covalent Organic Frameworks by Electron Diffraction Tomography. *Chinese J. Chem.* **2020**, *38* (10), 1153–1166.

(98) Freund, R.; Canossa, S.; Cohen, S. M.; Yan, W.; Deng, H.; Guillerm, V.; Eddaoudi, M.; Madden, D. G.; Fairen-Jimenez, D.; Lyu, H.; Macreadie, L. K.; Ji, Z.; Zhang, Y.; Wang, B.; Haase, F.; Wöll, C.; Zaremba,

O.; Andreo, J.; Wuttke, S.; Diercks, C. S. 25 Years of Reticular Chemistry. *Angew. Chemie - Int. Ed.* **2021**, *60* (45), 23946–23974.

(99) Sun, T.; Wei, L.; Chen, Y.; Ma, Y.; Zhang, Y. B. Atomic-Level Characterization of Dynamics of a 3D Covalent Organic Framework by Cryo-Electron Diffraction Tomography. *J. Am. Chem. Soc.* **2019**, *141* (28), 10962–10966.

(100) Cavka, J. H.; Jakobsen, S.; Olsbye, U.; Guillou, N.; Lamberti, C.; Bordiga, S.; Lillerud, K. P. A New Zirconium Inorganic Building Brick Forming Metal Organic Frameworks with Exceptional Stability. *J. Am. Chem. Soc.* **2008**, *130* (42), 13850–13851.

(101) Altomare, A.; Corriero, N.; Cuocci, C.; Falcicchio, A.; Moliterni, A.; Rizzi, R. EXPO Software for Solving Crystal Structures by Powder Diffraction Data: Methods and Application. *Cryst. Res. Technol.* **2015**, *50* (9–10), 737–742.

(102) Gándara, F.; Bennett, T. D. Crystallography of Metal-Organic Frameworks. *IUCrJ* **2014**, *1*, 563–570.

(103) Chen, Y.; Shi, Z. L.; Wei, L.; Zhou, B.; Tan, J.; Zhou, H. L.; Zhang, Y. B. Guest-Dependent Dynamics in a 3D Covalent Organic Framework. *J. Am. Chem. Soc.* **2019**, *141*(7), 3298-3303.

(104) Gándara, F.; Uribe-Romo, F. J.; Britt, D. K.; Furukawa, H.; Lei, L.; Cheng, R.; Duan, X.; O'Keeffe, M.; Yaghi, O. M. Porous, Conductive Metal-Triazolates and Their Structural Elucidation by the Charge-Flipping Method. *Chem. - A Eur. J.* **2012**, *18* (34), 10595–10601.

(105) Xie, D.; Baerlocher, C.; McCusker, L. B. Using Phases Retrieved from Two-Dimensional Projections to Facilitate Structure Solution from X-Ray Powder Diffraction Data. *J. Appl. Crystallogr.* **2011**, *44* (5), 1023–1032.

(106) Nguyen, H. L.; Hanikel, N.; Lyle, S. J.; Zhu, C.; Proserpio, D. M.; Yaghi, O. M. A Porous Covalent Organic Framework with Voided Square Grid Topology for Atmospheric Water Harvesting. *J. Am. Chem. Soc.* **2020**, *142* (5), 2218–2221.

(107) Nguyen, H. L.; Gropp, C.; Yaghi, O. M. Reticulating 1D Ribbons into 2D Covalent Organic Frameworks by Imine and Imide Linkages. *J. Am. Chem. Soc.* **2020**, *142* (6), 2771–2776.

(108) Suga, M.; Asahina, S.; Sakuda, Y.; Kazumori, H.; Nishiyama, H.; Nokuo, T.; Alfredsson, V.; Kjellman, T.; Stevens, S. M.; Cho, H. S.; Cho, M.; Han, L.; Che, S.; Anderson, M. W.; Schüth, F.; Deng, H.; Yaghi, O. M.; Liu, Z.; Jeong, H. Y.; Stein, A.; Sakamoto, K.; Ryoo, R.; Terasaki, O. Recent Progress in Scanning Electron Microscopy for the Characterization of Fine Structural Details of Nano Materials. *Prog. Solid State Chem.* **2014**, *42* (1–2), 1–21.

(109) Mayoral, A.; Ma, Y.; Terasaki, O. Some Efforts Toward Understanding Structural Features of MOF/COF. *Isr. J. Chem.* **2018**, *58* (9), 1157–1163.

(110) Tang, C. Y.; Yang, Z. Chapter 8 - Transmission Electron Microscopy (TEM). In *Membrane Characterization*; Hilal, N., Ismail, A. F., Matsuura, T., Oatley-Radcliffe, D., Eds.; Elsevier, 2017; pp 145–159.

(111) Zhan, G.; Cai, Z. F.; Strutyński, K.; Yu, L.; Herrmann, N.; Martínez-Abadía, M.; Melle-Franco, M.; Mateo-Alonso, A.; Feyter, S. De. Observing Polymerization in 2D Dynamic Covalent Polymers. *Nature* **2022**, *603* (7903), 835–840.

(112) Thommes, M.; Kaneko, K.; Neimark, A. V.; Olivier, J. P.; Rodriguez-Reinoso, F.; Rouquerol, J.; Sing, K. S. W. Physisorption of Gases, with Special Reference to the Evaluation of Surface Area and Pore Size Distribution (IUPAC Technical Report). *Pure Appl. Chem.* **2015**, *87* (9–10), 1051–1069.

(113) Kim, K. C.; Yoon, T. U.; Bae, Y. S. Applicability of Using CO2 Adsorption Isotherms to Determine BET Surface Areas of Microporous Materials. *Microporous Mesoporous Mater.* **2016**, *224*, 294–301.

(114) Tsao, C. S.; Yu, M. S.; Chung, T. Y.; Wu, H. C.; Wang, C. Y.; Chang, K. Sen; Chen, H. L. Characterization of Pore Structure in Metal-Organic Framework by Small-Angle X-Ray Scattering. *J. Am. Chem. Soc.* **2007**, *129* (51), 15997–16004.

(115) Plötze, M.; Niemz, P. Porosity and Pore Size Distribution of Different Wood Types as Determined by Mercury Intrusion Porosimetry. *Eur. J. Wood Wood Prod.* **2011**, *69* (4), 649–657.

(116) Beurroies, I.; Boulhout, M.; Llewellyn, P. L.; Kuchta, B.; Férey, G.; Serre, C.; Denoyel, R. Using Pressure to Provoke the Structural Transition of Metal-Organic Frameworks. *Angew. Chemie - Int. Ed.* **2010**, *49* (41), 7526–7529.

(117) Okolo, G. N.; Everson, R. C.; Neomagus, H. W. J. P.; Roberts, M. J.; Sakurovs, R. Comparing the Porosity and Surface Areas of Coal as Measured by Gas Adsorption, Mercury Intrusion and SAXS Techniques. *Fuel* **2015**, *141*, 293–304.

(118) Willems, T. F.; Rycroft, C. H.; Kazi, M.; Meza, J. C.; Haranczyk, M. Algorithms and Tools for High-Throughput Geometry-Based Analysis of Crystalline Porous Materials. *Microporous Mesoporous Mater.* **2012**, *149* (1), 134–141.

(119) Martin, R. L.; Haranczyk, M. Construction and Characterization of Structure Models of Crystalline Porous Polymers. *Cryst. Growth Des.* **2014**, *14* (5), 2431–2440.

(120) Ding, X.; Guo, J.; Feng, X.; Honsho, Y.; Guo, J.; Seki, S.; Maitarad, P.; Saeki, A.; Nagase, S.; Jiang, D. Synthesis of Metallophthalocyanine Covalent Organic Frameworks That Exhibit High Carrier Mobility and Photoconductivity. *Angew. Chemie - Int. Ed.* **2011**, *50* (6), 1289–1293.

(121) Rappe, A. K.; Goddard, W. A. Charge Equilibration for Molecular Dynamics Simulations. *J. Phys. Chem.* **1991**, *95* (8), 3358–3363.

(122) Furukawa, H.; Kim, J.; Ockwig, N. W.; O'Keeffe, M.; Yaghi, O. M. Control of Vertex Geometry, Structure Dimensionality, Functionality, and Pore Metrics in the Reticular Synthesis of Crystalline Metal-Organic Frameworks and Polyhedra. *J. Am. Chem. Soc.* **2008**, *130* (35), 11650–11661.

Chapter 2

A cubic 3D covalent organic framework with nbo topology

2.1 Author contributions

Dr. Linjiang Chen helped with the geometry optimization of the COFs. Dr. Zhiwei Fu helped with the synthesis of $(OH)_8PcCo$ monomer at the beginning of this project. Dr. Marc Little performed the single crystal measurement and refined the data of the model compounds. Dr. Alex James helped with the N_2 sorption measurement. Dr. Mounib Bahri performed the TEM measurement. Dr. Lunjie Liu performed the SEM measurement. Dr. Xiaoyan Wang, Dr. Yong Yan, Dr. Hongjun Niu and Dr. Alexandros Katsoulidis provided useful suggestions on supercritical CO_2 drying. Dr. Samantha Y. Chong helped with the PXRD refinement of COFs. Dr. Hongmei Chen helped with the ICP-OES measurement. Dr. Glyn Connolly helped with the analyse of ^{11}B NMR spectra. Solid-state NMR spectra was performed by the test service from University of Durham. All other work was performed by the thesis author.

2.2 Background

COFs with **dia**, **lon**, **bor**, **ctn**, **pts** and **ljh** topologies have been realized using organic tetrahedral units (like adamantane, tetraphenyl methane, tetraphenyl silane and their derivatives), while trigonal prism-shaped organic cages[1] and triptycene were used for constructing COFs of **acs**, **stp, ceq** and **hea** topologies, *etc*.[2] The limited choice of these polyhedral organic building blocks is one of the main reasons why the structural diversity of 3D COFs is far less explored compared with MOFs, where metal clusters with up to 24 points of extension have been reported.[3] Besides, the synthesis challenge of multi-linking organic polyhedral type building blocks further adds complexity to this route.

A second strategy for constructing 3D COFs is to control the alignment of planar (or near planar) building blocks to achieve the desired framework topology. Correct orientation of the building blocks to generate a 3D COF can be established through conformational flexibility in the organic linkages, such as rotatable imine bonds, as exemplified by 3D COFs with the **ffc**[4] or **tbo**[5] topology. However, conformational flexibility can be hard to control and hence it can be challenging to target specific topologies using a priori design. Indeed, the precise control of linker conformation was key to the synthesis of **fjh** COFs, and this involved setting up multiple dihedral angles, not just the rotatable imine bonds.[6] Alternatively, rigid linkages with a reliable polyhedral geometry can be used to connect and reticulate building blocks into 3D arrangements, for example, to create COFs with the **srs**[7] and **rra**[8] topology. Such predesigned linkages increase the likelihood of the building blocks adopting the desired arrangement while avoiding the synthetic complexity of 3D polyhedral building blocks. We use this latter strategy in this work to target 3D COFs with the **nbo** topology.

The **nbo** net is one of the edge-transitive topologies for building blocks of square geometry. As a rule of thumb, for a given set of building units, the edge-transitive nets are the most likely ones to form.[9] According to the Reticular Chemistry Structure Resource (RCSR),[10] there are five possible crystal nets for planar square building blocks (**Figure 2.1**).[11] Among them, the 2D **sql**[12] and **kgm**[13] topologies have been adopted for several COFs (**Figure 2.1a**).[14] Characteristic dihedral angles exist between neighbouring square planar units in the 3D **nbo**, **lvt** and **rhr** topologies (**Figure 2.1b**). The **lvt** and **rhr** nets require dihedral angles to be around 60°. The **nbo** net requires a 90° dihedral angle, which is synthetically addressable. The **nbo** net is also hetero-dual, which means it is less likely to self-interpenetrate compared to self-dual nets,[15] such as **dia** nets, which have been shown to exhibit up to 11-fold interpenetration.[16] We expect to increase the likelihood of obtaining a non-interpenetrated framework, to take the advantage of either a larger pore channel or simplify the following COFs crystal structures solve.

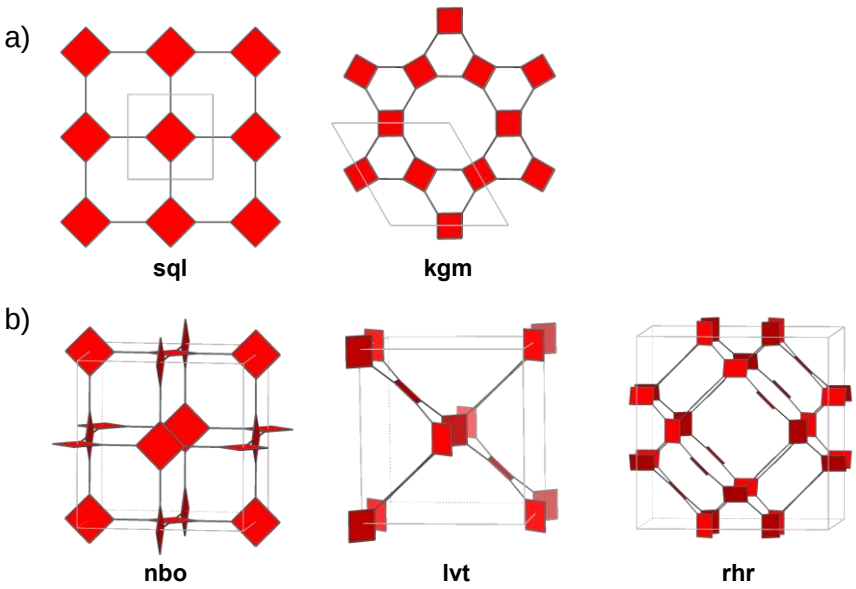

Figure 2.1. (a) 2D (b) 3D edge-transitive topologies build from single 4-connected (4-c) planar vertex. All topologies are shown as their corresponding augmented net. Grey line corresponds to unit cell.

In this work, we applied the easily synthesizable $(OH)_8PcCo$ units as the square planar building block and introduced the tetrahedra-shaped spiroborate linkage to reticulate the two neighbouring $(OH)_8PcCo$ units into perpendicular orientation. A conformer search result of the reported spiroborate molecule in the Cambridge Structure Database (CSD) supports our reticular design strategy (**Figure 2.2**). Spiroborate linkage have been widely used for the synthesis of organic macrocycles,[17] cages,[18] COFs[19,20] and, during the course of this study, mechanically entwined helical covalent polymers.[21] Spiroborate linkages can be formed reversibly, which well satisfies the general requirement for the synthesis of COFs because the linkages can undergo reversible error correction to give ordered crystalline frameworks while satisfying the precise 3D geometrical constraints. Also, the short spiroborate linkage increased the likelihood to obtain non-interpenetrated 3D COFs.

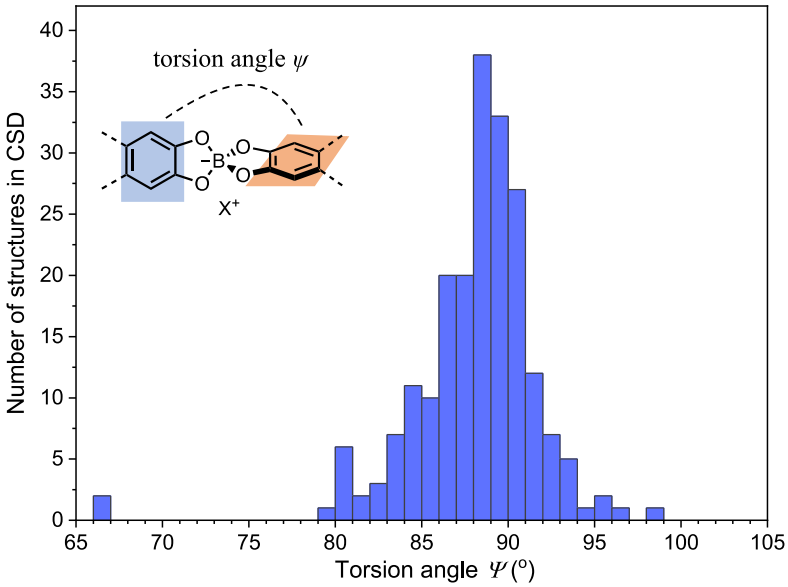

Figure 2.2. Distribution of the torsion angles expressed by spiroborate units as in the CSD at the time of this project (in total, 129 structure hits). The mostly reported angle is close to 90 degrees, supporting our reticular design strategy. X^+ in the graph corresponds to any type of counter cation.

2.3 Experimental section

2.3.1 Synthesis of monomers

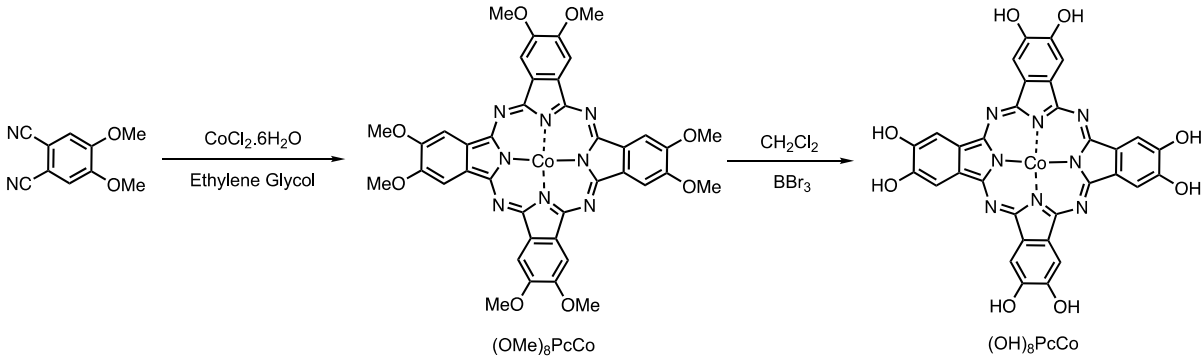

Figure 2.3. Scheme for the synthesis of $(OH)_8PcCo$.

$(OH)_8PcCo$ was synthesized according to a reported procedure with some modifications.[22,23]

Synthesis of $(OMe)_8PcCo$: Under N_2 atmosphere, 4,5-dimethoxyphthalodinitrile (1.129 g, 6.0 mmol) and cobalt (II) chloride hexahydrate (0.238 g, 1.0 mmol) were heated in 20 mL of ethylene glycol at 200 °C for 5 h, after which the mixture was cooled somewhat (below 100 ^oC), and an equal volume of water was added. The mixture was suction filtered while still hot using a Whatman PTFE membrane filter with pore size of 0.45 µm, and the filter cake was washed with hot water. The crude product was boiled at 120 ^oC for 2 h, first with 100 mL of 1 M HCl (aq.) and then with 100 mL of 1 M NaOH (aq.), hot filtered, and washed with hot water each time until the filtrate was colourless and neutral. The solid material was washed with methanol and dried in vacuo 6 h at 60 °C, yield 41.1% as black powders. MALDI-TOF MS for $C_{40}H_{32}CoN_8O_8$ (calcd. 811.17), found m/z = 811.17 ([M]+).

Synthesis of $(OH)_8PcCo$: under N_2 atmosphere, $(OMe)_8PcCo$ (0.5 g, 0.62 mmol) was suspended in 40 mL of anhydrous dichloromethane and this system was stirred under ice bath for 10 min. Then, boron tribromide (BBr_3) solution (1.0 M in methylene chloride) (24.7 mL, 24.70 mmol) was added into the system slowly under ice bath. Upon the complete addition of BBr_3 solution, the mixture was warmed to room temperature and stirred for 3 days. After that, 20 mL of methanol was added slowly (dropwise add in at the beginning) under ice bath to quench the reaction (open system). The solvent was removed, the residue liquid was washed by methanol and centrifuged. After repeating the cycle of wash and centrifuge more than 3 times, the precipitate was collected and dried in vacuum, to give $(OH)_8PcCo$ as a black solid in 70% yield. MALDI-TOF MS for $C_{32}H_{16}CoN_8O_8$ (Calc. 699.04), found m/z = 699.24 ([M]+).

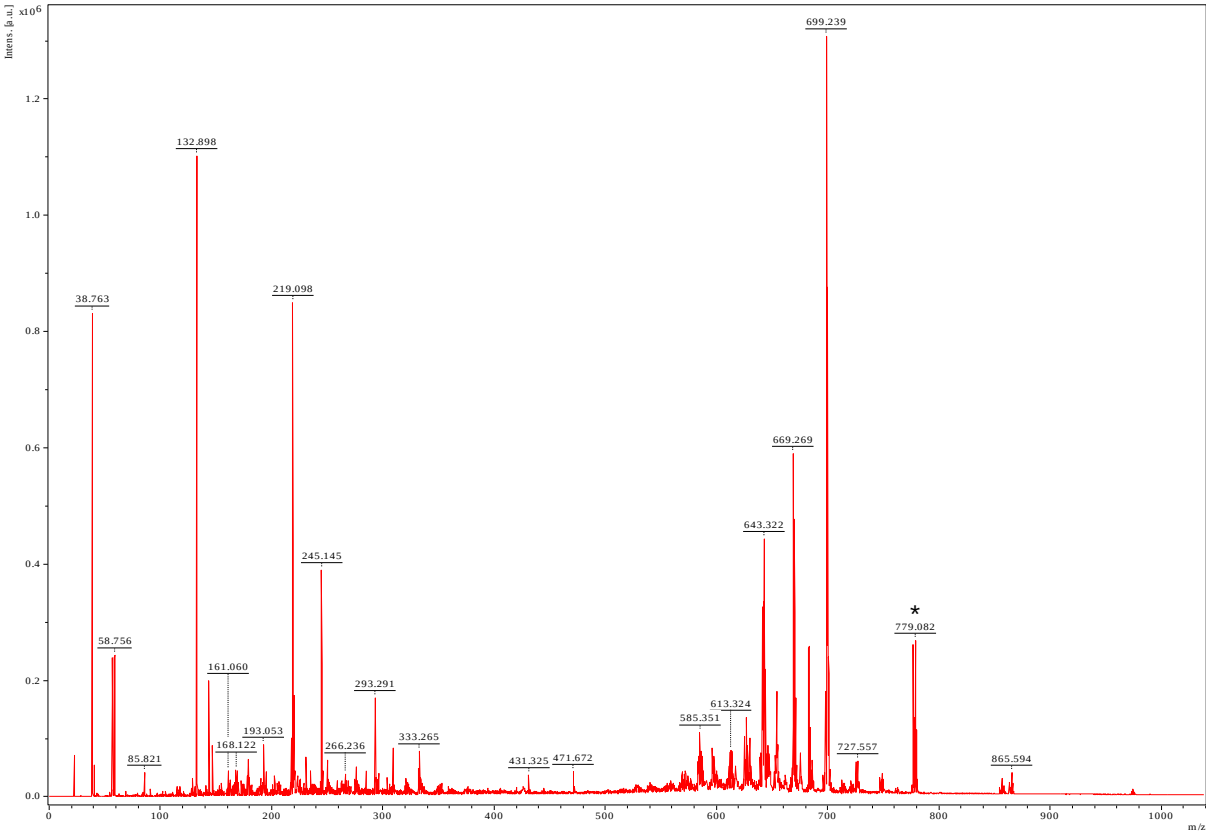

Figure 2.4. MALDI-TOF mass spectra of the as-synthesized $(OH)_8PcCo$, using 2-[(2E)-3-(4-tert-Butylphenyl)-2-methylprop-2-enylidene] malononitrile (DCTB) as the matrix, measured at positive mode. * Mass peak appeared at 779.082 can be [M+2Br]+, or [M+2K+2H]+.

2.3.2 Synthesis of COFs

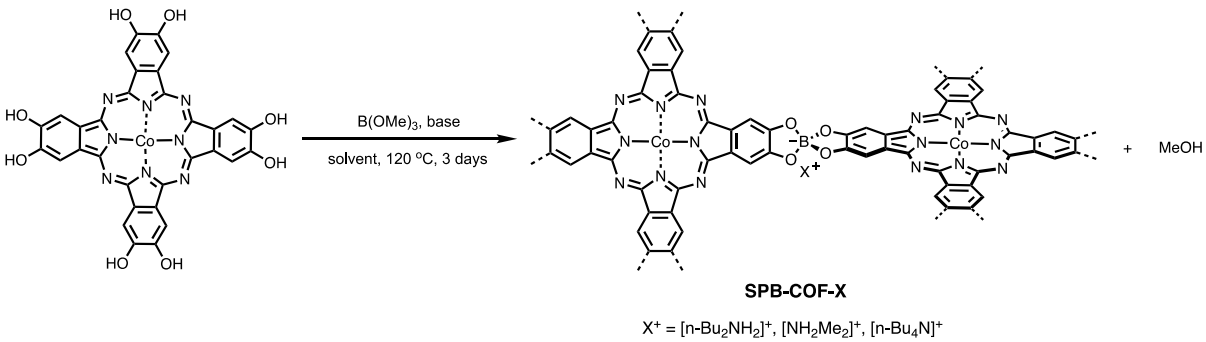

Figure 2.5. Scheme for the synthesis of SPB-COFs.

Synthesis of SPB-COF-DBA (X^+ = $[n\text{-}Bu_2NH_2]^+$): A 10 mL Pyrex tube was charged with $(OH)_8PcCo$ (21.0 mg, 0.03 mmol), $B(OMe)_3$ (7.0 µL, 0.06 mmol) and 1 mL *N,N*-dibutylformamide (DBF). The mixture was sonicated at room temperature for 2 mins, then flash frozen in liquid N_2 bath and degassed through three freeze-pump-thaw cycles and sealed under vacuum using a Schlenk line and oil pump. Upon warming to room temperature, the tube was put into 120 ^oC oven for 72 h and then taken out, which formed a black gel like product. After cooling to room temperature, the product was washed with anhydrous acetone to give a dark powder product. The obtained powder was immersed in anhydrous acetone, and the solvent was exchanged with fresh acetone for three times with an interval of 1.5 h. The wet sample was then transferred to a Critical Point Drier (Quorum-E3100AG), the sample was washed and exchanged with liquid CO_2 for four times with the interval of an hour. After the final exchange, the system was heated to reach the critical point of CO_2 and the formed supercritical CO_2 was then released slowly within an hour. After the chamber pressure returned to ambient, samples were then transferred into a gas adsorption test tube inside glove box and samples was then degassed at room temperature for 12 h, yield black powder 17.0 mg, 58.2%. Several batches of high crystallinity SPB-COF-DBA synthesised at such scale were combined after activation for the following measurements. This sample was directly used for gas adsorption test. This batch of SPB-COF-DBA was used in all the experiments/measurements unless otherwise specified. Anal. Cald for ($C_8H_2Co_{0.25}N_2O_2B_{0.5}$ + $C_4H_{10}N_{0.5}$ = $C_{48}H_{48}CoN_{10}O_8B_2$): C: 59.22; H: 4.97; N: 14.39. Found: C: 50.97; H: 4.15; N: 12.22. Theoretical Co content: 6.05 wt.%. ICP-OES analysis shows a Co content of 5.09 wt.%.

Synthesis of SPB-COF-DMA (X^+ = $[NH_2Me_2]^+$): The synthesis of SPB-COF-DMA follows the same reaction condition as for the synthesis of SPB-COF-DBA but introducing $NHMe_2$ solution (30.0 µL, 0.06 mmol, 2.0 M in THF) as base and 1.0 mL 1-methyl-2-pyrrolidinone (NMP) as the solvent. Yield black powders 17.2 mg, 71.19 %. Several batches of high crystallinity SPB-COF-

DMA synthesised at such scale were combined after activation for the following measurements. This batch of SPB-COF-DMA was used in all the experiments/measurements unless otherwise specified. Anal. Cald for ($C_8H_2Co_{0.25}N_2O_2B_{0.5}$ + $CH_4N_{0.5}$= $C_{36}H_{24}CoN_{10}O_8B_2$): C: 53.70; H: 3.00; N: 17.40. Found: C: 47.26; H: 3.69; N: 13.19. Theoretical Co content: 7.32 wt.%. ICP-OES analysis shows a Co content of 5.21 wt.%.

Synthesis of SPB-COF-TBA (X^+ = $[n\text{-}Bu_4N]^+$): The synthesis of SPB-COF-TBA follows the same reaction condition as for the synthesis of SPB-COF-DBA but introducing n-$Bu_4NOH.30H_2O$ (48.0 mg, 0.06 mmol) as base and 1.0 mL 1-methyl-2-pyrrolidinone (NMP) as the solvent. Yield black powders 30.0 mg, 83.5 %. Several batches of high crystallinity SPB-COF-TBA synthesised at such scale were combined after activation for the following measurements. This batch of SPB-COF-TBA was used in all the experiments/measurements unless otherwise specified. Anal. Cald for ($C_8H_2Co_{0.25}N_2O_2B_{0.5}$ + $C_8H_{18}N_{0.5}$= $C_{64}H_{80}CoN_{10}O_8B_2$): C: 64.17; H: 6.73; N: 11.69. Found: C: 54.74; H: 5.64; N: 10.98. Theoretical Co content: 4.92 wt.%. ICP-OES analysis shows a Co content of 4.54 wt.%.

Table 2.1. Synthetic conditions that were screened for synthesizing **SPB-COFs**.

Entry	Solvent 1	Solvent 2	Base	Temp (ºC)	Time (days)	Crystallinity
1	DMF	-	-	150	5	Poor
2	DMF	-	LiOH	120	3	amorphous
3	DMF	-	LiOH	120	7	poor
4	DMF (0.5)	mesitylene (0.5)	LiOH	120	3	poor
5	DMF (0.5)	mesitylene (0.5)	$NHMe_2$ (2.0 M in THF)	120	3	poor
6	DMAc	-	LiOH	120	7	amorphous
7	DMAc	-	$NHMe_2$ (2.0 M in THF)	120	7	amorphous
8	DEF	-	LiOH	120	3	amorphous
9	DBF	-	LiOH	120	3	high
10	DBF	-	pyridine	120	3	amorphous
11	DBF	-	-	120	3	high
12	NMP	-	LiOH	120	3	high
13	NMP	-	$NHMe_2$ (2.0 M in THF)	120	3	high
14	NMP	-	n-Bu_4NOH (10% in MeOH)	120	3	amorphous
15	NMP	-	n-$Bu_4NOH.30H_2O$	120	3	high
16	NMP	-	pyridine	120	3	poor
17	NMP	-	-	120	3	high

* All these synthetic conditions give product of high yield. Although we can also get crystalline product from synthesis entry 9, 12 and 17, we did not discuss them more in this paper since we cannot confirm the detailed type of counter cation in these structures (tried model compound synthesis at COF synthesis condition, did not get ideal NMR or any single crystal structures).

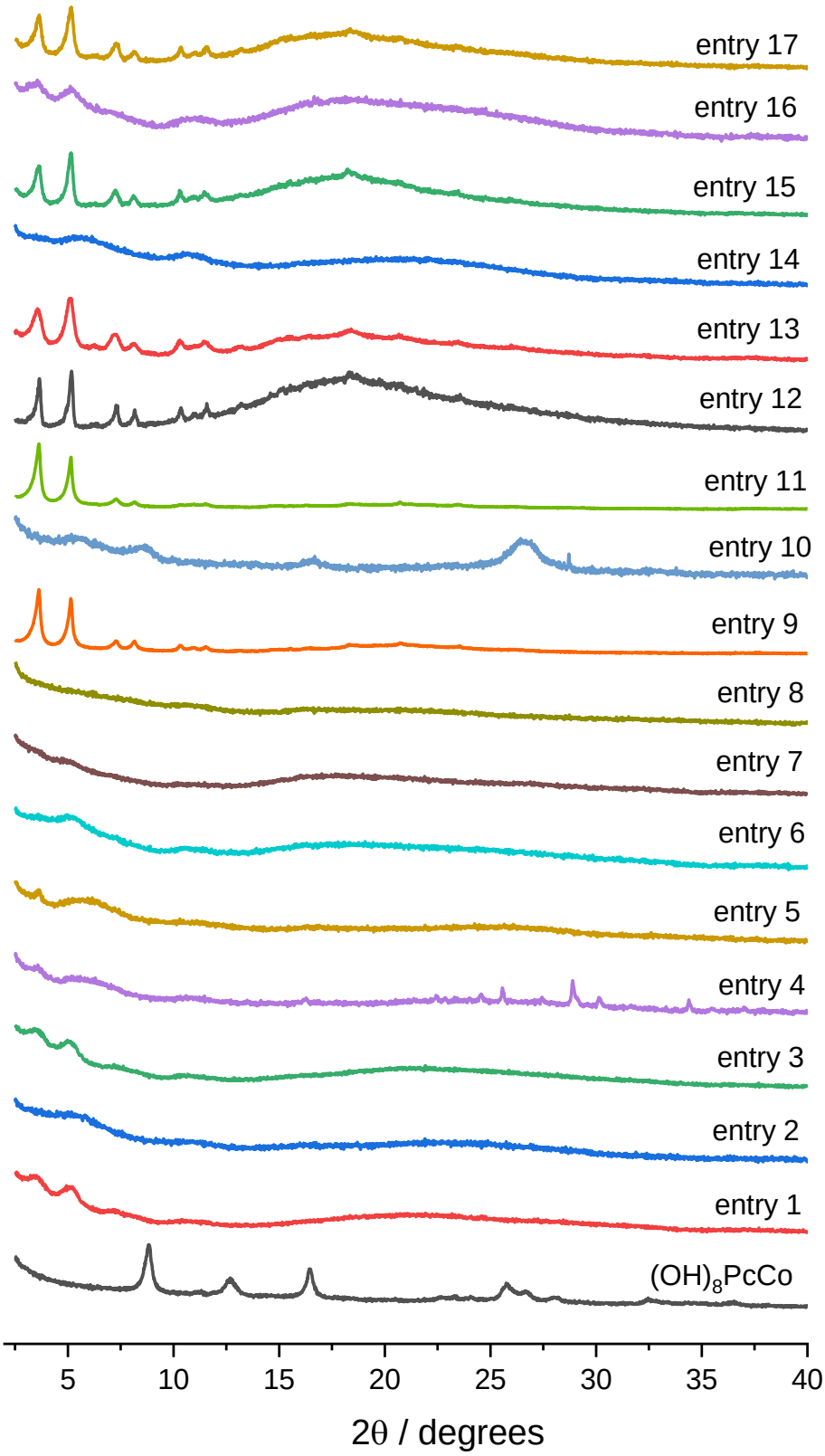

Figure 2.6. PXRD comparison of the SPB-COFs synthesis conditions screened.

2.3.3 Synthesis of model compounds

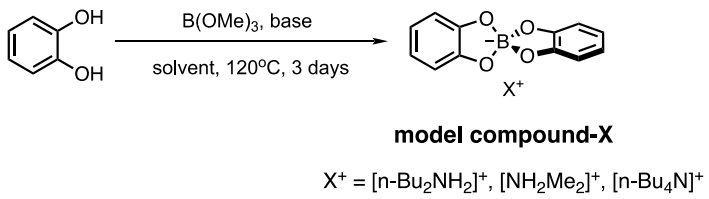

Figure 2.7. Scheme for the synthesis of model compounds.

Synthesis of model compound-DBA (X^+ = $[n\text{-}Bu_2NH_2]^+$): Under N_2 atmosphere, 1,2-dihydroxybenzene (1.05 g, 9.54 mmol) and $B(OMe)_3$ (0.53 mL, 4.77 mmol) were added into 50.0 mL *N*,*N*-dibutylformamide (DBF). The solution was then stirred at 120 °C for 3 days under reflux. During heating, the reaction changed from a transparent bright yellow solution to an opaque dark brown solution. After the reaction mixture was cooled to room temperature, solvent was removed using vacuum distillation. The residue brown oil like product was dissolved in very small amount of dichloromethane and then added dropwise into a stirred 300 mL cold diethyl ether to precipitate the product. The solid product was collected by filtration and dried in vacuum oven at 80 °C for 6 h to get 1.35 g pure product as light grey crystalline powders. Yield 79.3 %. Single crystals of model compound-DBA that were suitable for X-ray diffraction were grown from its saturated ethyl acetate solution at room temperature for a week.

^{1}H NMR (400 MHz, DMSO-d_6): δ = 8.06 (s, 2H), 6.48 (s, 8H), 2.86 (m, 4H), 1.53 (dt, 4H), 1.31 (m, 4H), 0.89 (t, 6H) ppm. ^{13}C NMR (100 MHz, DMSO-d_6): δ = 151.54, 117.29, 107.60, 46.54, 27.56, 19.22, 13.47 ppm. MS (ESI−) m/z calcd for $[C_{12}H_8BO_4]^-$ [M]−: 227.05. Found: 227.0526. MS (ESI+) m/z calcd for $[n\text{-}Bu_2NH_2]^+$ [M]+: 130.16. Found: 130.1588. Anal. Cald for $C_{20}H_{28}BNO_4$: C: 67.19, H: 7.92, N: 3.92. Found: C: 67.07, H: 7.94, N: 3.71.

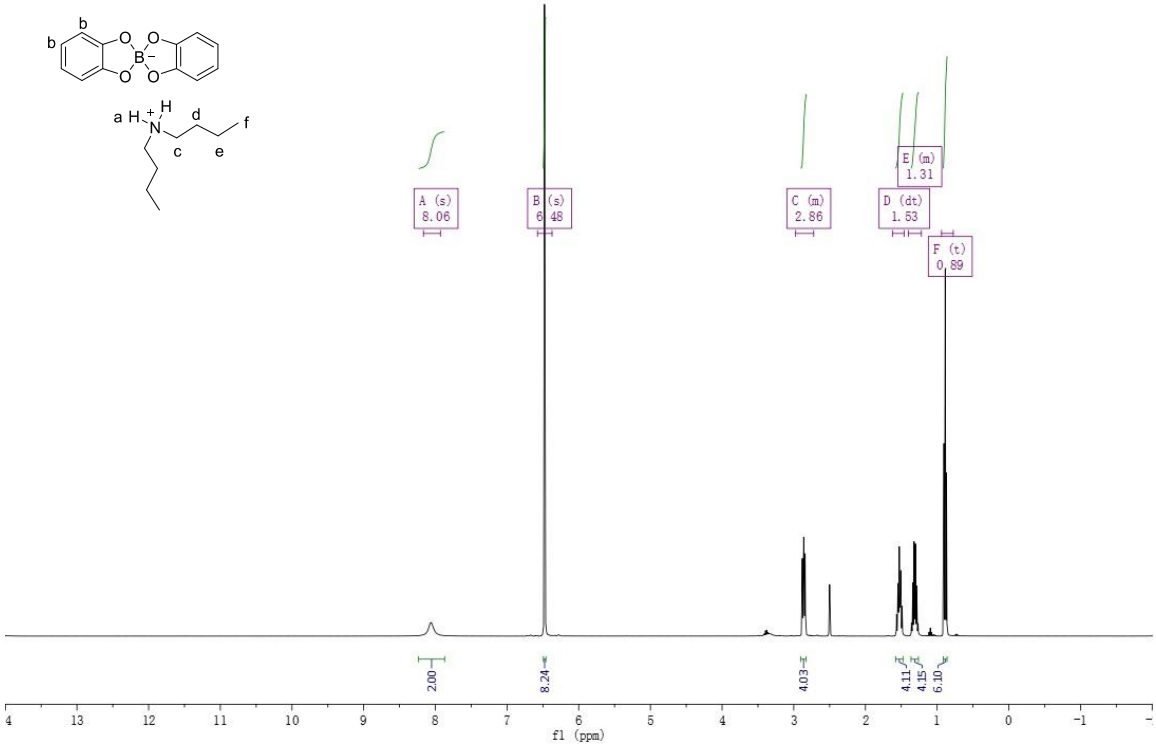

Figure 2.8. ^{1}H NMR spectra of **model compound-DBA** in DMSO-d_6. The four hydrogen atoms at the benzene unit is of the same chemical shift, which is in agreement with former reported similar structure.[24]

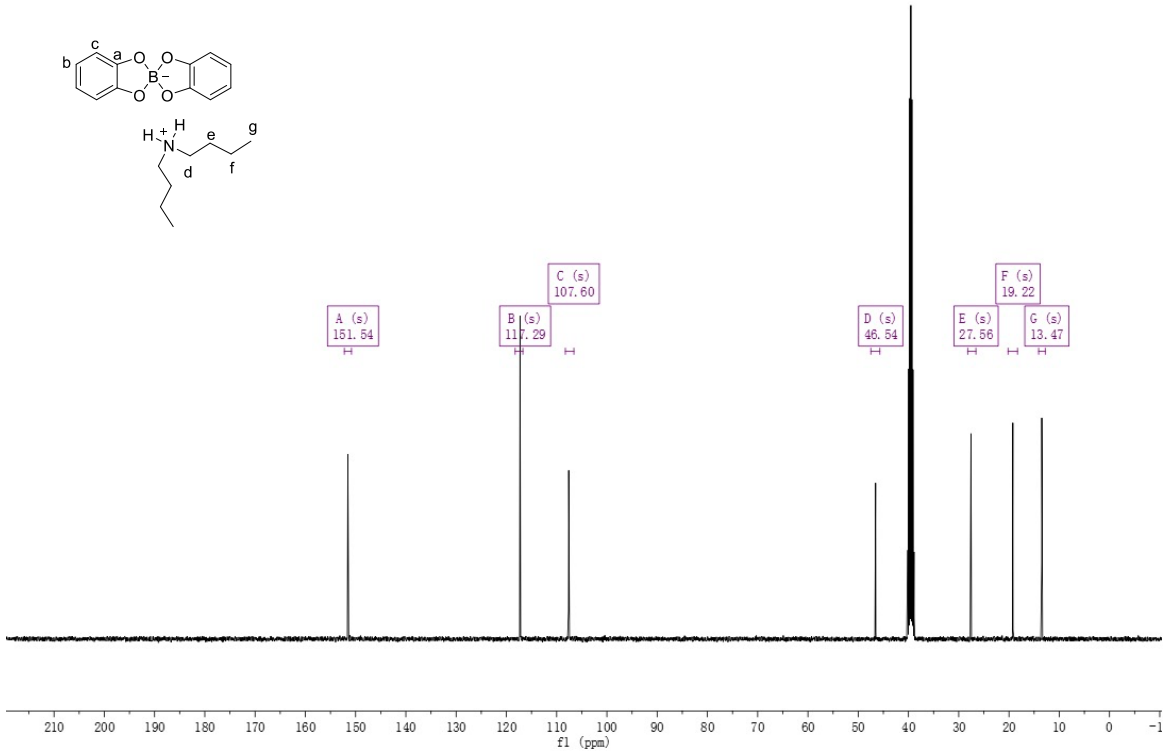

Figure 2.9. ^{13}C NMR spectra of **model compound-DBA** in DMSO-d_6.

Synthesis of model compound-DMA (X^+ = $[NH_2Me_2]^+$): model compound-DMA was synthesized from the similar method as above, but with $NHMe_2$ solution (2.4 mL, 4.77 mmol, 2.0 M in THF) as the base and using 1-methyl-2-pyrrolidinone (NMP) as the solvent. During heating, the reaction changed from a transparent light-yellow solution to an opaque dark red solution. Product was obtained as brown powders, yield 1.05 g, 81.0 %. No single crystal structure of this one obtained.

^{1}H NMR (400 MHz, DMSO-d_6): δ = 8.14 (s, 2H), 6.47 (m, 8H), 2.54 (s, 6H) ppm. ^{13}C NMR (100 MHz, DMSO-d_6): δ = 151.54, 117.28, 107.59, 34.38 ppm. MS (ESI−) m/z calcd for $[C_{12}H_8BO_4]^-$ [M]−: 227.05. Found: 227.0526. MS (ESI+) m/z calcd for $[NH_2Me_2]^+$ [M]+: 46.07. Found: 46.0657. Anal. Cald for $C_{14}H_{16}BNO_4$: C: 61.51, H: 5.92, N: 5.13. Found: C: 60.61, H: 5.91, N: 5.18.

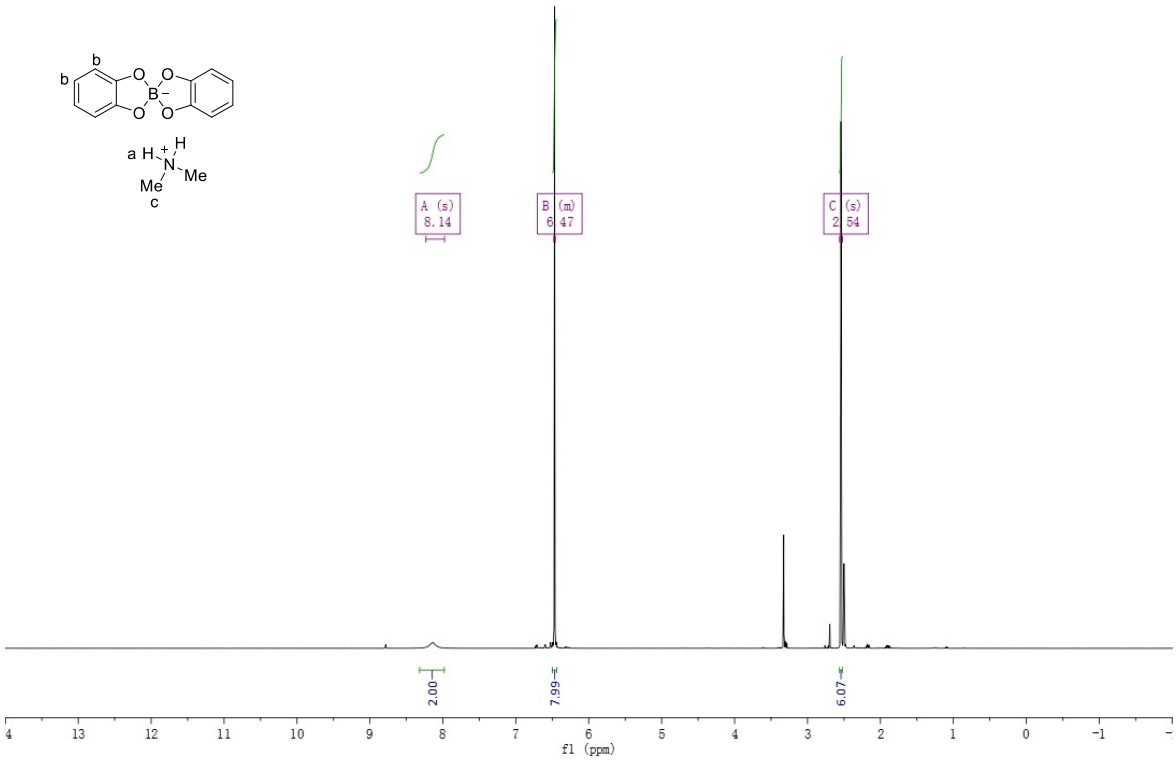

Figure 2.10. ^{1}H NMR spectra of **model compound-DMA** in DMSO-d_6.

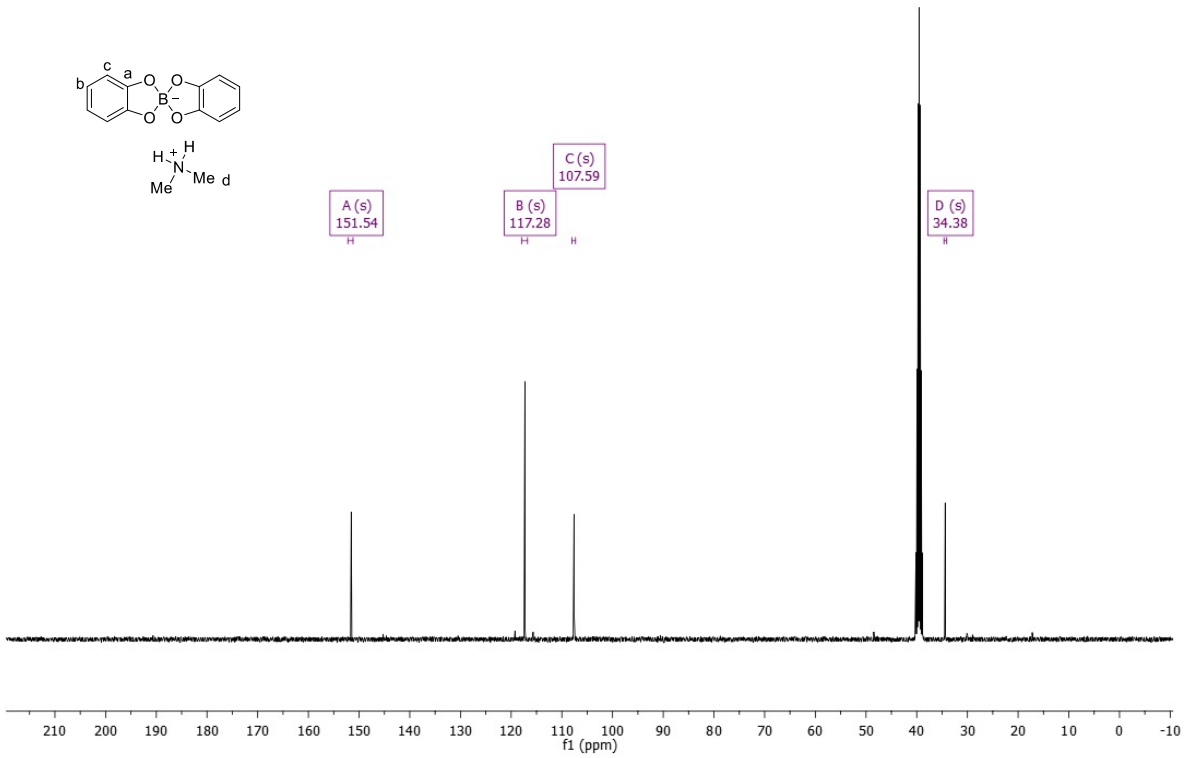

Figure 2.11. ^{13}C NMR spectra of **model compound-DMA** in DMSO-d_6.

Synthesis of model compound-TBA (X^+ = $[n\text{-}Bu_4N]^+$): model compound-TBA was synthesized from the similar method as above, but with n-$Bu_4NOH.30H_2O$ (3.81 g, 4.77 mmol) as the base and using 1-methyl-2-pyrrolidinone (NMP) as the solvent. During heating, the reaction changed from a transparent brown-yellow solution to an opaque dark brown solution. Product was obtained as brown powders, yield 1.80 g, 80.4 %. Single crystals of the model compound-TBA that were suitable for X-ray diffraction were grown by slow diffusion of diethyl ether into its saturated ethyl acetate or ethanol solution at room temperature for a week.

^{1}H NMR (400 MHz, DMSO-d_6): δ = 6.46 (m, 8H), 3.15 (m, 8H), 1.56 (m, 8H), 1.30 (m, 8H), 0.93 (t, 12H) ppm. ^{13}C NMR (100 MHz, DMSO-d_6): δ = 151.56, 117.25, 107.57, 57.49, 23.04, 19.19, 13.47 ppm. MS (ESI−) m/z calcd for $[C_{12}H_8BO_4]^-$ [M]−: 227.05. Found: 227.0491. MS (ESI+) m/z calcd for $[nBu_4N]^+$ [M]+: 242.28. Found: 242.2841. Anal. Cald for $C_{28}H_{44}BNO_4$: C: 71.59, H: 9.47, N: 2.98. Found: C: 70.82, H: 9.53, N: 3.24.

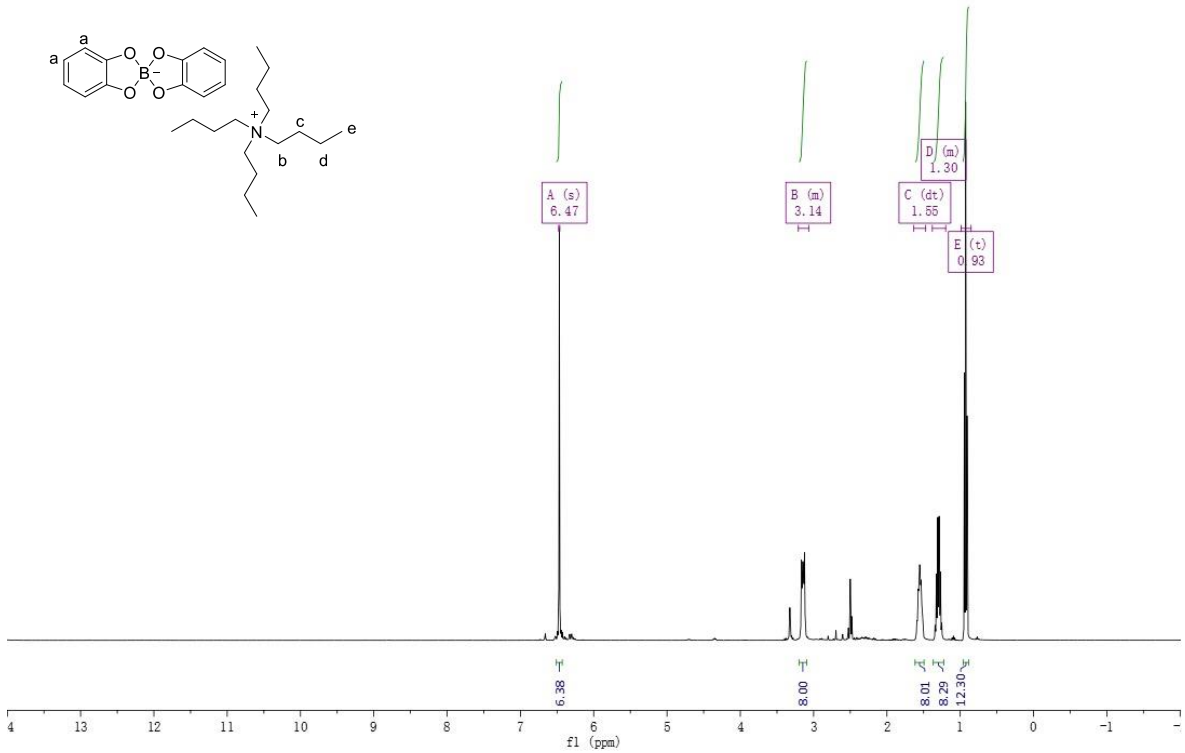

Figure 2.12. ^{1}H NMR spectra of of **model compound-TBA** in DMSO-d_6.

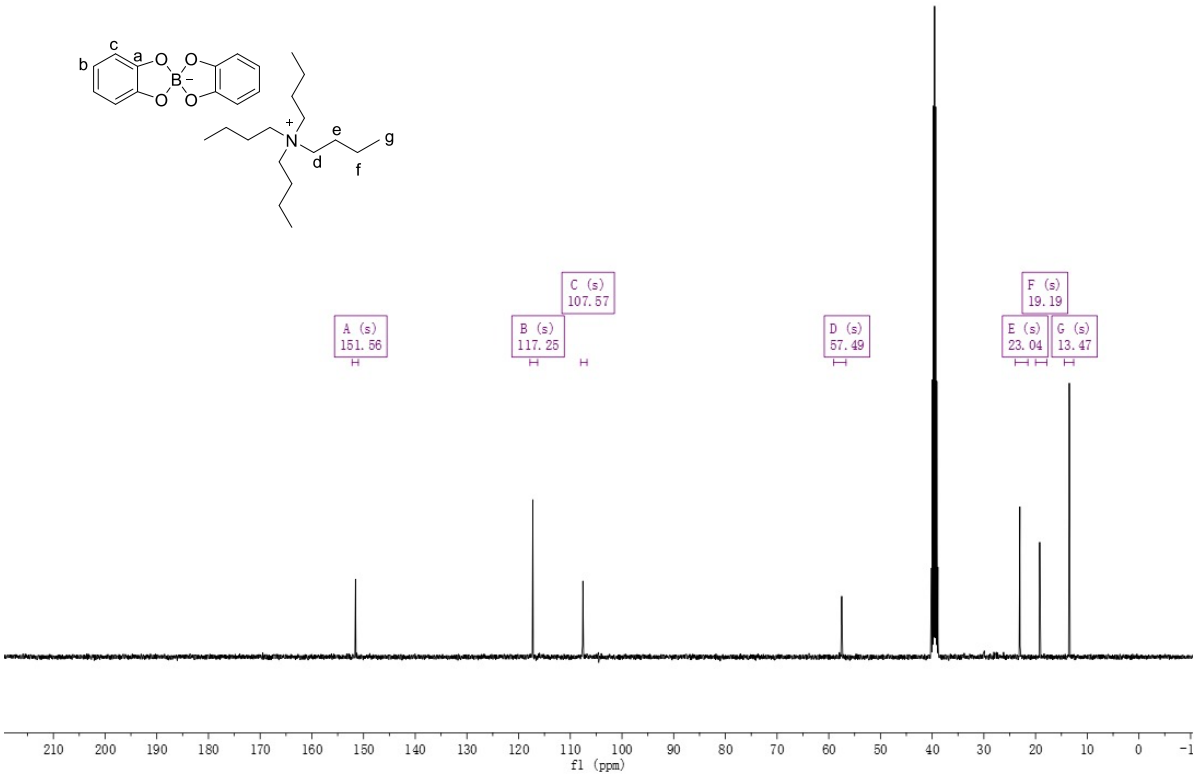

Figure 2.13. ^{13}C NMR spectra of **model compound-TBA** in DMSO-d_6.

2.4 Results and discussion

2.4.1 Powder X-ray diffraction analysis and structure modelling

Figure 2.14a shows the ChemDraw structure of the three SPB-COFs synthesised using our strategy. SPB-COF-DBA was synthesized from the reaction between $(OH)_8PcCo$ and $B(OMe)_3$ in neat *N*,*N*-dibutylformamide (DBF). The counter cation in SPB-COF-DBA is $[n\text{-}Bu_2NH_2]^+$, which is formed from the decomposition of DBF solvent under COFs synthesis conditions (120 °C /3 days) applied. SPB-COF-DMA and SPB-COF-TBA were synthesized from the same conditions as SPB-COF-DBA, but using 1-methyl-2-pyrrolidone (NMP) as the solvent and introduce $NHMe_2$ (2.0 M in THF) and $n\text{-}Bu_4NOH.30H_2O$ as the bases, which gave $[NH_2Me_2]^+$ and $[n\text{-}Bu_4N]^+$ as the counter cation, respectively. The existence of these two types of counter cations in SPB-COFs can be confirmed by the solid-state ^{13}C NMR spectra of the corresponding COFs and, by the solution ^{1}H NMR spectra and single crystal structure of the corresponding model compounds. These results will be discussed more detail in the latter part of this chapter.

The experimental PXRD pattern of SPB-COFs are shown in **Figure 2.14b**. The three SPB-COFs show a similar pattern, indicating the same framework structure and underlying topology. SPB-COF-DBA has the highest crystallinity and was chosen for full characterisation.

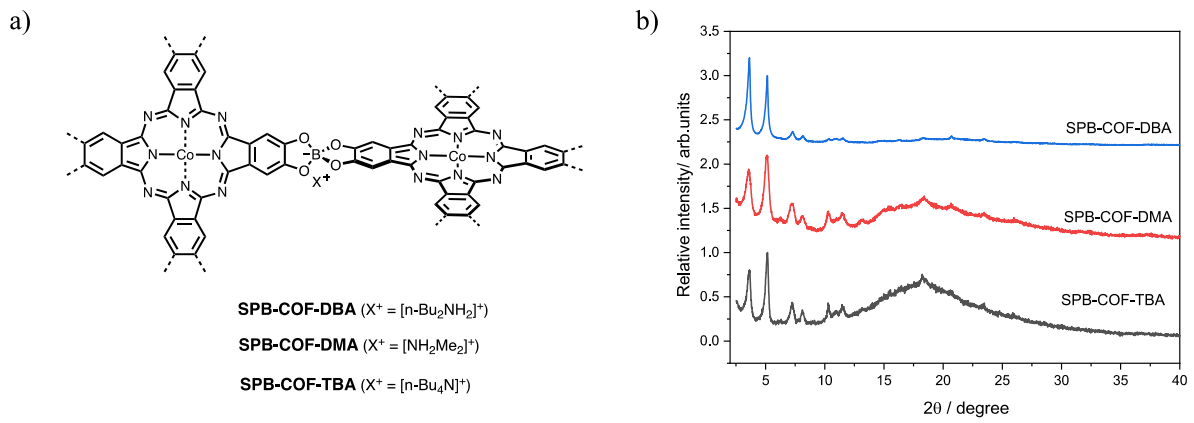

Figure 2.14. (a) scheme of the three **SPB-COFs**. **(b)** experimental PXRD comparison of the three **SPB-COFs**, as-synthesized sample.

Although we expect the spiroborate linkage can reticulate the two-neighbouring square PcCo unit into a perpendicular orientation and form the desired 3D COF **nbo** topology, there are four other possible topologies: **lvt**, **rhr**, **tcb** and **uks** (**Figure 2.15**) potentially accessible for building blocks of square planar geometry. To confirm the SPB-COFs structure, we built COFs models based on all of these topologies and compared the experimental PXRD with the simulated PXRD patterns.

A COF model of 2D **sql** topology (**Figure 2.1a**) was also built for comparison, supposing that the spiroborate linkage is of planar geometry (though, impossible from the CSD conformer search results, **Figure 2.2**). **Table 2.2** summarizes these 3D topologies, including the number of edges, calculated pore size and torsion angle between two neighbouring squares. This information is helpful for us to decide the final framework topology that formed. For example, topologies with only one kind of edge are more likely to form compared with others, and we can compare the calculated pore size with the experimental value to further confirm the actual framework structure. The PXRD comparisons are shown in **Figure 2.16**. The experimental PXRD can fit well with the simulated PXRD pattern based on the COF model of non-interpenetrated **nbo** topology.

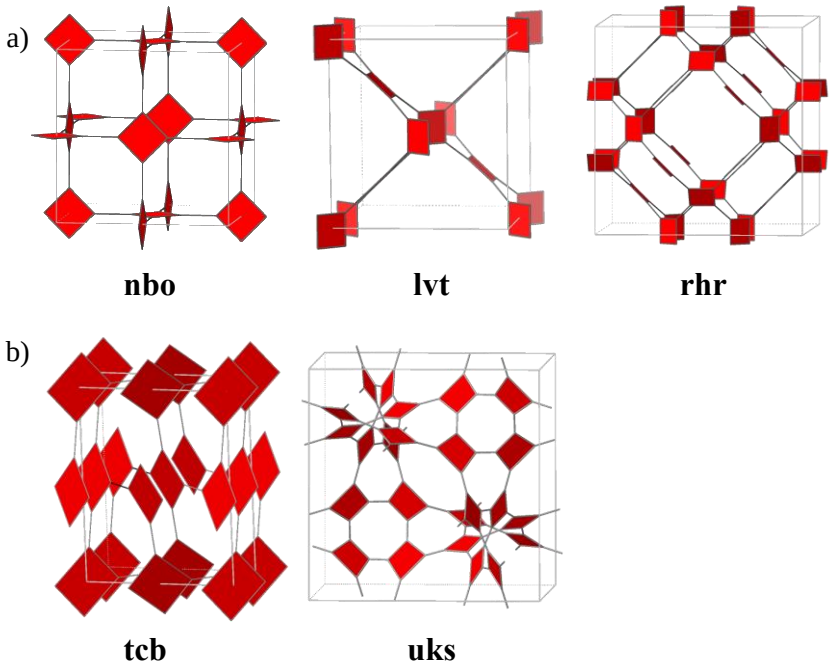

Figure 2.15. Possible topologies of **SPB-COFs (a)** edge-transitive nets; **(b)** nets with two edges.

Table 2.2. Structural and topological features of possible networks constructed from planar square building blocks.

Topology	Kinds of vertices	No.edge	Pore size[a] / Å	Torsion angle[b] / °	Space Group of COFs built
nbo	1	1	30.7	90	Im-3m (No.229)
lvt	1	1	29.3	60	I41/amd (No.141)
rhr	1	1	48.6	60	Im-3m (No.229)
tcb	1	2	13.1	82	P1 (No.1)
uks	1	2	54.5	42	P1 (No.1)

a. Calculated using zeo++.[25,26]
b. Torsion angle corresponds to the torsion angle between two neighbouring squares.

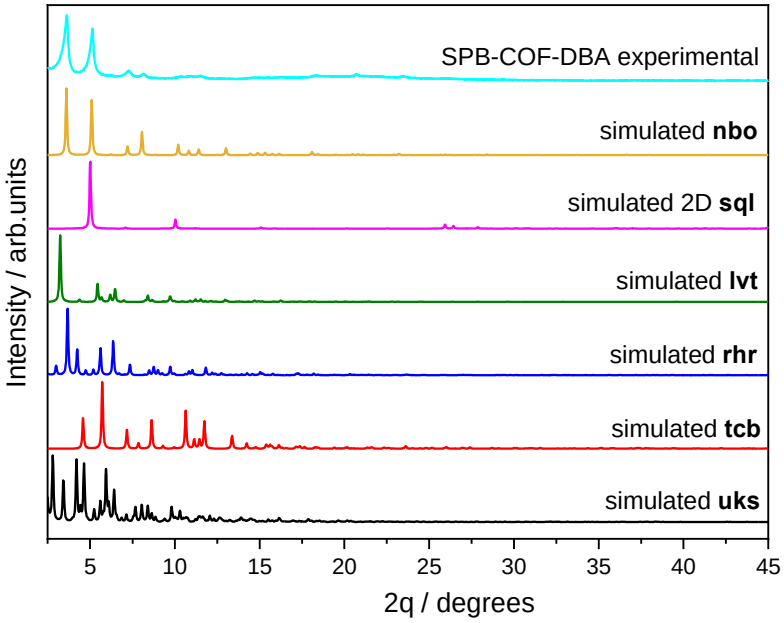

Figure 2.16. Overlay of the experimental and simulated PXRD patterns of **SPB-COF-DBA** based on non-interpenetrated 3D **nbo**, **lvt**, **rhr**, **tcb** and **uks** topologies and 2D **sql** topology (based-on SPC linkage).

To further confirm the non-interpenetration of SPB-COFs, we have built COFs models with up to 3-fold interpenetration (**Figure 2.17**) and compared the simulated PXRD pattern with the experimental pattern (**Figure 2.18**). The results confirmed that all SPB-COFs are of non-interpenetrated **nbo** topology. It is worth noting that the PXRD simulated from COFs models mentioned above, were all based on the spiro-orthocarbonate (SPC) linkage rather than the spiroborate (SPB linkage) itself. The reason why we use SPC-COFs models for PXRD comparison rather than SPB is that SPB-COFs are ionic frameworks, and we cannot accurately locate the position of the counter cations (though it seems in all three SPB-COFs, the type of counter cations shows no apparent influence on the peak positions in PXRD pattern). On the other hand, the SPC-COFs are much easier to optimize and the simulated PXRD patterns from COF models with either SPB or SPC linkages show no difference (**Figure 2.19a**). **Figure 2.19b** is a framework structure representation of SPB-COFs (non-interpenetrated 3D **nbo** topology) in space filling style. More details on the computational methods used for these COFs structural modelling can be found in the **Materials and methods** section of this chapter (**Section 2.6.13**, COFs structural modelling).

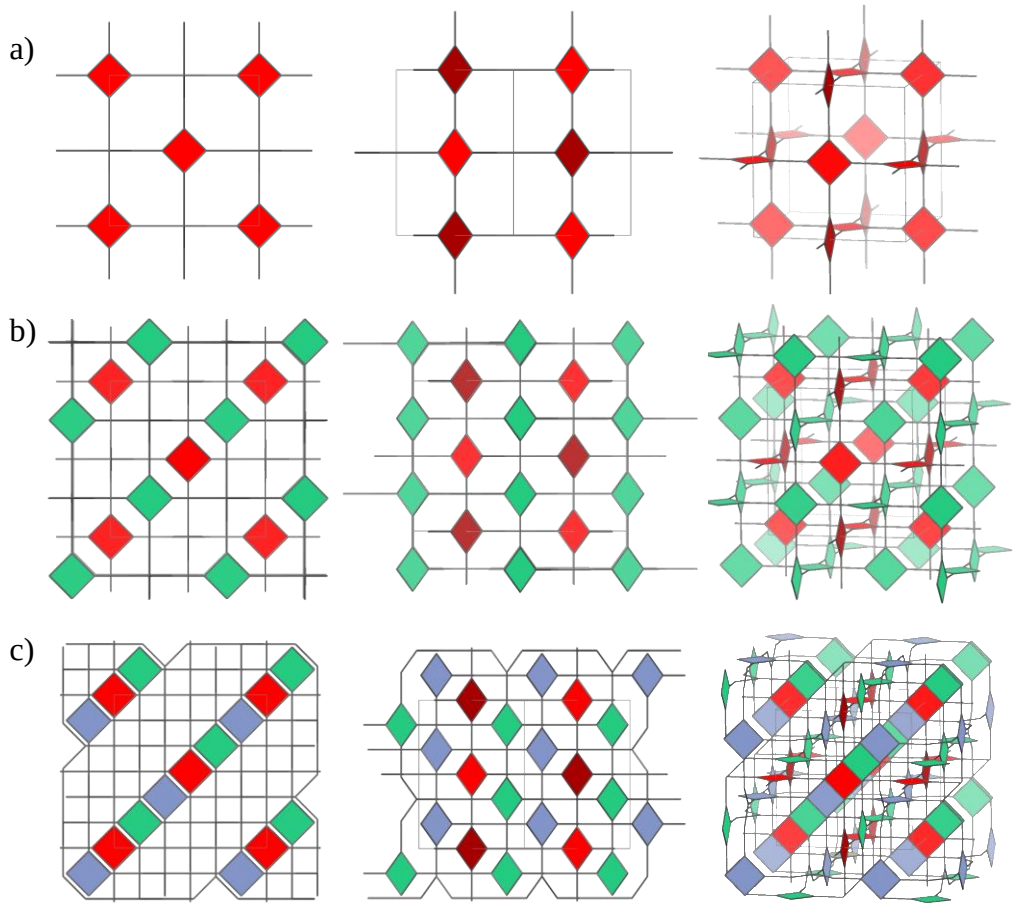

Figure 2.17. Three comparable views of **(a) nbo** crystal net; **(b)** 2-fold interpenetrated **nbo** crystal net and **(c)** 3-fold interpenetrated **nbo** crystal net. PcCo node belonging to different nets are coloured in red, green or violet.

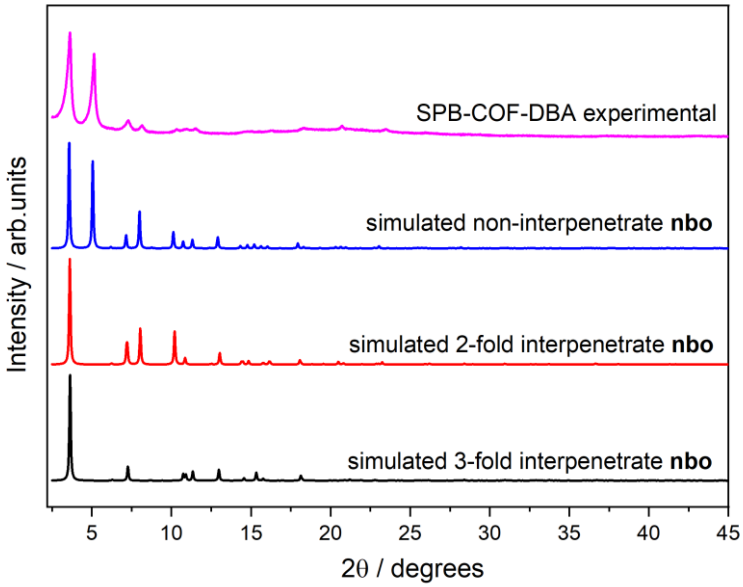

Figure 2.18. Comparison of the experimental PXRD pattern and simulated patterns for the **nbo** topology with the different degrees of interpenetration.

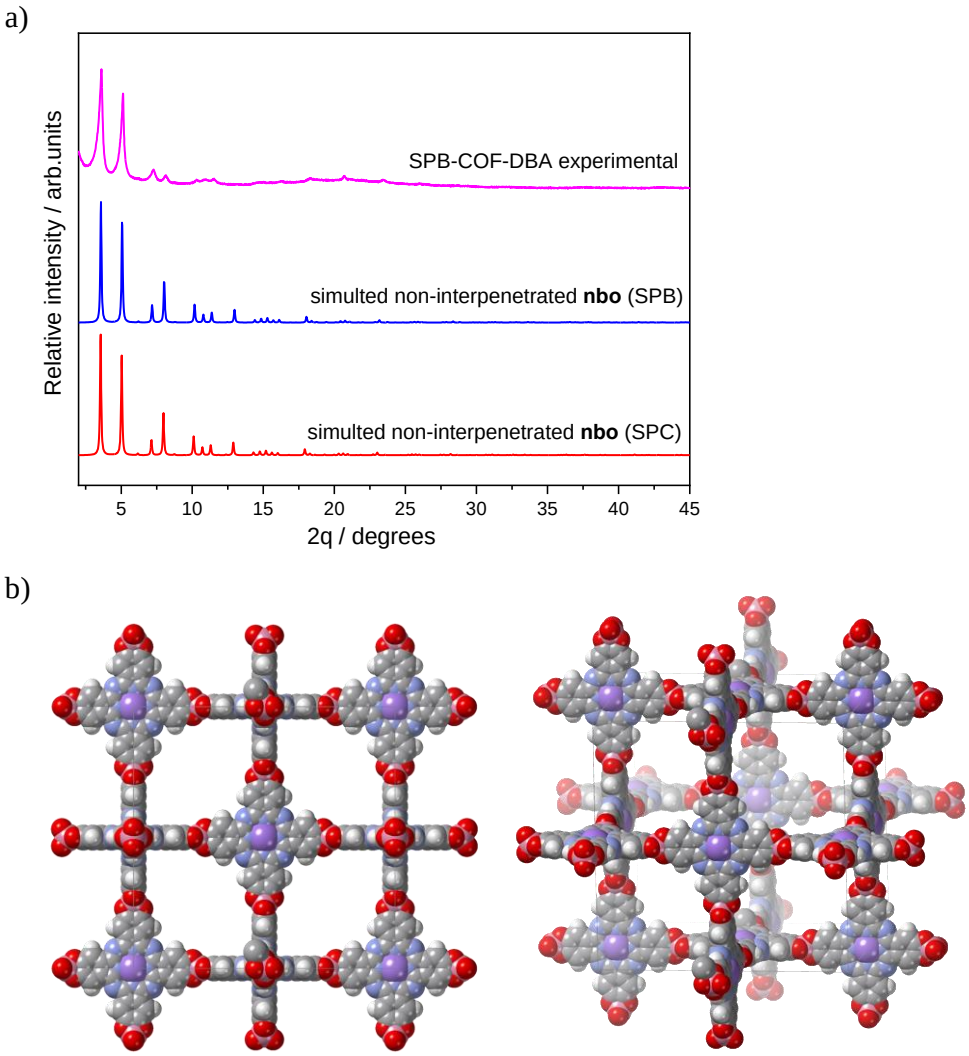

Figure 2.19. (a) Comparison of the experimental PXRD pattern and simulated patterns of the models based on the spiroborate (SPB) or spiro-orthocarbonate (SPC) linkage. (b) Framework structure representation of SPB-COFs. All counter cations ($[n\text{-}Bu_2NH_2]^+$, $[NH_2Me_2]^+$, $[n\text{-}Bu_4N]^+$) in the framework are omitted for clarity. White, pink, gray, blue, red and purple atoms represent hydrogen, boron, carbon, nitrogen, oxygen and cobalt, respectively; gray lines indicate the unit cell.

SPB-COF-DBA showed the best crystallinity among the three SPB-COFs, with 11 resolved diffraction peaks in the experimental PXRD pattern fitting well with the simulated pattern. The experimental diffraction pattern exhibited significant peaks at 3.64°, 5.15°, 7.30°, 8.15°, 10.35°, 10.97°, 11.51°, 16.39°, 18.35°, 20.75° and 23.46°. Pawley refinement confirmed that these correspond to the (110), (200), (220), (310), (400), (411), (420), (620), (640), (811) and (842) planes, respectively, in a cubic symmetry structure (space group Im$\bar{3}$m, No.229). The presence of the multiple well-defined reflections suggests that SPB-COF-DBA has high crystallinity and high periodicity in three dimensions. This experimental PXRD pattern is in good agreement with the simulated pattern obtained from a non-interpenetrated model with **nbo** topology (**Figure 2.20**). The refinement yielded a cubic *I* centered lattice with unit cell parameters of a = 34.744(2) Å, in excellent agreement with our simulated COF model (Im$\bar{3}$m, a = 34.707 Å). The SPB-COF model used for comparison has Li^+ as counter cations.

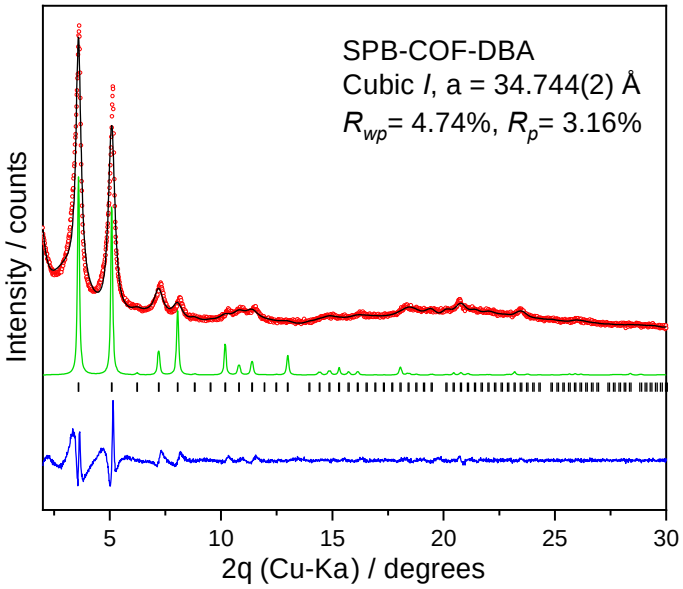

Figure 2.20. Experimental PXRD pattern (red), profile calculated from Pawley refinement (black) and residual (blue), and pattern simulated from the structural model (green) for **SPB-COF-DBA**. Reflection positions are shown by tick marks.

SPB-COF-DMA and SPB-COF-TBA show lower crystallinity compared with SPB-COF-DBA. The experimental PXRD pattern of SPB-COF-DMA shows peaks at 3.51°, 5.13°, 6.27°, 7.22°, 8.15°, 10.30°, 11.49°, 13.16°, 18.40° and 20.80°. Pawley refinement confirmed that these correspond to the (110), (200), (211), (220), (310), (400), (420), (510), (640) and (811) planes, respectively (**Figure 2.21**). The experimental PXRD pattern of SPB-COF-TBA exhibited peaks at 3.64°, 5.15°, 7.23°, 8.10°, 10.33° and 11.47°. Pawley refinement confirmed that these correspond to the (110), (200), (220), (310), (400) and (420) planes, respectively (**Figure 2.22**). SPB-COF-

DMA and SPB-COF-TBA are in a cubic symmetry structure as SPB-COF-DBA, but with a refined unit cell parameter of a = 34.690(5) Å and a = 34.685(7) Å, respectively. For all the three SPB-COFs, simulated PXRD was from a fully geometry-optimized SPB-COF model with lithium atoms as the counterions. For Pawley refinement, all the Li^+ counterions were omitted for obtaining higher crystal symmetry. The SPB-COF model used for comparison has Li^+ as counter cations.

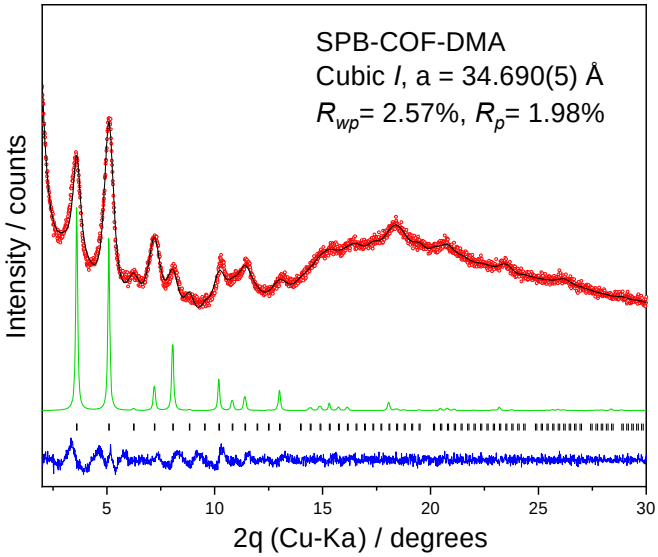

Figure 2.21. Experimental PXRD pattern (red), profile calculated from Pawley refinement (black) and residual (blue), and pattern simulated from the structural model (green) for **SPB-COF-DMA**. Reflection positions are shown by tick marks.

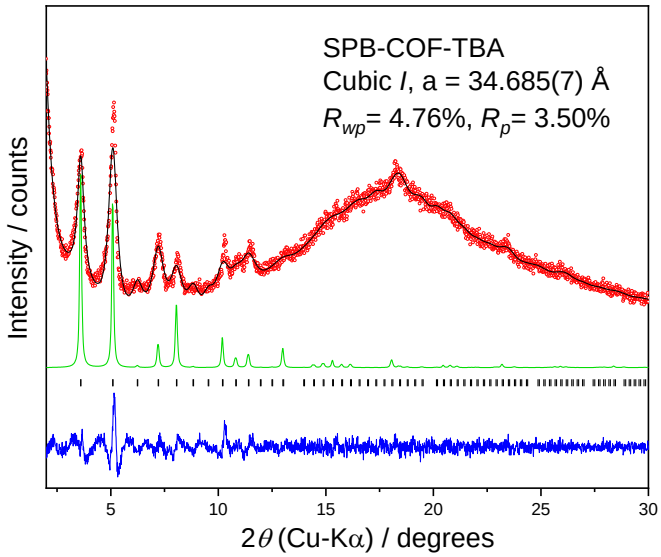

Figure 2.22. Experimental PXRD pattern (red), profile calculated from Pawley refinement (black) and residual (blue), and pattern simulated from the structural model (green) for **SPB-COF-TBA**. Reflection positions are shown by tick marks.

2.4.2 Single crystal structure of model compounds

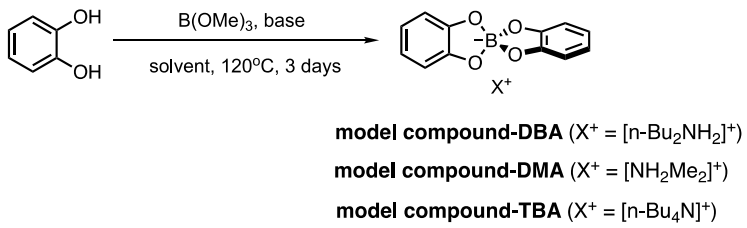

Figure 2.23. Scheme for the synthesis of **model compounds**.

To confirm the formation of the spiroborate linkage and its perpendicular geometry, three model compounds that correspond to each SPB-COF were prepared from the same reaction conditions as for the COF synthesis. The reaction scheme is shown above (**Figure 2.23**). The solution ^{1}H NMR spectra of these model compounds in dmso-d_6 confirms the desired product is formed (**Figure 2.8**, **Figure 2.10** and **Figure 2.12**). Single crystal of model compound-DBA was grown from a saturated ethyl acetate solution, while crystals of model compound-TBA can be obtained either by slow diffusion of diethyl ether into a saturated ethyl acetate or ethanol solution at room temperature for a week. No single crystal of model compound-DMA was obtained, possibly due to the small size of DMA cation.[27]

As is shown in **Figure 2.24**, the single crystal structure of model compound-DBA confirms the tetrahedral-shaped spiroborate linkage and the perpendicular orientation of the two neighbouring phenyl rings. The structure of the DBA cation ($[n\text{-}Bu_2NH_2]^+$), which is formed from the decomposition of DBF solvent during the reaction was also confirmed from these crystal structures. A similar result can be seen for model compound-TBA (**Figure 2.25**). The TBA cation ($[n\text{-}Bu_4N]^+$) is from the $n\text{-}Bu_4NOH.30H_2O$ salt added.

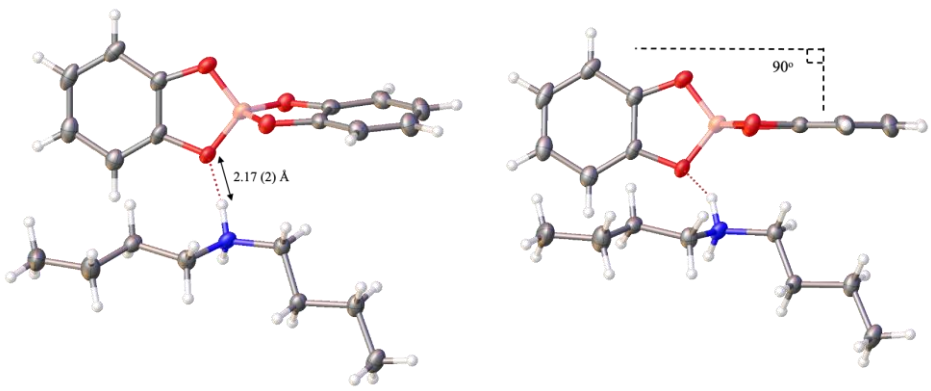

Figure 2.24. Displacement ellipsoid plots from the single crystal structure of **model compound-DBA**; two views are shown; ellipsoids are displayed at 50 % probability level. C = grey; H = white; N = blue; O = red; B = pink. As is shown in the graph, the two benzene rings connected with spiroborate linkage are of perpendicular orientation with each other.

Table 2.3. Single crystal refinement details for **model compound-DBA**.

Name	model compound-DBA
Crystallization solvent	ethyl acetate
Wavelength/ Å	0.71073 (Mo-Kα)
Formula	$C_{12}H_8BO_4,C_8H_{20}N$
Weight	357.24
Crystal size/mm^3	0.41*0.25*0.13
Crystal system	triclinic
Space group	P $\bar{1}$
***a*/ Å**	8.1206(6)
***b*/ Å**	10.1529(9)
***c*/ Å**	12.4939(10)
***α*/ °**	102.267(7)
***β*/ °**	104.960(7)
***γ*/ °**	93.689(6)
***V*/ Å^3**	964.68(14)
ρ_{calcd}/g cm-1	1.230
Z	2
T/K	100.00 (10)
μ/mm-1	0.084
F (000)	384.0
θ range/°	3.474 - 60.924
Reflections collected	12044
Independent reflections	4721
Data / restraints / parameters	4721/0/245
R_{int}	0.0376
Final R_1 values ($I > 2\sigma(I)$)	0.0495
Final R_1 values (all data)	0.0772
wR_2 (all data)	0.1297
Goodness-of-fit on F^2	1.052

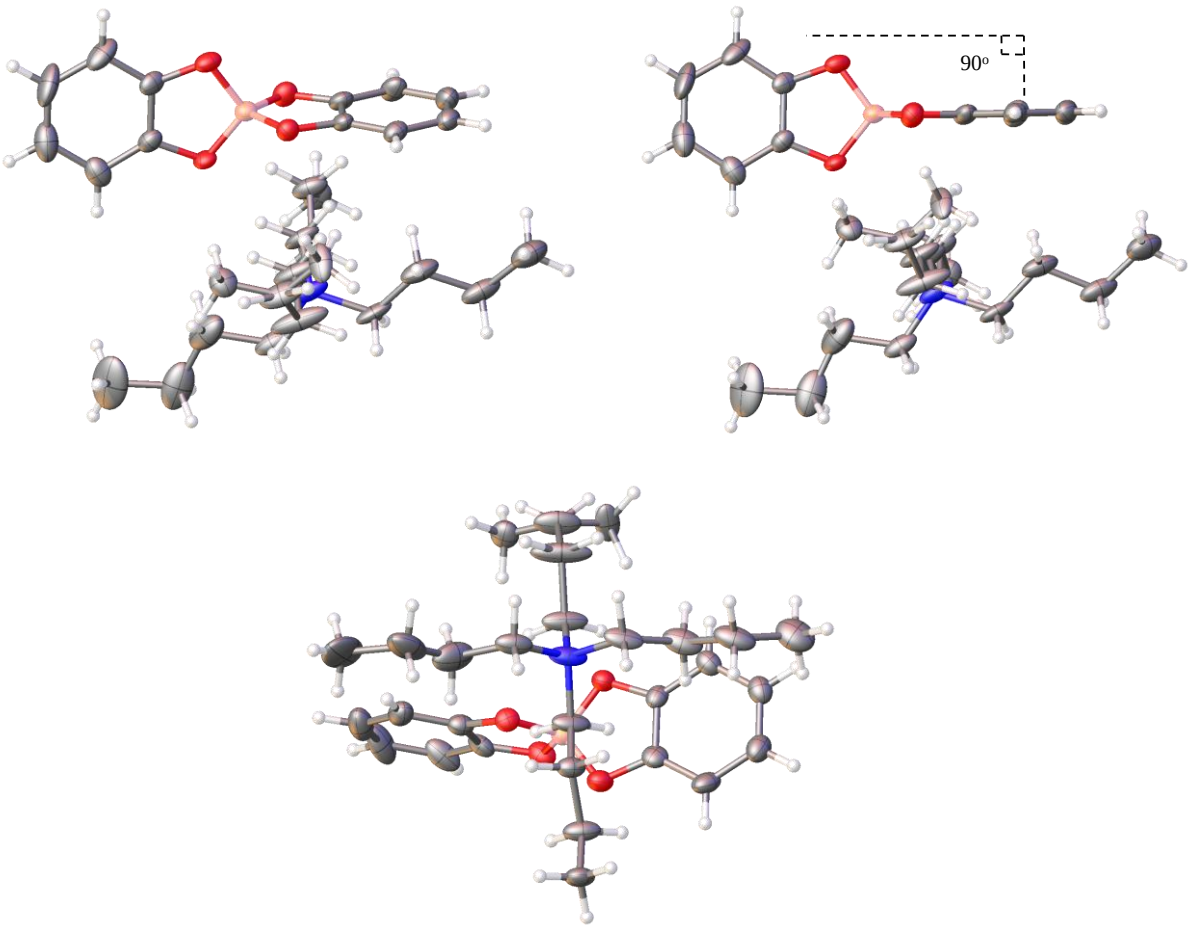

Figure 2.25. Displacement ellipsoid plots from the single crystal structure of **model compound-TBA**; three views are shown; ellipsoids are displayed at 50 % probability level. C = grey; H = white; N = blue; O = red; B = pink. As is shown in the graph, the two benzene rings connected with spiroborate linkage are of perpendicular orientation with each other.

Table 2.4. Single crystal refinement details for **model compound-TBA**.

Name	model compound-TBA
Crystallization solvent	Ethanol + Et_2O or ethyl acetate + Et_2O
Wavelength/ Å	0.71073 (Mo-Kα)
Formula	$C_{12}H_8BO_4$,$C_{16}H_{35}N$
Weight	468.44
Crystal size/mm^3	0.22*0.197*0.041
Crystal system	orthorhombic
Space group	$Pca2_1$
***a*/ Å**	15.5802(3)
***b*/ Å**	8.4052(2)
***c*/ Å**	20.6412(4)
***V*/ Å^3**	2703.05(10)
ρ_{calcd}/g cm^{-1}	1.151
Z	4
T/K	100.00(13)
μ/mm-1	0.075
F (000)	1020.00
θ range/°	3.946 – 58.296
Reflections collected	61889
Independent reflections	6998
Data / restraints / parameters	6998/2/322
R_{int}	0.0397
Final R_1 values (I > 2σ(*I*))	0.0881
Final R_1 values (all data)	0.0970
wR_2 (all data)	0.1742
Goodness-of-fit on F^2	1.145

2.4.3 FT-IR and solid-state ^{13}C and ^{11}B NMR

Fourier transform infrared spectra (FT-IR) of all three SPB-COFs shows a newly formed, strong absorption band between 1026 and 1032 cm^{-1} corresponding to the B−O stretching vibrations of $[BO_4]$ tetrahedra (**Figure 2.26**). This corroborates the successful formation of the spiroborate linkage in SPB-COFs. FT-IR spectra of the three model compounds gave similar results. The absorption band formed at 1053 cm^{-1} confirms the formation of $[BO_4]^-$ tetrahedral structure (**Figure 2.27**).[21,28]

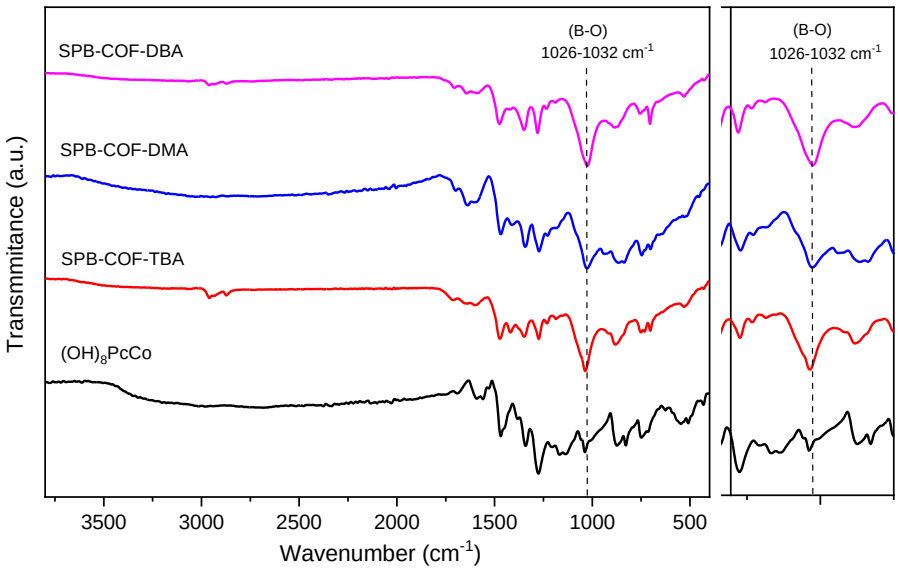

Figure 2.26. Attenuated total reflection (ATR)-FT-IR spectra of $(OH)_8PcCo$ and SPB-COFs.

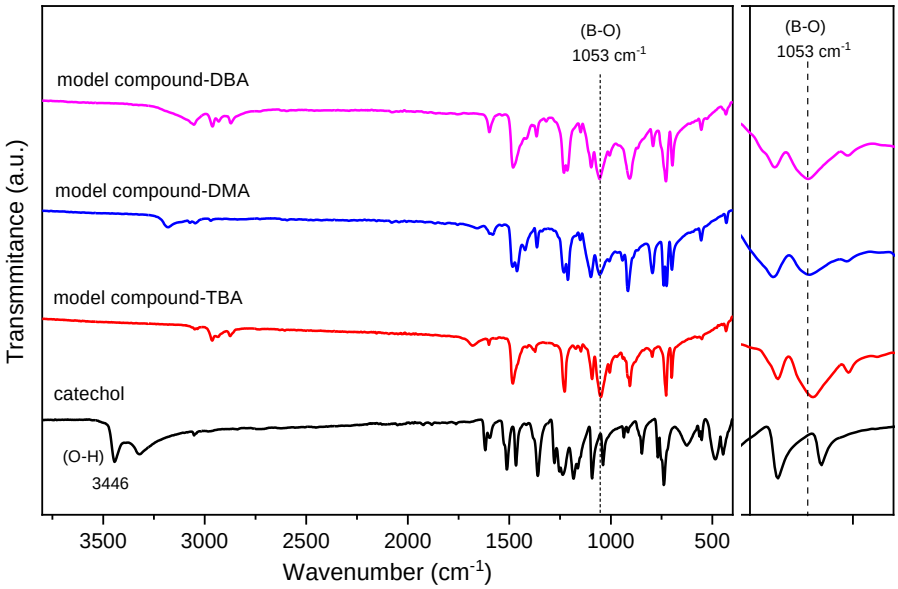

Figure 2.27. ATR-FT-IR spectra of catechol and model compounds.

In the solid-state ^{13}C CP/MAS NMR spectra of SPB-COF-DBA, signals between 170.7 and 105.8 ppm correspond to phthalocyanine carbons, which is in good accordance with literature reports.[29] Signals at 49.0, 27.5, 19.0 and 13.5 ppm correspond to carbons on the n-butyl group in $[n\text{-}Bu_2NH_2]^+$ cations (carbon signals of $[n\text{-}Bu_2NH_2]^+$ cation in the solution ^{13}C NMR spectra of model compound-DBA in **Figure 2.9** are at 46.54, 27.56, 19.22, 13.47 ppm) (**Figure 2.28**). SPB-COF-DMA and SPB-COF-TBA show a similar result, but the carbon signals from the counter cations varied from SPB-COF-DBA. The DMA cation shows a signal at 30.8 ppm for SPB-COF-DMA (**Figure 2.29**) which corresponds well with the solution ^{13}C nmr of model compound-DMA, at 34.38 ppm, in **Figure 2.11**. The TBA cation shows signals at 57.7, 21.2, 17.5 and 14.1 ppm (**Figure 2.30**), which is also in accordance with model compound-TBA, at 57.49, 23.04, 19.19, 13.47 ppm in **Figure 2.13**. The peak broadening in the solid-state ^{13}C NMR compared to solution ^{13}C NMR relates to: (1) quadrupolar and dipolar couplings and chemical shift anisotropy; (2) crystallinity of sample.[30,31]

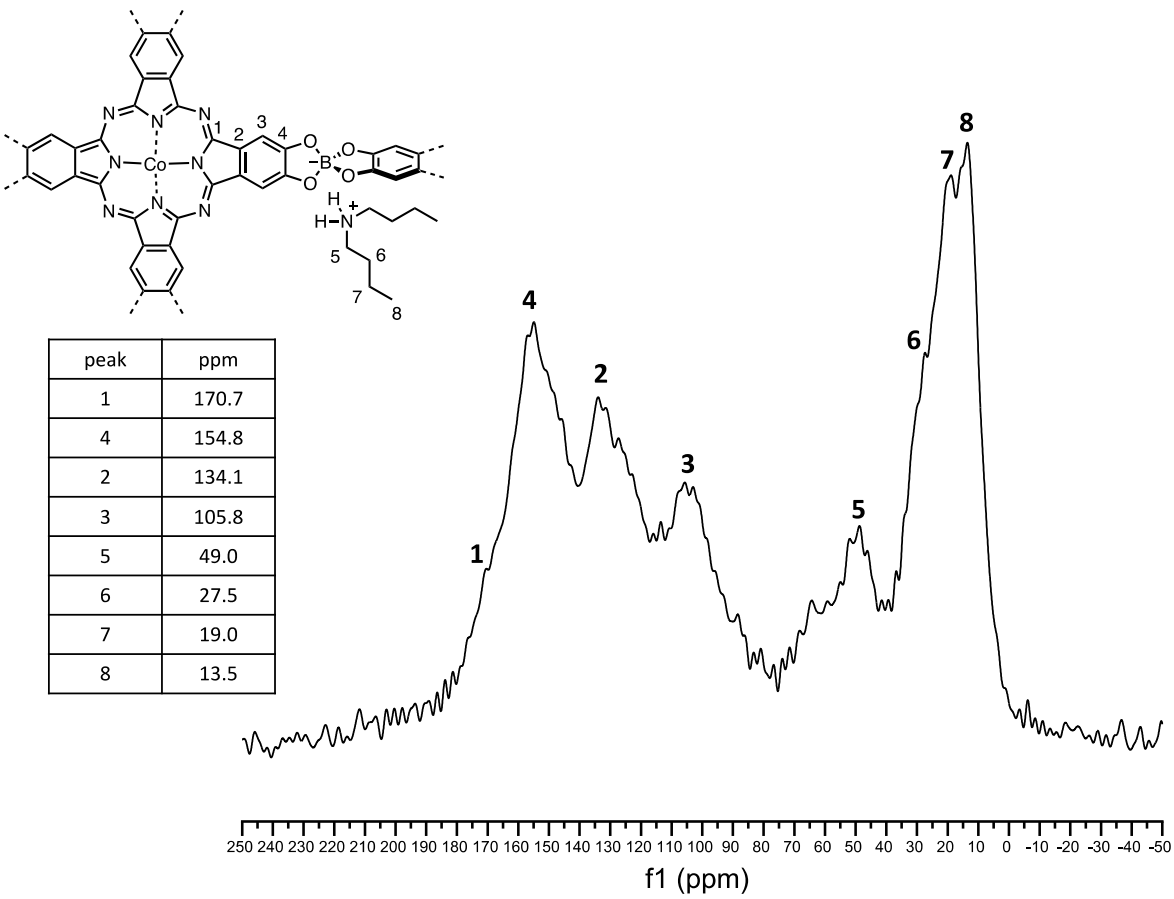

peak	ppm
1	170.7
4	154.8
2	134.1
3	105.8
5	49.0
6	27.5
7	19.0
8	13.5

Figure 2.28. Solid state ^{13}C CP/MAS NMR spectrum of **SPB-COF-DBA**. Supercritical CO_2 activated COF was used for the measurement.

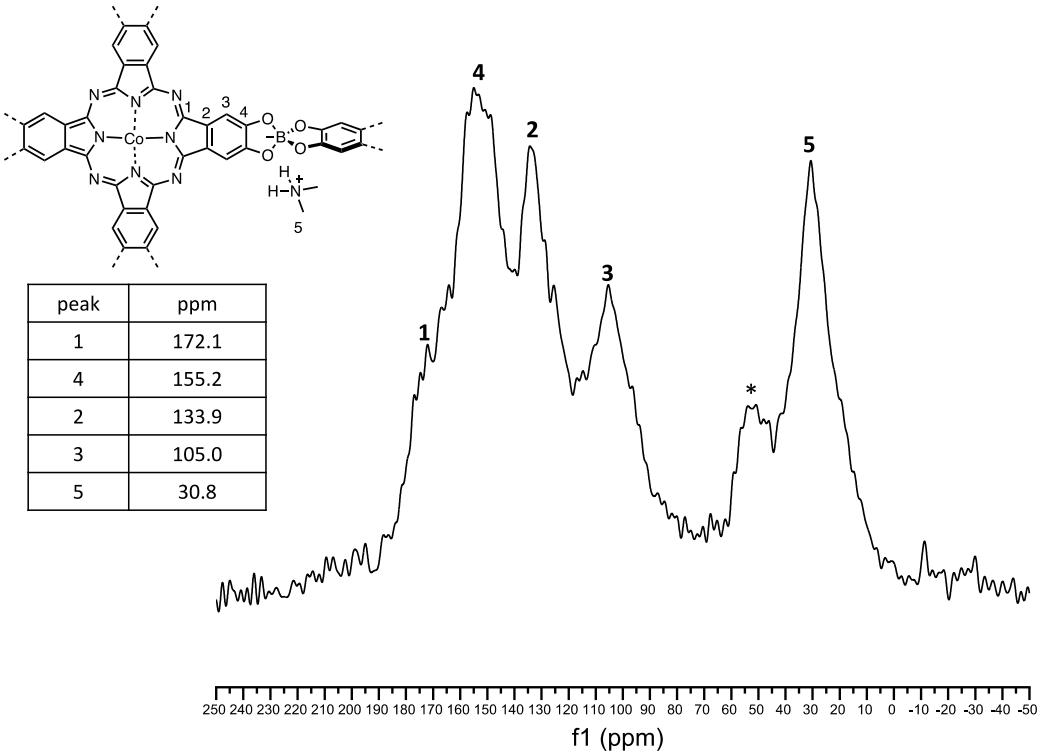

peak	ppm
1	172.1
4	155.2
2	133.9
3	105.0
5	30.8

Figure 2.29. Solid state ^{13}C CP/MAS NMR spectrum of **SPB-COF-DMA**. Supercritical CO_2 activated COF was used for the measurement. * Residual NMP.

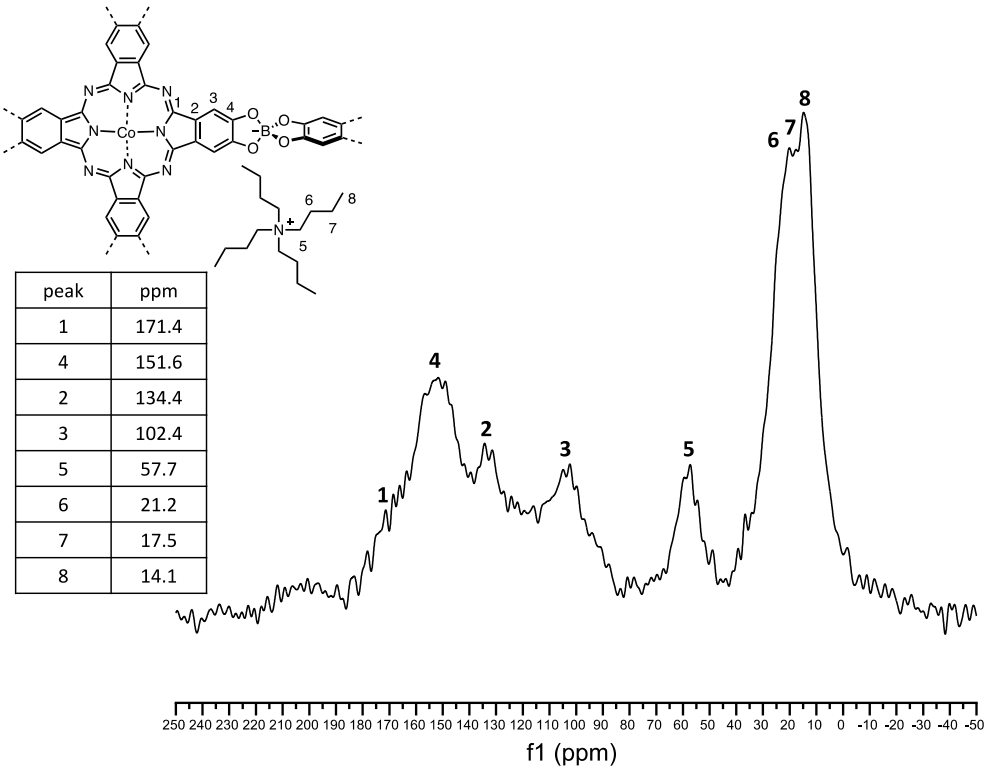

peak	ppm
1	171.4
4	151.6
2	134.4
3	102.4
5	57.7
6	21.2
7	17.5
8	14.1

Figure 2.30. Solid state ^{13}C CP/MAS NMR spectrum of **SPB-COF-TBA**. Supercritical CO_2 activated COF was used for the measurement.

The signal at 14.0 ppm in the solid-state ^{11}B MAS NMR spectra of SPB-COF-DBA corresponds to the sp^3 hybridized spiroborate boron atom (**Figure 2.31**). This agrees with the literature[19] and our model compound, confirming that boron has been incorporated into the framework as tetrahedral $[BO_4]^-$. SPB-COF-DMA (**Figure 2.32**) and SPB-COF-TBA (**Figure 2.33**) show similar results. Solid-state ^{11}B MAS NMR spectra comparisons are shown below.

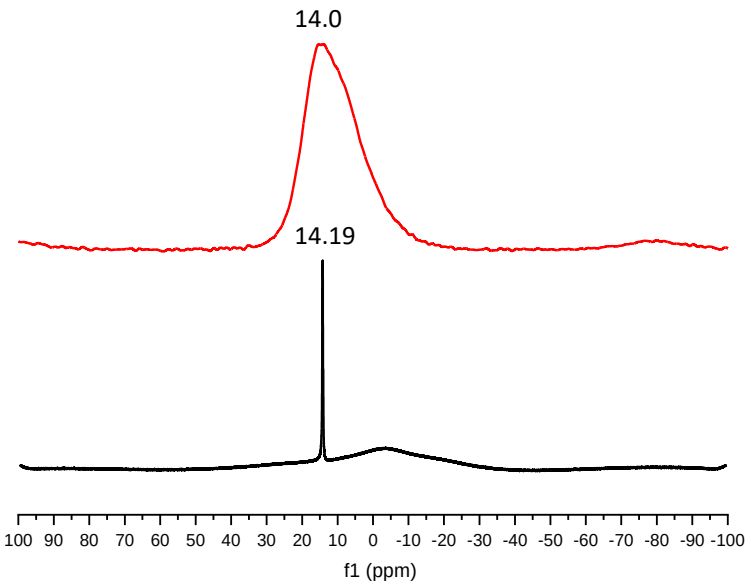

Figure 2.31. Solid-state ^{11}B MAS NMR spectrum of **SPB-COF-DBA** (red) compare with ^{11}B solution NMR spectrum of **model-compound-DBA** (black). Supercritical CO_2 activated COF was used for the measurement.

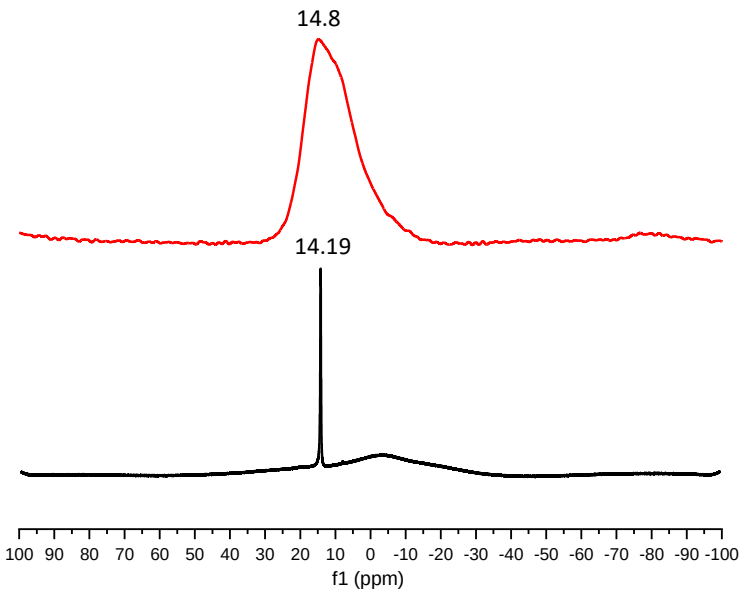

Figure 2.32. Solid-state ^{11}B MAS NMR spectrum of **SPB-COF-DMA** (red) compare with ^{11}B solution NMR spectrum of **model-compound-DMA** (black). Supercritical CO_2 activated COF was used for the measurement.

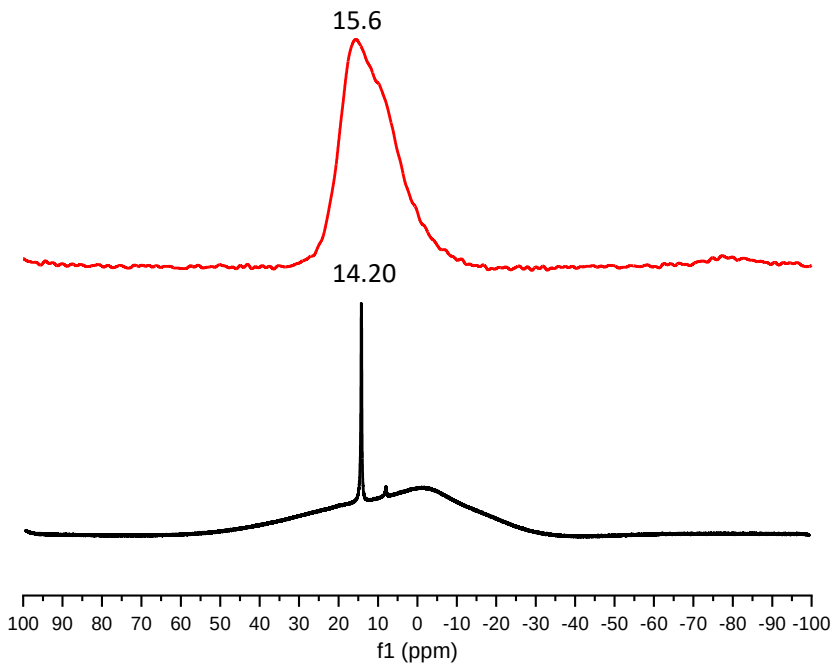

Figure 2.33. Solid-state ^{11}B MAS NMR spectrum of **SPB-COF-TBA** (red) compare with ^{11}B solution NMR spectrum of **model-compound-TBA** (black). Supercritical CO_2 activated COF was used for the measurement.

2.4.4 Thermogravimetric analysis

The thermogravimetric analysis (TGA) curve of SPB-COF-DBA shows around 20% weight loss below 300 °C and another 25% weight loss at around 950 °C. SPB-COF-DMA shows around 27% weight loss below 400 °C and another 28% weight loss when heated to 950 °C. SPB-COF-TBA shows 6% weight loss below 200 °C and another 54% weight loss when heated to 950 °C (**Figure 2.34**). The weight loss below 150 °C in all the three COFs can be attributed to loss of moisture (H_2O) and free DBF solvent (boiling point = 120 °C). By comparing the TGA curve between these three COFs with the four COFs (BPDA-COF, BPDA-2-COF, BPDA-4-COF and PA-COF) made in chapter 3 (**Figure 3.57**), we assume that the weight loss between 150 ~ 400 °C in the three SPB-COFs here are possibly from the decomposition of $[n\text{-}Bu_2NH_2]^+$ during heating. Weight loss above 400 °C can be attributed to partial structure decompose .[32,33] All the measurements were done under a N_2 atmosphere.

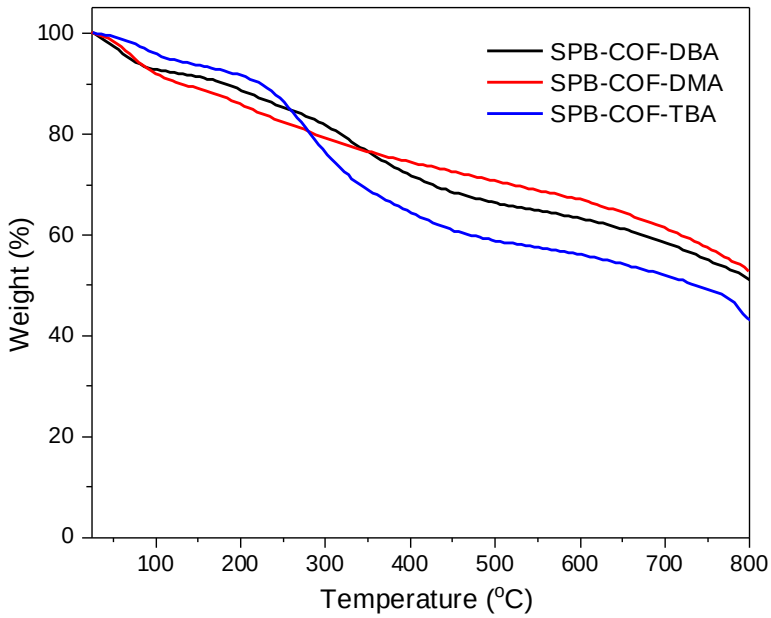

Figure 2.34. TGA curves of SPB-COFs in N_2 atmosphere.

2.4.5 Scanning electron microscopy images

Scanning electron microscopy (SEM) images of SPB-COF-DBA show a homogeneous morphology of cube-shaped crystals with dimensions of 80−100 nm (**Figure 2.35**). No apparent morphology can be distinguished from the SEM image of SPB-COF-DMA (**Figure 2.36**) and SPB-COF-TBA (**Figure 2.37**) due to the small particle size. As the samples will be vacuumed before sending into the chamber for SEM measurement, considering the pore frangibility in these SPB-COFs, we are not sure if the vacuum operations will influence the particle morphology, though generally it will not.

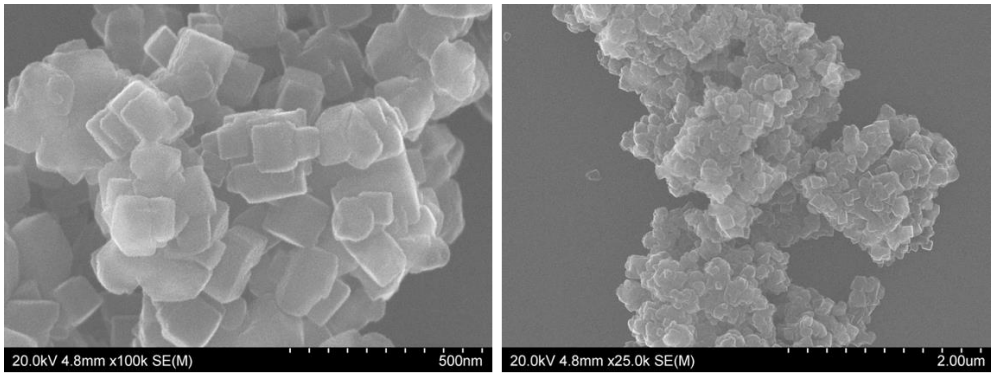

Figure 2.35. SEM images of **SPB-COF-DBA**. As-synthesized COF material was used for measurement.

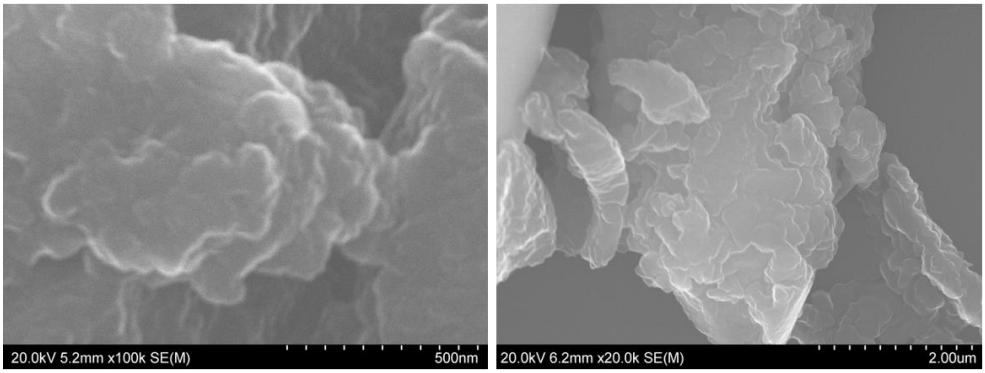

Figure 2.36. SEM images of **SPB-COF-DMA**. As-synthesized COF material was used for measurement.

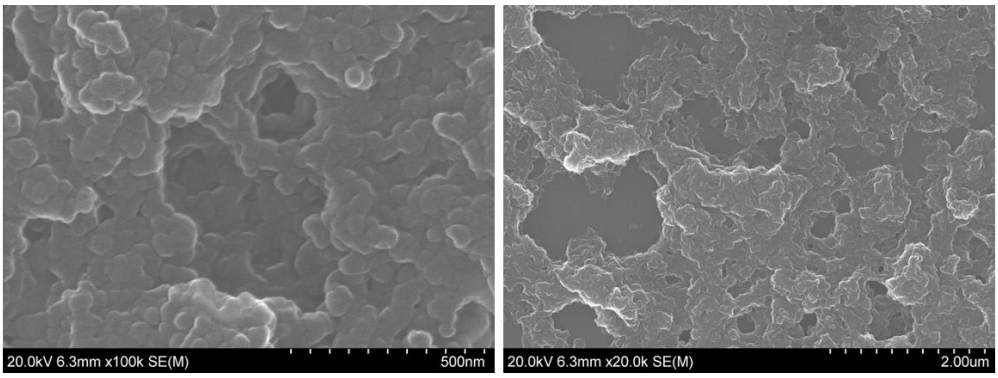

Figure 2.37. SEM images of **SPB-COF-TBA**. As-synthesized COF material was used for measurement.

2.4.6 Transmission electron microscope images

The highly ordered, periodic structure of SPB-COF-DBA was also apparent in high-resolution transmission electron microscope (HR-TEM) images. **Figure 2.38a** shows an 80 nm sized crystal, illustrating the long-range ordered square lattice in the **nbo** net. The cobalt (II) phthalocyanine (PcCo) units can be identified unambiguously (**Figure 2.38a**) as bright spots at the vertices of the squares. The PcCo units that are perpendicular to the electron beam appear brighter than the PcCo units that are parallel to the electron beam. The dark areas between the bright spots and the dimmer spots correspond to the pore space in the framework. This contrast is better resolved in the inverse fast Fourier transform (IFFT) image (**Figure 2.38b and 2.38c**). The periodic structural features in the HR-TEM images are consistent with the experimental unit cell (**Figure 2.39**): the distance between two bright spots, through a dimmer spot, is 3.47 nm, which agrees well with the Pawley refined unit-cell lengths of 3.4744(2) nm. More TEM images of SPB-COF-DBA are shown in **Figure 2.40**; this is a rare example of clear structural assignment of the repeating crystal lattice for a 3D COF using HR-TEM. Due to the lower crystallinity of SPB-COF-DMA (**Figure 2.41**) and SPB-COF-TBA (**Figure 2.42**), no clear lattice could be distinguished from their TEM images. Similarly, as the samples will be vacuumed before sending into the chamber for TEM measurement, considering the pore frangibility in these SPB-COFs, we are not sure if this vacuum operations will influence the TEM image quality, though generally it will not.

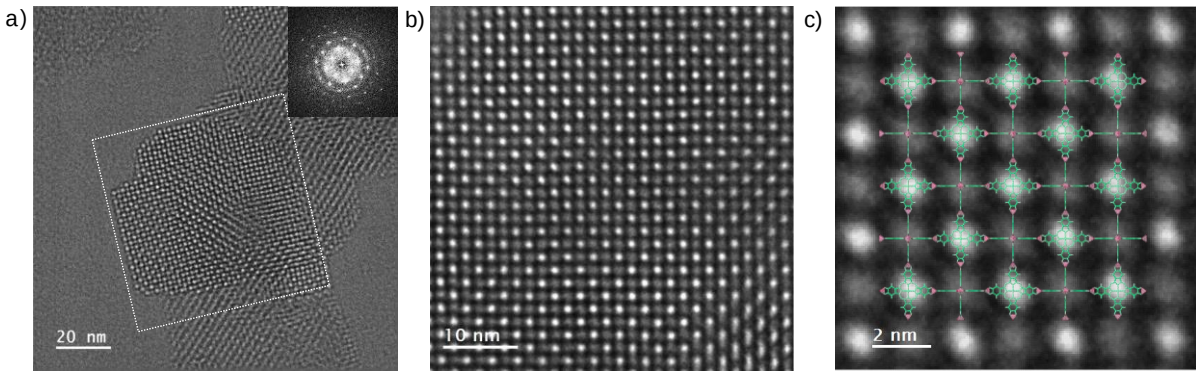

Figure 2.38. (a) HR-TEM image of as-synthesized SPB-COF-DBA. Inset: fast Fourier transform (FFT) of the selected area in white frame. (b) Image obtained by performing the inverse FFT (IFFT) on the spots at the FFT image in (a). Periodic mask was applied on the FFT image in (a) before operating IFFT, to remove unwanted noise and to enhance periodic elements in image. (c) Enlarged IFFT image in graph (b) with the COF model superimposed. Counter cations are omitted for clarity; the SPB linkages are shown as pink tetrahedra.

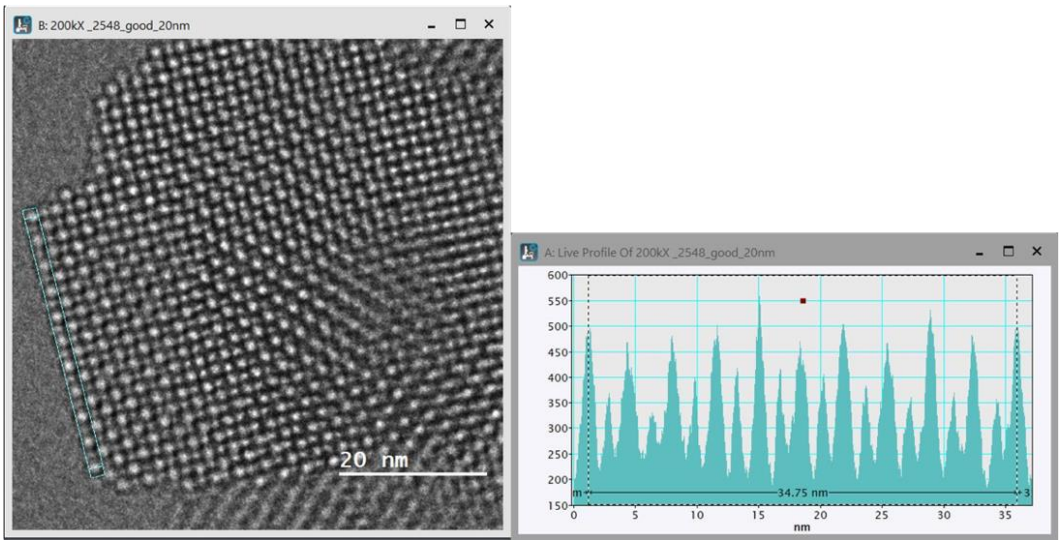

Figure 2.39. The distance measured between the brightest PcCo unit columns (= 3.47 nm) in the HR-TEM image of **SPB-COF-DBA**.

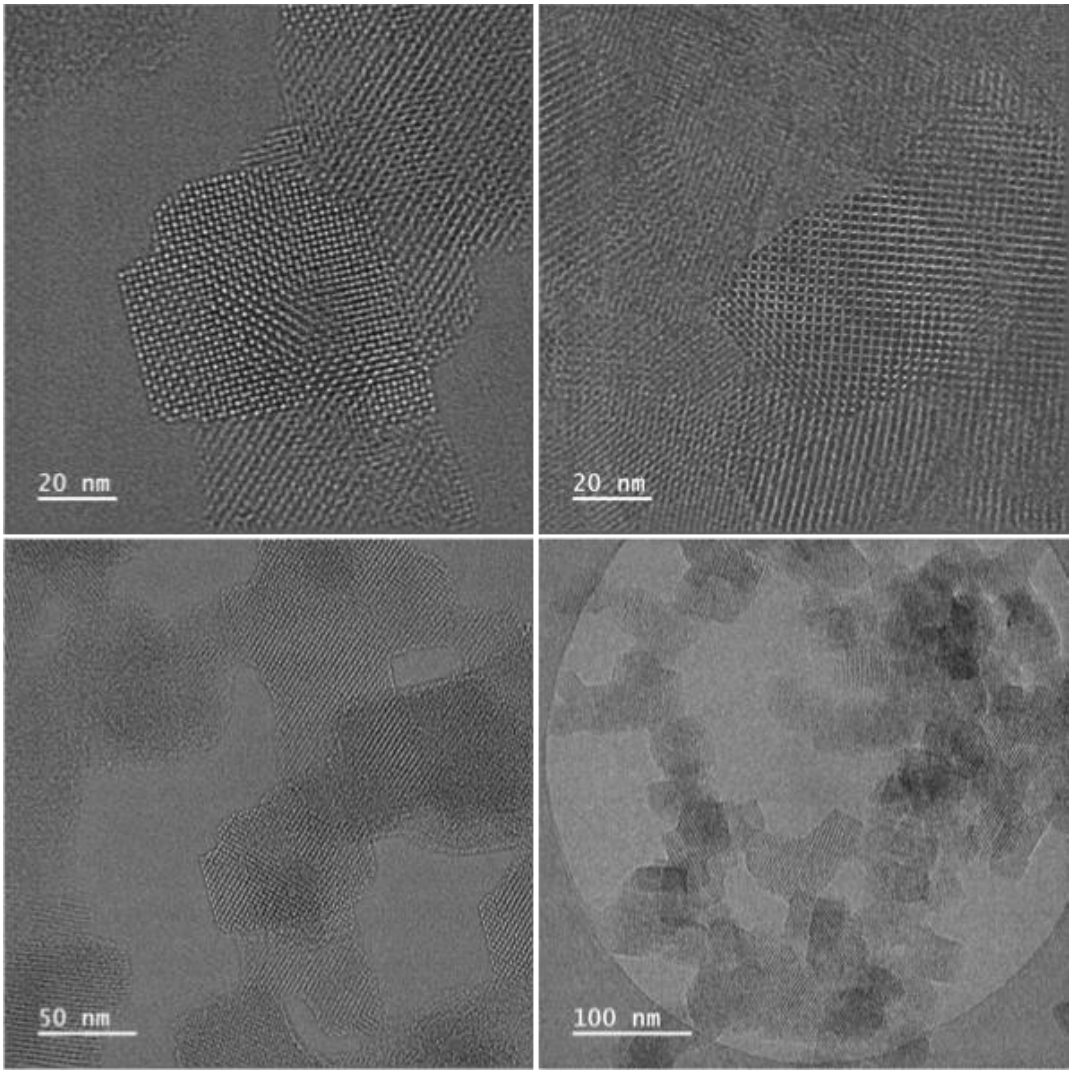

Figure 2.40. HR-TEM images of **SPB-COF-DBA** as-synthesized, inside the first image is the FFT.

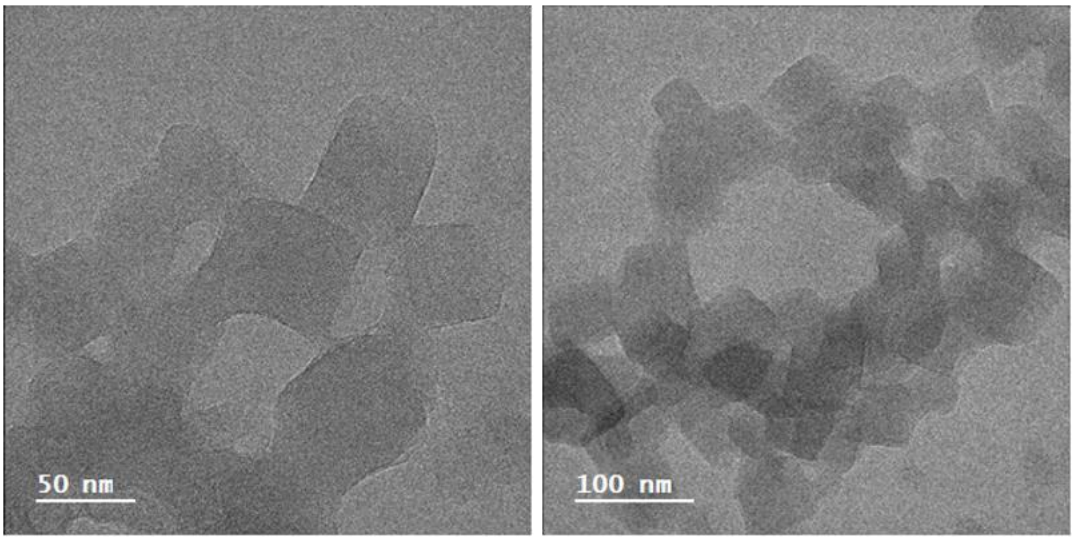

Figure 2.41. HR-TEM images of as-synthesized **SPB-COF-DMA**.

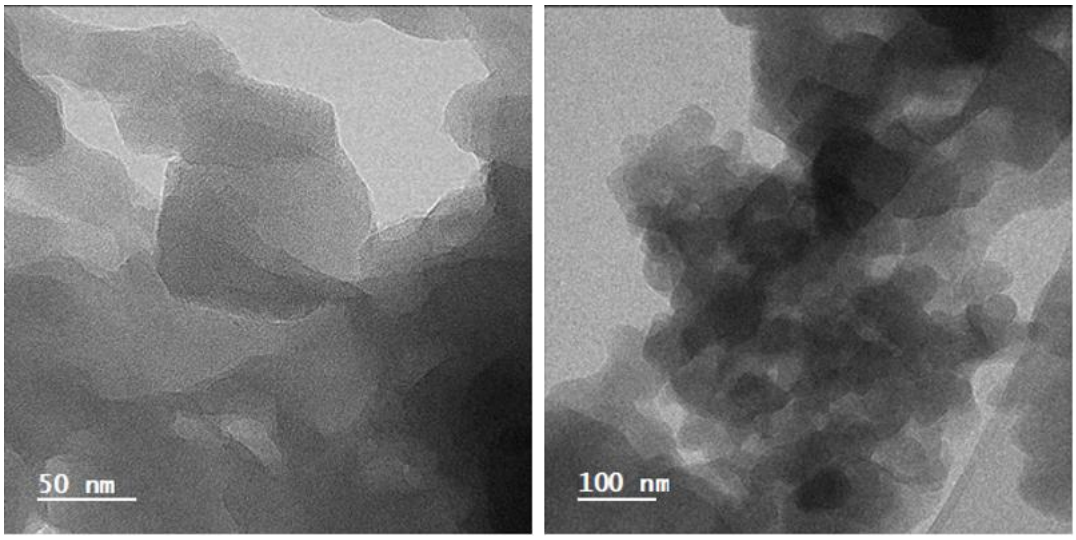

Figure 2.42. HR-TEM images of as-synthesized **SPB-COF-TBA**.

2.4.7 Gas sorption isotherms

2.4.7.1 Activation of SPB-COFs

The activation of SPB-COFs was not trivial, considering it has a non-interpenetrated open channel framework structure and cubic pore with the largest expected pore volume of 3.5×3.5×3.5 nm^3 (do not consider the cations included). To screen activation conditions we used SPB-COF-DBA. Various conditions were investigated to activate SPB-COF-DBA (**Table 2.5**) but only supercritical CO_2 activation ($scCO_2$) provided us with satisfactory results when comparing the PXRD pattern of the as-synthesized COFs with the pattern after activation (**Figure 2.43**). The successful SPB-COF-DBA activation by applying supercritical CO_2 can be attributed to the elimination of solvent (CO_2) surface tension (capillary forces), and therefore to prevents pore collapse upon solvents removal, at temperatures and pressures above CO_2 critical point.[34] We then used this batch of activated COFs for N_2 sorption measurement.

In order to maintain the COF crystallinity during $scCO_2$ activation, the best crystalline as-synthesized SPB-COFs should be used for activations. Also, one of the most important steps that decide the crystallinity of the activated SPB-COFs is the venting process after liquid CO_2 reached its critical point. The venting process should be as slow as possible, especially at the beginning. Venting too fast will lead to recondensation of liquid CO_2 which is detrimental to the activation process.

Table 2.5. Activation conditions screened for **SPB-COF-DBA**.

sample	Activation Condition (all done in sealed vial)
AC-1	DBF + $CHCl_3$ (16 h + 6 h), 50 ºC vacuum oven/2 h
AC-2	DBF + Acetone (16 h + 6 h), 50 ºC vacuum oven/2 h
AC-3	DMF + $CHCl_3$ (16 h + 6 h), 50 ºC vacuum oven/2 h
AC-4	DMF + Acetone (16 h + 6 h), 50 ºC vacuum oven/2 h
AC-5	DMF + Acetone (2 h + 2 h), 80 ºC vacuum oven/2 h
AC-6	DMF + Acetone (2 h + 2 h), 120 ºC vacuum oven/2 h
AC-7	DMF + MeOH (2 h + 2 h), 80 ºC vacuum oven/2 h
AC-8	DMF + MeOH (2 h + 2 h), 120 ºC vacuum oven/2 h
AC-9	DMF + CH_2Cl_2 (2 h + 2 h), 80 ºC vacuum oven/2 h
AC-10	DMF + CH_2Cl_2 (2 h + 2 h), 120 ºC vacuum oven/2 h
AC-11	DMF + $CHCl_3$ (2 h + 2 h), 80 ºC vacuum oven/2 h
AC-12	DMF + $CHCl_3$ (2 h + 2 h), 120 ºC vacuum oven/2 h
AC-13	120 ºC vacuum oven/2 h
AC-14	2-propanol/1 h + Acetone/1 h + n-pentane/1 h, RT vacuum*/ 1 h
AC-15	THF/1 h + n-pentane/1 h, RT vacuum/ 1 h
AC-16	DMF/1 h + acetone/1 h, RT vacuum/ 1 h
AC-17	DMF/1 h + acetone/1 h, RT vacuum/1 h + 110 ºC vacuum oven/0.5 h
AC-18	DMF/1 h + acetone/1 h + n-pentane/1 h, RT vacuum oven/1 h
AC-19	DMF/1 h + acetone/1 h + n-pentane/1 h, RT vacuum/1 h + 110 ºC/0.5 h
AC-20	MeOH/1 h + Acetone/1 h + n-pentane/1 h, RT vacuum/1 h
AC-21	Supercritical CO_2 activation, exchange for five times with interval of 1 hour (acetone)

* RT vacuum is done in Schlenk line with oil pump.

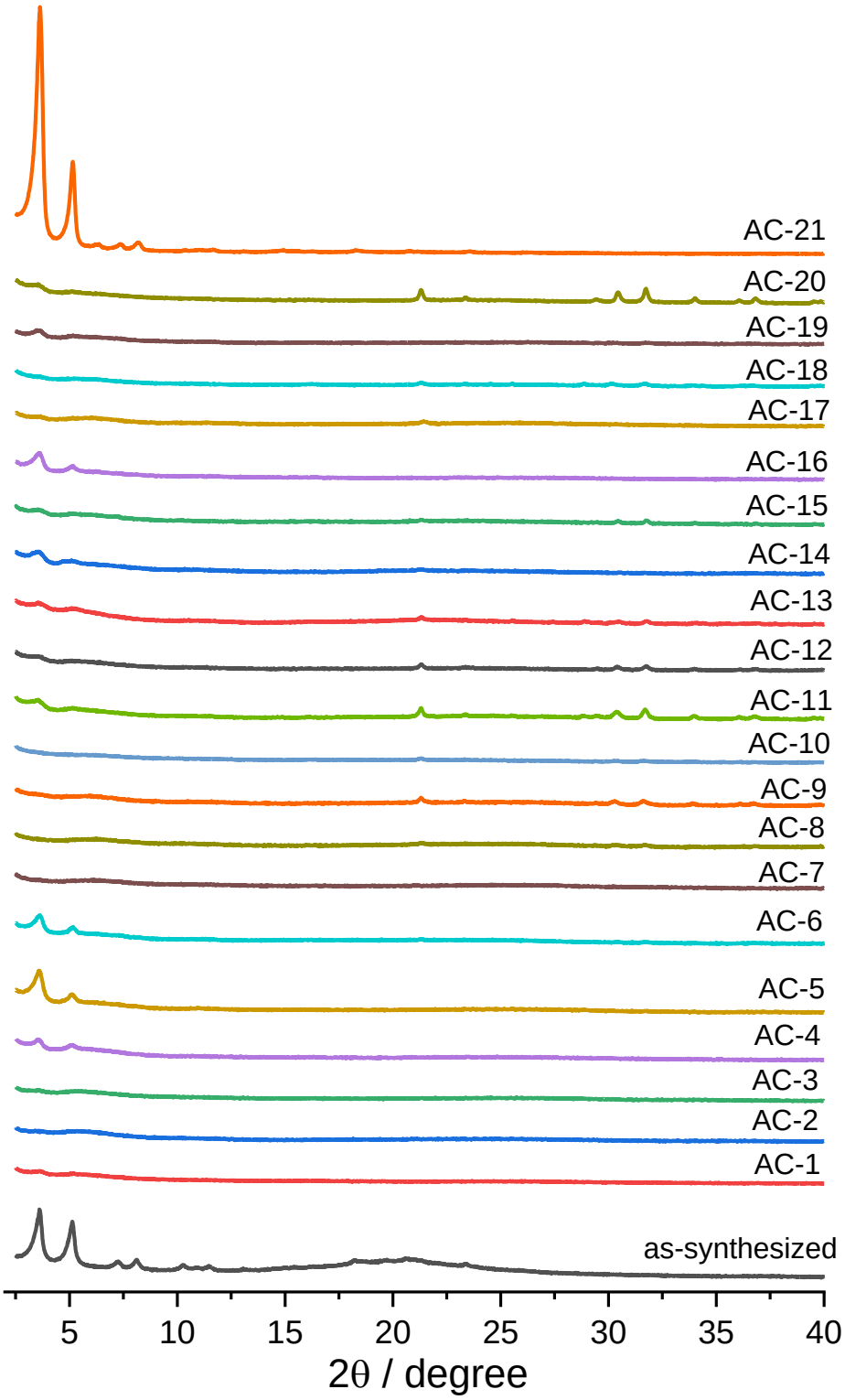

Figure 2.43. PXRD comparison of different activation conditions screened for **SPB-COF-DBA**.

2.4.7.2 Gas sorption isotherms of SPB-COFs

The porosity of SPB-COF-DBA was evaluated by nitrogen sorption measurements at 77 K (**Figure 2.44**). The Brunauer−Emmett−Teller (BET) and Langmuir surface areas were found to be 1726 and 2179 $m^2 g^{-1}$, respectively, which equates to 31% or 40% of the calculated N_2 accessible surface area (5495 $m^2 g^{-1}$) based on the SPB-COF framework without the counter cations. The difference between the theoretical and experimental values may be attributed, in part, to the partial structural collapse during activation as indicated by the PXRD comparison before and after $scCO_2$ activation (**Figure 2.44d**). SPB-COF-DBA exhibited a nitrogen adsorption isotherm shape that is consistent with mesoporosity and a pore volume of 0.9 $m^3 g^{-1}$. The pore size derived for SPB-COF-DBA by fitting a nonlocal density functional theory (NL-DFT) model to the N_2 isotherm was 2.45 nm.

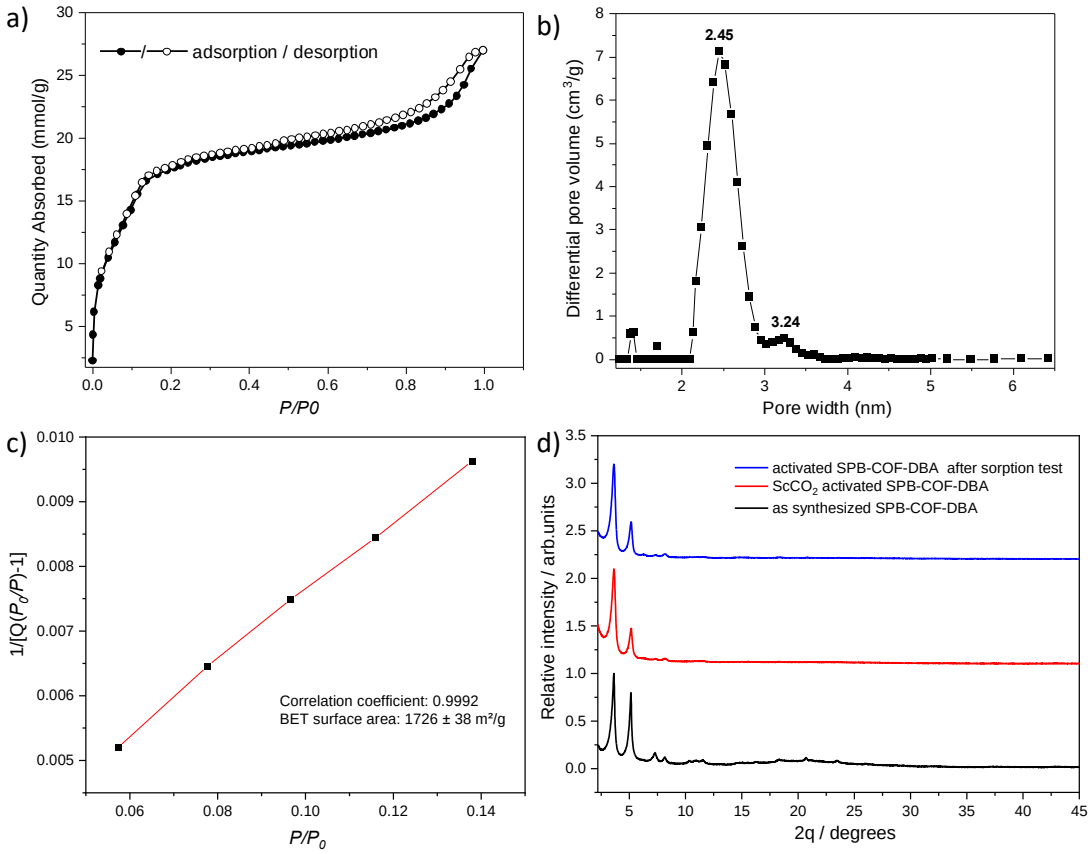

Figure 2.44. (a) Nitrogen adsorption/desorption isotherms for **SPB-COF-DBA** recorded at 77 K. (b) Pore size distribution profiles of **SPB-COF-DBA** calculated by NL-DFT. (c) BET surface area plot for **SPB-COF-DBA**. The x axis range was selected from P/P_0 = 0.05~0.3 to satisfy both a correlation coefficient > 0.995 and a positive C value. (d) PXRD comparison of **SPB-COF-DBA**, as synthesized, after $scCO_2$ activation and after sorption test. We used $scCO_2$ activated samples for sorption measurements.

The activation of SPB-COF-DMA and SPB-COF-TBA were both unsuccessful. Possibly due to unknown effects from the NMP solvent applied for these two COFs synthesis. After the $scCO_2$ activation, the crystallinity was lost in both SPB-COF-DMA (**Figure 2.45d**) and SPB-COF-TBA (**Figure 2.46d**). We are still not sure about the reason why the activation of these two COFs was unsuccessful. Due to the amorphous nature of these two COFs after activation, SPB-COF-DMA and SPB-COF-TBA gave a low BET surface area of 180 $m^2\ g^{-1}$ and 271 $m^2\ g^{-1}$, respectively. The pore size distribution profiles from these two COFs are thus not so reliable also.

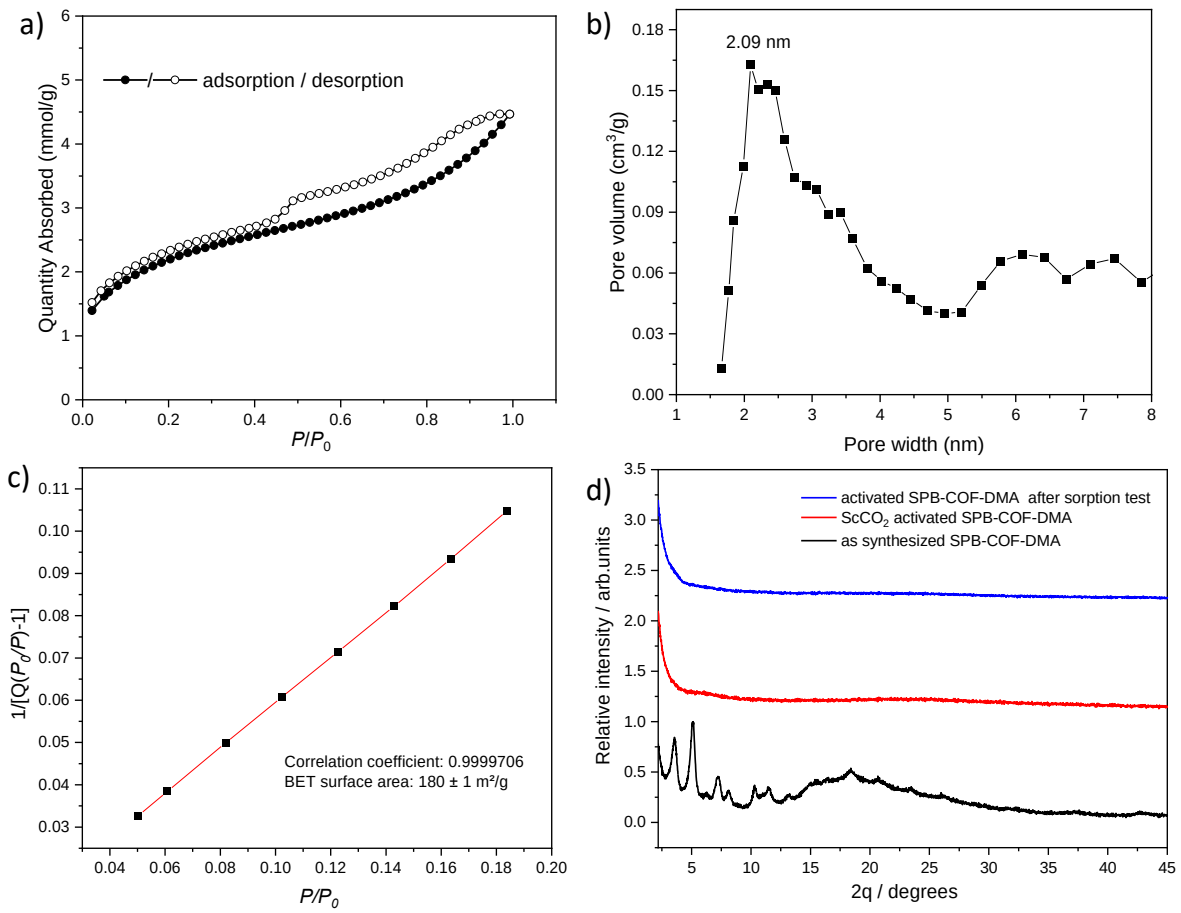

Figure 2.45. (a) Nitrogen adsorption/desorption isotherms for **SPB-COF-DMA** recorded at 77 K. (b) Pore size distribution profiles of **SPB-COF-DMA** calculated by NL-DFT. (c) BET surface area plot for **SPB-COF-DMA**. The x axis range was selected from P/P_0 = 0.05~0.3 to satisfy both a correlation coefficient > 0.995 and a positive C value. (d) PXRD comparison of **SPB-COF-DMA**, as synthesized, after $scCO_2$ activation and after sorption test. We used $scCO_2$ activated samples for sorption measurements. The activation of **SPB-COF-DMA** using $scCO_2$ was not successful.

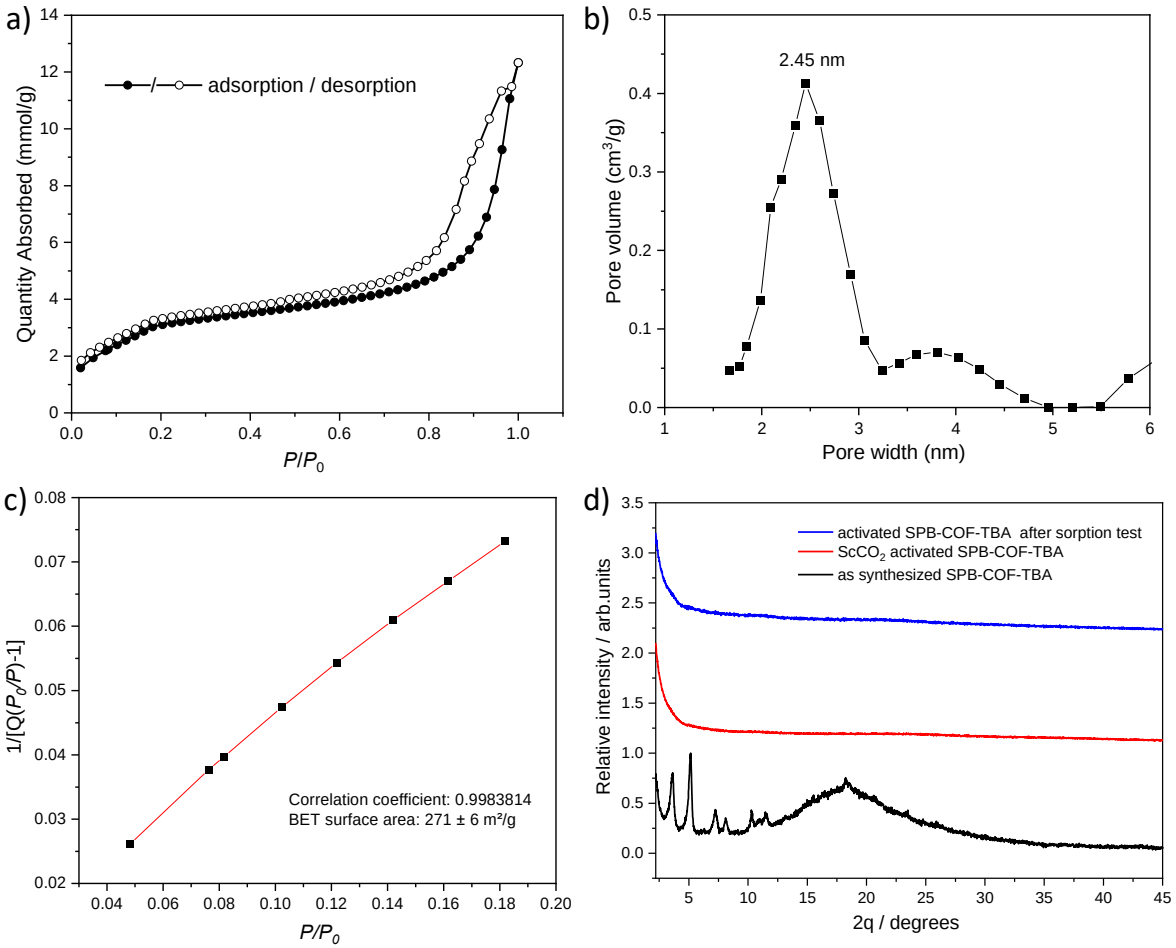

Figure 2.46. (a) Nitrogen adsorption/desorption isotherms for **SPB-COF-TBA** recorded at 77 K. (b) Pore size distribution profiles of **SPB-COF-TBA** calculated by NL-DFT. (c) BET surface area plot for **SPB-COF-TBA**. The x axis range was selected from P/P_0 = 0.05~0.3 to satisfy both a correlation coefficient > 0.995 and a positive C value. (d) PXRD comparison of **SPB-COF-TBA**, as synthesized, after $scCO_2$ activation and after sorption test. We used $scCO_2$ activated samples for sorption measurements. The activation of **SPB-COF-TBA** using $scCO_2$ was not successful.

2.4.8 Solvent stability test

As-synthesized SPB-COF powders (20 mg) were immersed in different organic solvents or aqueous solutions (3.0 mL) at room temperature for 24 hours. The SPB-COFs were then separated by centrifugation and washed with anhydrous acetone three times. The PXRD of these samples was then measured without further purification. The SPB-COF samples were dried in an 80 °C vacuum oven for 6 hours before FT-IR measurement. These samples were the same batch as used for PXRD measurements. As shown below in **Figure 2.47-2.49**, SPB-COFs are stable in all the organic solvents tested and aqueous solutions except acidic solutions – we propose this is due to the intrinsic susceptibility of spiroborate units to hydrolyse in acidic conditions.[35,36]

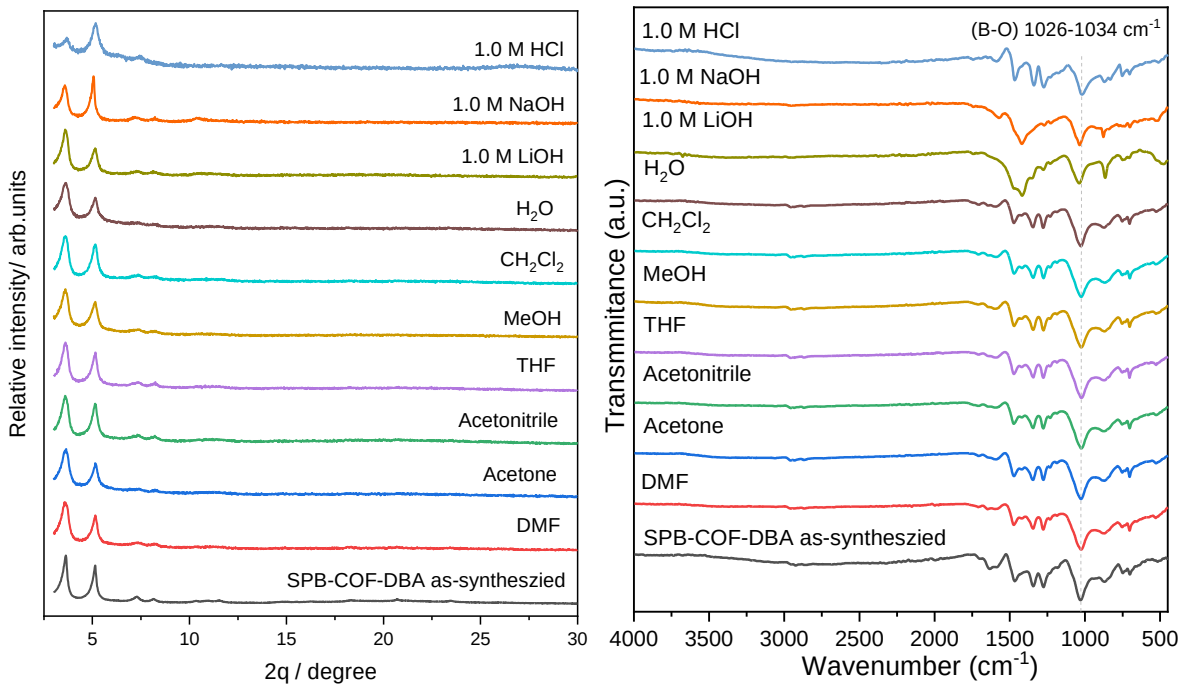

Figure 2.47. (a) PXRD patterns and (b) FT-IR spectra of **SPB-COF-DBA** before and after immersion in solvent for 24 h.

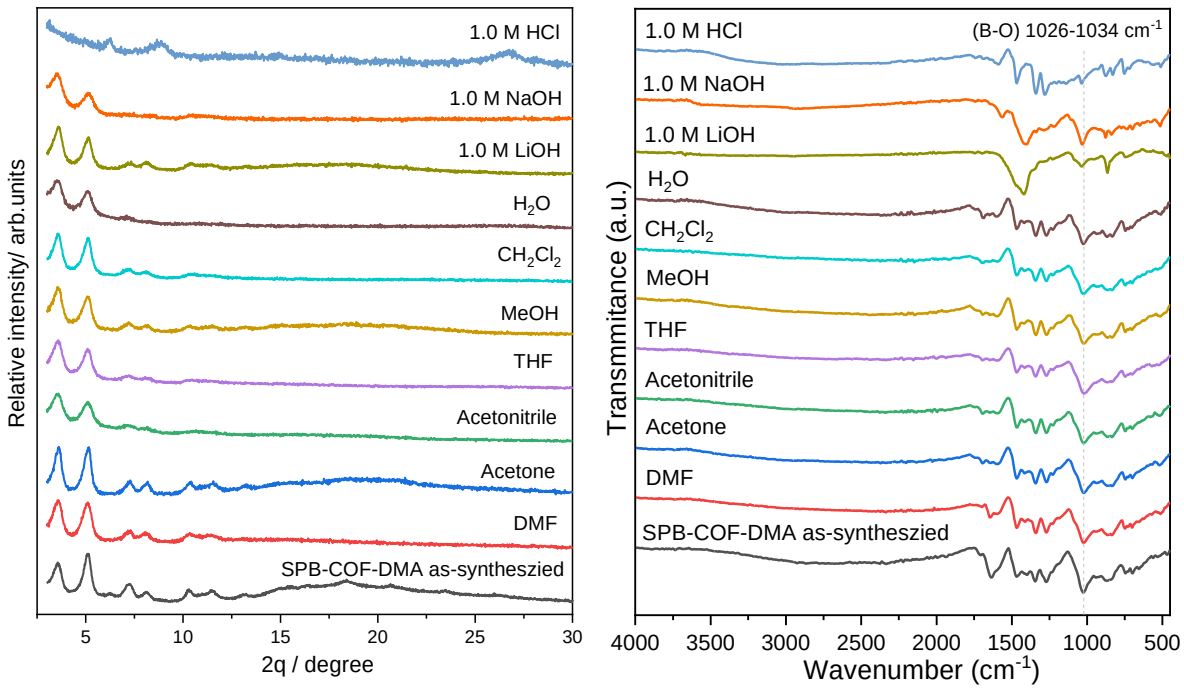

Figure 2.48. (a) PXRD patterns and (b) FT-IR spectra of **SPB-COF-DMA** before and after immersion in solvent for 24 h.

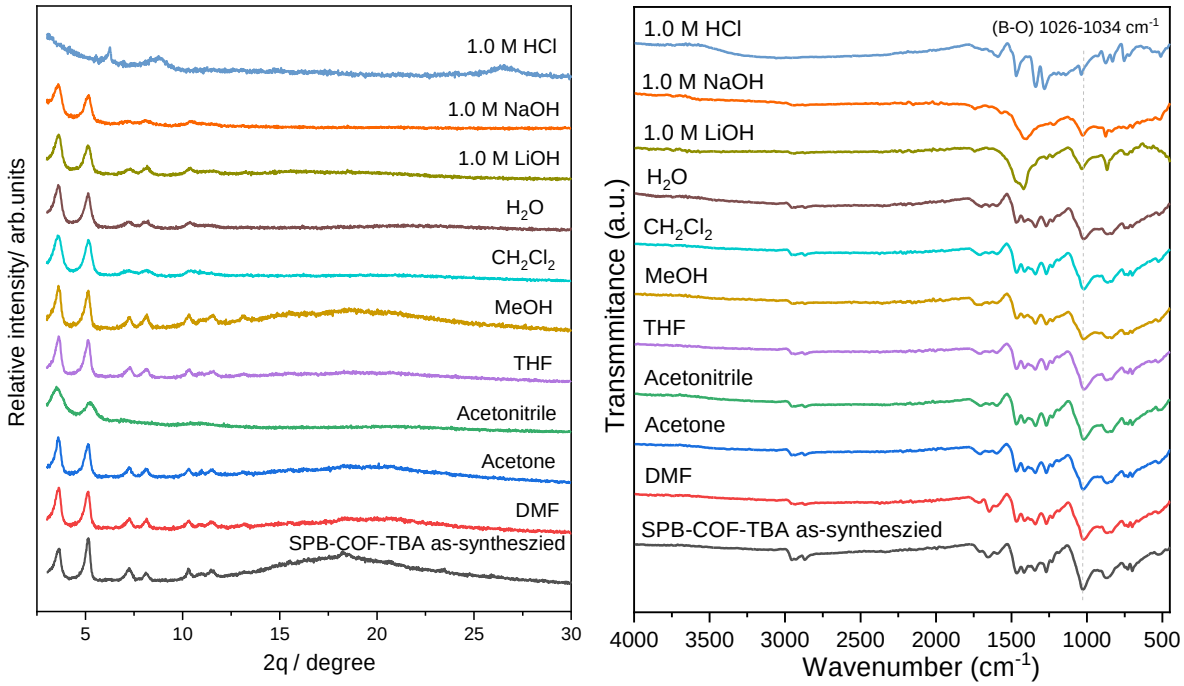

Figure 2.49. (a) PXRD patterns and (b) FT-IR spectra of **SPB-COF-TBA** before and after immersion in solvent for 24 h.

2.5 Conclusion

In this work, we connected the square planar cobalt(II) phthalocyanine (PcCo) units by tetrahedral-shaped spiroborate linkages to realise 3D COFs with non-interpenetrated **nbo** topology. The successful formation of spiroborate linkage was corroborated by FT-IR and solid-state ^{11}B NMR spectra. One of the three SPB-COFs obtained, SPB-COF-DBA, showed high crystallinity and long-range order, with 11 resolved diffraction peaks in the experimental powder X-ray diffraction (PXRD) pattern. This well-ordered crystal lattice allowed clear visualization of the cubic crystal lattice using HR-TEM. SPB-COF-DBA has cube-shaped pores and exhibits permanent porosity with a Brunauer−Emmett−Teller (BET) surface area of 1726 m^2 g^{-1}. This work provides a potential general strategy for targeting 3D COFs structures from easily accessible planar or near planar organic building blocks.

2.6 Materials and methods

All reagents were obtained from Sigma-Aldrich, Manchester Organics, or TCI Europe. Anhydrous solvents were purchased from Sigma-Aldrich, Acros Organics or Fisher Scientific. All chemicals were used without further purification. All gases for sorption analysis were supplied by BOC at a purity of ≥99.9%. Reactions were carried out under nitrogen atmosphere using standard Schlenk techniques.

2.6.1 Solution nuclear magnetic resonance

NMR spectra were recorded on a Bruker Avance 400 NMR spectrometer, operating at frequencies of 400 MHz (^{1}H) and 100 MHz (^{13}C) and referenced against the residual ^{1}H or ^{13}C signal of the solvent. ^{11}B spectra operating at 128 MHz used deuterium lock for referencing.

2.6.2 Solid-state ^{13}C CP MAS and ^{11}B MAS nuclear magnetic resonance

Solid-state NMR experiments were performed on a Bruker Avance III HD spectrometer using the Durham University (UK) solid-state NMR service. Carbon-13 magic-angle spinning measurements were carried out at 100.63 MHz using a Bruker Avance III HD spectrometer and 4 mm (rotor o.d.) probe. Spectra were acquired at a spin rate of 10 kHz. Cross-polarisation (CP) spectra were recorded with TOSS spinning sideband suppression, 0.8 ms contact time and with a recycle delay of 1 s. Carbon spectral referencing is relative to neat tetramethylsilane, carried out by setting the high-frequency signal from an external sample of adamantane to 38.5 ppm. 50 Hz of line broadening was added to improve the signal to noise. Boron-11 magic-angle spinning measurements were carried out at 128.39 MHz using a Bruker Avance III HD spectrometer and 4 mm (rotor o.d.) probe. Spectra were acquired at a spin rate of 20 kHz. All direct excitation ^{11}B spectra were acquired with a 1 us 30-degree solid pulse which was determined from a 6 us solution pulse determined on BF_3/OEt_2. The spectra were acquired with a recycle delay of 1 s determined on the sample. Boron spectral referencing is relative to BF_3/OEt_2. Since the probe used has a boron background, a spectrum of an empty rotor was collected, and this was subtracted from all spectra.

2.6.3 Mass spectrometry

High resolution mass spectrometry (HR-MS) as performed on an Agilent Technologies 6530B accurate- mass QTOF mixed ESI/APCI mass spectrometer (capillary voltage 4000 V, fragmentor 225 V) in positive-ion detection mode. Matrix-assisted laser desorption ionization time-of-flight mass (MALDI-TOF MS) spectra were recorded on an Applied Biosystems BioSpectrometry model Voyager-DE-STR spectrometer in reflector or linear mode.

2.6.4 Elemental analysis

CHN analysis was performed on a Thermo EA1112 Flash CHNS-O Analyzer using standard microanalytical procedures.

2.6.5 Inductively coupled plasma optical emission spectrometry

Inductively coupled plasma optical emission spectrometry (ICP-OES) measurements were conducted on an ICP-OES Agilent 5110. Samples were digested in concentrated nitric acid (67-69%, trace metal analysis grade) by microwave, and then diluted using distilled water.

2.6.6 Powder X-ray diffraction

Laboratory powder X-ray diffraction (PXRD) data patterns were collected in transmission mode on samples held on thin Mylar film in aluminium well plates on a Panalytical Empyrean diffractometer equipped with a high throughput screening (HTS) XYZ stage, X-ray focusing mirror, and PIXcel detector, using Cu-Kα radiation, λ = 1.54184 Å. For HT screening, PXRD patterns were measured over the 2θ range 1-56° in 0.013° steps over 30 minutes.

2.6.7 Single crystal X-ray diffraction

Single crystal X-ray data for the model compounds were measured on a Rigaku MicroMax-007 HF rotating anode diffractometer (Mo-Kα radiation, λ = 0.71073 Å, Kappa 4-circle goniometer, Rigaku Saturn724+ detector), and data reduction was performed using CrysAlisPro. Structures were solved with SHELXL[37] and refined by full-matrix least squares on $|F|^2$ by SHELXL,[38] interfaced through the programme OLEX2.[39] All non- H atoms were refined anisotropically. H atoms bonded to C atoms were fixed in geometrically estimated positions and refined using the riding model. H atoms bonded to N atoms were located in the different maps and refined isotropically. For full refinement details, see **Tables 2.3** and **Table 2.4**.

2.6.8 Fourier-transform infrared spectroscopy

Attenuated total reflection (ATR)-FT-IR spectra were obtained with an ATR method on a Bruker Tensor-27 spectrometer at room temperature.

2.6.9 Thermogravimetric analysis

TGA analysis was carried out using a TA Q5000IR analyzer with an automated vertical overhead thermobalance. Samples were heated at a rate of 10 °C/min under a dry nitrogen gas flow.

2.6.10 Scanning electron microscopy

SEM images were recorded using a Hitachi S-4800 cold field emission scanning electron microscope (FE- SEM). Samples were prepared by depositing the dry powders on a silicon disk and then coating the samples with Chromium using an Emitech K550X automated sputter coater.

2.6.11 Transmission electron microscopy

TEM images were obtained using a JEOL 2100+ microscope operating at 200 KV equipped with a Gatan Rio Camera. Since COF materials are electron beam sensitive, the electron beam damage to the specimen was minimized as much as possible. A single HR-TEM image was recorded with an exposure time of 2 seconds. After drift compensation, some frames can be superimposed to increase the signal-to-noise (SN) ratio.

SPB-COF crystals were dispersed in anhydrous acetone by ultrasonication and drop-cast on a holey carbon film on 200 mesh copper grids.

2.6.12 Gas sorption analysis

Surface areas were measured by nitrogen sorption at 77.3 K. Powder samples were degassed offline at room temperature, followed by degassing on the analysis port under vacuum at room temperature for 12 hours. Isotherms were measured using a Micromeritics 2420 volumetric adsorption analyzer. Surface areas were calculated from a selected range within the relative pressure (P/P_0) range from 0.05 to 0.30 of the adsorption branch, to satisfy both a correlation coefficient > 0.995 and a positive C value.

2.6.13 COFs structure modelling

As we discussed in **Section 2.4.1** (powder X-ray diffraction analysis and structure modelling) in this chapter: according to RCSR database,[40] 5 topologies are possible for square-planar building blocks of a single type: edge-transitive **nbo**, **lvt** and **rhr** nets, and **tcb** and **uks** nets that have two edges (**Figure 2.15**).[11] Moreover, although the conformer search result of the spiroborate unit in the Cambridge Structural Database (CSD) showed that this linkage can hardly be planar (**Figure 2.2**), for more accurate results, here, we considered the possibility of forming a 2D planar **sql** topology (**Figure 2.1a**). Based on these assumptions, we constructed SPB-COF models for each topology using zeo++ code[26] and Material Studio software, and compared PXRD patterns simulated from the models with the experimental diffraction pattern. PXRD comparison results was concluded in **Figure 2.16** and the result showed that the experimental phase of SPB-COFs is of **nbo** topology. For 3D COFs structures, interpenetration needs to be considered. Here, we constructed SPB-COF models of two-fold and three-fold interpenetrated **nbo** nets. The comparison result was summarized in **Figure 2.18** and the result reaffirms that the experimental phase of SPB-COFs is of non-interpenetrated **nbo** topology.

For all the COF models included in **Figures 2.16** and **Figure 2.18**, we used spiro-orthocarbonate (SPC) linkages, instead of spiroborate (SPB) linkages, to connect the cobalt(II) phthalocyanine (PcCo) units. In doing so, we rendered all the frameworks charge neutral, hence allowing for their geometry optimizations without having to consider the counter ions (we are unable to accurately position these counter ions within frameworks). All the geometry optimizations made use of the Universal force field, implemented in the Forcite module of the BIOVIA Materials Studio software. We also fully relaxed an SPB-COF model, with charge-balancing lithium cations, for the **nbo** topology, using density functional theory (DFT). The position of lithium cation toward the spiroborate linkage was decided by referring a related single crystal structure in CSD, with Li^+ as the counter cation (CSD Identifier: ODOWEJ).[24] The reason why we apply this lithium cation counterbalanced SPB-COF model for PXRD comparison is because the small lithium size would minimize the counter cations influence toward simulated PXRD pattern. To confirm the rationality of using SPC-linked COF models for structure solution, we compared the SPC-based model and the SPB-based model, both with a non-interpenetrated **nbo** topology, the PXRD comparison result shown in **Figure 2.19** evidenced that these two models yielded almost identical PXRD patterns.

Periodic DFT calculations were carried out within the plane-wave pseudopotential formalism, using the Vienna *ab initio* Simulation Package code.[41] A kinetic-energy cutoff of 500 eV was used to define the plane-wave basis set, and the electronic Brillouin zone was integrated using Γ-centred

Monkhorst−Pack grids with the smallest allowed spacing between k-points (KSPACING) being 0.25 $Å^{-1}$. Geometry optimizations, involving both lattice parameters and atomic positions, were performed employing the Perdew−Burke−Ernzerhof exchange−correlation functional with the DFT-D3(BJ) dispersion correction. Tolerances of 10^{-6} eV and 10^{-2} eV $Å^{-1}$ were applied during the optimization of the Kohn−Sham wavefunctions and the geometry optimizations, respectively. This periodic DFT calculations were performed by Dr. Linjiang Chen. The Li^+ counterbalanced spiroborate-based COF model was shown in **Figure 2.50a**.

To confirm the rationality of the final SPB-COF model used for PXRD comparison (Li^+ counterbalanced) after geometry optimization, we checked: (1) the torsion angle of the two phenyl units alongside the spiroborate linkage has a torsion angle of 86º, in good accordance with the conformer search result of the reported spiroborate units (**Figure 2.2**), where the torsion angle mainly locates within a range of 80 ~ 95º; (2) the average C-C bond length in the benzene rings of the optimized SPB-COF models is at around 1.4 Å, in good agreement with former studies (**Figure 2.50b**).[41] These results can be good evidence to reaffirm the accuracy of the optimized SPB-COF models.

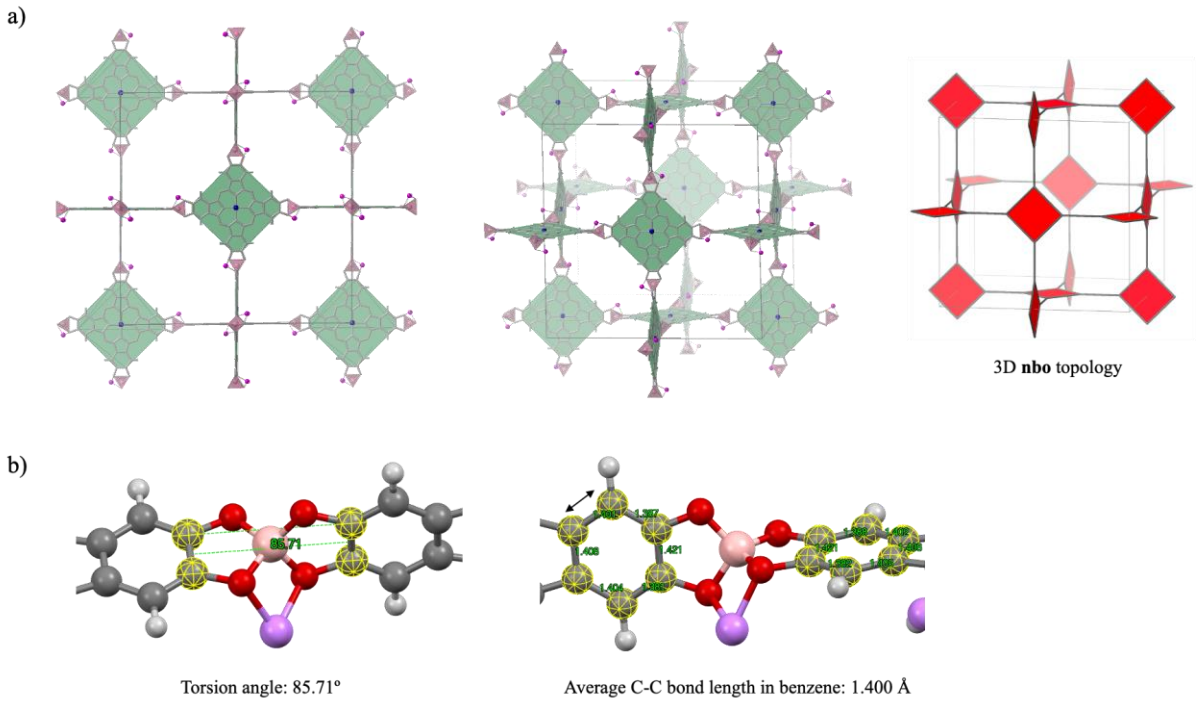

Figure 2.50. (a) Two views of the optimized SPB-COF model with Li^+ as the counter cation, and the graph representation of the 3D **nbo** topology shown as its corresponding augmented net. The green square represents the PcCo unit, pink tetrahedral represents the spiroborate linkage and Li^+ counter cation was coloured in purple. (b) SPB-COF model structure accuracy checking through spiroborate linkage torsion angle and the average C-C bond length in the benzene rings.

2.7 Atomic coordinates of the fitted COF models

Fractional atomic coordinates and unit cell parameters of the 3D non-interpenetrated SPB-based COF model (Li^+ as counter cation) with **nbo** topology.

Name: 3D non-interpenetrated SPB-COF model (Li^+ as counter cation) of **nbo** topology				
Space Group: R-3 (No.146) a=b=c= 34.7072 (Å), α=β=γ= 89.6530°				
Atom Name	**x**	**y**	**z**	**Occupancy**
C	-0.01979	-0.11888	0.49952	1.00
C	-0.96773	-0.07885	0.49855	1.00
C	-0.15300	-0.95743	0.50240	1.00
C	-0.18684	-0.97851	0.50203	1.00
C	-0.52064	-0.61873	-0.00133	1.00
C	-0.46820	-0.57913	-0.00074	1.00
C	-0.65297	-0.45671	-0.00134	1.00
C	-0.68678	-0.47785	-0.00186	1.00
C	-0.97923	-0.11896	0.49841	1.00
C	-0.03178	-0.07884	0.49985	1.00
C	-0.84690	-0.95869	0.50000	1.00
C	-0.81352	-0.98059	0.49951	1.00
C	-0.48008	-0.61902	-0.00120	1.00
C	-0.53225	-0.57851	-0.00088	1.00
C	-0.34696	-0.45933	0.00081	1.00
C	-0.31358	-0.48121	0.00129	1.00
C	-0.11886	-0.01995	0.50067	1.00
C	-0.07891	-0.96785	0.50154	1.00
C	-0.95721	-0.15293	0.49718	1.00
C	-0.97827	-0.18678	0.49729	1.00
C	-0.61888	-0.51921	-0.00048	1.00
C	-0.57878	-0.46722	-0.00010	1.00
C	-0.45856	-0.65341	-0.00134	1.00
C	-0.48036	-0.68658	-0.00150	1.00
C	-0.11900	-0.97941	0.50159	1.00
C	-0.07880	-0.03189	0.50049	1.00
C	-0.95888	-0.84684	0.50001	1.00
C	-0.98082	-0.81350	0.50091	1.00
C	-0.61893	-0.47865	-0.00055	1.00
C	-0.57891	-0.53127	-0.00033	1.00
C	-0.45750	-0.34746	0.00180	1.00
C	-0.47870	-0.31344	0.00192	1.00
O	-0.96764	-0.77593	0.50000	1.00
O	-0.46478	-0.27696	0.00239	1.00
O	-0.03576	-0.77664	0.50410	1.00
O	-0.53297	-0.27576	0.00094	1.00
O	-0.77596	-0.96740	0.50079	1.00
O	-0.27606	-0.46794	0.00104	1.00
O	-0.77656	-0.03550	0.49714	1.00

O	-0.27659	-0.53615	0.00285	1.00
H	-0.92750	-0.84685	0.49932	1.00
H	-0.42614	-0.34790	0.00211	1.00
H	-0.07413	-0.84729	0.50395	1.00
H	-0.57283	-0.34645	0.00162	1.00
H	-0.84698	-0.92730	0.50061	1.00
H	-0.34716	-0.42795	0.00112	1.00
H	-0.84716	-0.07392	0.49667	1.00
H	-0.34711	-0.57466	0.00158	1.00
N	-0.06849	-0.06859	0.50020	1.00
N	-0.56885	-0.56801	-0.00062	1.00
N	-0.93115	-0.06874	0.49806	1.00
N	-0.43150	-0.56932	-0.00029	1.00
N	0.00015	-0.05478	0.49941	1.00
N	-0.50016	-0.55476	-0.00060	1.00
N	-0.05479	0.00006	0.50082	1.00
N	-0.55478	-0.49944	-0.00007	1.00
B	-0.00358	-0.74997	0.50387	1.00
B	-0.74992	-0.00327	0.49714	1.00
Li	-0.24966	-0.45410	0.95663	1.00
Li	-0.45312	-0.75114	0.04308	1.00
Co	0.00000	-0.50000	0.50000	1.00
Co	-0.50000	-0.00000	-0.00000	1.00

Fractional atomic coordinates and unit cell parameters of the 3D non-interpenetrated SPC-based COF model with **nbo** topology.

Name: 3D non-interpenetrated SPC-COF model of **nbo** topology				
Space Group: Im-3m (No.229) a=b=c= 34.9302 (Å), α=β=γ= 90°				
Atom Name	**x**	**y**	**z**	**Occupancy**
C	0.02058	0.11964	0.50000	1.00
C	0.96798	0.08199	0.50000	1.00
C	0.15569	0.95751	0.50000	1.00
C	0.18913	0.97947	0.50000	1.00
O	0.96611	0.77377	0.50000	1.00
H	0.92655	0.84368	0.50000	1.00
N	0.07081	0.07081	0.50000	1.00
N	0.00000	0.05617	0.50000	1.00
C	0.00000	0.75000	0.50000	1.00
Co	0.00000	0.50000	0.50000	1.00

2.8 Reference

(1) Zhu, Q.; Wang, X.; Clowes, R.; Cui, P.; Chen, L.; Little, M. A.; Cooper, A. I. 3D Cage COFs: A Dynamic Three-Dimensional Covalent Organic Framework with High-Connectivity Organic Cage Nodes. *J. Am. Chem. Soc.* **2020**, *142* (39), 16842–16848.

(2) Nguyen, H. L. Reticular Design and Crystal Structure Determination of Covalent Organic Frameworks. *Chem. Sci.* **2021**, *12* (25), 8632–8647.

(3) Guillerm, V.; Kim, D.; Eubank, J. F.; Luebke, R.; Liu, X.; Adil, K.; Lah, M. S.; Eddaoudi, M. A Supermolecular Building Approach for the Design and Construction of Metal-Organic Frameworks. *Chem. Soc. Rev.* **2014**, *43* (16), 6141–6172.

(4) Lan, Y.; Han, X.; Tong, M.; Huang, H.; Yang, Q.; Liu, D.; Zhao, X.; Zhong, C. Materials Genomics Methods for High-Throughput Construction of COFs and Targeted Synthesis. *Nat. Commun.* **2018**, *9* (1), 5274.

(5) Kang, X.; Han, X.; Yuan, C.; Cheng, C.; Liu, Y.; Cui, Y. Reticular Synthesis of Tbo Topology Covalent Organic Frameworks. *J. Am. Chem. Soc.* **2020**, *142* (38), 16346–16356.

(6) Nguyen, H. L.; Gropp, C.; Ma, Y.; Zhu, C.; Yaghi, O. M. 3D Covalent Organic Frameworks Selectively Crystallized through Conformational Design. *J. Am. Chem. Soc.* **2020**, *142* (48), 20335–20339.

(7) Yahiaoui, O.; Fitch, A. N.; Hoffmann, F.; Fröba, M.; Thomas, A.; Roeser, J. 3D Anionic Silicate Covalent Organic Framework with Srs Topology. *J. Am. Chem. Soc.* **2018**, *140* (16), 5330–5333.

(8) Zhang, Y.; Duan, J.; Ma, D.; Li, P.; Li, S.; Li, H.; Zhou, J.; Ma, X.; Feng, X.; Wang, B. Three-Dimensional Anionic Cyclodextrin-Based Covalent Organic Frameworks. *Angew. Chemie - Int. Ed.* **2017**, *56* (51), 16313–16317.

(9) Kalmutzki, M. J.; Hanikel, N.; Yaghi, O. M. Secondary Building Units as the Turning Point in the Development of the Reticular Chemistry of MOFs. *Sci. Adv.* **2018**, *4* (10), eaat9180.

(10) O'Keeffe, M.; Peskov, M. A.; Ramsden, S. J.; Yaghi, O. M. The Reticular Chemistry Structure Resource (RCSR) Database of, and Symbols for, Crystal Nets. *Acc. Chem. Res.* **2008**, *41* (12), 1782–1789.

(11) Eddaoudi, M.; Kim, J.; Vodak, D.; Sudik, A.; Wachter, J.; O'Keeffe, M.; Yaghi, O. M. Geometric Requirements and Examples of Important Structures in the Assembly of Square Building Blocks. *Proc. Natl. Acad. Sci. U. S. A.* **2002**, *99* (8), 4900–4904.

(12) Fu, Z.; Wang, X.; Gardner, A. M.; Wang, X.; Chong, S. Y.; Neri, G.; Cowan, A. J.; Liu, L.; Li, X.; Vogel, A.; Clowes, R.; Bilton, M.; Chen, L.; Sprick, R. S.; Cooper, A. I. A Stable Covalent Organic Framework for Photocatalytic Carbon Dioxide Reduction. *Chem. Sci.* **2020**, *11* (2), 543–550.

(13) Zhou, T.-Y.; Xu, S.-Q.; Wen, Q.; Pang, Z.-F.; Zhao, X. One-Step Construction of Two Different Kinds of Pores in a 2D Covalent Organic Framework. *J. Am. Chem. Soc.* **2014**, *136* (45), 15885–15888.

(14) Li, Z.; He, T.; Gong, Y.; Jiang, D. Covalent Organic Frameworks: Pore Design and Interface Engineering. *Acc. Chem. Res.* **2020**, *53* (8), 1672–1685.

(15) Topology. In *Introduction to Reticular Chemistry*; John Wiley & Sons, Ltd, 2019; pp 429–452.

(16) Guan, X.; Ma, Y.; Li, H.; Yusran, Y.; Xue, M.; Fang, Q.; Yan, Y.; Valtchev, V.; Qiu, S. Fast, Ambient Temperature and Pressure Ionothermal Synthesis of Three-Dimensional Covalent Organic Frameworks. *J. Am. Chem. Soc.* **2018**, *140* (13), 4494–4498.

(17) Danjo, H.; Hashimoto, Y.; Kidena, Y.; Nogamine, A.; Katagiri, K.; Kawahata, M.; Miyazawa, T.; Yamaguchi, K. Nestable Tetrakis(Spiroborate) Nanocycles. *Org. Lett.* **2015**, *17* (9), 2154–2157.

(18) Danjo, H.; Masuda, Y.; Kidena, Y.; Kawahata, M.; Ohara, K.; Yamaguchi, K. Preparation of Cage-Shaped Hexakis(Spiroborate)S. *Org. Biomol. Chem.* **2020**, *18* (19), 3717–3723.

(19) Du, Y.; Yang, H.; Whiteley, J. M.; Wan, S.; Jin, Y.; Lee, S.-H.; Zhang, W. Ionic Covalent Organic Frameworks with Spiroborate Linkage. *Angew. Chem. Int. Ed.* **2016**, *55* (5), 1737–1741.

(20) Zhang, Y.; Duan, J.; Ma, D.; Li, P.; Li, S.; Li, H.; Zhou, J.; Ma, X.; Feng, X.; Wang, B. Three-Dimensional Anionic Cyclodextrin-Based Covalent Organic Frameworks. *Angew. Chem. Int. Ed.* **2017**, *56* (51), 16313–16317.

(21) Hu, Y.; Teat, S. J.; Gong, W.; Zhou, Z.; Jin, Y.; Chen, H.; Wu, J.; Cui, Y.; Jiang, T.; Cheng, X.; Zhang, W. Single Crystals of Mechanically Entwined Helical Covalent Polymers. *Nat. Chem.* **2021**, *13* (7), 660–665.

(22) Metz, J.; Schneider, O.; Hanack, M. Synthesis and Properties of Substituted (Phthalocyaninato)-Iron and -Cobalt Compounds and Their Pyridine Adducts. *Inorg. Chem.* **1984**, *23* (8), 1065–1071.

(23) Ding, X.; Feng, X.; Saeki, A.; Seki, S.; Nagai, A.; Jiang, D. Conducting Metallophthalocyanine 2D Covalent Organic Frameworks: The Role of Central Metals in Controlling π-Electronic Functions. *Chem. Commun.* **2012**, *48* (71), 8952–8954.

(24) Downard, A.; Nieuwenhuyzen, M.; Seddon, K. R.; van den Berg, J.-A.; Schmidt, M. A.; Vaughan, J. F. S.; Welz-Biermann, U. Structural Features of Lithium Organoborates. *Cryst. Growth Des.* **2002**, *2* (2), 111–119.

(25) Willems, T. F.; Rycroft, C. H.; Kazi, M.; Meza, J. C.; Haranczyk, M. Algorithms and Tools for High-Throughput Geometry-Based Analysis of Crystalline Porous Materials. *Microporous Mesoporous Mater.* **2012**, *149* (1), 134–141.

(26) Martin, R. L.; Haranczyk, M. Construction and Characterization of Structure Models of Crystalline Porous Polymers. *Cryst. Growth Des.* **2014**, *14* (5), 2431–2440.

(27) Danjo, H.; Kidena, Y.; Kawahata, M.; Sato, H.; Katagiri, K.; Miyazawa, T.; Yamaguchi, K. Multilayered Inclusion Nanocycles of Anionic Spiroborates. *Org. Lett.* **2015**, *17* (10), 2466–2469.

(28) Gaafar, M. S.; El-Aal, N. S. A.; Gerges, O. W.; El-Amir, G. Elastic Properties and Structural Studies on Some Zinc-Borate Glasses Derived from Ultrasonic, FT-IR and X-Ray Techniques. *J. Alloys Compd.* **2009**, *475* (1–2), 535–542.

(29) Neti, V. S. P. K.; Wu, X.; Hosseini, M.; Bernal, R. A.; Deng, S.; Echegoyen, L. Synthesis of a Phthalocyanine 2D Covalent Organic Framework. *CrystEngComm* **2013**, *15* (36), 7157–7160.

(30) Park, S.; Johnson, D. K.; Ishizawa, C. I.; Parilla, P. A.; Davis, M. F. Measuring the Crystallinity Index of Cellulose by Solid State 13C Nuclear Magnetic Resonance. *Cellulose* **2009**, *16* (4), 641–647.

(31) Kimura, H.; Dohi, H.; Kotani, M.; Matsunaga, T.; Yamauchi, K.; Kaji, H.; Kurosu, H.; Asakura, T. Molecular Dynamics and Orientation of Stretched Rubber by Solid-State 13C NMR. *Polym. J.* **2010**, *42*, 25–30.

(32) Seoudi, R.; El-Bahy, G. S.; El Sayed, Z. A. FTIR, TGA and DC Electrical Conductivity Studies of Phthalocyanine and Its Complexes. *J. Mol. Struct.* **2005**, *753* (1-3), 119–126.

(33) Kumar, P.; Kumar, A.; Sreedhar, B.; Sain, B.; Ray, S. S.; Jain, S. L. Cobalt Phthalocyanine Immobilized on Graphene Oxide: An Efficient Visible-Active Catalyst for the Photoreduction of Carbon Dioxide. *Chem. – A Eur. J.* **2014**, *20* (20), 6154–6161.

(34) Nelson, A. P.; Farha, O. K.; Mulfort, K. L.; Hupp, J. T. Supercritical Processing as a Route to High Internal Surface Areas and Permanent Microporosity in Metal−Organic Framework Materials. *J. Am. Chem. Soc.* **2009**, *131* (2), 458–460.

(35) Ito, M.; Ikai, T.; Yamamoto, S.; Taura, D.; Ousaka, N.; Yashima, E. Chiral Guest-Induced Catalytic Deracemization of a Spiroborate-Based Double-Stranded Helicate Bearing a Bisporphyrin Unit with Acids. *Chem. Lett.* **2020**, *49* (9), 1030–1033.

(36) Narkar, A. R.; Barker, B.; Clisch, M.; Jiang, J.; Lee, B. P. PH Responsive and Oxidation Resistant Wet Adhesive Based on Reversible Catechol-Boronate Complexation. *Chem. Mater.* **2016**, *28* (15), 5432–5439.

(37) Sheldrick, G. M. SHELXT - Integrated Space-Group and Crystal-Structure Determination. *Acta Crystallogr. Sect. A Found. Crystallogr.* **2015**, *A71* (1), 3–8.

(38) Sheldrick, G. M. Crystal Structure Refinement with SHELXL. *Acta Crystallogr. Sect. C Struct. Chem.* **2015**, *C71* (1), 3–8.

(39) Dolomanov, O. V.; Bourhis, L. J.; Gildea, R. J.; Howard, J. A. K.; Puschmann, H. OLEX2: A Complete Structure Solution, Refinement and Analysis Program. *J. Appl. Crystallogr.* **2009**, *42* (2), 339–341.

(40) Keeffe, M. O.; Peskov, M. a; Ramsden, S. J.; Yaghi, O. M. (RCSR) Database of , and Symbols for , Crystal. *Acc. Chem. Res.* **2008**, *41* (12), 1782–1789.

(41) Kresse, G.; Furthmüller, J. Efficiency of Ab-Initio Total Energy Calculations for Metals and Semiconductors Using a Plane-Wave Basis Set. *Comput. Mater. Sci.* **1996**, *6* (1), 15–50.

Chapter 3

Unexpected spiroborate linkage formation in covalent organic framework synthesis

3.1 Author contributions

Dr. Linjiang Chen helped with the computational geometry optimization of COFs. Dr. Tom Fellowes performed the single crystal measurement and refined the data of model compounds. Dr. Tom Fellowes carried out the PXRD refinement of COFs. Dr. Mounib Bahri performed the TEM measurement. Xiang Zhou helped with GS-MS measurement. Sriram Vijayakrishnan helped with the LC-MS measurements. Rob Clowes helped with the N_2 sorption measurement. Dr. Hongjun Niu helped with supercritical CO_2 drying. Solid-state NMR spectra was performed by the test service from University of Durham. All other work was performed by the thesis author.

3.2 Background

In the last chapter, we successfully synthesised a series of spiroborate-based 3D COFs of **nbo** topology. The obtained SPB-COF-DBA showed the highest BET surface area of 1726 $m^2 g^{-1}$, which is still far lower than the calculated theoretical value of 5495 $m^2 g^{-1}$ (based on a framework model without any counter cations included). We attributed this lower experimental BET surface area to two factors: (1) partial structure collapse during COFs activation, as evidenced by the PXRD comparison before and after activation; (2) the ionic nature of spiroborate linkage allows counter cations to locate inside the COF porosities, thus decreased the exposed accessible surface. To get closer to the high theoretical BET surface area of 3D COFs of **nbo** topology, in this chapter we proposed another strategy to target **nbo** topology with a neutral boronate ester linkage. Boronate ester linkages have long been used for COF synthesis due to their good reversibility, for example, the first 2D[1] and 3D COFs[2] reported were all based on boronate ester linkage. With no counter cations to block the pores, we can expect larger porosity (5.5 nm *vs.* 3.7 nm) and higher BET surface areas could be realized and thus endow these COFs with good performance in gas storage/separations.

The strategy we propose here to target 3D COFs of **nbo** topology follows the same design principle for the preparation of the first MOF with **nbo** topology (MOF-601, **Figure 3.1**).[3] In this example, the dimensionality of MOFs was adjusted from 2D **sql** topology (MOF-118) to 3D **nbo** topology (MOF-601, MOF-602 and MOF-603) by twisting the two carboxylic acid groups on each side of the ligand to near perpendicular orientation by introducing two bulky substitutions at the 2,2' position of the biphenyl unit in the linker (**Figure 3.2**). The bulky groups include cyano (-C≡N), methyl (-CH_3) and iodo (-I), with van der Waals radius of 220, 200 and 198 pm, respectively, which are much larger than the hydrogen atom with a van der Waals radius of 120 ppm.[3] The van der Waals radius of cyano group is calculated based on the equation: (cyano C-N bond length + van der Waals radius of carbon atom + van der Waals radius of nitrogen atom)/2. In linker BPDC, the repulsion induced by the small H atoms at the 2,2' and 6,6' positions of the biphenyl unit are negligible (**Figure 3.2**). Moreover, the carboxyl group on each side of linker BPDC was in good co-planarity with the benzene that it directly connected with. These two factors together endow an overall near planar geometry of linker BPDC, and the reaction between this planar linear linker and a planar 4-c (c = connected) metal cluster $Cu_2(CH_3COO)_4$ yielded a 2D MOF-118 of **sql** topology. Replacing the two hydrogen atoms at the 2,2' positions of the biphenyl unit in linker BPDC by the larger -C≡N, -CH_3 or -I groups increased repulsion and bringing the two carboxylic group on each side of linkers to near perpendicular orientation. Such sterically enforced 90° twist of the carboxyl

groups in these three linkers will reticulates the 4-c planar metal cluster $Cu_2(CH_3COO)_4$ into 3D spatial arrangement to give MOF-601, MOF-602 and MOF-603 with 3D **nbo** topology.

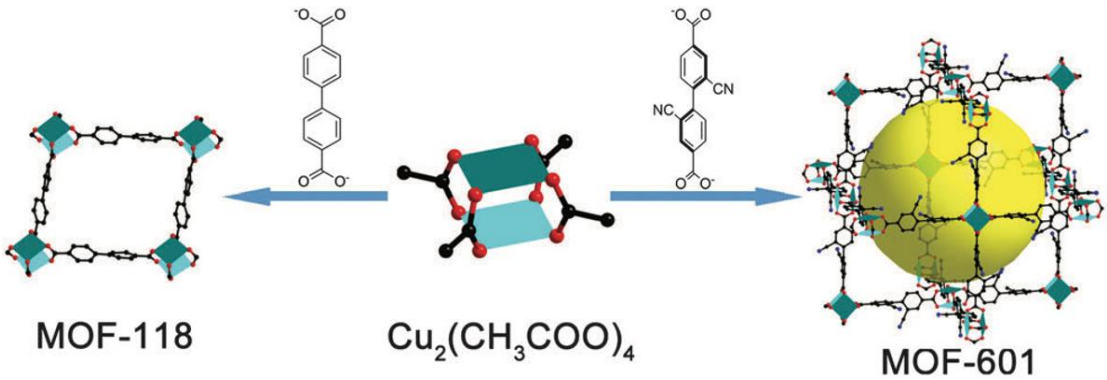

Figure 3.1. An example of MOF dimensionality tuning through linker geometry control.[4]

atom/group	Vander Waals radius/pm
-H	120
-C≡N	220
-Me	200
-I	198

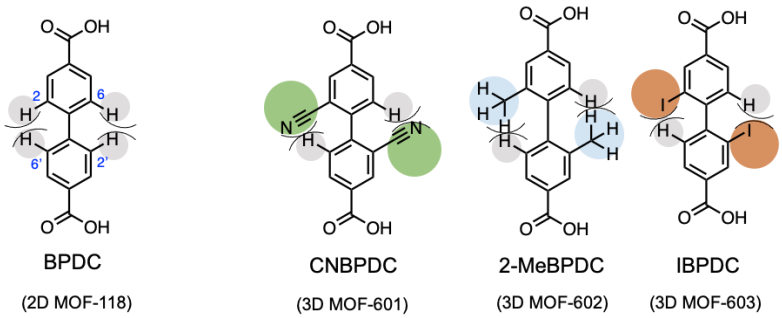

Figure 3.2. The repulsion between H atom and other functional groups/atoms on adjacent phenyl rings.[3]

In this work, we plan to apply the same linker geometry directed control to synthesize COFs of **nbo** topology by introducing two or four $-CH_3$ (methyl) substitutions on the 2,2' (linker BPDA-2) or 2,2',6,6' positions (linker BPDA-4) of the biphenyl unit in 4,4′-biphenylenediboronic acid (linker BPDA) (**Figure 3.3**). As control experiment, we will also synthesize COFs from planar linker BPDA under the same reaction conditions for comparison, although this is an already reported COF structure.[5] Here, we still use $(OH)_8$PcCo as the square planar building block. The detailed proposed reaction scheme is shown in **Figure 3.3**. As is shown in Figure 3.3, we expect the reaction between $(OH)_8$PcCo and the near planar linker BPDA will form a 2D COF of **sql** topology, while the reaction between $(OH)_8$PcCo and the two new linkers will give us 3D COFs of **nbo** topology. Both based on the neutral boronate ester linkage. Conformer search results from the Cambridge Structure Database (CSD) of the biphenyl unit, 2,2'-dimethyl-1,1'-biphenyl unit, 2,2',6,6'-tetramethyl-1,1'-biphenyl units and 2-phenylbenzo[d][1,3,2]-dioxaborole unit supports our design principle (**Figure 3.4**). However, the reaction between $(OH)_8$PcCo and the two new linkers: BPDA-2 and BPDA-4, yielded unexpected spiroborate-linked products, under our reaction condition. Details will be discussed later in the "**Result and Discussion**" section in this chapter.

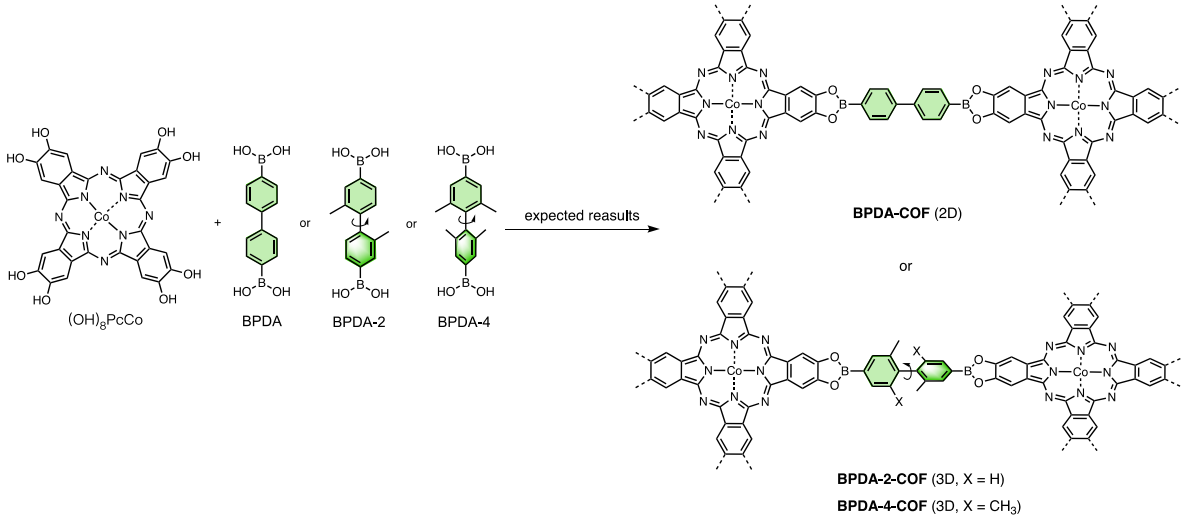

Figure 3.3. Our proposed approach to target 3D COFs of **nbo** topology through linker geometry control and the expected experimental outcomes, based-on boronate ester linkage.

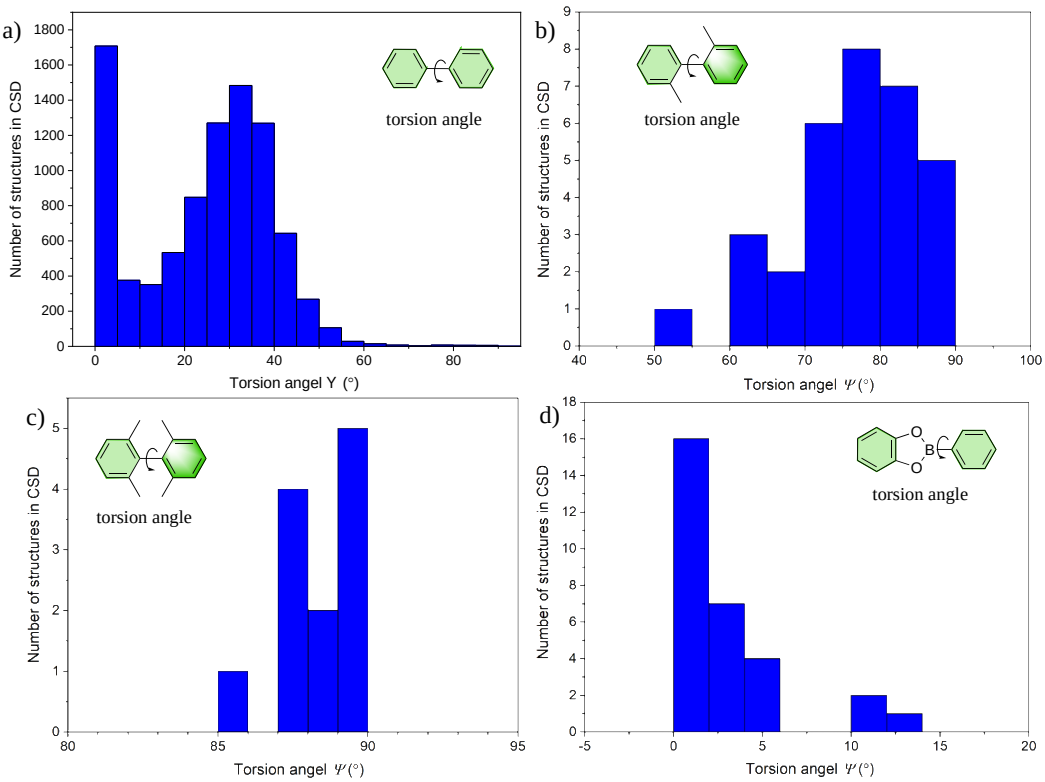

Figure 3.4. Distribution of the torsion angles expressed by (a) biphenyl unit, 8934 crystals hit, the angle distribution is mostly within 0-15°. (b) 2,2‘-dimethyl-1,1’-biphenyl unit, 32 crystals hit, the most reported angle is between 60-90°. (c) 2,2',6,6'-tetramethyl-1,1'-biphenyl units, 12 crystals hit, the most reported angle is close to 90°. (d) 2-phenylbenzo[d][1,3,2]dioxaborole unit, 10 crystals hit, the most commonly reported angle is between 0-5°. All the result are from Cambridge Structure Database (CSD), by the time we work on this project. Any crystals with above mention fragments were included. The above conformer searching result support our reticular design strategy.

3.3 Experimental section

3.3.1 Synthesis of monomers

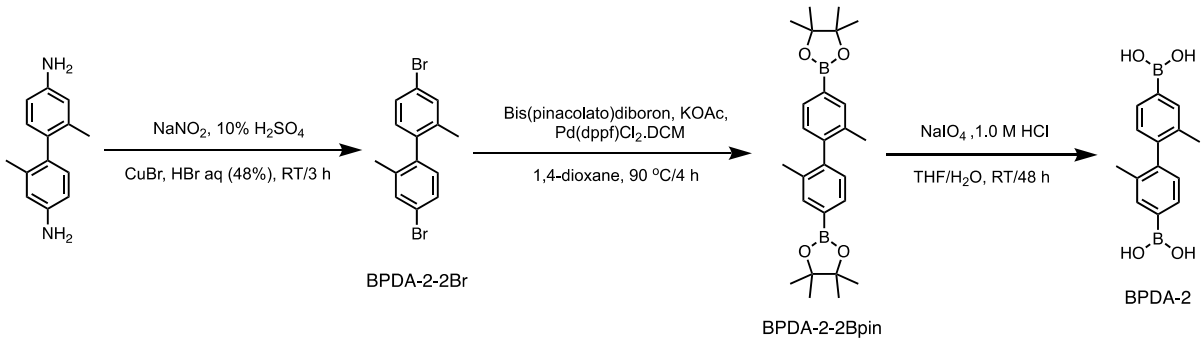

Figure 3.5. Scheme for the synthesis of linker **BPDA-2**.

The synthesis of BPDA-2-2Br follows a modified literature procedure.[6]

Synthesis of 4,4'-dibromo-2,2'-dimethyl-1,1'-biphenyl (BPDA-2-2Br): *m*-tolidine (1.06 g, 5.0 mmol, 1.0 equiv.) was dissolved in in 10% aqueous H_2SO_4 (11.0 mL) at 10 °C and $NaNO_2$ (0.76, 11.0 mmol, 2.2 equiv.) in H_2O (6.2 mL) was added dropwise to the solution at 10 °C to form a diazonium salt. After stirring at 10 °C for 30 minutes, this diazonium salt solution was added dropwise to a cold solution (ice bath) of CuBr (7.17 g, 50.0 mmol, 10.0 equiv.) in 48% aqueous HBr (69.0 mL). The reaction was slowly heated to 50 °C and stirred for 3 h, after which it was cooled to room temperature. The solution was extracted with Et_2O (3*50 mL) (be careful!!! the mix of the cooled reaction system and Et_2O is exothermic, for safety concern, recommend operate this extraction step and the following washing in an open beaker or Erlenmeyer flask, rather than in the closed separating funnel), the Et_2O fractions were washed with 3.0 M HCl (aq.) followed by H_2O and then dried with anhydrous $MgSO_4$ and the solvent was removed under reduced pressure. The product was purified by silica gel column chromatography (eluent = hexane) to give pure product as a transparent oil, which will solidify to white solids upon cooling down. Yield 0.83 g, 49.0%.

CuBr activation (as-ordered CuBr is of deep green colour): CuBr was suspended in very small amount of concentrated HCl (37%) aqueous solution, the system was stirred at room temperature for around 30 min, which forms a dark green suspension. Then large amount of distilled water was added into the suspension to precipitate the white CuBr powders, this mixture was stirred at room temperature for around 1.5 h and then filtrate. The filtrate cake was washed with distilled water and EtOH and then put at 80 °C vacuum oven overnight to obtain CuBr as pale-yellow powders.

^{1}H NMR (400 MHz, $CDCl_3$): δ 7.43 (d, *J*=4.0 Hz, 2H), 7.36 (dd, J_1=4.0 Hz, J_2=8.0 Hz, 2H), 6.94 (d, *J*=8.0 Hz, 2H), 2.03 (s, 6H) ppm. ^{13}C NMR (100 MHz, $CDCl_3$): δ 139.40, 138.25, 132.92, 130.87, 128.95, 121.45, 19.78 ppm. MS (ESI+) m/z calcd for $C_{14}H_{12}Br_2$ [M]+: 337.93. Found: 338.3421. Anal. Cald for $C_{14}H_{12}Br_2$: C: 49.45, H: 3.56. Found: C: 49.86, H: 3.51.

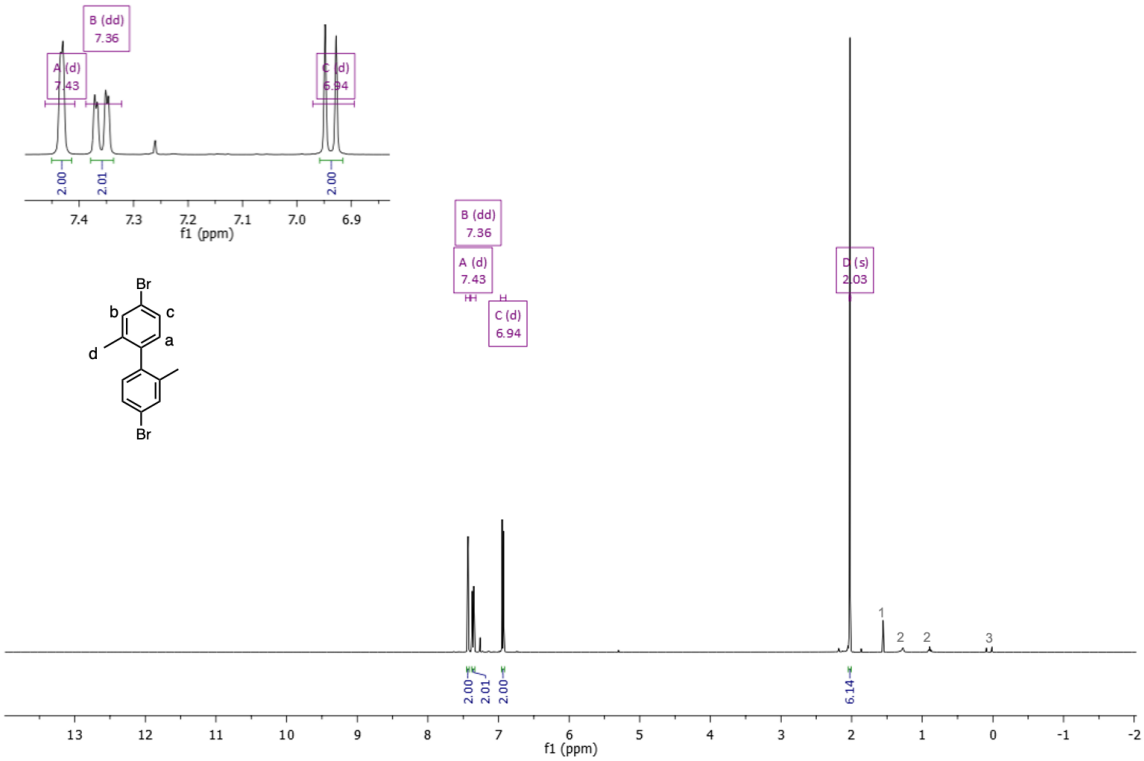

Figure 3.6. ^{1}H NMR spectrum of **BPDA-2-2Br** in $CDCl_3$. Chemical shift referenced to $CHCl_3$ protons at 7.26 ppm. Extra peaks in spectrum: 1. H_2O (s, 1.55 ppm); 2. n-hexane (m, 1.28 ppm; t, 0.89 ppm); 3. $(CH_3)_4Si$ (TMS) (s, 0.09 ppm; s, 0.01 ppm).

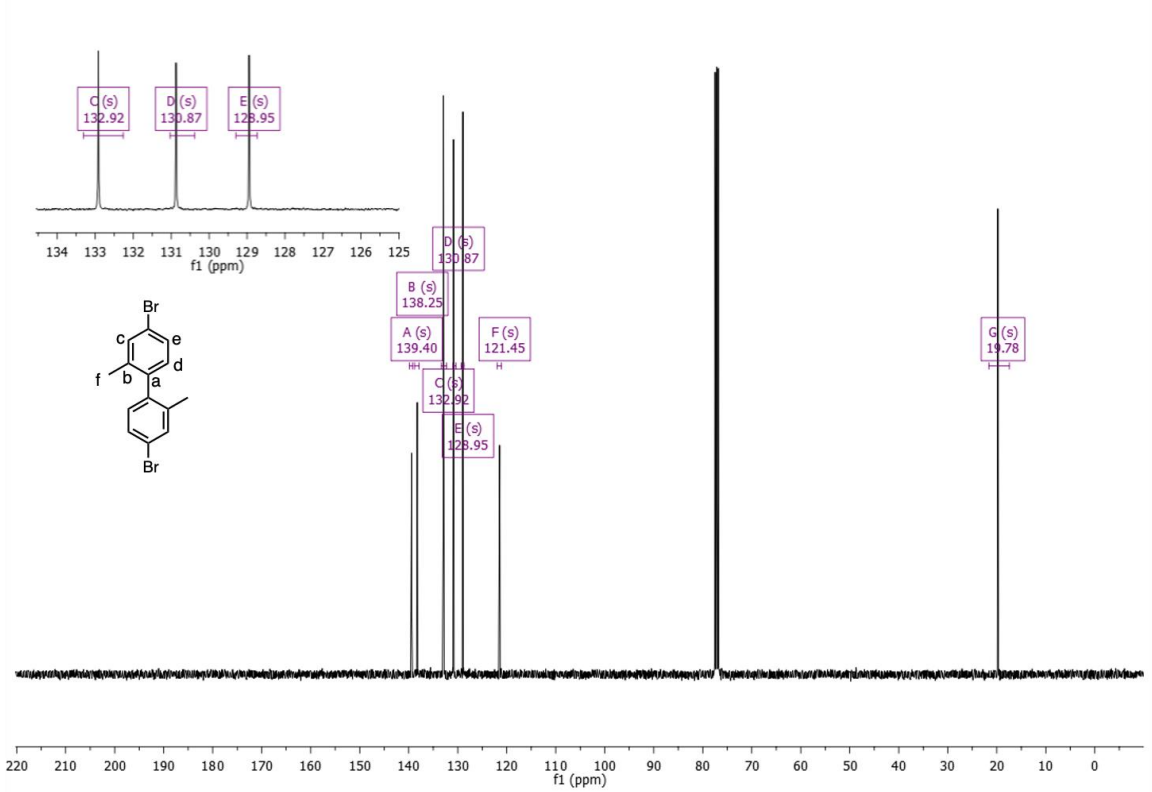

Figure 3.7. ^{13}C NMR spectrum of **BPDA-2-2Br** in $CDCl_3$.

Synthesis of 2,2‘-(2,2’-dimethyl-[1,1‘-biphenyl]-4,4’-diyl)bis(4,4,5,5-tetramethyl-1,3,2-dioxaborolane) (BPDA-2-2Bpin): BPDA-2-2Br (0.68 g, 2.0 mmol, 1.0 equiv.), bis(pinacolato) diboron (1.27 g, 5.0 mmol, 2.5 equiv.) and dry KOAc (0.59 g, 6.0 mmol, 3.0 equiv.) were suspended in anhydrous 1,4-dioxane (20 mL) and degassed for 30 min to remove air. Under nitrogen, Pd(dppf)Cl_2.DCM (0.16 g, 0.2 mmol, 0.1 equiv.) was added and the mixture was stirred at 90 °C overnight. The reaction mixture was cooled to room temperature, 10 mL H_2O was added to dilute the system and then using diethyl ether for extraction. Organic phase was combined and washed with water, then dried with anhydrous $MgSO_4$. The solvent was removed by rotary evaporator. The resulting residue was purified via silica gel column chromatography using dichloromethane: petroleum ether (2:1, v/v) as the eluent. The solution obtained was evaporated to dryness to obtain white powders as the pure product. Yield 0.64 g, 74%.

^{1}H NMR (400 MHz, $CDCl_3$): δ 7.72 (s, 2H), 7.67 (d, *J*=8.0 Hz, 2H), 7.10 (d, *J*=8.0 Hz, 2H), 2.04 (s, 6H), 1.36 (s, 24H) ppm. ^{13}C NMR (100 MHz, $CDCl_3$): δ 144.75, 136.38, 135.09, 132.14, 128.67, 83.91, 25.03, 19.66 ppm. MS (ESI+) m/z calcd for $C_{26}H_{36}B_2O_4$ [M]+: 434.28. Found: 435.2882. Anal. Cald for $C_{26}H_{36}B_2O_4$: C: 71.92, H: 8.36. Found: C: 72.07, H: 8.50.

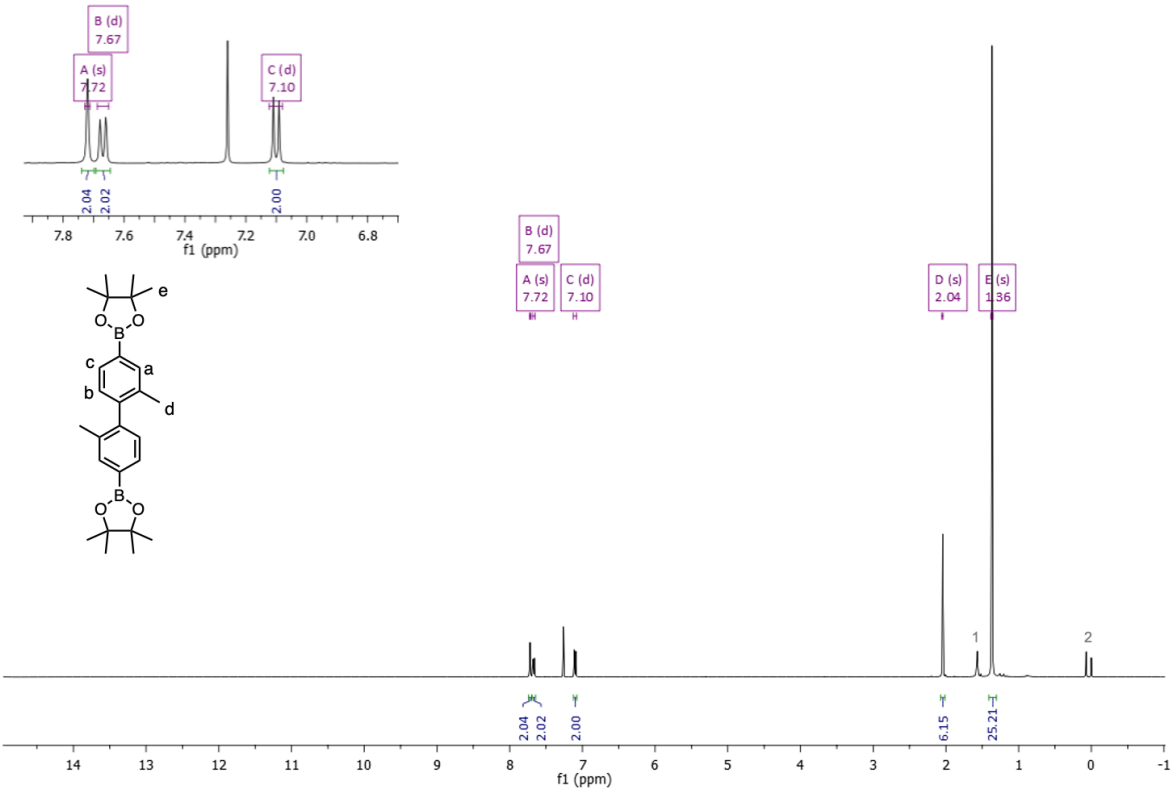

Figure 3.8. ^{1}H NMR spectrum of **BPDA-2-2Bpin** in $CDCl_3$. Chemical shift referenced to $CHCl_3$ protons at 7.26 ppm. Extra peaks in spectrum: 1. H_2O (s, 1.57 ppm); 2. $(CH_3)_4Si$ (TMS) (s, 0.08 ppm; s, 0.00 ppm).

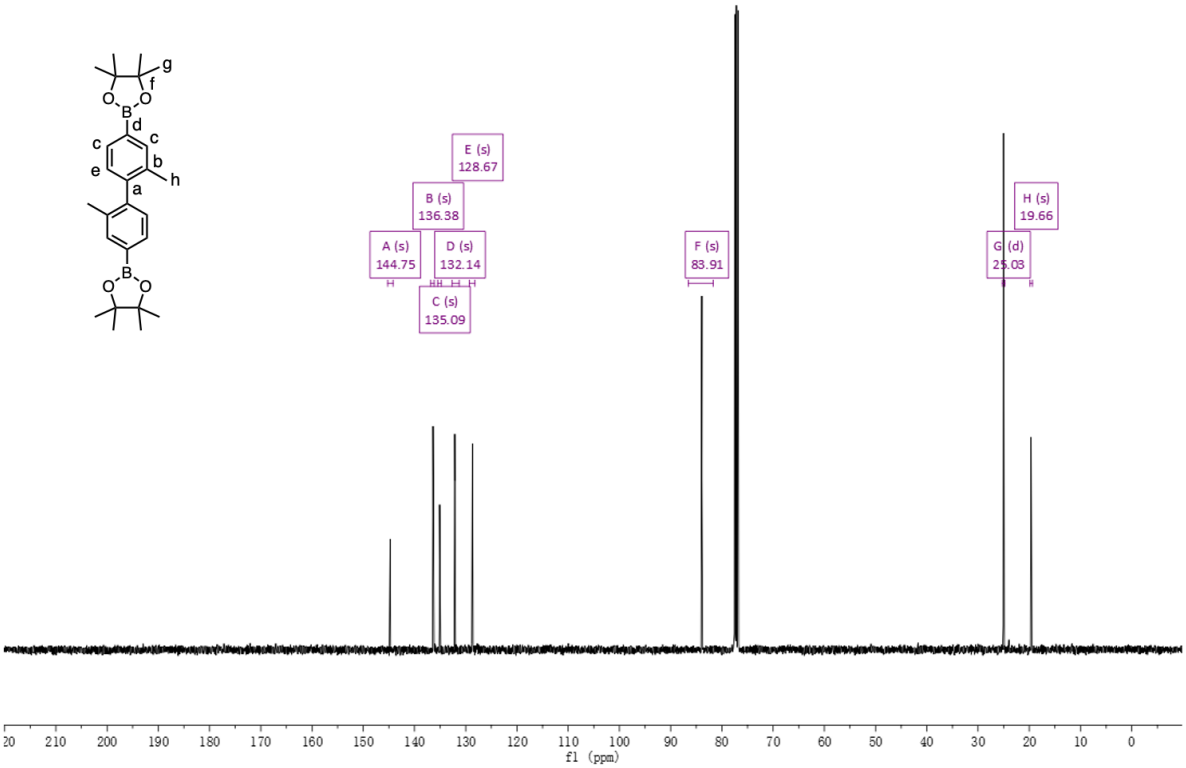

Figure 3.9. ^{13}C NMR spectrum of **BPDA-2-2Bpin** in $CDCl_3$.

Synthesis of (2,2‘-dimethyl-[1,1’-biphenyl]-4,4‘-diyl)diboronic acid (BPDA-2): BPDA-2-2Bpin (0.16 g, 0.37 mmol, 1.0 equiv.) was dissolved in THF/H_2O (v : v = 4:1, 15 mL) and sodium periodate ($NaIO_4$) (0.64 g, 3.0 mmol, 8.14 equiv.) was added. The suspension was stirred at room temperature for 40 min, then 1M HCl (1.0 mL) was added, and the mixture was stirred at room temperature for 48 h. The suspension was diluted with water (15 mL) and extracted with ethyl acetate (3*50 mL). The combined organic phases were washed with brine (2*10 mL) and H_2O (2*10 mL), dried over $MgSO_4$ and the solvent was removed under reduced pressure. The residue solids were washed with hexane (3*100 mL) and dried in vacuo to give product as white powders. Yield 0.09 g, 92%.

^{1}H NMR (400 MHz, DMSO-d_6): δ 8.00 (s, 4H), 7.70 (s, 2H), 7.64 (d, J=8.0 Hz, 2H), 7.01 (d, J=8.0 Hz, 2H), 1.98 (s, 6H) ppm. ^{13}C NMR (100 MHz, DMSO-d_6): δ 142.88, 135.77, 133.63, 131.48, 127.94, 19.49 ppm. MS (ESI+) m/z calcd for $C_{14}H_{16}B_2O_4$[M]+: 270.12. Found: 269.1162.

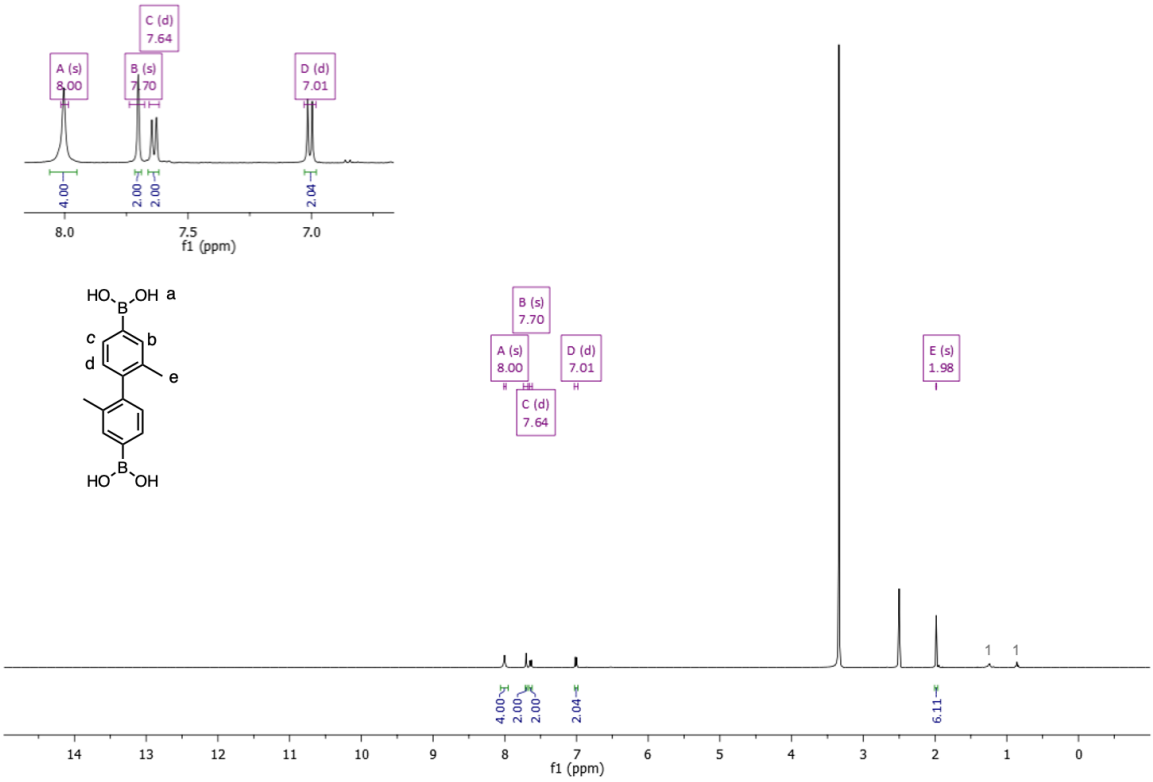

Figure 3.10. ^{1}H NMR spectrum of **BPDA-2** in DMSO-d_6. Chemical shift referenced to DMSO protons at 2.50 ppm. Extra peaks in spectrum: 1. n-hexane (m, 1.24 ppm; t, 0.86 ppm).

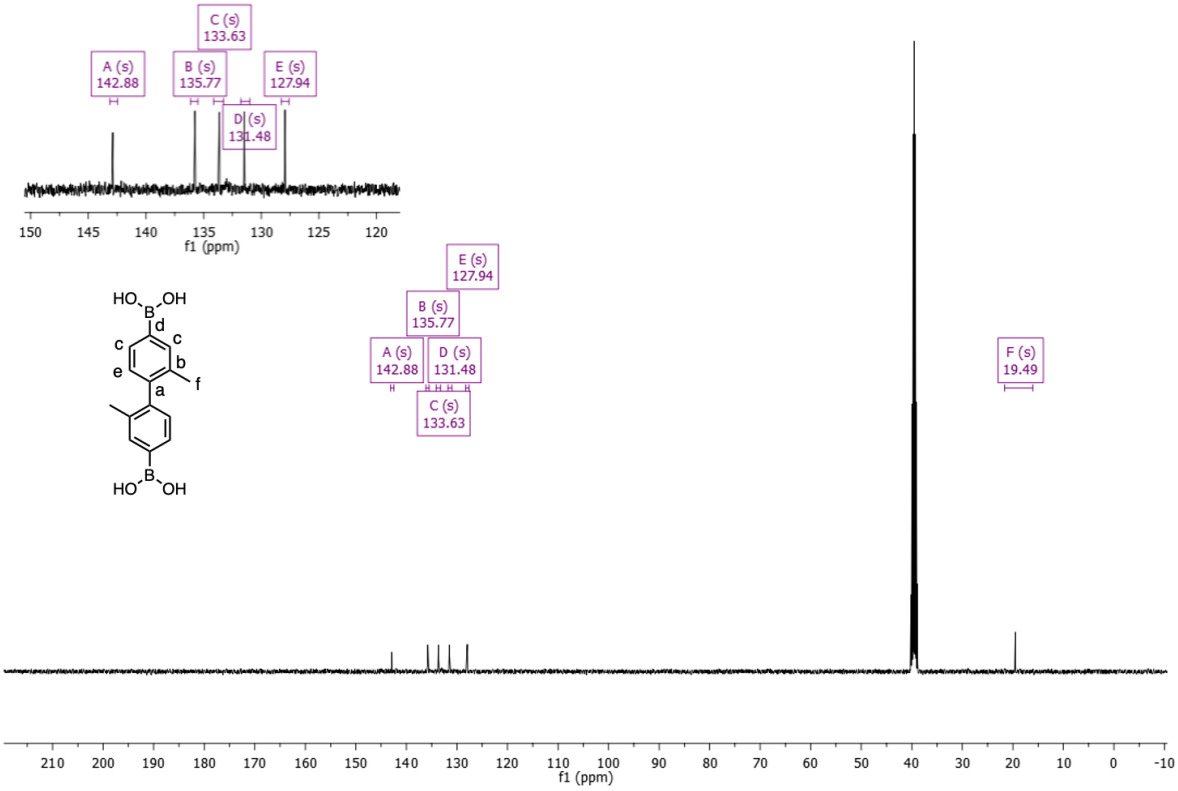

Figure 3.11. ^{13}C NMR spectrum of **BPDA-2** in DMSO-d_6.

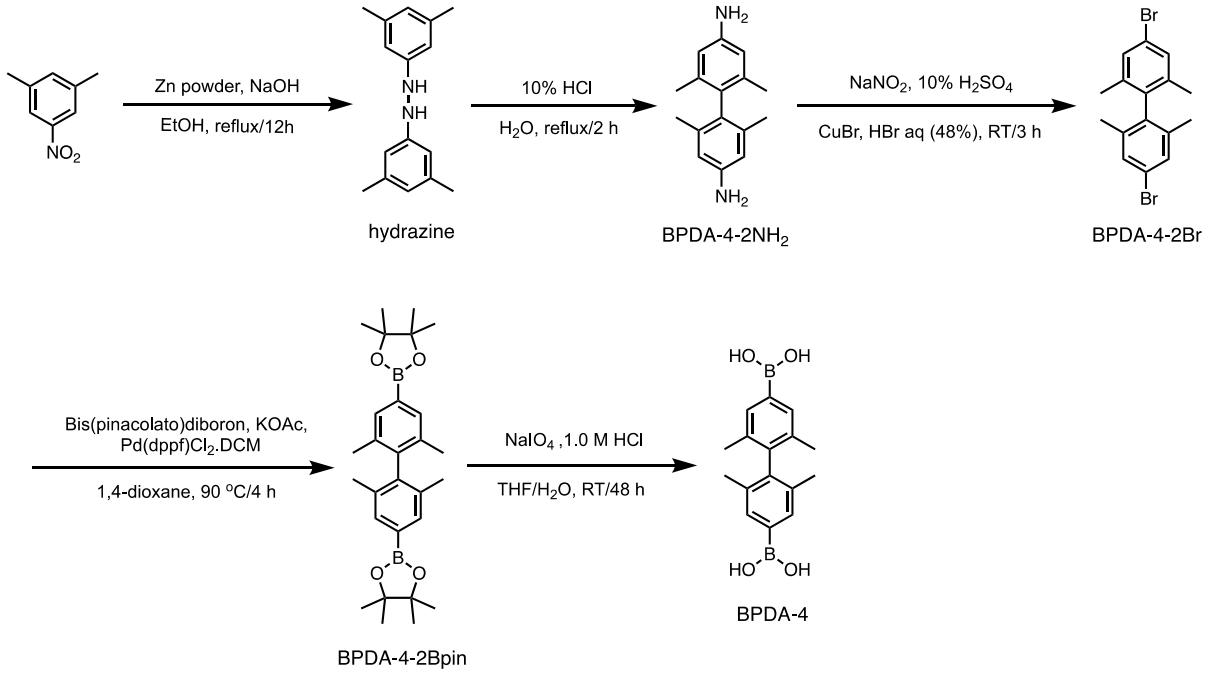

Figure 3.12. Scheme for the synthesis of linker **BPDA-4**.

The synthesis of hydrazine and BPDA-4-2NH_2 follows a modified literature procedure.[7]

Synthesis of 1,2-bis(3,5-dimethylphenyl) hydrazine (hydrazine): A suspension of 3,5-dimethylnitrobenzene (10.0 g, 66.2 mmol, 1 equiv.), zinc powder (25.0 g, 384.0 mmol, 5.8 equiv.), and EtOH (40 mL) was heated to reflux over 30 minutes under N_2 atmosphere. A solution of sodium hydroxide (15.0 g, 377.0 mmol, 5.7 equiv.) in water (50 mL) was added dropwise to the zinc suspension to keep steady reflux, resulting in an orange solution with suspended zinc. Heating was continued at reflux overnight, while more zinc powder (10.0 g, 150.0 mmol, 2.3 equiv.) was added in portions over the first 4 hours. The hot suspension was then filtered over a bed of Celite into a solution of sodium bisulfite (1.0 g, 9.6 mmol, 0.15 equiv.) in 30% aqueous acetic acid (150 mL), and the filter cake was rinsed with hot EtOH. The slurry was cooled in an ice bath and filtered, yielding an orange solid, which was recrystallized from hot heptane (80 mL) to yield the desired pure product as large yellow crystals. Yield 6.0 g, 75%.

^{1}H NMR (400 MHz, $CDCl_3$): δ 6.50 (s, 6H),5.46 (s, 2H), 2.25 (d, *J*= 4.0 Hz, 12H) ppm. ^{13}C NMR (100 MHz, $CDCl_3$): δ 149.39, 139.26, 121.87, 110.22, 21.51 ppm. MS (ESI+) m/z calcd for $C_{16}H_{20}N_2$ [M]+: 240.16. Found: 241.1703. Anal. Cald for $C_{16}H_{20}N_2$: C: 79.96, H: 8.39, N: 11.66. Found: C: 79.46, H: 8.43, N: 11.78.

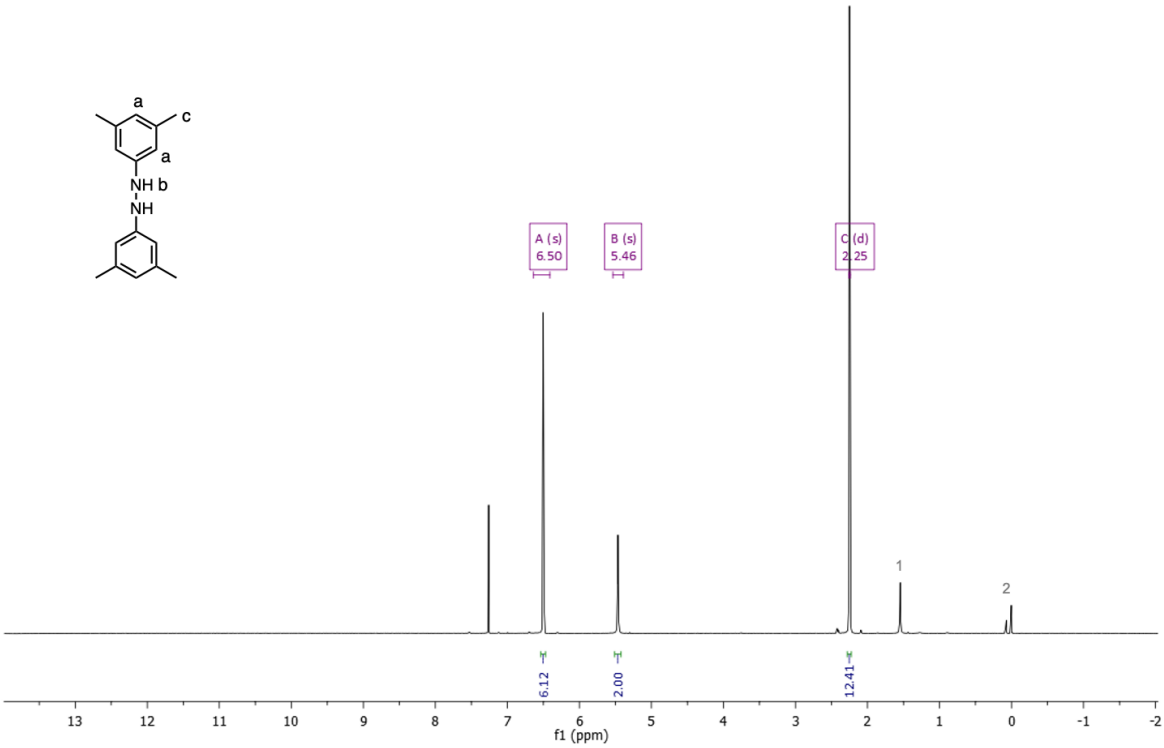

Figure 3.13. ^{1}H NMR spectrum of **hydrazine** in $CDCl_3$. Chemical shift referenced to $CHCl_3$ protons at 7.26 ppm. Extra peaks in spectrum: 1. H_2O (s, 1.54 ppm); 2. $(CH_3)_4Si$ (TMS) (d, 0.08 ppm; m, 0.01 ppm). ^{1}H NMR result is in accordance with literature reports.[7]

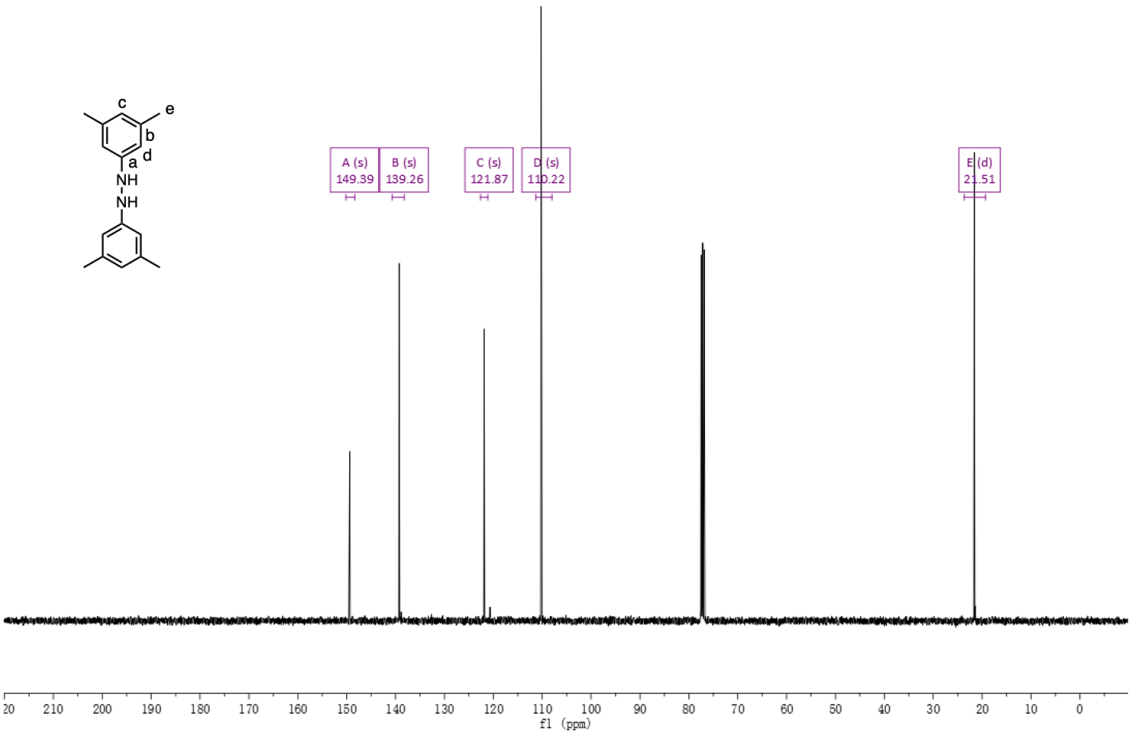

Figure 3.14. ^{13}C NMR spectrum of **hydrazine** in $CDCl_3$.

Synthesis of 4,4'-diamino-2,2',6,6'-tetramethylbiphenyl (BPDA-4-2NH$_2$): hydrazine (0.8 g, 3.32 mmol) was added to a degassed (30 min) 10% HCl (40 mL) and the reaction mixture was heated at reflux. After 2 hours, thin-layer chromatography (TLC), with ethyl acetate: hexane = 1: 2 as the eluent, sees full conversion of the starting material. The reaction mixture was cooled to room temperature and the pH was raised to >=10 with 1 M NaOH. The product was extracted using diethyl ether, washed with brine, dried over anhydrous $MgSO_4$, filtered, and concentrated in vacuo to afford light brown-red product. The crude product was purified by column chromatography on silica gel (ethyl acetate: hexane = 1: 2), to give pure product as pink-white powders. Yield 0.4 g, 50%.

^{1}H NMR (400 MHz, $CDCl_3$): δ 6.48 (s, 4H), 3.52 (s, 4H), 1.82 (s, 12H) ppm. ^{13}C NMR (100 MHz, $CDCl_3$): δ 144.72, 137.41, 130.82, 114.45, 20.13 ppm. MS (ESI+) m/z calcd for $C_{16}H_{20}N_2$ [M]+: 240.16. Found: 241.1704. Anal. Cald for $C_{16}H_{20}N_2$: C: 79.96, H: 8.39, N: 11.66. Found: C: 79.05, H: 8.42, N: 11.72.

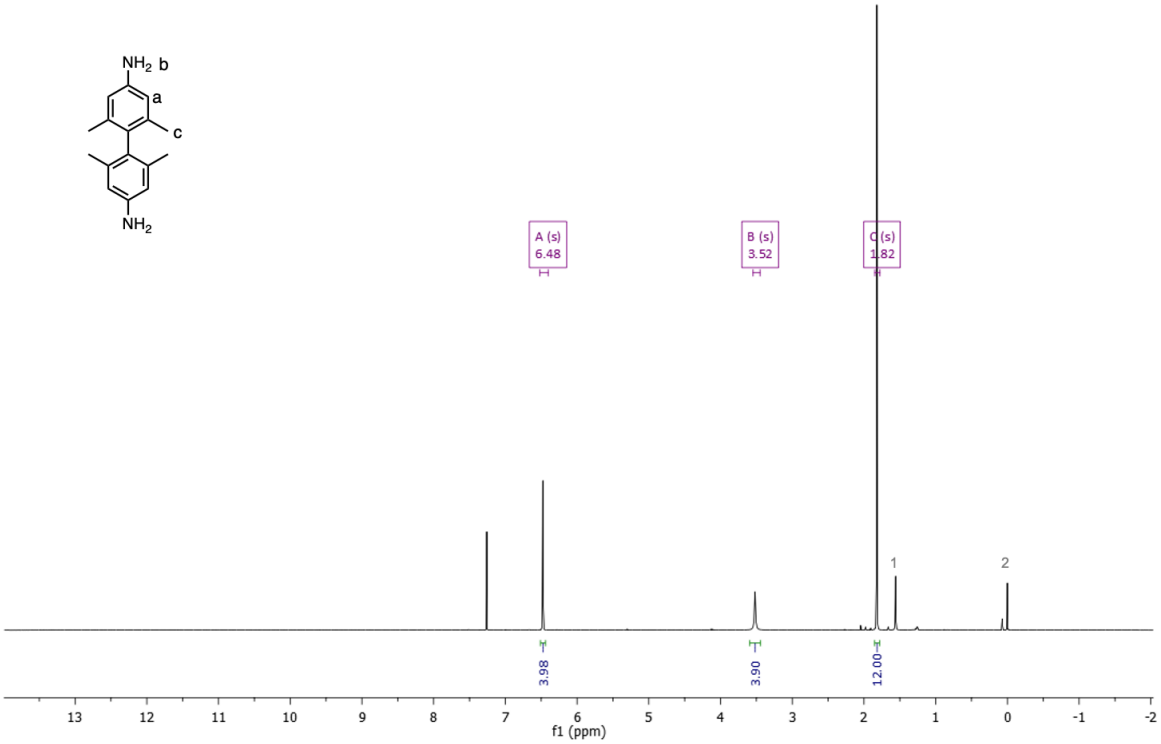

Figure 3.15. ^{1}H NMR spectrum of **BPDA-4-2NH$_2$** in $CDCl_3$. Chemical shift referenced to $CHCl_3$ protons at 7.26 ppm. Extra peaks in spectrum: 1. H_2O (s, 1.56 ppm); 2. $(CH_3)_4Si$ (TMS) (s, 0.07 ppm; s, 0.00 ppm).

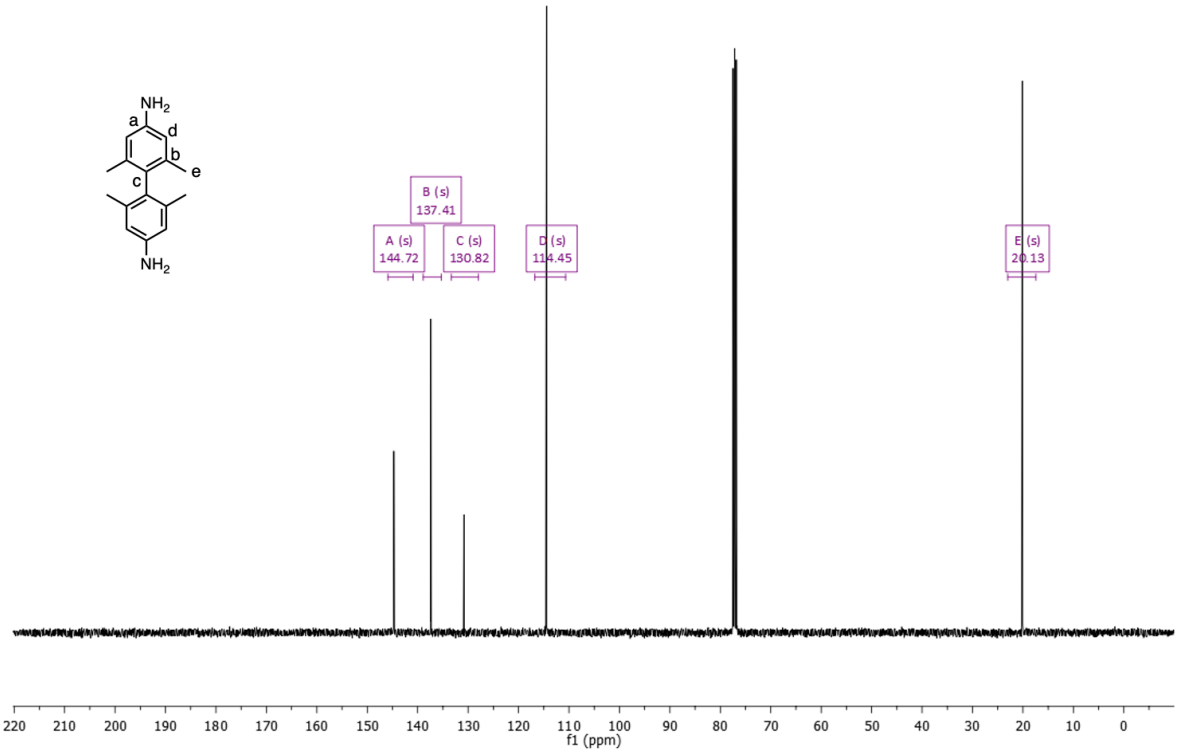

Figure 3.16. ^{13}C NMR spectrum of **BPDA-4-2NH$_2$** in $CDCl_3$.

Synthesis of 4,4'-dibromo-2,2',6,6'-tetramethyl-1,1'-biphenyl (BPDA-4-2Br): The synthesis of BPDA-4-2Br follows the same procedure for the synthesis of BPDA-2-2Br. Yield white powders 0.29 g, 40.0%.

^{1}H NMR (400 MHz, $CDCl_3$): δ 7.28 (s, 4H), 1.86 (s, 12H) ppm. ^{13}C NMR (100 MHz, $CDCl_3$): δ 137.88, 130.63, 121.00, 19.75 ppm. Anal. Cald for $C_{16}H_{16}Br_2$: C: 52.21, H: 4.38. Found: C: 52.53, H: 4.36.

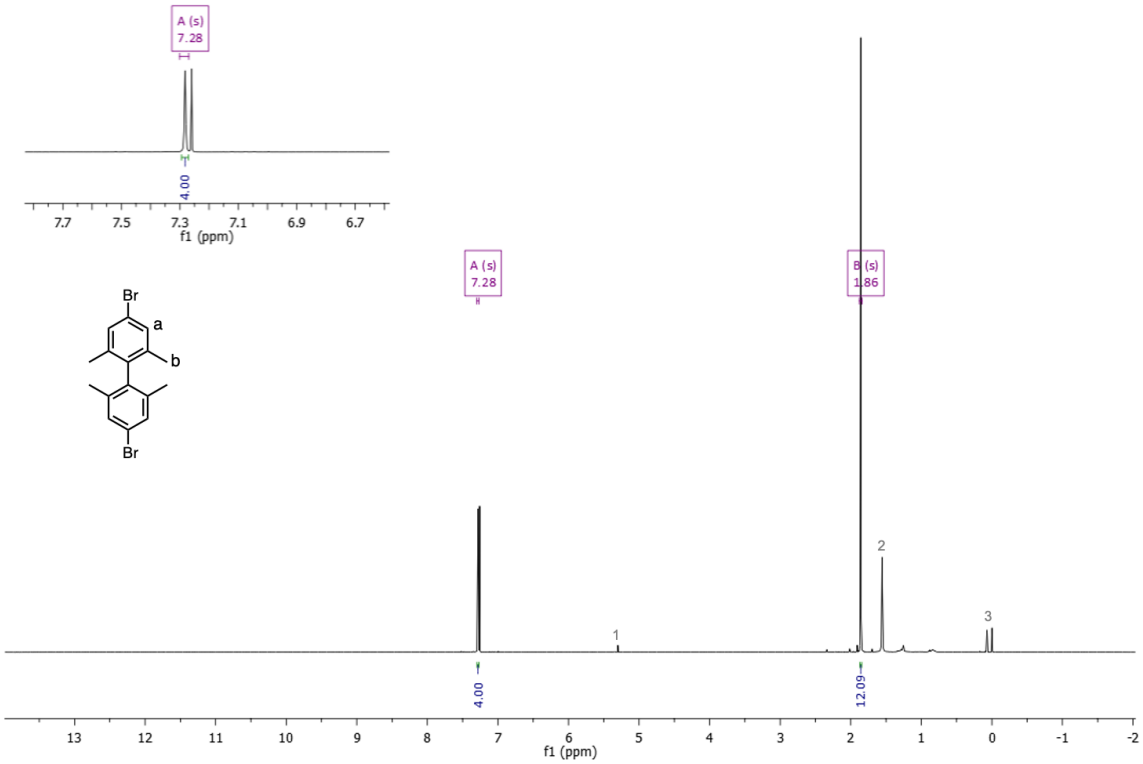

Figure 3.17. ^{1}H NMR spectrum of **BPDA-4-2Br** in $CDCl_3$. Chemical shift referenced to $CHCl_3$ protons at 7.26 ppm. Extra peaks in spectrum: 1. CH_2Cl_2 (s, 5.32 ppm); 2. H_2O (s, 1.56 ppm); 2. $(CH_3)_4Si$ (TMS) (s, 0.07 ppm; s, 0.00 ppm).

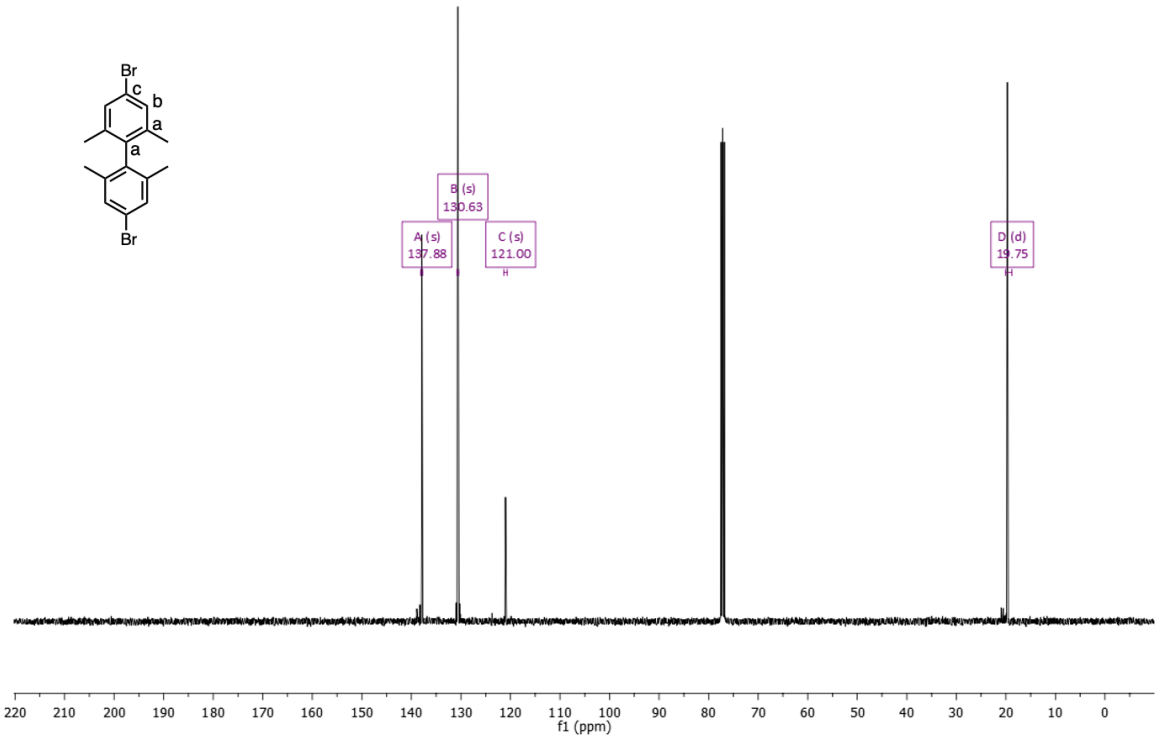

Figure 3.18. ^{13}C NMR spectrum of **BPDA-4-2Br** in $CDCl_3$.

Synthesis of 2,2'-(2,2',6,6'-tetramethyl-[1,1'-biphenyl]-4,4'-diyl)bis(4,4,5,5-tetramethyl-1,3,2-dioxaborolane) (BPDA-4-2BPin): The synthesis of BPDA-4-2BPin follows the same procedure for the synthesis of BPDA-2-2BPin. Yield 50% as white powders.

^{1}H NMR (400 MHz, $CDCl_3$): δ 7.57 (s, 4H), 1.88 (s, 12H), 1.37 (s, 24H) ppm. ^{13}C NMR (100 MHz, $CDCl_3$): δ 143.41, 134.79, 133.99, 83.86, 25.07, 19.68 ppm. MS (ESI+) m/z calcd for $C_{28}H_{40}B_2O_4$ [M]+: 462.31. Found: 463.3200. Anal. Cald for $C_{28}H_{40}B_2O_4$: C: 72.76, H: 8.72. Found: C: 72.37, H: 8.75.

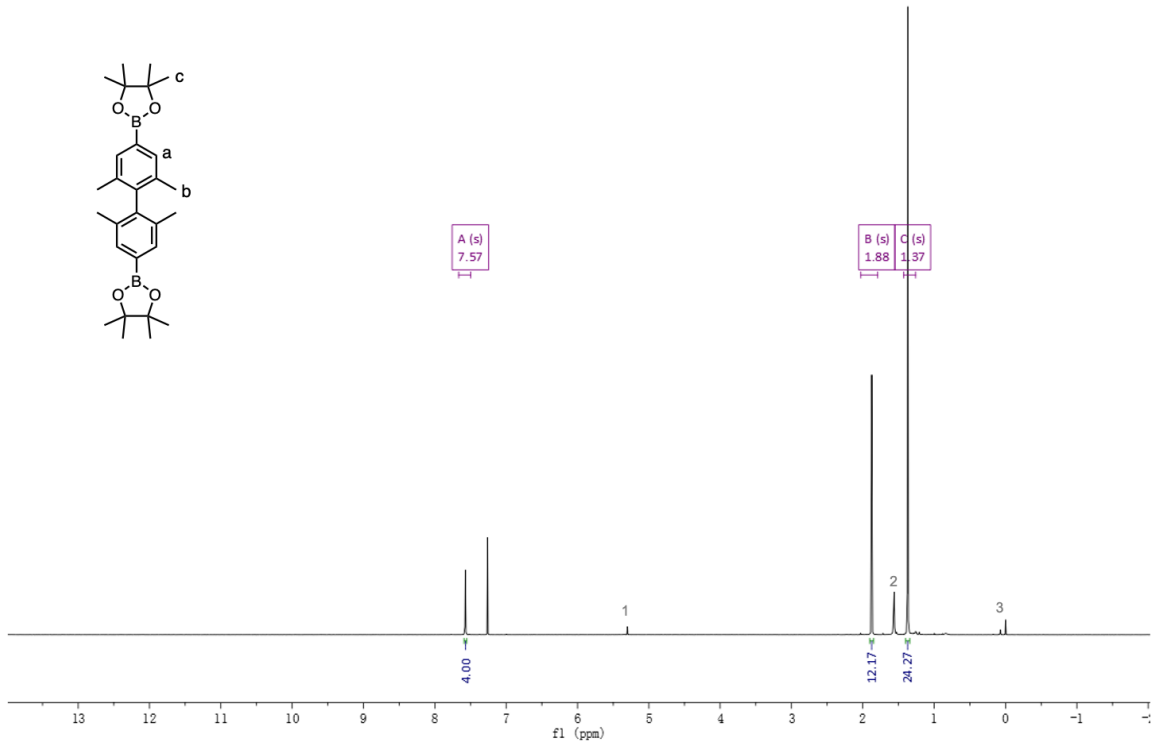

Figure 3.19. ^{1}H NMR spectrum of **BPDA-4-2BPin** in $CDCl_3$. Chemical shift referenced to $CHCl_3$ protons at 7.26 ppm. Extra peaks in spectrum: 1. CH_2Cl_2 (s, 5.30 ppm); 2. H_2O (s, 1.54 ppm); 2. $(CH_3)_4Si$ (TMS) (s, 0.08 ppm; s, 0.00 ppm).

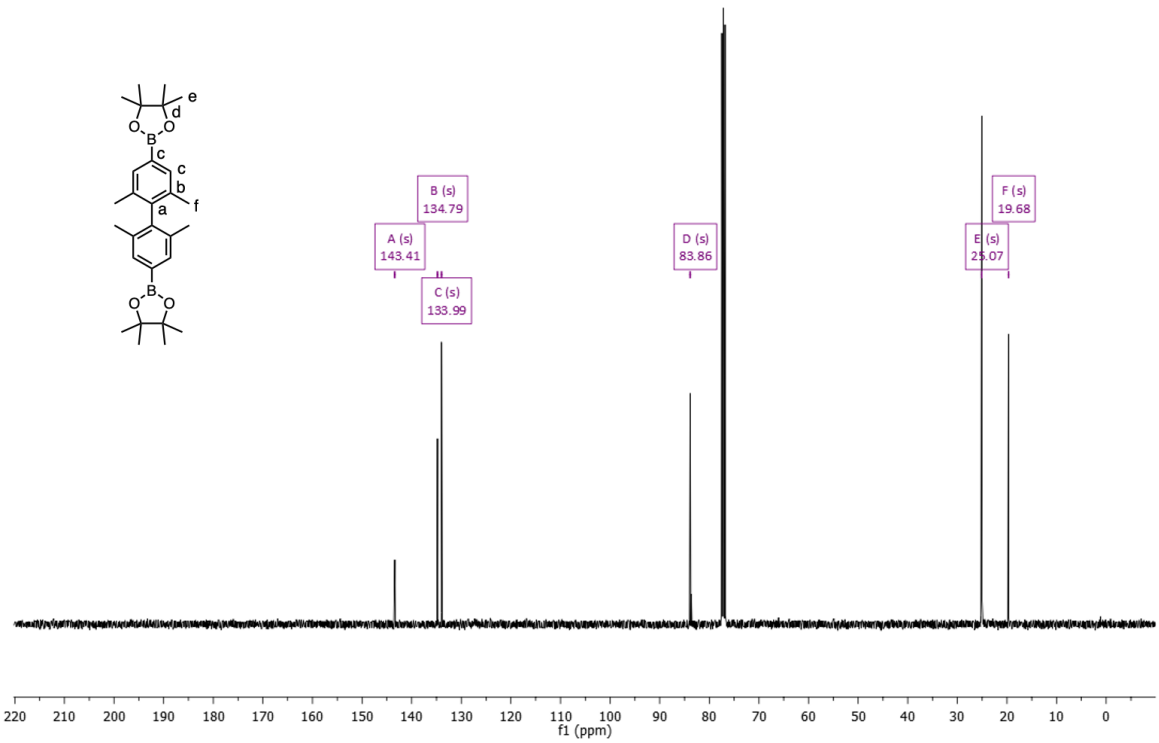

Figure 3.20. ^{13}C NMR spectrum of **BPDA-4-2BPin** in $CDCl_3$.

Synthesis of (2,2',6,6'-tetramethyl-[1,1'-biphenyl]-4,4'-diyl)diboronic acid (BPDA-4): The synthesis of BPDA-4 follows the same procedure for the synthesis of BPDA-2. Yield 90% as white powders.

^{1}H NMR (400 MHz, DMSO-d_6): δ 7.94 (s, 4H), 7.55 (s, 4H), 1.81 (s, 12H) ppm. ^{13}C NMR (100 MHz, MeOH-d_4): δ 135.46, 135.18, 134.28, 133.86, 19.98 ppm. MS (ESI+) m/z calcd for $C_{16}H_{20}B_2O_4$ [M]+: 298.15. Found: 301.1411. Anal. Cald for $C_{16}H_{20}B_2O_4$: C: 64.50, H: 6.77. Found: C: 64.68, H: 6.27.

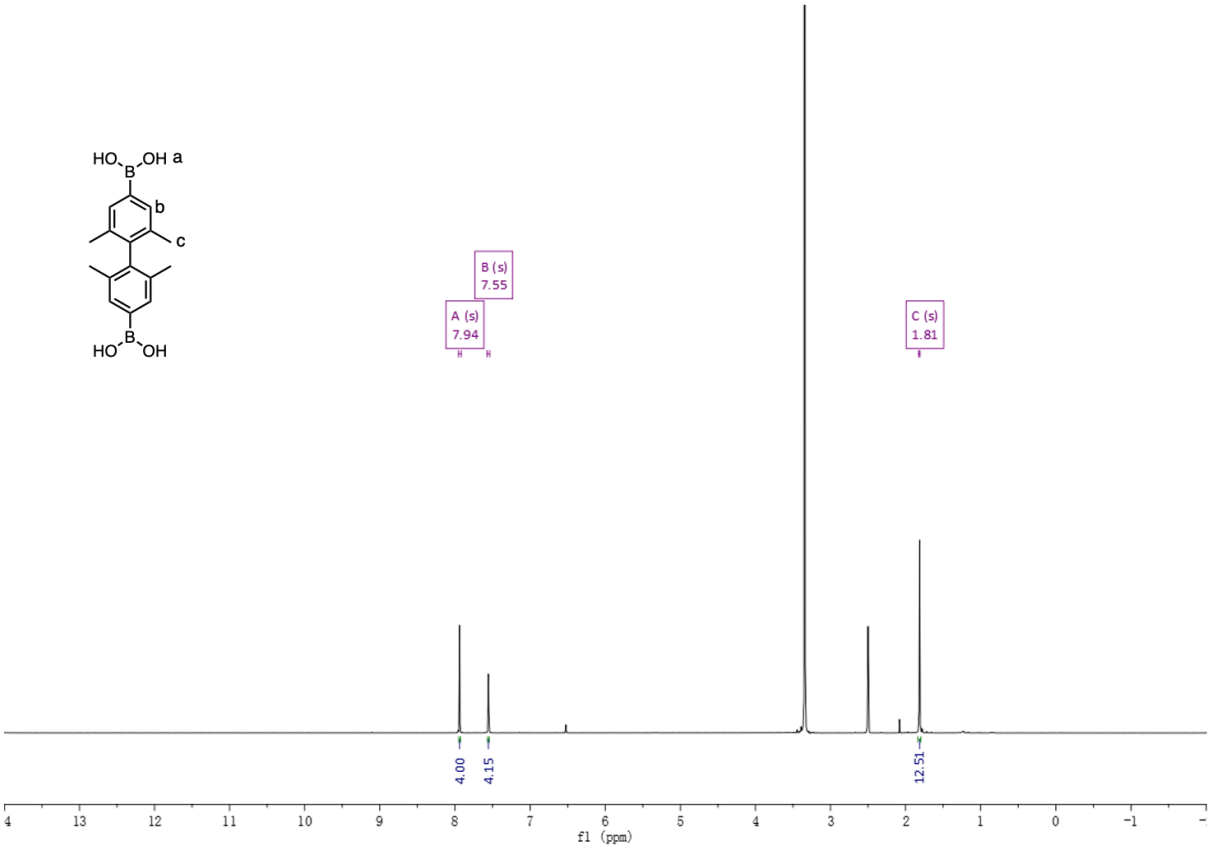

Figure 3.21. ^{1}H NMR spectrum of **BPDA-4** in DMSO-d_6.

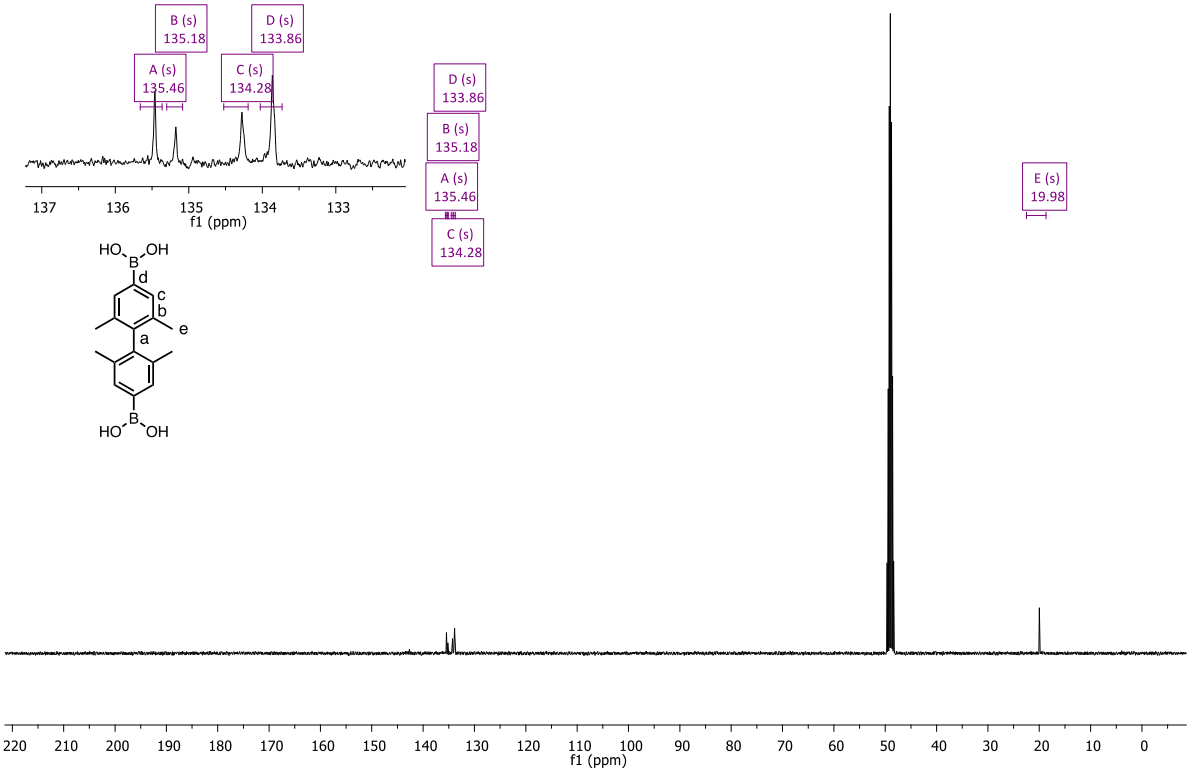

Figure 3.22. ^{13}C NMR spectrum of **BPDA-4** in MeOH-d_4.

3.3.2 Synthesis of COFs

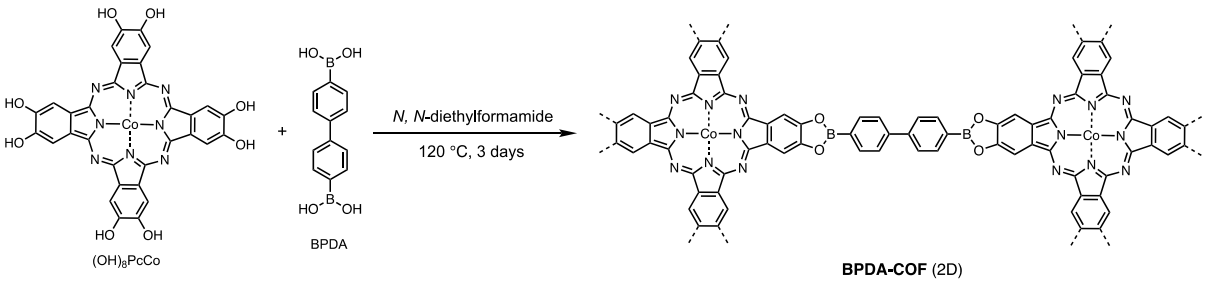

Figure 3.23. Scheme for the synthesis of **BPDA-COF**.

Synthesis of BPDA-COF: A 10 mL Pyrex tube was charged with $(OH)_8PcCo$ (10.5 mg, 0.015 mmol), BPDA (7.3 mg, 0.03 mmol) and *N*,*N*-diethylformamide (DEF) (1.0 mL). The mixture was sonicated at room temperature for 2 minutes, then flash frozen in a liquid N_2 bath and degassed through three freeze-pump-thaw cycles and sealed under vacuum using a Schlenk line and oil pump. Upon warming to room temperature, the tube was put into a 120 °C oven for 72 hours and then taken out of the oven, which yielded a black product. After cooling to room temperature, the product was washed with anhydrous acetone to give a dark powder. The obtained powder was immersed in anhydrous acetone, and the solvent was exchanged with fresh acetone three times with intervals of 24 hour. The wet sample was transferred to a Critical Point Drier (Quorum-E3100AG); the sample was then washed and exchanged with liquid CO_2 for 4–5 times with an interval of 1-2 hours, until all acetone in the material was successfully exchanged. After the final exchange, the system was heated to reach the critical point and the supercritical CO_2 was then released slowly over 1 hour. After the chamber pressure returned to ambient, samples were then transferred into a gas adsorption test tube inside the glove box and degassed at room temperature for 12 h affording **BPDA-COF** in 77% yield (12.0 mg) as a black powder. This sample was directly used for gas adsorption (several batches were combined for N_2 sorption). This batch of **BPDA-COF** was used in all the experiments/measurements unless otherwise specified. Anal. Cald for $C_{60}H_{28}N_4B_4O_8Co$: C: 64.74; H: 2.33; N: 10.79. Found: C: 62.64; H: 5.28; N: 8.80. Theoretical Co content: 5.67 wt.%. ICP-OES analysis shows a Co content of 4.29 wt.%.

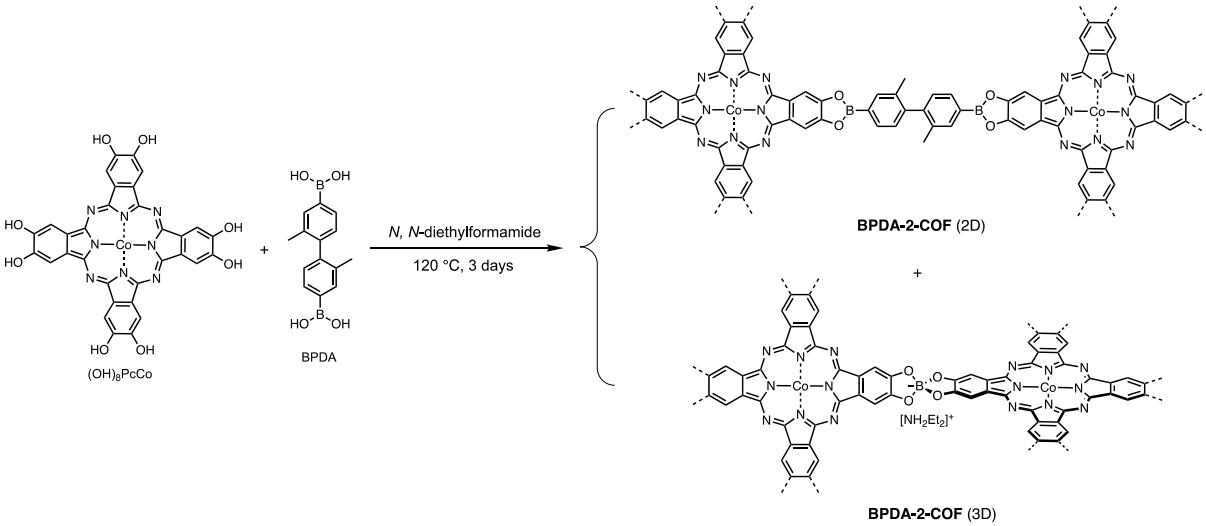

Figure 3.24. Scheme for the synthesis of **BPDA-2-COF**.

Synthesis of BPDA-2-COF: The synthesis of BPDA-2-COF follows the same procedure for the synthesis of BPDA-COF, but with BPDA-2 (8.1 mg, 0.03 mmol) as the linker. 14.0 mg BPDA-2-COF was obtained as black powders (100% yield calculated from boronate ester linkage = 16.4 mg. 100% yield calculated from spiroborate linkage = 12.9 mg.). This batch of BPDA-2-COF was used in all the experiments/measurements unless otherwise specified. Anal. Cald for $C_{60}H_{32}N_8O_8B_4Co$ (presume 100% boronate ester linkage): C: 65.81; H: 2.95; N: 10.23. Anal. Cald for $C_{40}H_{32}N_{10}O_8B_2Co$ (persume 100% spiroborate linkage): C: 55.78; H: 3.75; N: 16.26. Found: C: 54.25; H: 4.38; N: 10.54. Theoretical Co content: 5.38 wt.% (based-on 100 % boronate ester linkage, 2D) or 6.84 wt.% (based-on 100 % spiroborate linkage, 3D). ICP-OES analysis shows a Co content of 5.05 wt.%.

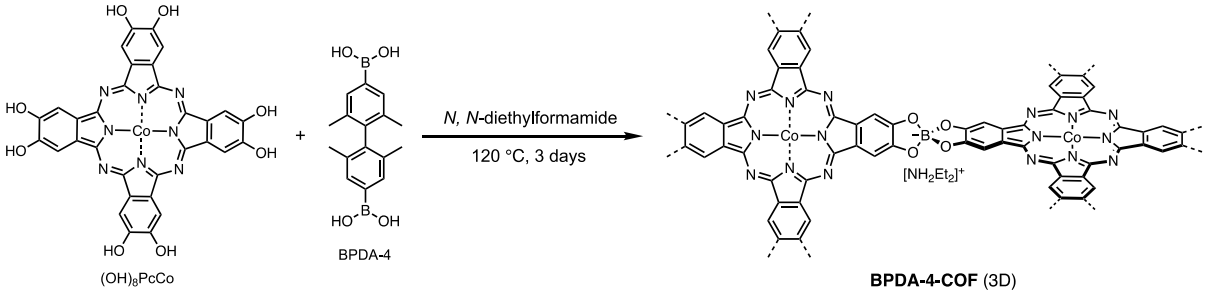

Figure 3.25. Scheme for the synthesis of **BPDA-4-COF**.

Synthesis of BPDA-4-COF: The synthesis of BPDA-4-COF follows the same procedure for the synthesis of BPDA-COF, but with BPDA-4 (9.0 mg, 0.03 mmol) as the linker. 9.0 mg BPDA-4-COF was obtained as black powders in 70% yield (calculated based on spiroborate linkage). This batch of BPDA-4-COF was used in all the experiments/measurements unless otherwise specified. Anal. Cald for $C_{40}H_{32}N_{10}O_8B_2Co$ (presume 100 % spiroborate linkage): C: 55.78; H: 3.75; N: 16.26. Found: C: 50.12; H: 3.99; N: 15.31. Theoretical Co content: 5.12 wt.% (based-on 100 % boronate ester linkage, 2D) or 6.84 wt.% (based-on 100 % spiroborate linkage, 3D). ICP-OES analysis shows a Co content of 5.44 wt.%.

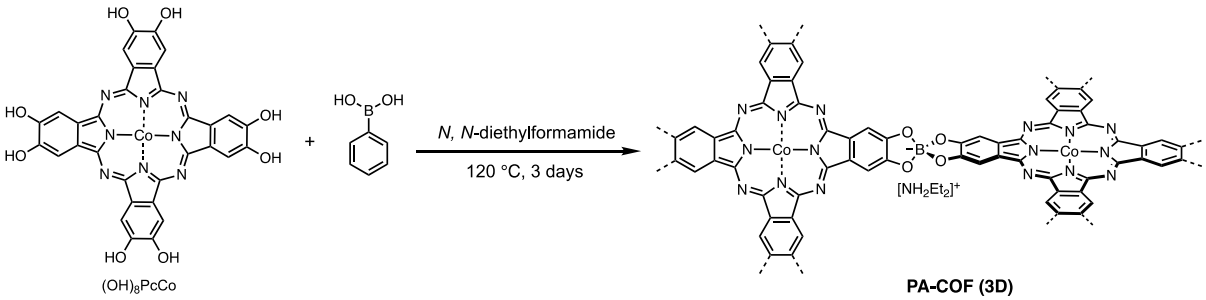

Figure 3.26. Scheme for the synthesis of **PA-COF**.

Synthesis of PA-COF: The synthesis of PA-COF follows the same procedure for the synthesis of BPDA-COF, but with phenylboronic acid (3.7 mg, 0.03 mmol) to replace the linker. 8.0 mg PA-COF was obtained in 61.5 % yield (calculated based on spiroborate linkage) as black powders. This batch of PA-COF was used in all the experiments/measurements unless otherwise specified. Anal. Cald for $C_{40}H_{32}N_{10}O_8B_2Co$: C: 55.78; H: 3.75; N: 16.26. Found: C: 52.97; H: 4.18; N: 12.22. Theoretical Co content: 6.84 wt.%. ICP-OES analysis shows a Co content of 5.40 wt.%.

3.3.3 Synthesis of model compounds

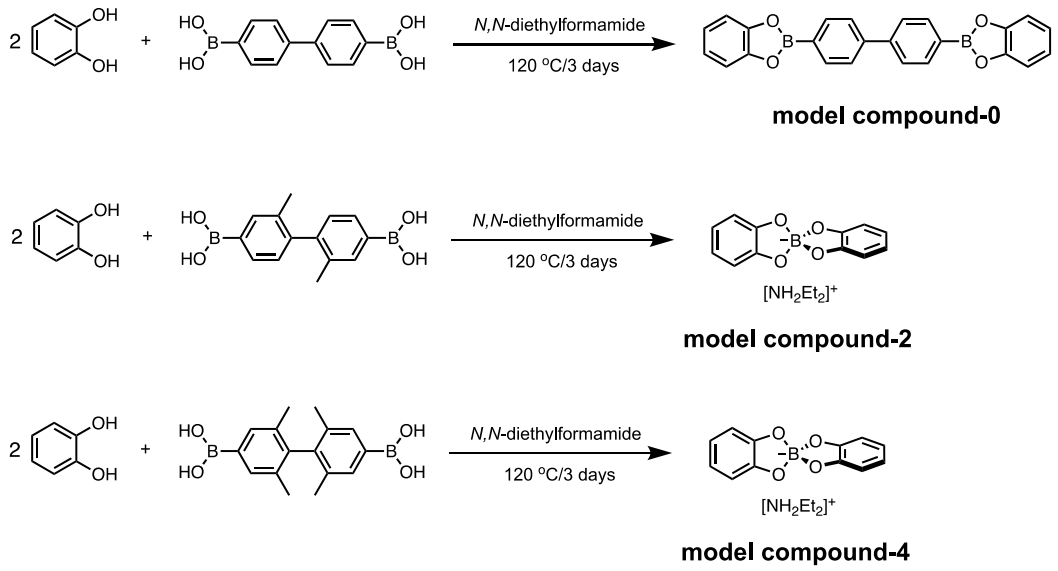

Figure 3.27. Scheme for the synthesis of **model compounds**.

Synthesis of model compound-0: Under a N_2 atmosphere, to a mixture of 4,4′-biphenyldiboronic acid (linker BPDA) (0.121 g, 0.5 mmol, 1.0 *equiv.*) and 1,2-dihydroxybenzene (0.115 g, 1.04 mmol, 2.08 *equiv.*) were added 12 mL of *N,N*-diethylformamide (DEF). The solution was stirred at 120 °C for 3 days with a Dean-Stark trap filled half full with 3 Å sieves. During this time a white solid began to precipitate from the transparent light-yellow solution. After the reaction mixture was cooled to room temperature, the white precipitate in the reaction system was collected through centrifugation and washed with hexane for three times, then dried in 80 °C vacuum oven to get the first batch of solid product in 55.4 % yield (0.11 g, yield calculated based on 4,4′-biphenyldiboronic acid) as white crystalline powders. The residue solvent was removed using vacuum distillation to get very small amount of the second batch white powder products. ^{1}H NMR spectra comparison of these two batches of solid product shows the first batch give purely model compound-0 while the second batch contains a mixture of model compound-0 and 1,2-dihydroxybenzene.

^{1}H NMR (400 MHz, $CDCl_3$): δ 8.20 (d, *J* = 8.0 Hz, 4H), 7.80 (d, *J* = 8.0 Hz, 4H), 7.34 (m, 4H), 7.15 (m, 4H) ppm. Due to the poor solubility of this compound, no solution ^{13}C NMR spectrum was obtained. Anal. Cald for $C_{24}H_{16}B_2O_4$: C: 73.91, H: 4.14. Found: C: 72.31, H: 4.04.

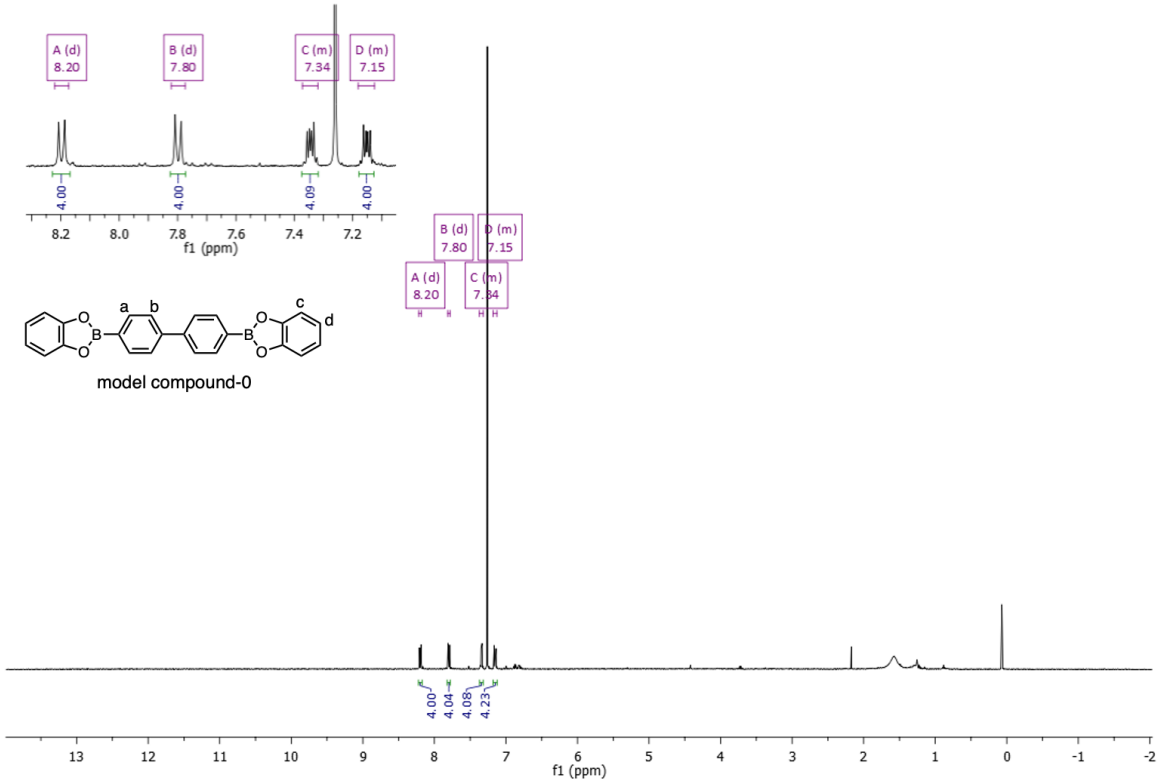

Figure 3.28. ^{1}H NMR spectrum of **model compound-0** in $CDCl_3$.

Synthesis of model compound-2: Under a N_2 atmosphere, to a mixture of (2,2'-dimethyl-[1,1'-biphenyl]-4,4'-diyl) diboronic acid (linker BPDA-2) (0.108 g, 0.4 mmol, 1.0 *equiv.*) and 1,2-dihydroxybenzene (0.092 g, 0.832 mmol, 2.08 *equiv.*) were added 12 mL of *N*,*N*-diethylformamide (DEF). The solution was stirred at 120 °C for 3 days with a Dean-Stark trap filled half full with 3 Å sieves. During this time, the reaction solution changed from a transparent light-yellow solution to an opaque dark brown solution. After the reaction mixture was cooled to room temperature, the solvent was removed using vacuum distillation. The brown oil residue was then dissolved in very small amount of dichloromethane and added dropwise to a stirred cold diethyl ether solution (300 mL) to precipitate the product. The solid product was collected by filtration and dried in a vacuum oven at 80 °C for 6 hours to give product in 62.7% yield (0.078 g, yield calculation based on 1,2-dihydroxybenzene) as brown powders. Single crystal of model compound-2 suitable for X-ray diffraction were grown from its saturated ethyl acetate solution at room temperature for one week.

^{1}H NMR (400 MHz, DMSO-d_6): δ 8.13 (s, 2H), 6.47 (s, 8H), 2.92 (q, J = 8.0 Hz, 4H), 1.15 (t, J = 8.0 Hz, 6H) ppm. ^{13}C NMR (100 MHz, DMSO-d_6): δ 151.55, 117.27, 107.58, 41.38, 11.05 ppm. MS (ESI+) m/z calcd for $[NH_2Et_2]^+$ [M]+: 74.15. Found: 74.0968. Anal. Cald for $C_{16}H_{20}BNO_4$: C: 63.81, H: 6.69, N: 4.65. Found: C: 65.16, H: 4.96.

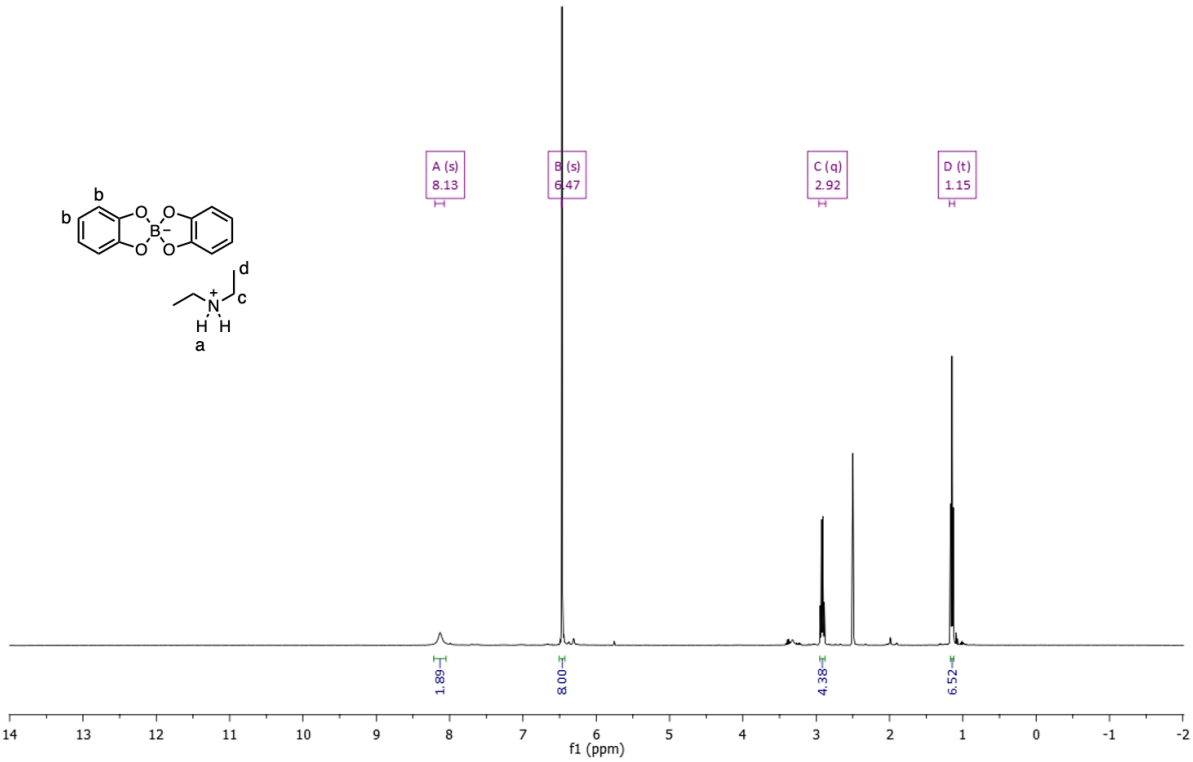

Figure 3.29. ^{1}H NMR spectrum of **model compound-2** in DMSO-d_6.

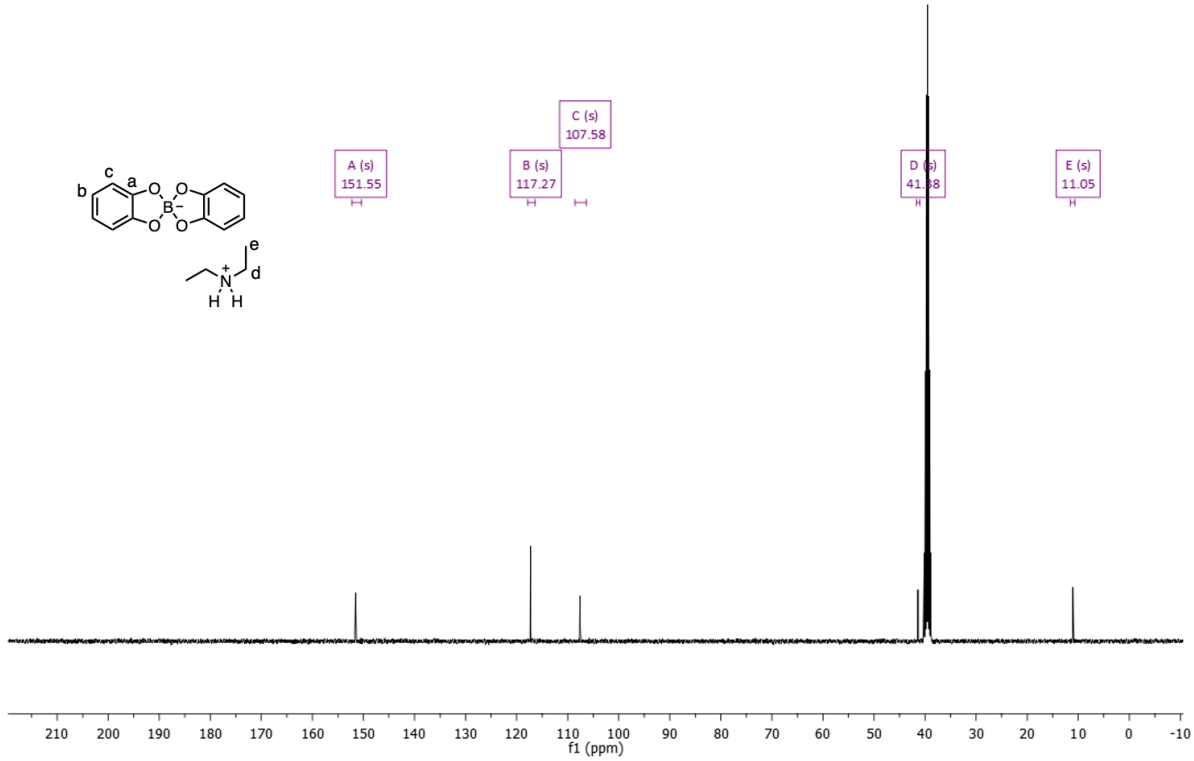

Figure 3.30. ^{13}C NMR spectrum of **model compound-2** in DMSO-d_6.

Synthesis of **model compound-4**: Under a N_2 atmosphere, to a mixture of (2,2',6,6'-tetramethyl-[1,1'-biphenyl]-4,4'-diyl) diboronic acid (linker BPDA-4) (0.104 g, 0.35 mmol, 1.0 *equiv.*) and 1,2-dihydroxybenzene (0.081 g, 0.728 mmol, 2.08 *equiv.*) were added 12 mL of *N*,*N*-diethylformamide (DEF). The solution was stirred at 120 °C for 3 days with a Dean-Stark trap filled half full with 3 Å sieves. During this time, the reaction solution changed from a transparent light-yellow solution to an opaque dark brown solution. After the reaction mixture was cooled to room temperature, the solvent was removed using vacuum distillation. The brown oil residue was then dissolved in very small amount of dichloromethane and added dropwise to stirred cold diethyl ether solution (300 mL) to precipitate the product. The solid product was collected by filtration and dried in a vacuum oven at 80 °C for 6 hours to give product in 66.3% yield (0.072 g, yield calculation based on 1,2-dihydroxybenzene) as pale brown powders. Single crystal of model compound-4 suitable for X-ray diffraction were grown from its saturated ethyl acetate solution at room temperature for one week.

^{1}H NMR (400 MHz, DMSO-d_6): δ 8.19 (s, 2H), 6.47 (s, 8H), 2.91 (q, J = 8.0 Hz, 4H), 1.15 (t, J = 8.0 Hz, 6H) ppm. ^{13}C NMR (100 MHz, DMSO-d_6): δ 151.55, 117.27, 107.58, 41.38, 11.09 ppm. MS (ESI+) m/z calcd for $[NH_2Et_2]^+$ [M]+: 74.15. Found: 74.0967.

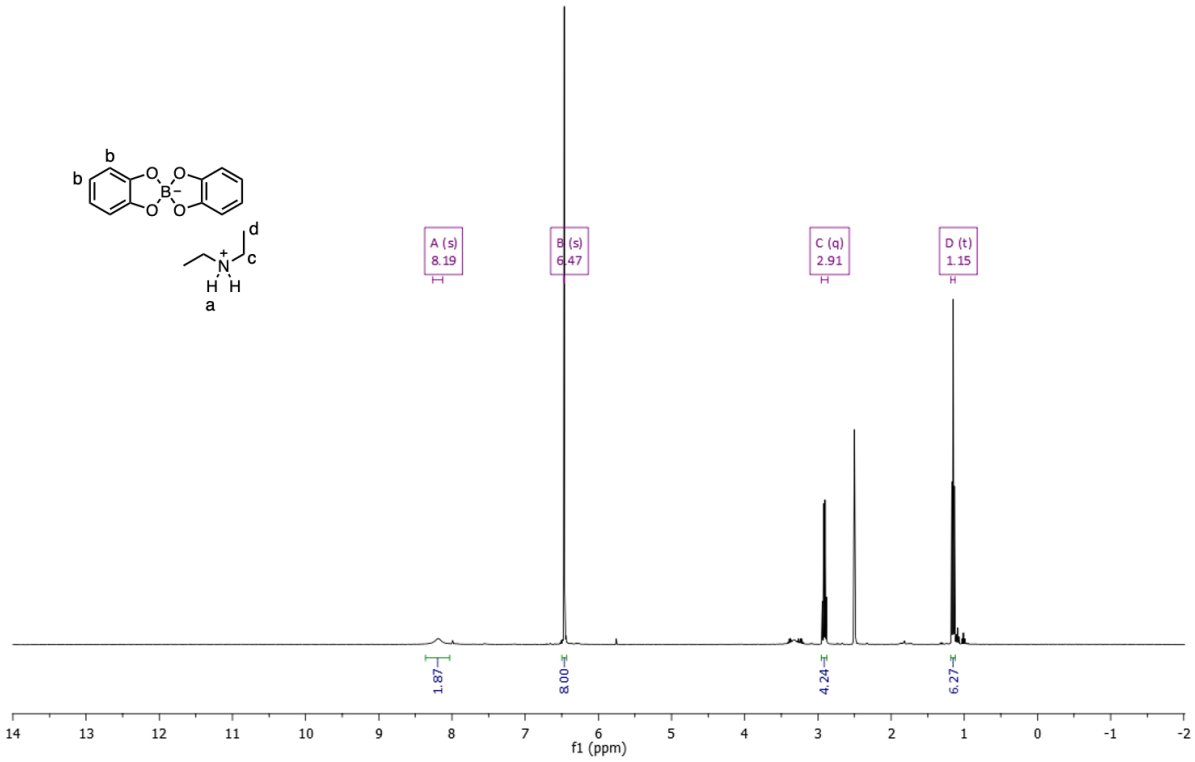

Figure 3.31. ^{1}H NMR spectrum of **model compound-4** in DMSO-d_6.

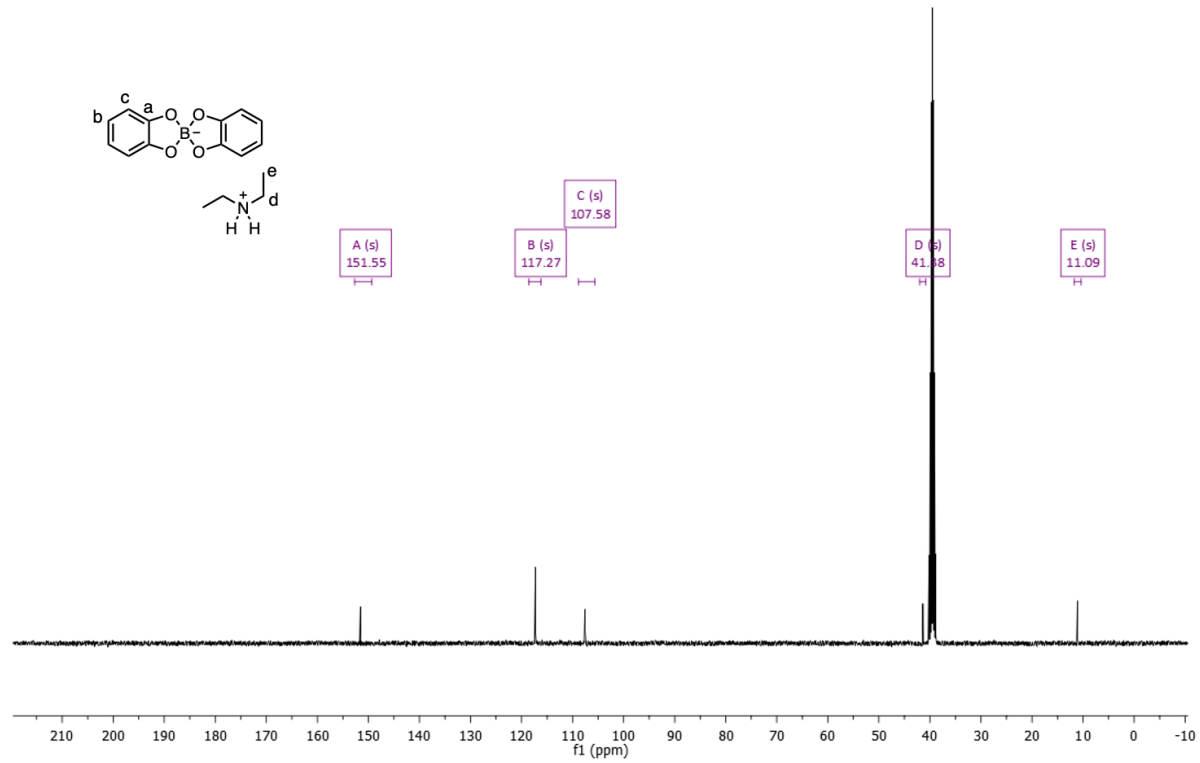

Figure 3.32. ^{13}C NMR spectrum of **model compound-4** in DMSO-d_6.

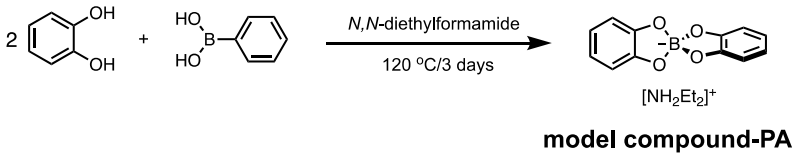

Figure 3.33. Scheme for the synthesis of **model compound-PA**.

Synthesis of model compound-PA: Under a N_2 atmosphere, to a mixture of phenylboronic acid (0.183 g, 1.5 mmol, 1.0 *equiv.*) and 1,2-dihydroxybenzene (0.344 g, 3.12 mmol, 2.08 *equiv.*) were added 15 mL of *N*,*N*-diethylformamide (DEF). The solution was stirred at 120 °C for 3 days with a Dean-Stark trap filled half full with 3 Å sieves. During this time, the reaction solution changed from a transparent light-yellow solution to transparent dark brown solution. After the reaction mixture was cooled to room temperature, the solvent was removed using vacuum distillation. The brown oil residue was then dissolved in very small amount of dichloromethane and added dropwise to a stirred cold diethyl ether solution (300 mL) to precipitate the product. The solid product was collected by filtration and dried in a vacuum oven at 80 °C for 6 hours to give product in 74.7% yield (0.17 g, yield calculation based on 1,2-dihydroxybenzene) as a pink-white powders. Single crystal of model compound-PA suitable for X-ray diffraction were grown from its saturated ethyl acetate solution at room temperature for one week.

^{1}H NMR (400 MHz, DMSO-d_6): δ 8.16 (s, 2H), 6.47 (m, 8H), 2.92 (q, J = 8.0 Hz, 4H), 1.15 (m, 6H) ppm. ^{13}C NMR (100 MHz, DMSO-d_6): δ 151.55, 117.27, 107.58, 41.37, 11.04 ppm. MS (ESI-) m/z calcd for $C_{12}H_8BO_4$ [M]−: 227.05. Found: 227.0519. MS (ESI+) m/z calcd for $[NH_2Et_2]^+$ [M]+: 74.15. Found: 74.0967. Anal. Cald for $C_{16}H_{20}BNO_4$: C: 63.81, H: 6.69, N: 4.65. Found: C: 63.58, H: 6.33, N: 4.66.

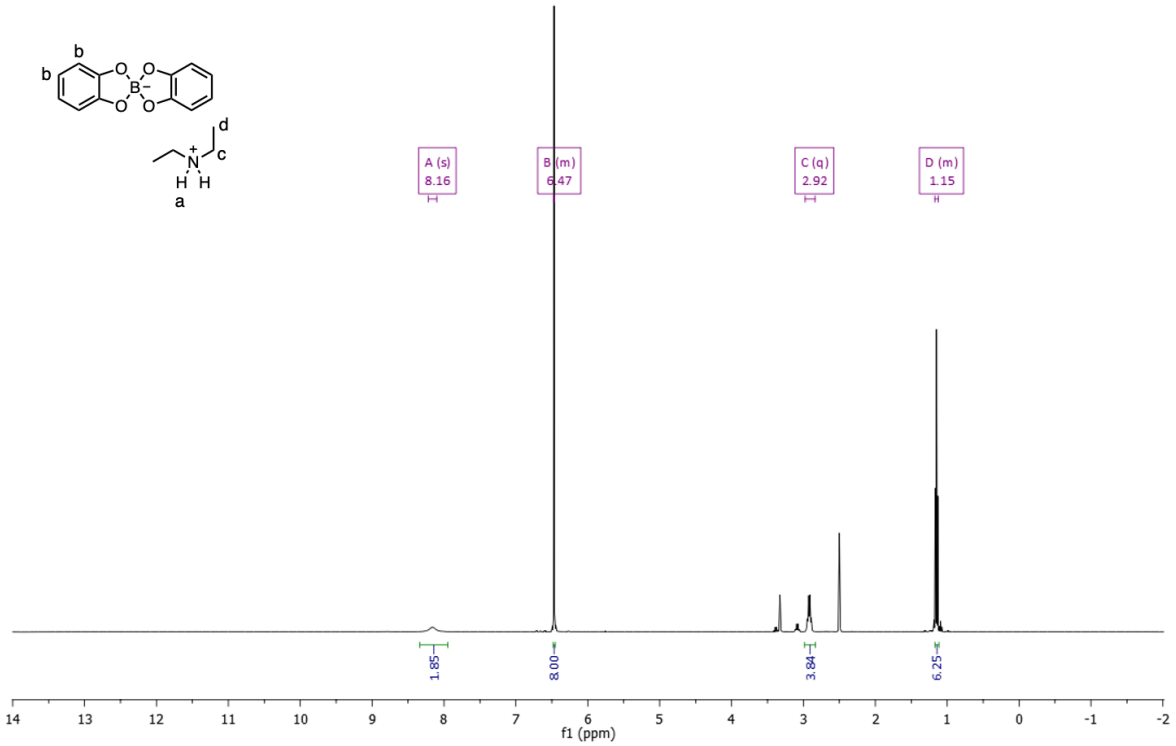

Figure 3.34. ^{1}H NMR spectrum of **model compound-PA** in DMSO-d_6.

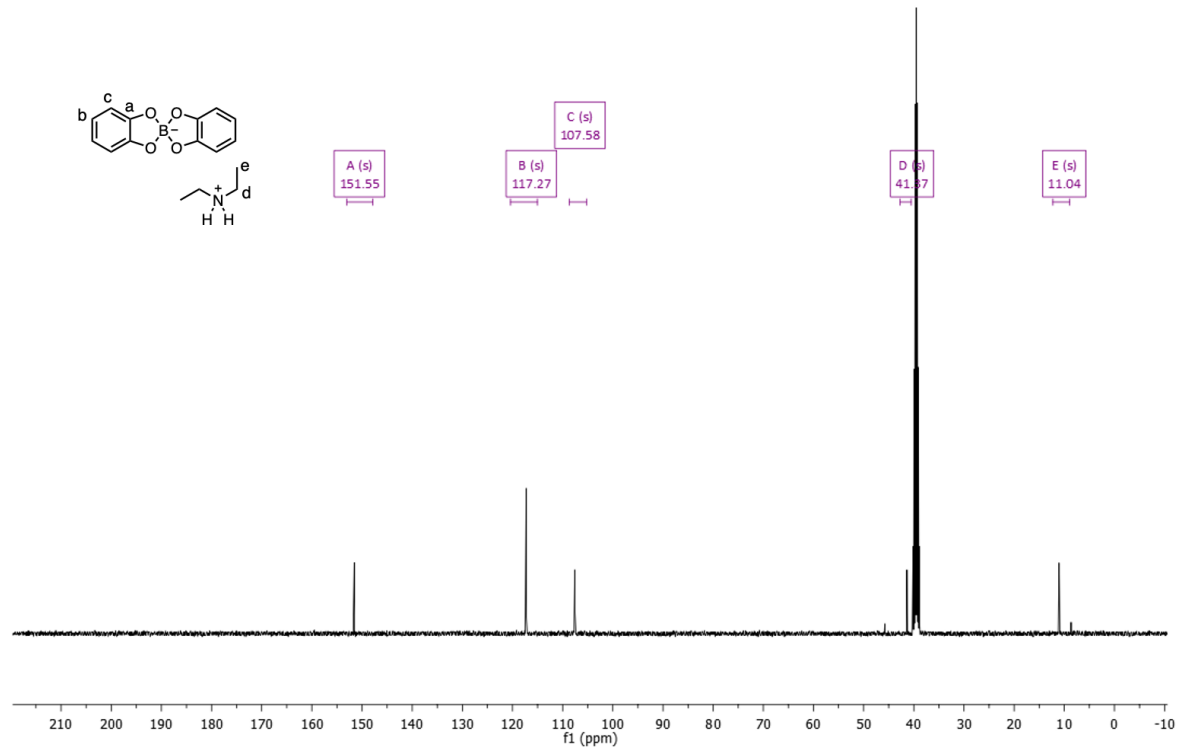

Figure 3.35. ^{13}C NMR spectrum of **model compound-PA** in DMSO-d_6.

3.4 Results and discussion

3.4.1 Powder X-ray diffraction analysis

BPDA-COF, BPDA-2-COF and BPDA-4-COF were synthesised by reacting $(OH)_8PcCo$ with linker BPDA, BPDA-2 and BPDA-4, respectively. Reactions were put in a 120 °C oven for 3 days, with *N*,*N*-diethylformamide (DEF) as the solvent. Although BPDA-COF is a reported structure, which was synthesized from a mixed solvent of *N*,*N*-dimethylacetamide (DMAc): 1,2-dichlorobenzene (o-DCB) = 2:1 (v : v) before,[5] here, as a control experiment, we prepared BPDA-COF in the same condition as for the synthesis of the other two COFs, using DEF as the solvent.

For the experimental results, though crystalline frameworks were obtained in all three cases, the results were different from what we expected (**Figure 3.36**). While the experimental PXRD pattern of BPDA-COF fit with the reported 2D boronate ester COF of **sql** topology, BPDA-4-COF gave a similar experimental PXRD pattern as the 3D SPB-COFs in the last chapter, in either its shape or peaks positions, indicating an underlying 3D **nbo** topology, based-on spiroborate linkage. BPDA-2-COF showed a more interesting PXRD pattern which looks like an addition of BPDA-COF and BPDA-4-COF, indicating a possible mixed 2D and 3D phase state.

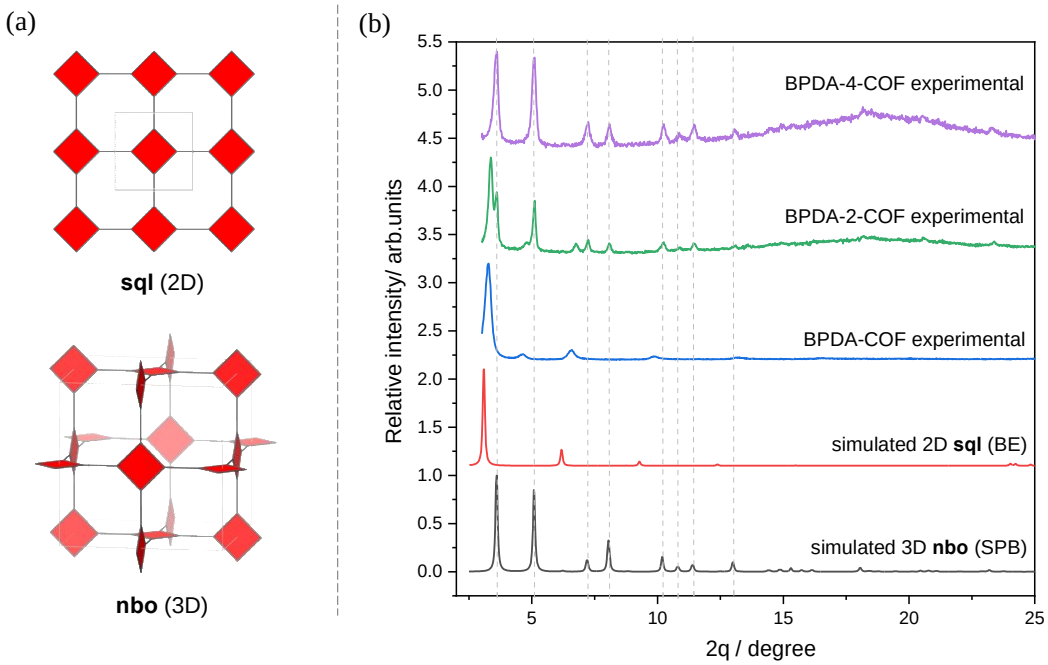

Figure 3.36. (a) Graph illustration of the 2D **sql** and the 3D **nbo** topology. All topologies are shown as their corresponding augmented net. (b) PXRD comparison between the experimental pattern of **BPDA-COF**, **BPDA-2-COF**, **BPDA-4-COF** and the simulated pattern based on the 2D **sql** topology (COF model based on boronate ester linkage, abbreviated as BE) and 3D **nbo** topology (COF model based on spiroborate linkage, abbreviated as SPB). For clarity, all the peaks that fits the 3D COF model (SPB) were marked out by grey dash lines.

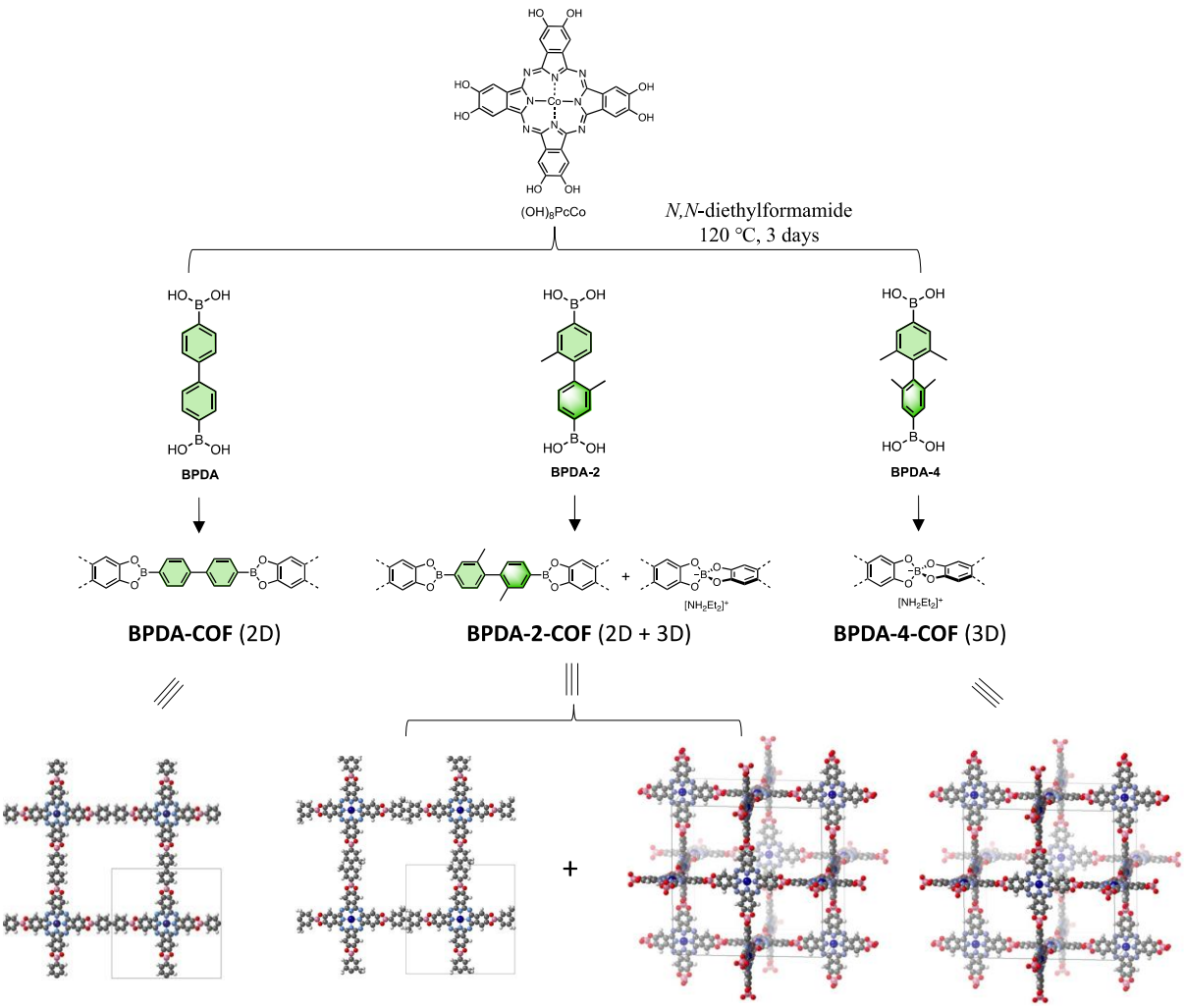

Figure 3.37. Reaction scheme between $(OH)_8PcCo$ and the three diboronic acid linkers based on the experimental PXRD results. The reaction between $(OH)_8PcCo$ with linker BPDA gave a 2D **BDDA-COF** with boronate ester (BE) linkage; the reaction between $(OH)_8PcCo$ with linker BPDA-2 yield **BDDA-2-COF**, which is a mixed phase of 2D BE-based COF and 3D spiroborate (SPB)-based COF; the reaction between $(OH)_8PcCo$ with linker BPDA-4 gave **BDDA-4-COF** of SPB-based 3D phase.

Based on the experimental PXRD comparison results discussed above, we proposed an unexpected reaction scheme between $(OH)_8PcCo$ and the three linear diboronic acid linkers (**Figure 3.37**). To exclude the possibility of forming an interpenetrated **nbo** topology based on the boronate ester linkage in BPDA-2-COF and BPDA-4-COF, 3D COF models with up to 5-fold interpenetration were built. Since the 3D phase that appeared in BPDA-2-COF is of the same structure as BPDA-4-COF (**Figure 3.36b**), here, we only use BPDA-4-COF for structure elucidation. Frameworks of **nbo** topology with different degrees of interpenetration are shown in **Figure 3.38** using a simplified representation style. None of the simulated PXRD patterns from these models can fit with the experimental PXRD pattern of BPDA-4-COF (**Figure 3.39**), thus excluding the possibility of forming boronate ester-linked 3D frameworks of **nbo** topology.

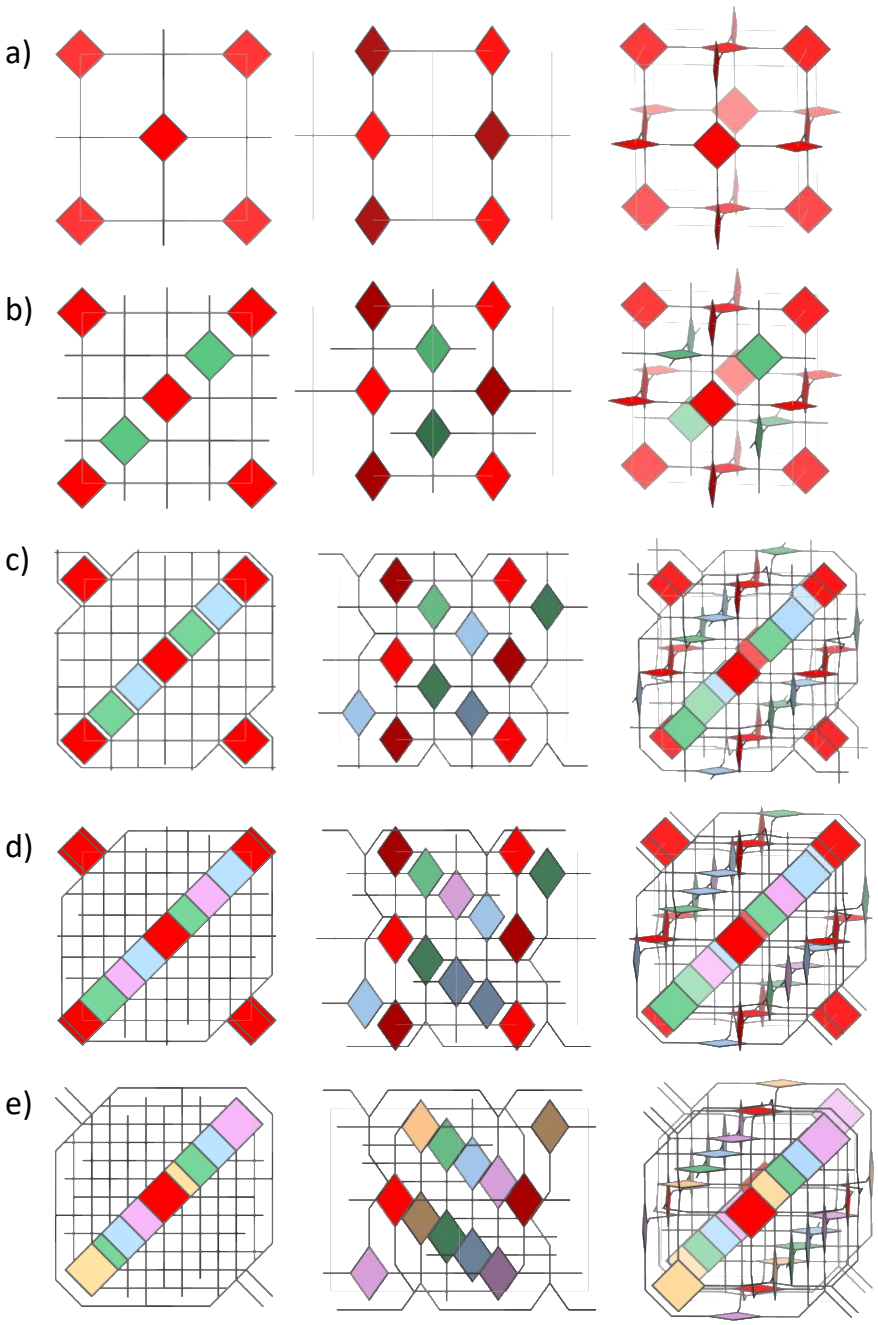

Figure 3.38. Three comparable views of (a) non-interpenetrated; (b) 2-fold; (c) 3-fold; (d) 4-fold and (e) 5-fold interpenetrated **nbo** net, based on boronate ester linked COFs. PcCo nodes belonging to first, second or third fold are coloured in red, green, blue, violet, and yellow, respectively.

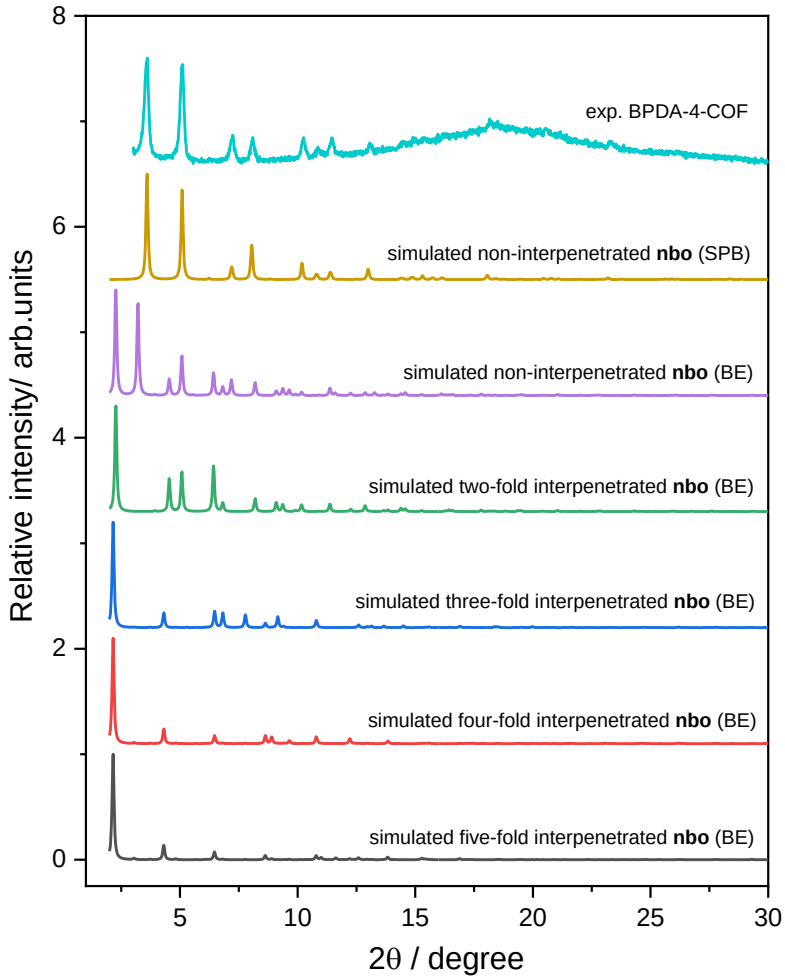

Figure 3.39. Comparison of the experimental PXRD pattern and simulated patterns for the **nbo** topology with different degrees of interpenetration. Spiroborate linkage is abbreviated as SPB while boronate ester linkage is abbreviated as BE.

The experimental diffraction pattern of BPDA-COF (**Figure 3.40**) exhibited significant peaks at 3.27°, 4.65°, 6.60°, 9.85°, 13.22°, 16.57° and 26.75°; Pawley refinement confirmed that these correspond to the (100), unknown, (200), (300), (400), (430) and (001) planes, respectively, in a tetragonal symmetry structure (space group P4/mmm), in good accordance with the literature reported structure.[5] The refinement gave unit cell parameters of a = 27.037(6) Å, c = 3.375(0) Å, in good agreement with our simulated COF model (P4/mmm, a = 27.558 Å, c = 3.468 Å).

The experimental diffraction pattern of BPDA-4-COF (**Figure 3.41**) exhibited significant peaks at 3.61°, 5.10°, 7.24°, 8.09°, 10.25°, 10.86°, 11.46°, 13.06°, 18.17° and 23.30°. Pawley refinement confirmed that these correspond to the (110), (200), (220), (310), (400), (330), (420), (510), (710) and (910) planes, respectively, in a cubic symmetry structure (space group Im$\bar{3}$m). The experimental PXRD pattern agrees with the simulated pattern obtained from a non-interpenetrated

model with **nbo** topology using the spiroborate linkage. The refinement yielded a cubic *I* centered lattice with unit cell parameters of a = 34.315(0) Å, in good agreement with our simulated COF model ($Im\bar{3}m$, a = 34.707 Å). Here, we used the same SPB-COF model from the former chapter for both PXRD simulation and as the initial lattice parameters for Pawley refinement.

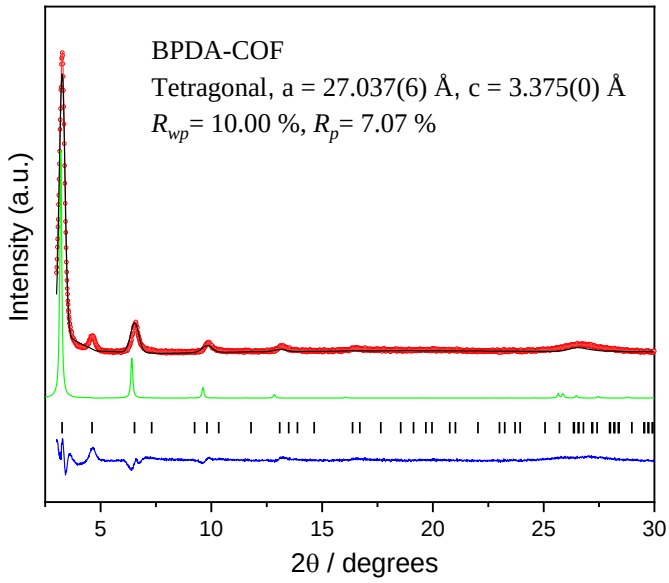

Figure 3.40. Experimental PXRD pattern (red), profile calculated from Pawley refinement (black) and residual (blue), and pattern simulated from the structural model (green) for **BPDA-COF**. Reflection positions are shown by tick marks.

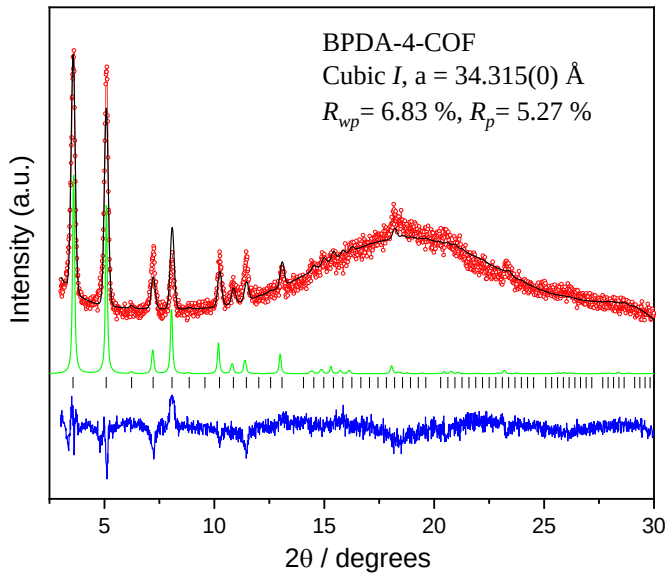

Figure 3.41. Experimental PXRD pattern (red), profile calculated from Pawley refinement (black) and residual (blue), and pattern simulated from the structural model (green) for **BPDA-4-COF**. Reflection positions are shown by tick marks.

The experimental diffraction pattern of BPDA-2-COF (**Figure 3.42**) exhibited significant peaks at 3.35°, 3.60°, 4.77°, 5.10°, 6.76°, 7.21°, 8.08°, 10.21°, 10.85°, 11.42°, 13.06°, 14.48°, 14.93°, 15.35°, 16.21°, 18.16°, 18.55°, 20.57° and 23.29°. The presence of the multiple well-defined reflections suggests that BPDA-2-COF has high crystallinity and high periodicity in two/three dimensions. Among these diffractions, Pawley refinement confirmed that peaks at 3.35°, 4.77° and 6.76° correspond to the (100), unknown and (200) planes of the 2D phase with **sql** topology, respectively, in a tetragonal symmetry structure (space group P4/mmm), the refinement gave unit cell parameters of a = 26.349(9) Å, c = 3.460(2) Å, in good agreement with our simulated COF model (P4/mmm, a = 27.558 Å, c = 3.468 Å). Pawley refinement confirmed that peaks at 3.60°, 5.10°, 7.21°, 8.08°, 10.21°, 10.85°, 11.42°, 13.06°, 14.48°, 14.93°, 15.35°, 16.21°, 18.16°, 18.55°, 20.57° and 23.29° corresponds to (110), (200), (220), (310), (400), (330), (420), (510), (440), (530), (611), (541), (710), (721), (811) and (910) planes of the 3D phase with **nbo** topology, respectively, based on spiroborate linkage. The refinement yielded a cubic *I* centered lattice with unit cell parameters of a = 34.761(1) Å, in excellent agreement with our simulated COF model (Im$\bar{3}$m, a = 34.707 Å).

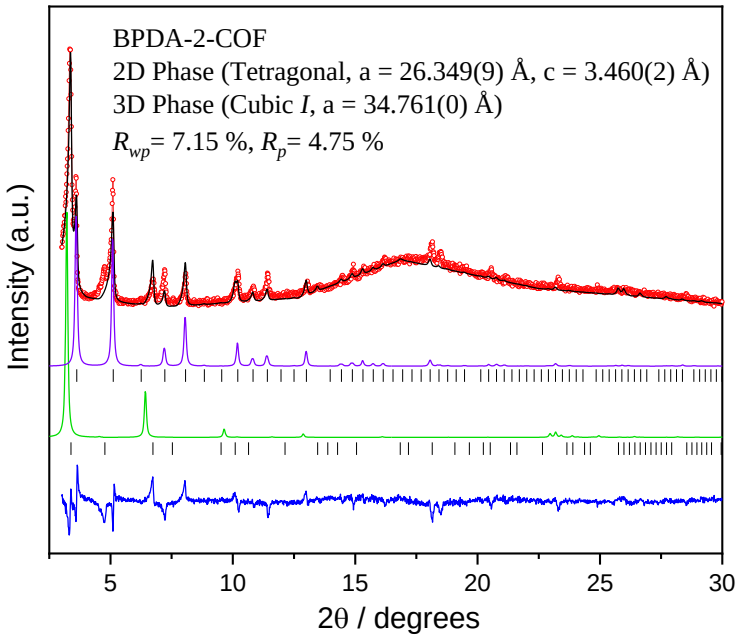

Figure 3.42. Experimental PXRD pattern (red), profile calculated from Pawley refinement (black) and residual (blue), and pattern simulated from the structural model (green) for **BPDA-2-COF**. Reflection positions are shown by tick marks.

3.4.2 Model compound synthesis and the proposed reaction mechanism

To confirm the type of linkage in all three COFs, particularly to make sure the formation of the spiroborate linkage in BPDA-2-COF and BPDA-4-COF, three model compounds were synthesized by reacting 1,2-dihydroxylbenzene with linker BPDA, BPDA-2 and BPDA-4, to yield model compound-0, model compound-2 and model compound-4, respectively. All model reactions were performed under COF synthesis conditions. It is worth noting that the colour change of the three model systems over the 3 days is different. While model compound-0 system remained a transparent light-yellow solution with a large amount of white precipitate, both model compound-2 and model compound-4 system changed from the same transparent light-yellow solution to a dark brown opaque solution within three days. Solution ^{1}H NMR spectra of the isolated precipitates from the model compound-0 system confirmed the 4,4'-bis(benzo[d][1,3,2]dioxaborol-2-yl)-1,1'-biphenyl structure (**Figure 3.43**) in 55% yield and in good accordance with boronate ester-linked 2D BPDA-COF. Powder products of model compound-2 and model compound-4 were precipitated from cold diethyl ether solution, after removing all the DEF solvent by vacuum distillation, which gave light-brown powder products with yields of 63% and 66%, respectively. Solution ^{1}H NMR spectra of these two powders confirmed their spiroborate-based structures (**Figure 3.43**). These results corroborated the formation of spiroborate linkage in BPDA-2-COF and BPDA-4-COF.

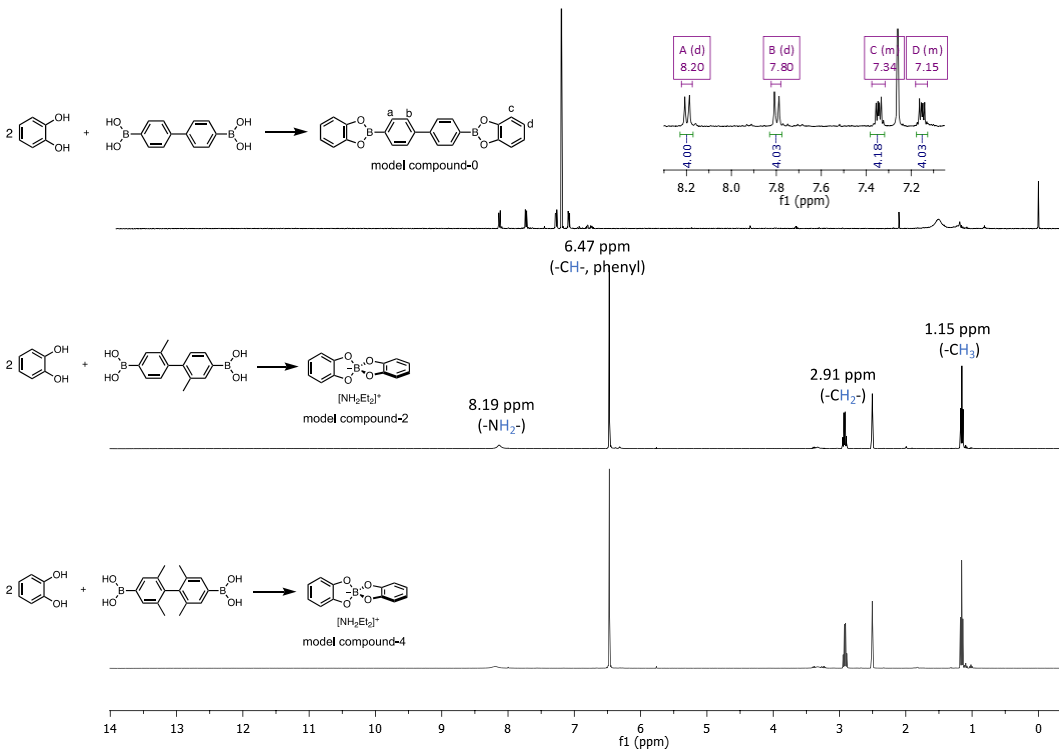

Figure 3.43. ^{1}H NMR spectra of **model compound-0** in $CDCl_3$, **model compound-2** and **model compound-4** in dmso-d_6. All model compounds were synthesized from the same reaction condition as for COF synthesis.

We then investigated the reason why the spiroborate linkage formed when $(OH)_8PcCo$ reacted with linker BPDA-2 and BPDA-4, while under the same condition, its reaction with linker BPDA yielded 2D BPDA-COF with the expected boronate ester linkage.

After literature searches, we found a similar example of an unexpected spiroborate linkage formation while researchers tried to synthesize a boronate ester-linked small molecule from benzene-1,4-diboronic acid (**Figure 3.44a**).[8] By varying the molar ratio of the bromide salts and benzene-1,4-diboronic acid from 1:1 to 2:1 and 4:1, they found that all reactions gave similar yield of the spiroborate molecule, indicating each benzene-1,4-diboronic acid linker provides two borons during the reaction. Moreover, they successfully identified the existence of phenylboronic acid in the crude reaction mixture by solution ^{1}H NMR, which corroborated the B-C bond cleavage in benzene-1,4-diboronic acid during the reaction. Further trials using phenylboronic acid to replace the benzene-1,4-diboronic acid yielded the same spiroborate product at a similar yield as when using the same *equiv*. benzene-1,4-diboronic acid. The possible reaction mechanism they proposed is shown in **Figure 3.44b**. They suppose, the reaction between the bromide salt and benzene-1,4-diboronic acid forms the boronate ester linkage which enhanced the Lewis acidity of this boron and leads to the direct nucleophilic attack by another bromide salts to give the spiroborate product.

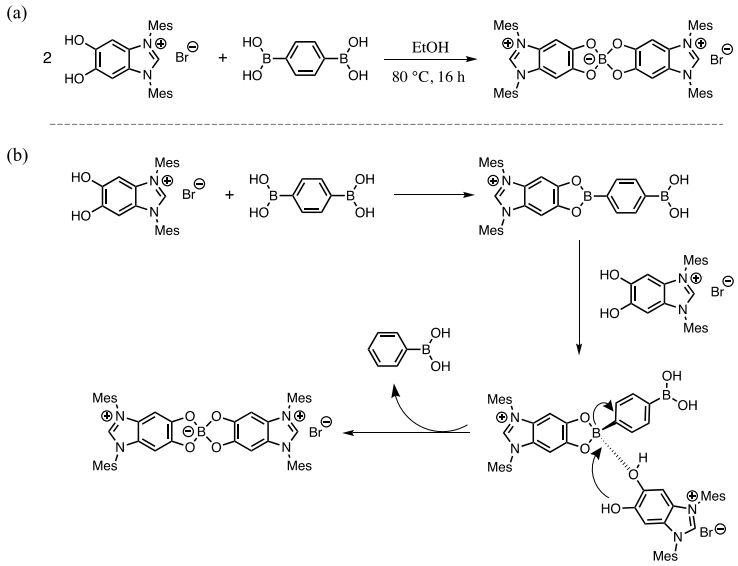

Figure 3.44. (a) The reaction scheme in the example reported. (b) The proposed reaction mechanism.[8]

In our case, particularly in the example of the formation of the spiroborate linked BPDA-4-COF, it seems that linker BPDA-4 only serves as the boron source. Inspired by this, we also tried to use phenylboronic acid replacing the biphenyl-diboronic acid linkers, under the same conditions for the synthesis of the BPDA-series COFs. We successfully obtained a 3D PA-COF of **nbo** topology

with spiroborate linkage in a 61.5% yield (**Figure 3.45**). The experimental diffraction pattern of PA-COF (**Figure 3.46**) exhibited significant peaks at 3.58°, 5.10°, 6.25, 7.21°, 8.08°, 10.28°, 10.86°, 11.46°, 13.06°, 14.97°, 18.18° and 23.41°. Pawley refinement confirmed that these correspond to the (110), (200), (211), (220), (310), (400), (330), (420), (510), (530), (710) and (910) planes, respectively, in a cubic symmetry structure (space group Im$\bar{3}$m). The experimental PXRD pattern is in good agreement with the simulated pattern obtained from a non-interpenetrated model with **nbo** topology. The refinement yielded a cubic *I* centered lattice with unit cell parameters of a = 35.018(7) Å, in excellent agreement with our simulated COF model (Im$\bar{3}$m, a = 34.707 Å). Here, we used the same SPB-COF model from the former chapter for both PXRD simulation and as the initial lattice parameters for Pawley refinement.

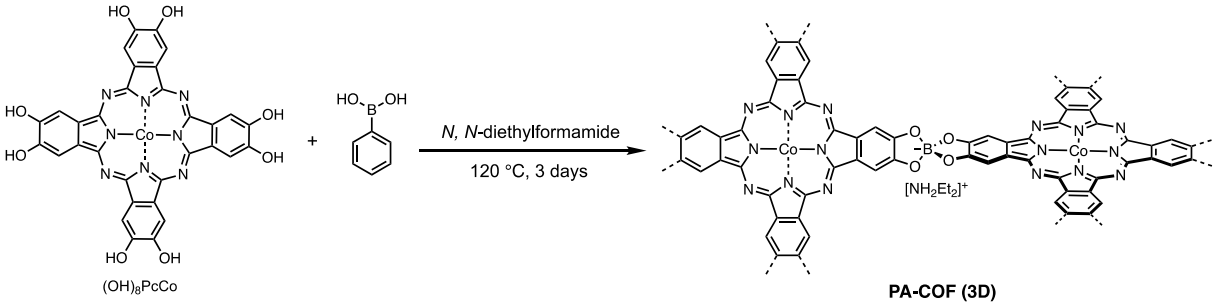

Figure 3.45. Scheme for the synthesis of **PA-COF**.

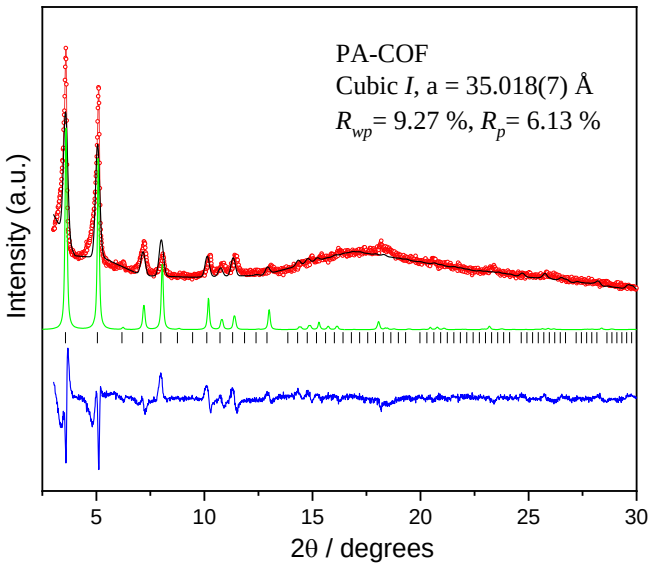

Figure 3.46. Experimental PXRD pattern (red), profile calculated from Pawley refinement (black) and residual (blue), and pattern simulated from the structural model (green) for **PA-COF**. Reflection positions are shown by tick marks.

Model compound-PA was synthesized by reacting phenylboronic acid with 1,2-dihydroxylbenzene under COF synthesis conditions to give the isolated product as pure spiroborate structures (**Figure 3.47a**). Single crystals of model compound-PA were grown from its saturated ethyl acetate solution at room temperature. The single crystal structure of model compound-PA confirmed its spiroborate structure and the $[NH_2Et_2]^+$ counter cation (**Figure 3.47b**). Single crystal refinement details for model compound-PA were summarized in **Table 3.1**.

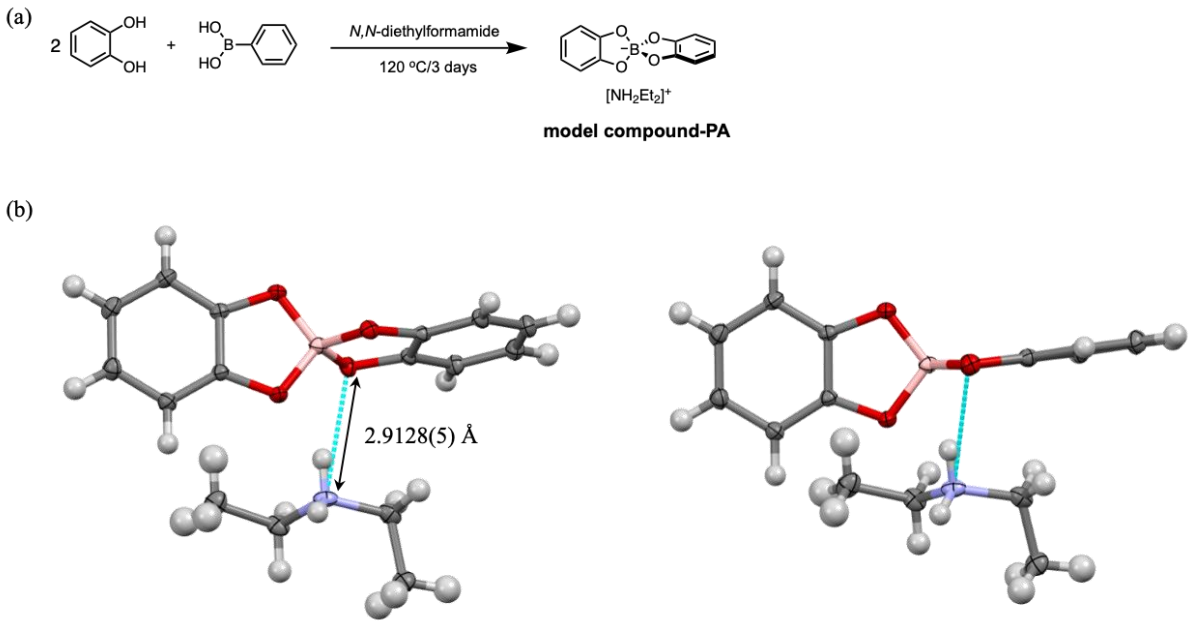

Figure 3.47. (a) Scheme for the synthesis of **model compound-PA**. (b) Displacement ellipsoid plots from the single crystal structure of **model compound-PA**; two views are shown; ellipsoids are displayed at 50% probability level. C = grey; H = white; N = blue; O = red; B = pink. Single crystals of **model compound-2** and **model compound-4** were also grown from their saturated ethyl acetate solution, since the single crystal measurement of **model compound-2** and **model compound-4** gives the same unit cell parameter as model compound-PA, so we did not carry on the measurement further for them.

Table 3.1. Single crystal refinement details for **model compound-PA**.

Name	**model compound-PA**
Crystallization solvent	ethyl acetate
Wavelength/ Å	0.71073 (Mo-Kα)
Formula	$C_{12}H_8BO_4,C_4H_{12}N$
Weight	301.14
Crystal size/mm^3	0.238 × 0.225 × 0.173
Crystal system	monoclinic
Space group	$P2_1/n$
***a*/ Å**	11.3054(2)
***b*/ Å**	8.22080(10)
***c*/ Å**	16.9376(5)
***α*/ °**	90
***β*/ °**	105.506(2)
***γ*/ °**	90
***V*/ Å^3**	1516.87(6)
ρ_{calcd}/g cm-1	1.319
Z	4
T/K	100.00(10)
μ/mm-1	0.093
F (000)	640.0
θ range/°	3.9 to 101.984
Reflections collected	56792
Independent reflections	13473
Data / restraints / parameters	13473/0/207
R_{int}	0.0232
Final R1 values (I > 2σ(I))	0.0452
Final R1 values (all data)	0.0684
wR_2 (all data)	0.1470
Goodness-of-fit on F^2	1.038

Since our case here is similar to the "B-C bond cleavage in benzene-1,4-diboronic acid" example discussed above,[8] based-on their work, we proposed a possible reaction mechanism to explain the unexpected spiroborate linkage formation during the synthesis of BPDA-2-COF and BPDA-4-COF in our example. We take linker BPDA-4 for reaction mechanism illustration. As is shown in **Figure 3.48**, we suppose, under the reaction condition applied, initial reaction between $(OH)_8$PcCo and linker BPDA-4 yielded a mono-boronate ester compound 1. Since boron in the boronate ester structure exhibited enhanced Lewis acidity toward the corresponding boronic acid,[9] this boronate ester linkage was then transformed to the first batch of spiroborate molecules through the nucleophilic attack by another $(OH)_8$PcCo, which will release a mono-functional boronic acid substituted compound 2 that can further act as the boron source to give the second batch of spiroborate molecules.

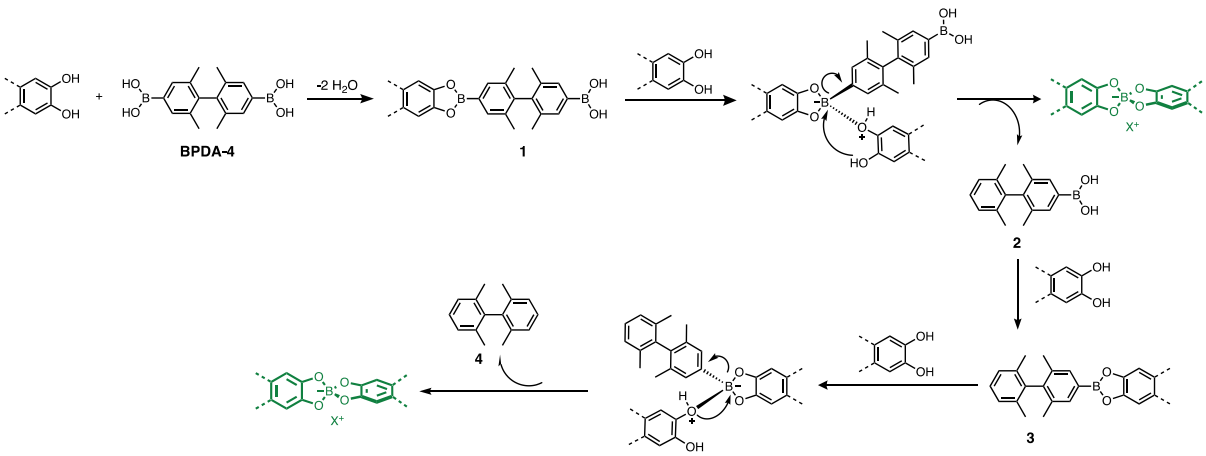

Figure 3.48. Possible reaction mechanism proposed for the formation of spiroborate linkage in **BPDA-4-COF**.

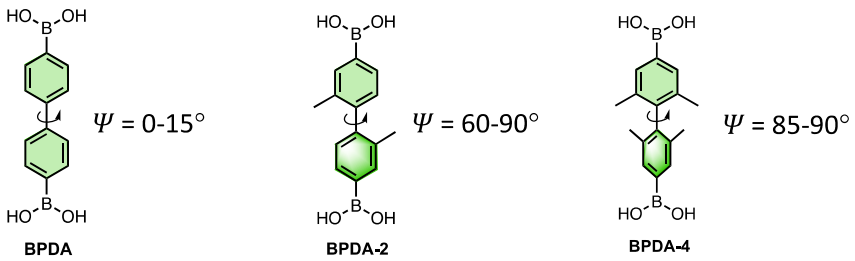

Figure 3.49. Conformation of the three linkers, Ψ = torsion angle of the two phenyls. Torsion angle concluded from the conformer search result of the single crystal structures of the corresponding biphenyl fragment in the Cambridge Structure Database (CSD) shown in **Figure 3.4**.

As for the reason why under the same reaction condition, the reaction between $(OH)_8$PcCo and linker BPDA yielded a 2D boronate ester-linked COF, we propose the near planar linker BPDA reacts with $(OH)_8$PcCo formed a closely stacked 2D layers (d-spacing = 3.5 Å), which protects the boron from being attacked by another $(OH)_8$PcCo. As the stacking enhanced 2D boronate ester

linked COFs formation rate and stability had been reported before.[10] Linker BPDA-4 has a torsion angle of 85-90°, which prohibited the close packing between each layer and thus spared some space for the nucleophilic attack reaction by other $(OH)_8PcCo$ units. The torsion angle of the two phenyl units in linker BPDA-2 is between 60-90°, which is smaller than linker BPDA-4 but larger than linker BPDA, this might explain its mixed phases of 2D boronate ester structures and 3D spiroborate structures. Under the reaction condition we applied, despite the stacking-induced protection effect in the 2D BPDA-COF, we hypothesize that the spiroborate structure should be the favoured since the formation of the sp^3 hybridized tetrahedra boron will significantly release the angle strain from the sp^2 hybridized triangle boron of 120° to 109°, as reported before.[11]

3.4.3 FT-IR and solid-state ^{13}C and ^{11}B NMR spectra

Figure 3.50 shows the FT-IR spectra comparison between the four model compounds and their precursors. As can be seen in **Figure 3.50a**, model compound-0 showed a strong adsorption band at 1329 cm^{-1}, corresponding to the stretching vibrations of the B–O bond in the trigonal boronate ester linkage, while the strong adsorption band at 1053 cm^{-1} in model compound-2, model compound-4 and model compound-PA can be assigned to the B−O stretching vibrations in $[BO_4]^-$ tetrahedra.[12,13] The attenuation of the adsorption at 1327-1329 cm^{-1} and the enhanced adsorption at 1053 cm^{-1} in model compounds-2, model compounds-4 and model compounds-PA compared to the four diboronic acid precursors also supported the successful formation of sp^3 hybridized boron based spiroborate linkage in these model compounds. Similarly, in **Figure 3.51a**, while the FT-IR spectra of the 2D BPDA-COF showed a strong absorption band at 1338 cm^{-1}, indicating its boronate ester linkage, BPDA-2-COF exhibited an adsorption band both at 1338 and 1037 cm^{-1}, corroborated its mixed boronate ester and spiroborate linkage. BPDA-4-COF and PA-COF showed strong adsorption band at 1037-1041 cm^{-1}, confirming their spiroborate linkage. The absorption band between 2800-3000 cm^{-1} in COFs can be attributed to the C-H stretching vibration in the aldehyde group (-CHO) from DEF, indicating a trace amount of DEF solvent residue after $ScCO_2$ activation of COFs. Further FT-IR spectra comparison between COFs and their precursors gave similar results as we concluded from model compounds (**Figure 3.51b**).

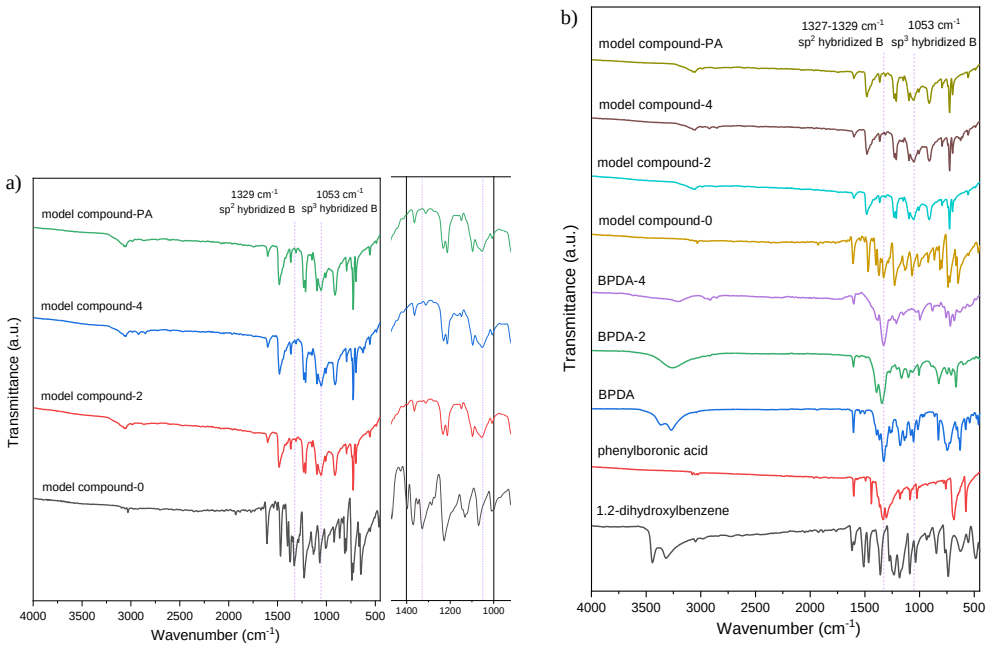

Figure 3.50. FT-IR spectra of (a) the four **model compounds** and (b) the comparison between model compounds and precursors.

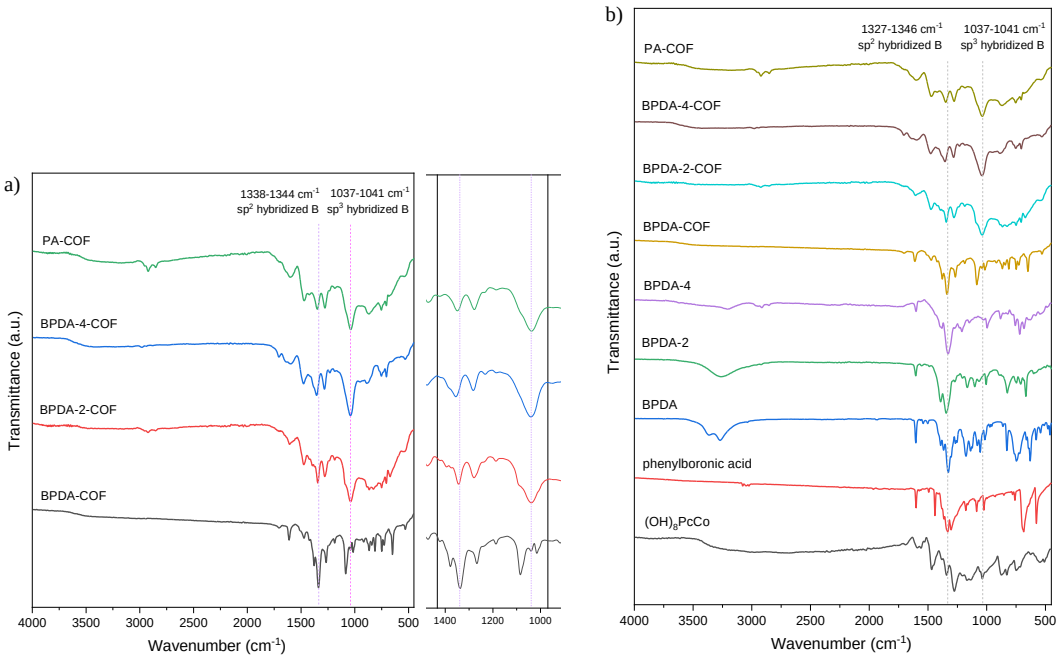

Figure 3.51. FT-IR spectra of (a) the four **COFs** and (b) the comparison between COFs and precursors. The $scCO_2$ activated COFs were used for measurement.

Figure 3.52-3.55 shows the solid-state ^{13}C CP/MAS NMR spectra of the four COFs. **Figure 3.52** shows the spectra of the 2D BPDA-COF, while signals at 136.9 and 106.7 ppm correspond to phthalocyanine carbons, the signal at 126.5 ppm can be attributed to carbons on the phenyl units in linker BPDA. **Figure 3.53** shows the spectra of the mixed phased BPDA-2-COF, while signals at 154.9 and 106.2 ppm correspond to phthalocyanine carbons, the signal at 132.6 ppm is the added signal of the phthalocyanine carbons and the carbons on the phenyl units in linker BPDA-2. Signals at 42.2 and 12.3 ppm correspond to carbons on $[NH_2Et_2]^+$ counter cation, while the signal at 16.6 ppm can be assigned to the methyl carbon in linker BPDA-2. **Figure 3.54** shows the spectra of the BPDA-4-COF, while the signals at 150.8, 134.0 and 107.1 ppm corresponds to phthalocyanine carbons, signals at 43.6 and 13.7 ppm can be attributed to carbons on $[NH_2Et_2]^+$. **Figure 3.55** shows the spectra of the PA-COF, similar to BPDA-4-COF, while the signals at 149.3, 133.8 and 106.2 ppm correspond to phthalocyanine carbons, signals at 44.9 and 14.0 ppm can be attributed to the carbons on $[NH_2Et_2]^+$.

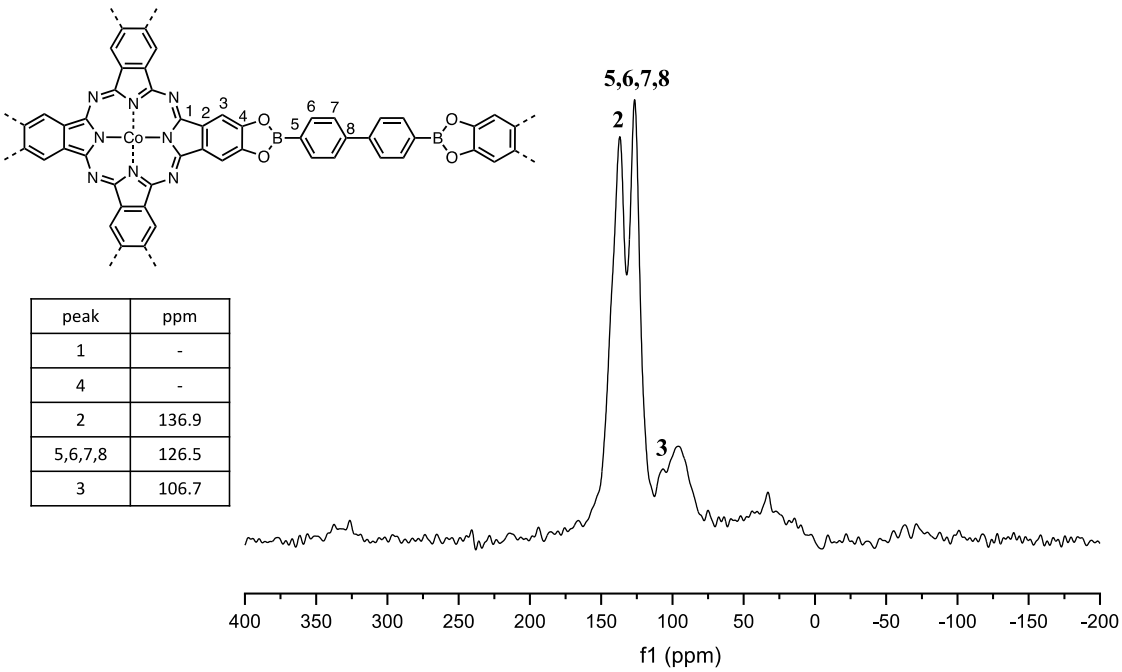

peak	ppm
1	-
4	-
2	136.9
5,6,7,8	126.5
3	106.7

Figure 3.52. Solid state ^{13}C solid state NMR CP/MAS spectrum of **BPDA-COF**. The $scCO_2$ activated COF was used for measurement.

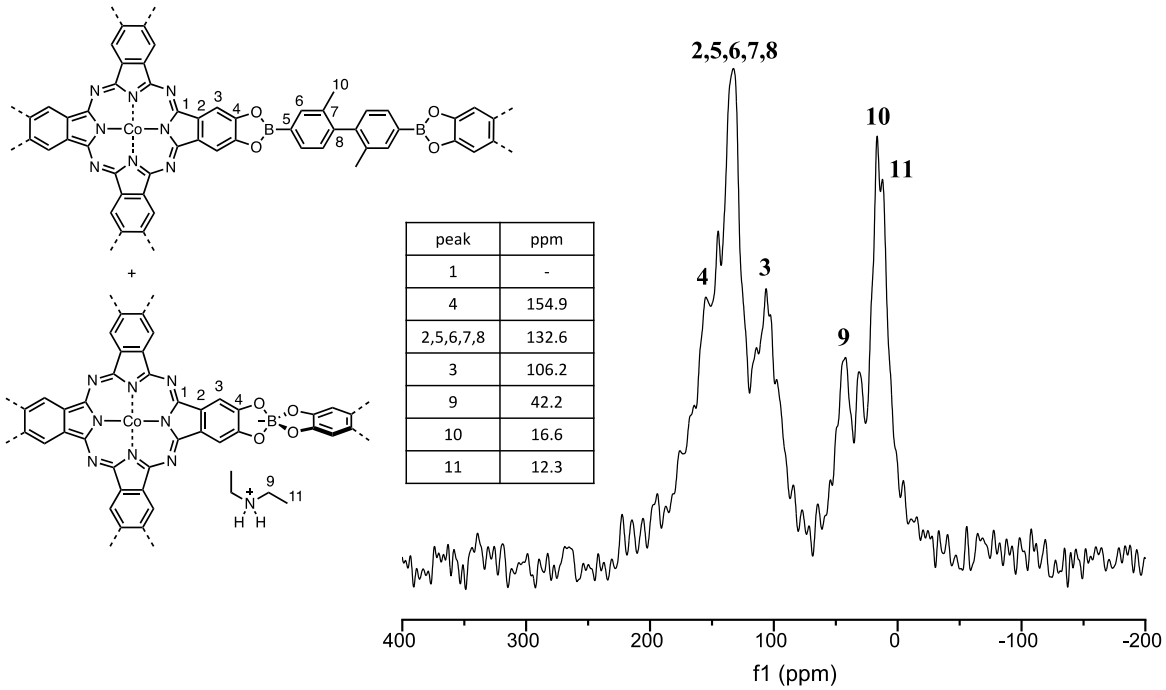

peak	ppm
1	-
4	154.9
2,5,6,7,8	132.6
3	106.2
9	42.2
10	16.6
11	12.3

Figure 3.53. Solid state ^{13}C solid state NMR CP/MAS spectrum of **BPDA-2-COF**. The $scCO_2$ activated COF was used for measurement.

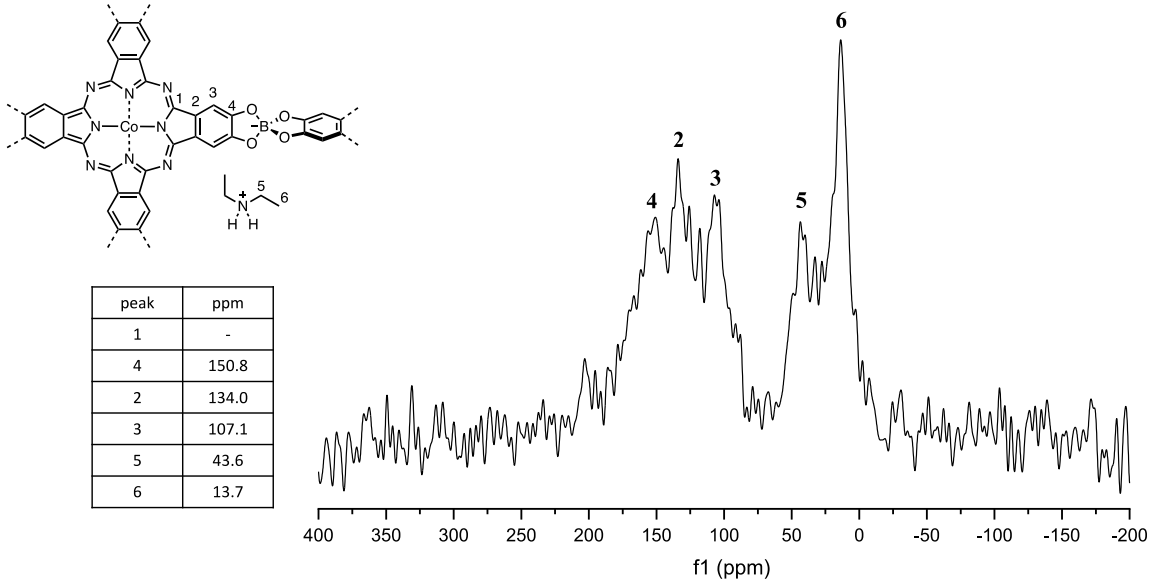

peak	ppm
1	-
4	150.8
2	134.0
3	107.1
5	43.6
6	13.7

Figure 3.54. Solid state ^{13}C solid state NMR CP/MAS spectrum of **BPDA-4-COF**. The $scCO_2$ activated COF was used for measurement.

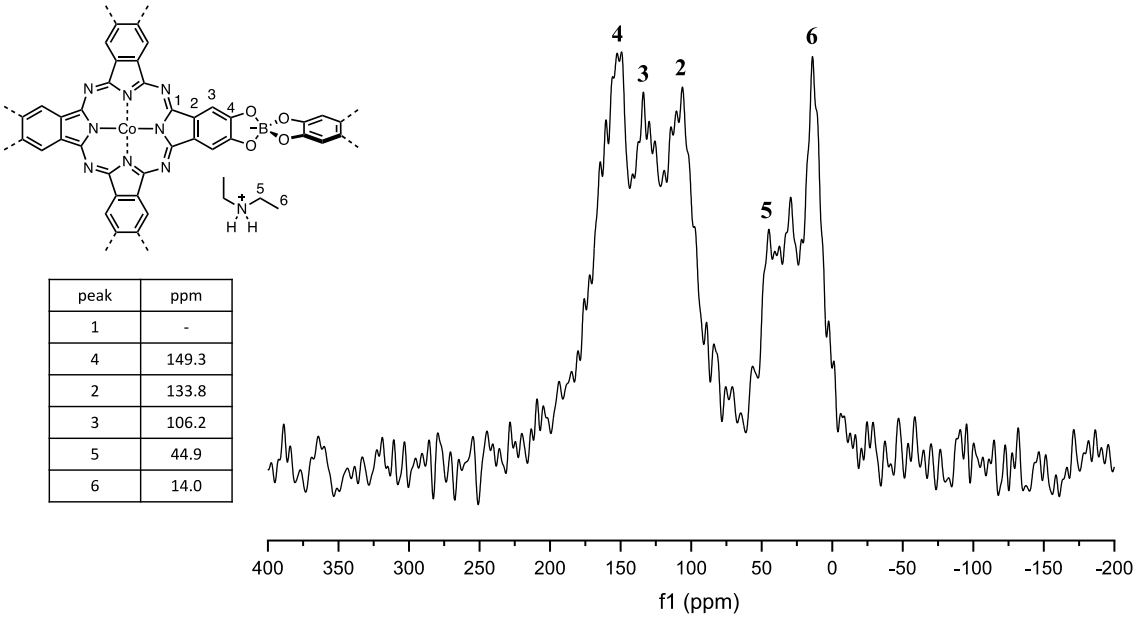

peak	ppm
1	-
4	149.3
2	133.8
3	106.2
5	44.9
6	14.0

Figure 3.55. Solid state ^{13}C solid state NMR CP/MAS spectrum of **PA-COF**. The $scCO_2$ activated COF was used for measurement.

Figure 3.56 shows the solid-state ^{11}B MAS NMR spectrum and the solution ^{11}B NMR spectrum comparison between COFs, model compounds and the corresponding boronic acid precursors. As can be seen in **Figure 3.56**, the solid-state ^{11}B NMR signal gradually shifted from 19.96 ppm in the 2D BPDA-COF to 16.16, 11.41 and 13.31 ppm in BPDA-2-COF, BPDA-4-COF and PA-COF, respectively. Comparison between this trend and the solution ^{11}B NMR signal of the spiroborate based model compounds (model compound-2, -4 and -PA), which locates at 14.19 ppm, confirms that boron has been incorporated into BPDA-2-COF, BPDA-4-COF and PA-COF as a sp^3 hybridized tetrahedral spiroborate state. In addition, solid-state ^{11}B NMR signal of the 2D BPDA-COF (19.96 ppm) is close to the reported value of the solid-state ^{11}B NMR signal for 1,4-bis(benzodioxaborol-2-yl)benzene, an analogue of model compound-0, which locates at 18.0 ppm, corroborating the formation of the sp^2 hybridized boron based boronate ester linkage in BPDA-COF.[14] The solid-state ^{11}B NMR spectrums of the linker BPDA, BPDA-2 and BPBA-4 are also measured, which showed signals at 19.51, 15.70 and 17.13 ppm, respectively. For reference, the reported solid-state ^{11}B NMR signal of phenylboronic acid locates at 24.2 ppm.[15]

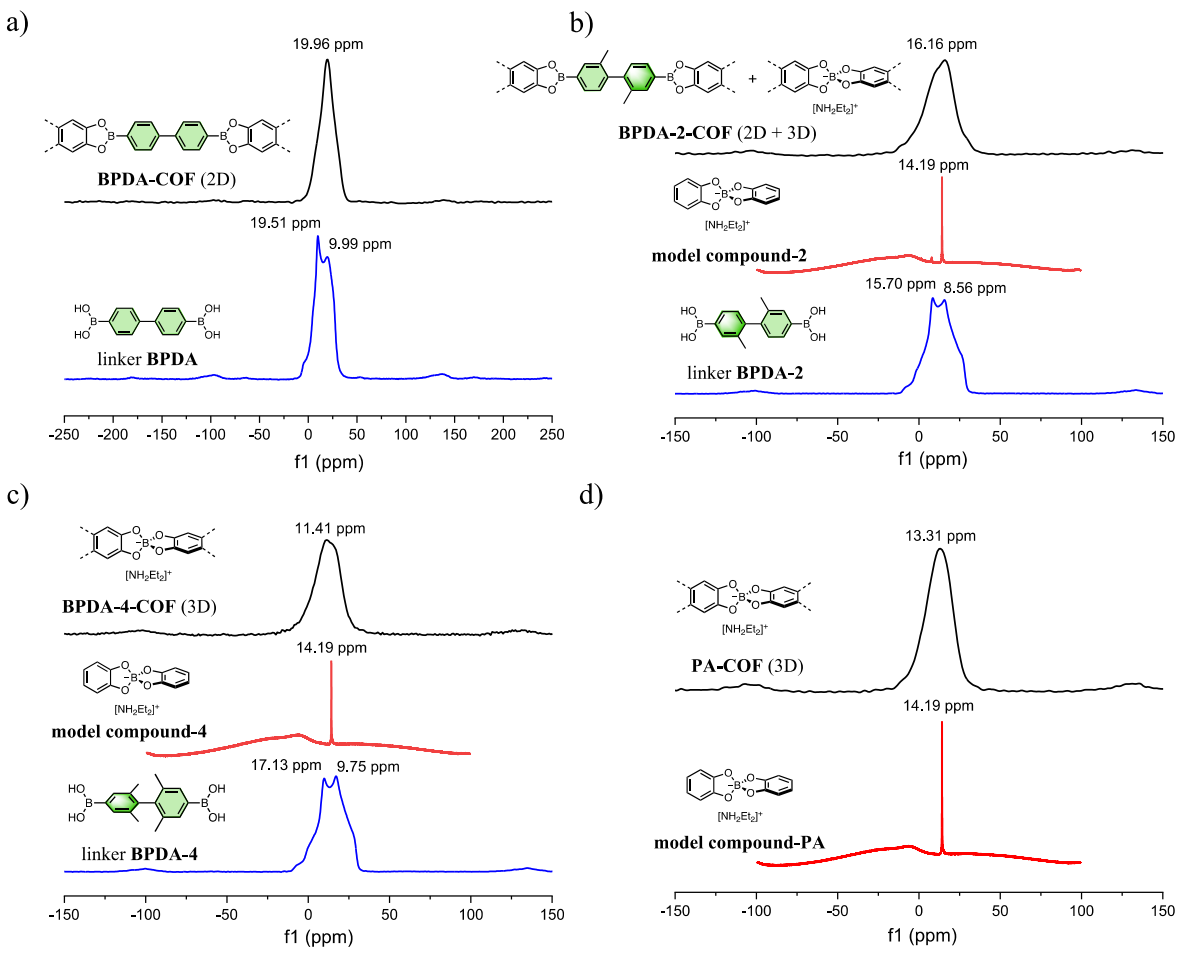

Figure 3.56. Solid-state ^{11}B MAS NMR spectrum comparison with ^{11}B solution NMR spectrum between (a) **BPDA-COF** (black, solid-state) and linker **BPDA** (blue, solid-state); (b) **BPDA-2-COF** (black, solid-state), **isolated model compound-2** (red, solution state) and linker **BPDA-2** (blue, solid-state); (c) **BPDA-4-COF** (black, solid-state), **isolated model compound-4** (red, solution state) and linker **BPDA-4** (blue, solid-state); (d) **PA-COF** (black, solid-state) and **isolated model compound-PA** (red, solution state). Supercritical CO_2 activated COF was used for the measurement. For reference, the reported solid-state ^{11}B NMR spectrum signal for 1,4-bis(benzodioxaborol-2-yl)benzene (CAS: 98494-81-6. an analogue of **model compound-0**) locates at 18.0 ppm.[14] The reported solid-state ^{11}B NMR spectrum signal for phenyl boronic acids locates at 24.2 ppm.[15]

3.4.4 Thermogravimetric analysis

Thermogravimetric analysis (TGA) of BPDA-COF showed the best thermal stability among the four COFs with only around 5% weight loss below 500 °C and another 30% weight loss when heated to 950 °C under a nitrogen atmosphere. BPDA-2-COF, BPDA-4-COF and PA-COF showed similar thermal stability, with around 30% weight loss at around 400 °C and another 20% weight loss when heated to 950 °C. By comparing the TGA curve between the 2D boronate ester-linked BPDA-COF and the other three COFs with ionic spiroborate linkage included, we can draw several conclusions: (1) the similar TGA curve of BPDA-2-COF, BPDA-4-COF and PA-COF can serve as another evidence to support their similar chemical and framework structure; (2) the weight loss below 200 °C in BPDA-2-COF, BPDA-4-COF and PA-COF can be attributed to loss of moisture (H_2O) and free DEF solvents (boiling point = 177 °C); (3) the extra weight loss (compared to the 2D BPDA-COF) between 200 ~ 400 °C in BPDA-2-COF, BPDA-4-COF and PA-COF are possibly from the decomposition of $[NH_2Et_2]^+$ during heating; (4) weight loss above 400 °C can be attributed to partial structure decompose.[16,17] All the measurements were done under a N_2 atmosphere.

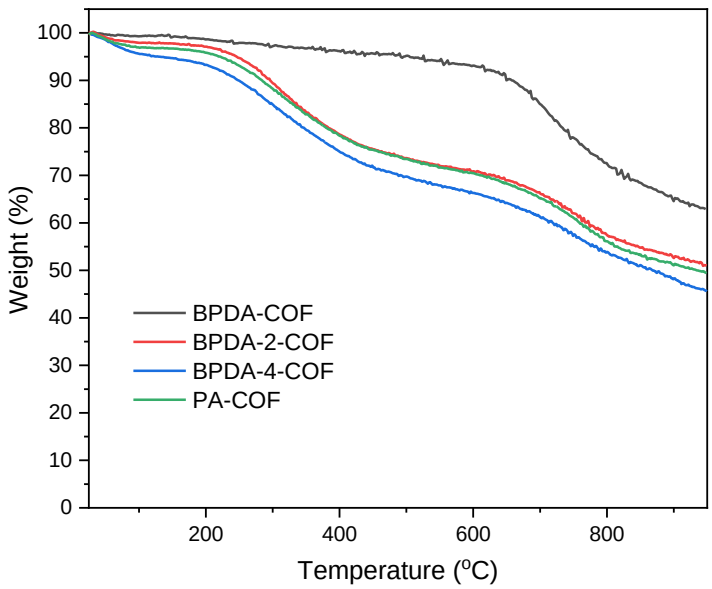

Figure 3.57. TGA curves of the four COFs in N_2 atmosphere.

3.4.5 Scanning electron microscopy images

Scanning electron microscopy (SEM) images of the four COFs are shown in **Figure 3.58-3.61**. The 2D BPDA-COF showed an overall sphere-like morphology with average size at around 2.0 μm, which formed from the aggregation of number of band-like structures (**Figure 3.58**). Considering the cubic unit cell of **nbo** topology, SEM images of the 3D BPDA-4-COF and PA-COF were supposed to show cube-like morphology. However, due to the small particle size at around 100 nm in the SEM images of BPDA-4-COF (**Figure 3.60**), no clear morphology can be identified, while the SEM images of PA-COF showed uniform cube-like morphology as we expected, with cube edge length at around 500 nm (**Figure 3.61**), though these cubes intergrown with each other. Two kinds of morphologies were identified from the SEM images of the mixed phase BPDA-2-COF in **Figure 3.59**, one is band-like structures with width at around 70 nm, the other one is uniform cubes with size varies from 250 nm to 400 nm. By comparing the SEM images of BPDA-2-COF with BPDA-COF and PA-COF, we suppose the band like structure corresponds to the 2D phase, while the cubes can be assigned to the 3D phase part. The 2D and 3D phase did not distribute evenly in BPDA-2-COF.

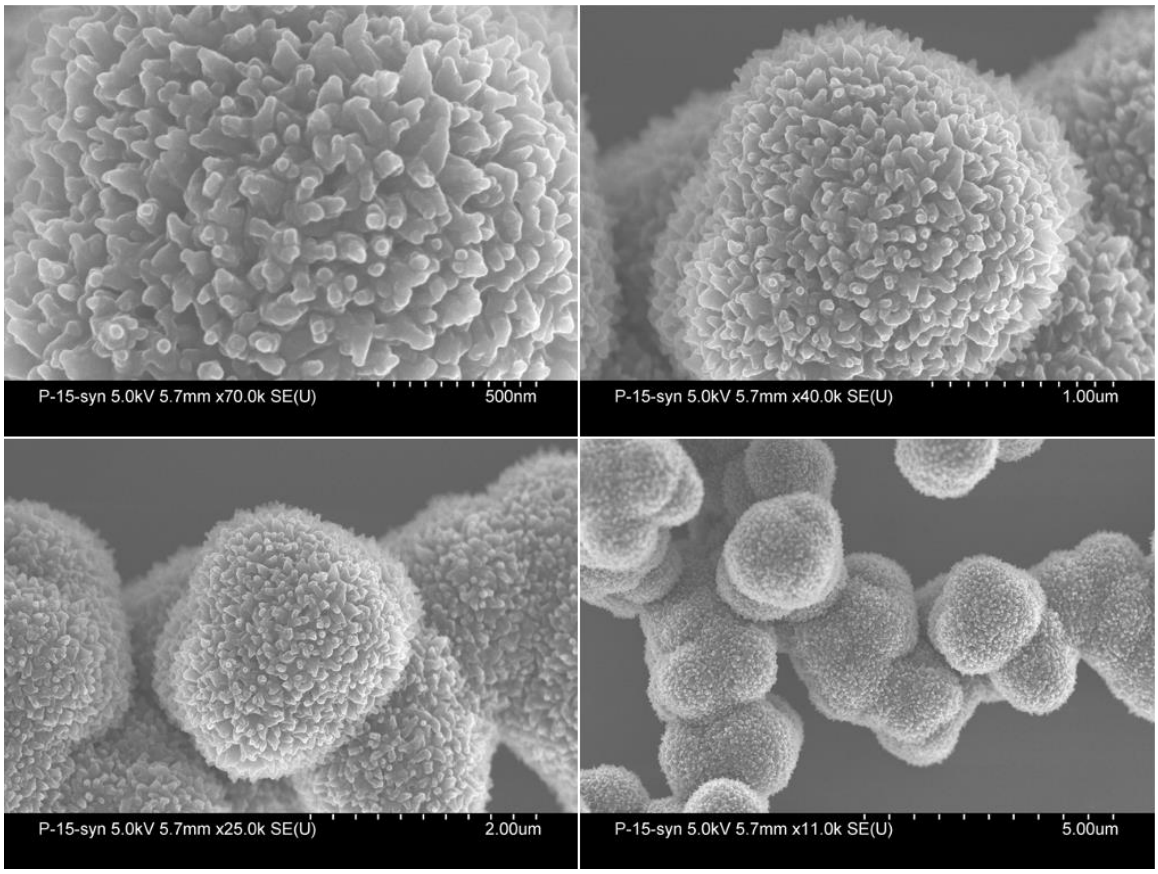

Figure 3.58. SEM images of **BPDA-COF**. As-synthesized COF materials was used for measurement.

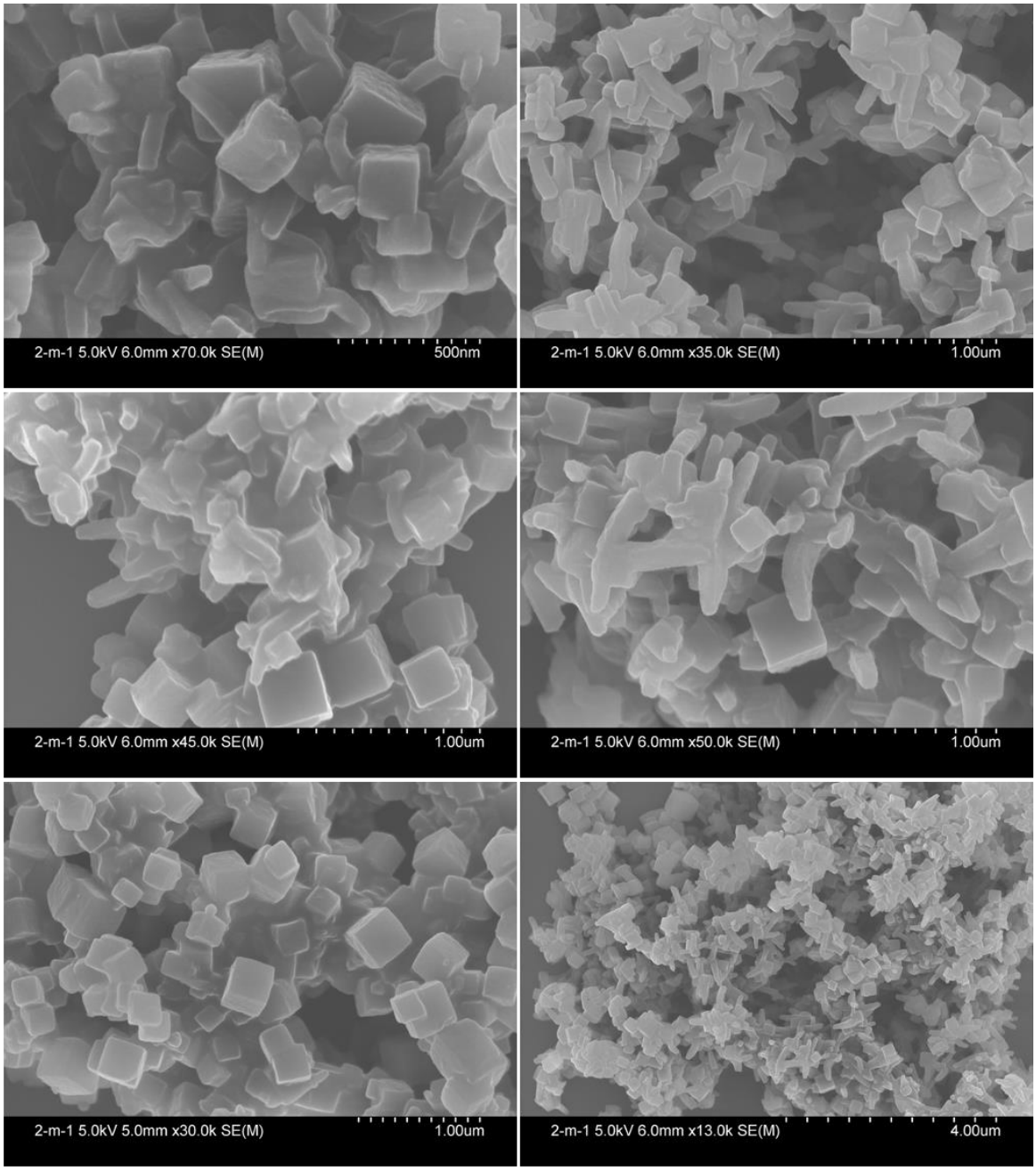

Figure 3.59. SEM images of **BPDA-2-COF**. As-synthesized COF materials was used for measurement.

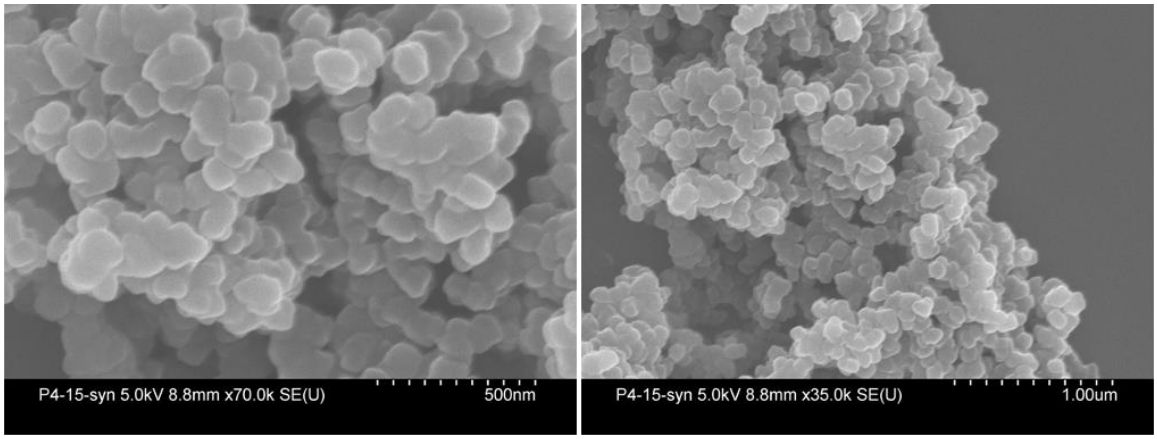

Figure 3.60. SEM images of **BPDA-4-COF**. As-synthesized COF materials was used for measurement.

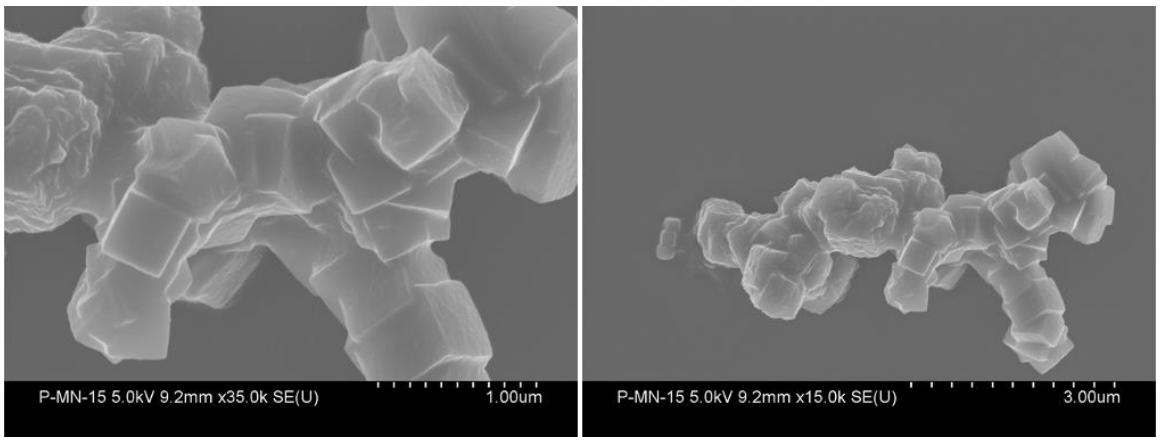

Figure 3.61. SEM images of **PA-COF**. As-synthesized COF materials was used for measurement.

3.4.6 Transmission electron microscopy images

The structure of the four COFs was further investigated by transmission electron microscopy (TEM) analysis. Ordered tetragonal pore structures could be observed in the TEM images of the 2D BPDA-COF in **Figure 3.62**, with identified d-spacing of 2.70 nm, corresponding to (100) plane, which represents the in-plane pore channels of 2.76 nm in the idealized AA-stacking COF model. **Figure 3.63** showed the TEM image of BPDA-2-COF. As can be seen, both the band-like and cube-like morphologies, which had been observed in the SEM images of BPDA-2-COFs can also be clearly identified from the TEM images. While the TEM image of the cube phase and its corresponding fast Fourier transform (FFT) (**Figure 3.63 (e)** and **(f)**) in BPDA-2-COF corroborated its spiroborate based 3D structure, with a d-spacing of 2.35 and 1.67 nm, corresponding to (110) and (200) plane of the spiroborate COF model, the identified d-spacing (2.35 nm) of the band like morphology also fits with the 3D phase rather than the 2D structure. We did not distinguish the 2D phase here. TEM images of BPDA-4-COF exhibited average particle size of 80 ~ 100 nm (**Figure 3.64**), however, due to its relatively poor crystallinity, no ordered domains or clear lattice can be found. TEM images of PA-COF were shown in **Figure 3.65**, as can be seen, PA-COF showed uniform cube like morphology with average cube edge size of ~500 nm. PA-COF showed highly ordered crystalline domains (area > 50 nm) with identified d-spacing of 1.75 nm, which can be attributed to the (200) planes in the spiroborate based 3D COF of **nbo** topology.

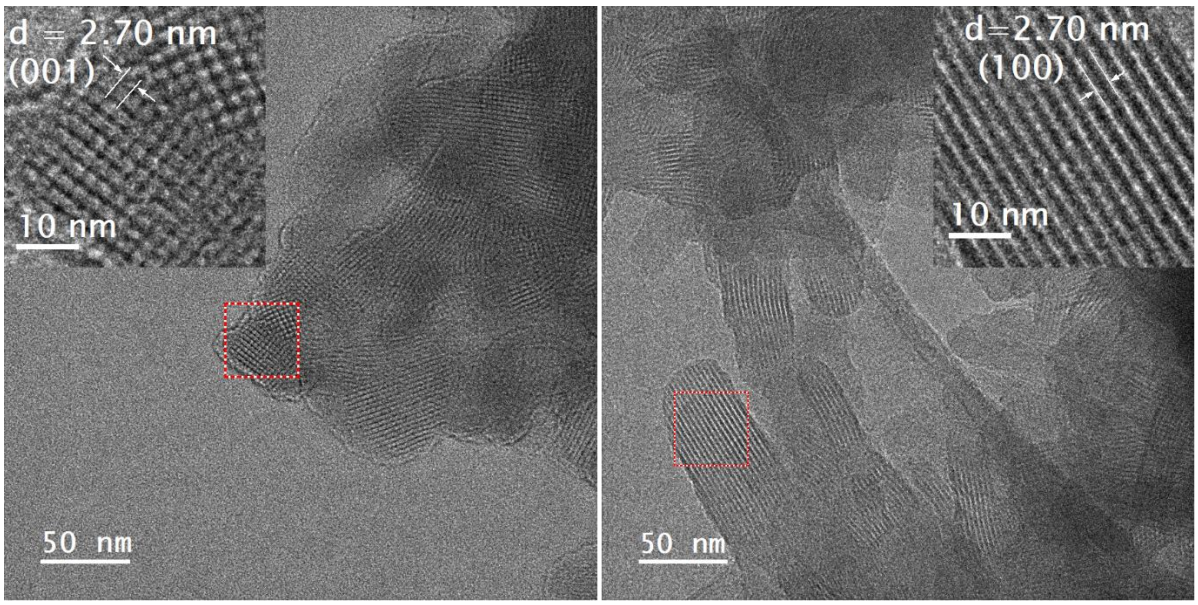

Figure 3.62. TEM images of **BPDA-COF**. As-synthesized COF materials was used for measurement.

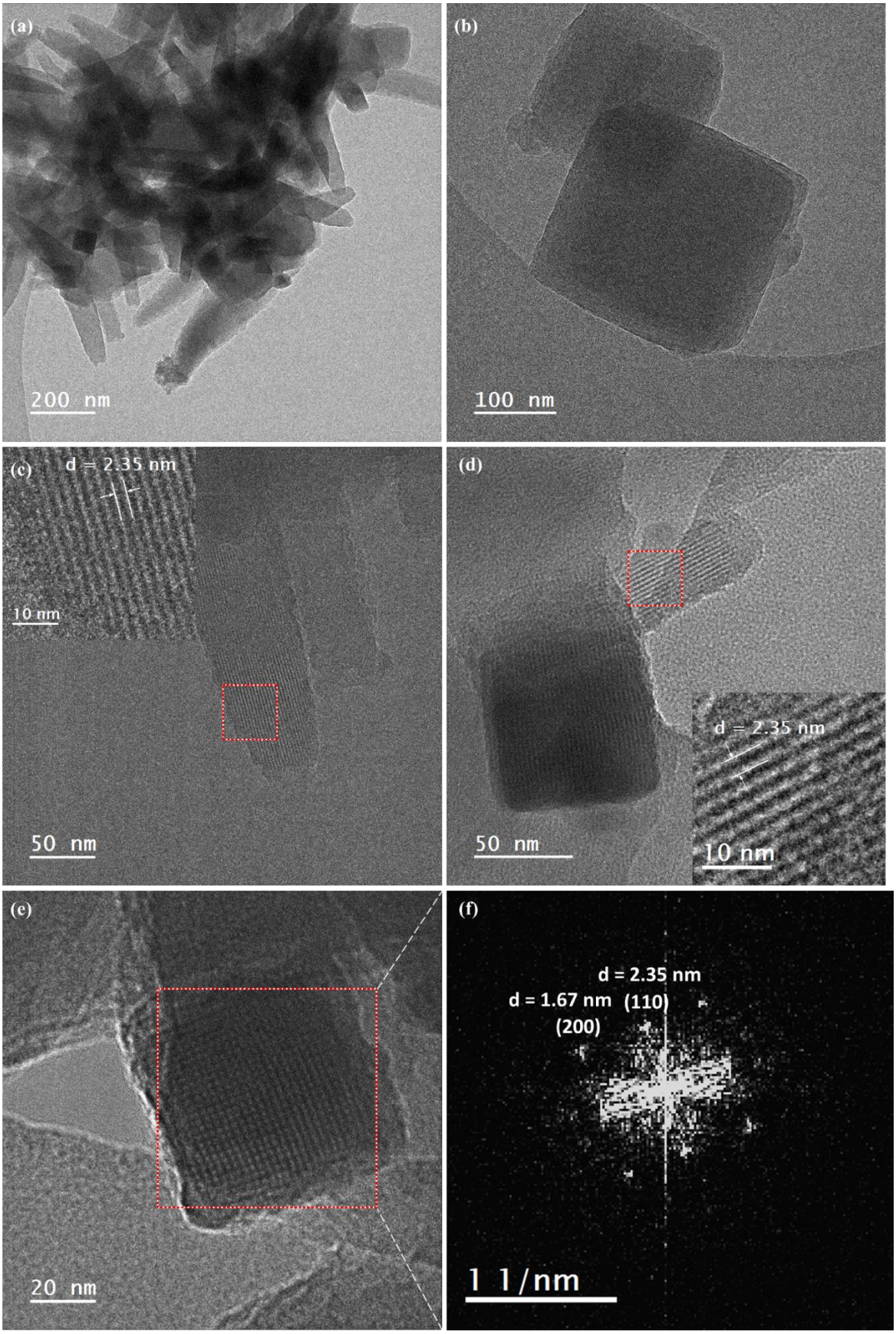

Figure 3.63. TEM images of **BPDA-2-COF**. (f) shows the fast Fourier transform (FFT) of the selected area in (e). As-synthesized COF materials was used for measurement.

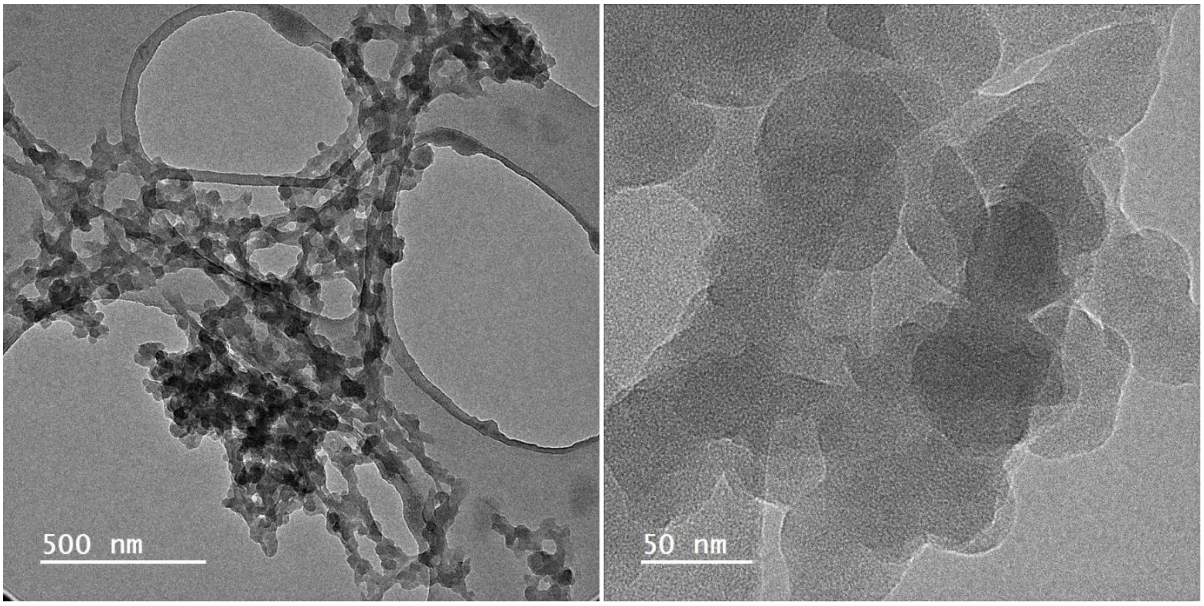

Figure 3.64. TEM images of **BPDA-4-COF**. As-synthesized COF materials was used for measurement.

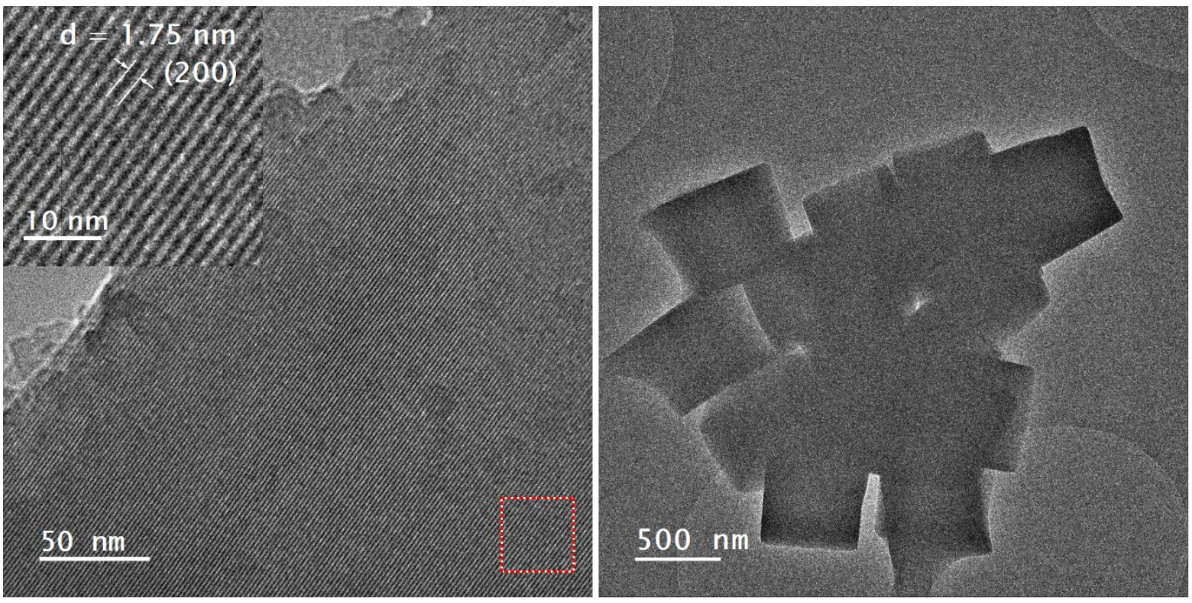

Figure 3.65. TEM images of **PA-COF**. As-synthesized COF materials was used for measurement.

3.4.7 Gas sorption isotherms

The porosity of the four COFs was evaluated by nitrogen sorption measurements at 77 K (**Figure 3.66-3.69**). All COFs gave type IV sorption isotherm with shapes consistent with mesoporosity and sequential, multilayer pore filling. The Brunauer− Emmett−Teller (BET) surface areas of BPDA-COF, BPDA-2-COF, BPDA-4-COF and PA-COF were found to be 1371, 1307, 1246 and 1282 m^2 g^{-1}, respectively, after supercritical CO_2 activation ($scCO_2$). The measured surface area of the 2D BPDA-COF equates to 89% of the calculated nitrogen-accessible surface area (1546 m^2 g^{-1}) for the idealized, AA-stacking COF model. For comparison, BET surface area of the reported 2D BPDA-COF is 1087 m^2 g^{-1}, which is synthesised from a mixed solvent of dimethylacetamide (DMAc) : 1,2-dichlorobenzene (o-DCB) = 2:1 (v : v) at 120 °C for 3 days.[5] The higher BET surface area in our case can be attributed to $scCO_2$ activation.[18] The theoretical surface area calculated for BPDA-2-COF is 1689 m^2 g^{-1} and 5469 m^2 g^{-1}, corresponding to the idealized AA-stacking 2D phase and 3D phase, respectively. As for the 3D phase, here, we used the fully optimized spiroborate based COF model with Li^+ as counter cations for the theoretical surface area calculation, since the small Li^+ was expected to bring the minimum influence toward the simulated PXRD pattern, single crystal structure of the model compound is not strong enough to help us accurately allocate the position of $[NH_2Et_2]^+$ cations within COFs. The low experimental BET surface area of BPDA-2-COF, BPDA-4-COF and PA-COF compared to the calculated value can be attributed to three reasons: Firstly, the size of the $[NH_2Et_2]^+$ counter cation (van der Waals radius, shortest =365 pm, longest = 540 pm) is larger than Li^+ (van der Waals radius = 182 pm), which was used for COF model built and for theoretical surface are calculation. Secondly, there was still trace amount of DEF solvent left in COFs after $scCO_2$ activation, as can be evidenced by FT-IR spectra of COFs. Finally, partial structural collapse after activation can be observed as indicated by PXRD (**Figure 3.67d**, **3.68d and 3.69d**). Theoretical surface areas were calculated by zeo++[19] with N_2 as the probe molecule, using a probe radius of 182 pm.

The pore diameters derived for BPDA-COF, BPDA-2-COF, BPDA-4-COF and PA-COF by fitting nonlocal-density functional theory (NL-DFT) models to the N_2 isotherms were mainly located at 2.31, 3.10, 3.02 and 3.10 nm, respectively. These values are in good agreement with the pore size shown in the 2D and 3D phase COF models, which showed tetragonal or cube-shaped pores with diameters of 2.3 and 3.4 nm, respectively. The small shoulder peaks in the pore size distribution (PSD) profile of BPDA-COF and BPDA-4-COF can be attributed to the relatively lower crystallinity, similar results were observed in several other COFs reported.[20,21,22] The PSD profile of the mixed phased BPDA-2-COF showed a single peak at 3.10 nm, corresponding to the pore size of 3D phase, no peaks belonging to 2D phase can be distinguished.

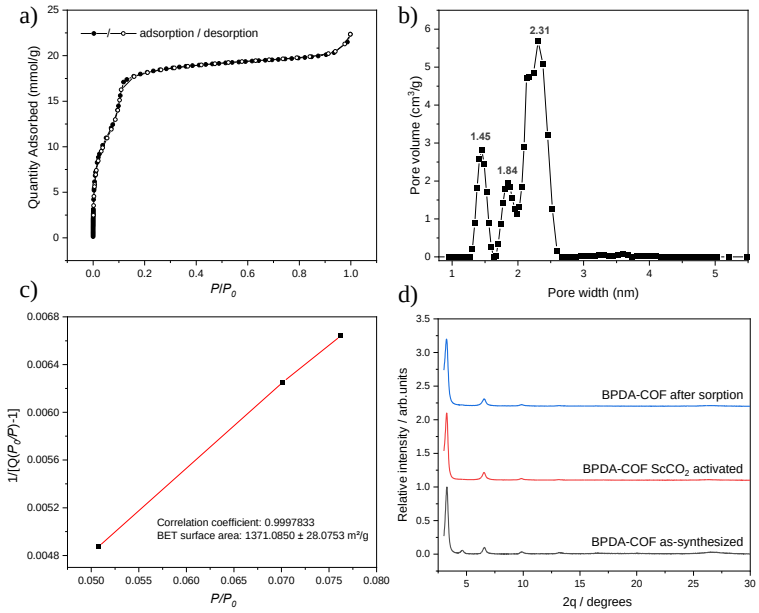

Figure 3.66. (a) Nitrogen adsorption/desorption isotherms for **BPDA-COF** recorded at 77 K. (b) Pore size distribution profiles of **BPDA-COF** calculated by NL-DFT. (c) BET surface area plot for **BPDA-COF**. The x axis range was selected from P/P_0 = 0.05~0.3 to satisfy both a correlation coefficient > 0.995 and a positive C value. (d) PXRD comparison of **BPDA-COF**, as synthesized, after $scCO_2$ activation and after sorption test. We used $scCO_2$ activated samples for sorption measurements.

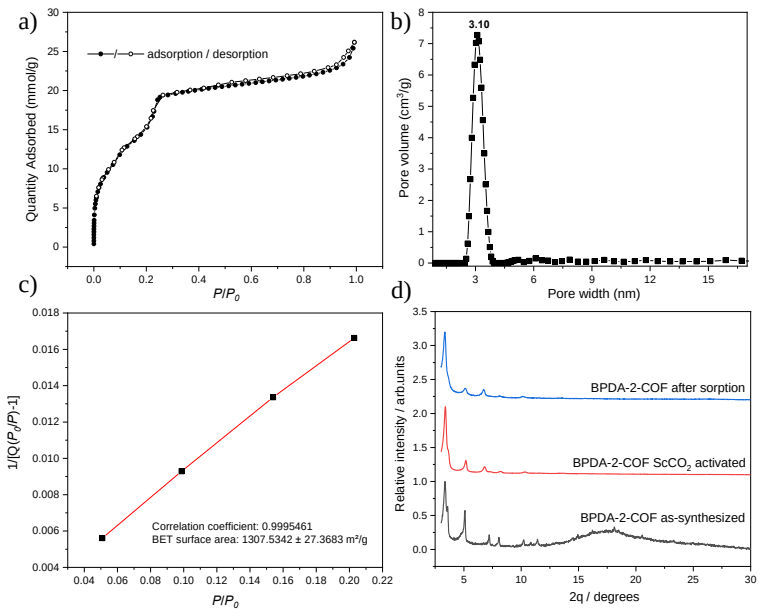

Figure 3.67. (a) Nitrogen adsorption/desorption isotherms for **BPDA-2-COF** recorded at 77 K. (b) Pore size distribution profiles of **BPDA-2-COF** calculated by NL-DFT. (c) BET surface area plot for **BPDA-2-COF**. The x axis range was selected from P/P_0 = 0.05~0.3 to satisfy both a correlation coefficient > 0.995 and a positive C value. (d) PXRD comparison of **BPDA-2-COF**, as synthesized, after $scCO_2$ activation and after sorption test. We used $scCO_2$ activated samples for sorption measurements.

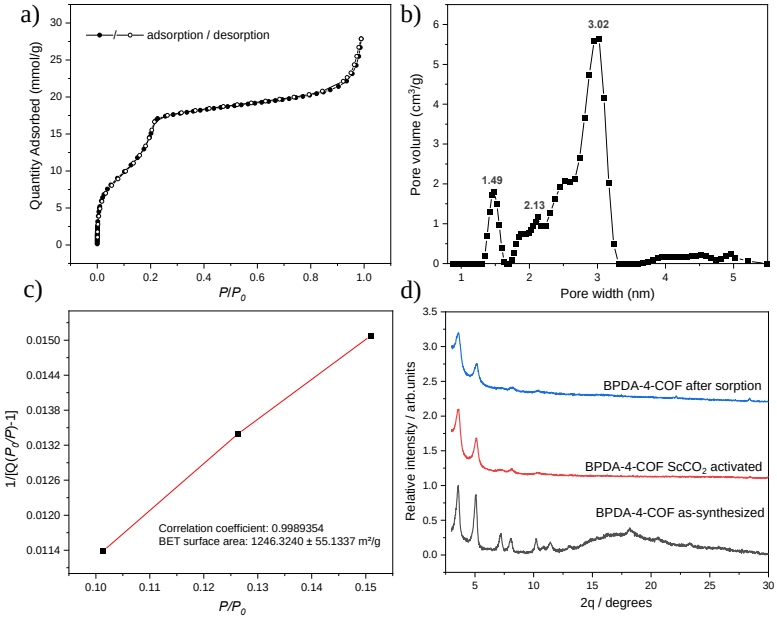

Figure 3.68. (a) Nitrogen adsorption/desorption isotherms for **BPDA-4-COF** recorded at 77 K. (b) Pore size distribution profiles of **BPDA-4-COF** calculated by NL-DFT. (c) BET surface area plot for **BPDA-4-COF**. The x axis range was selected from P/P_0 = 0.05~0.3 to satisfy both a correlation coefficient > 0.995 and a positive C value. (d) PXRD comparison of **BPDA-4-COF**, as synthesized, after $scCO_2$ activation and after sorption test. We used $scCO_2$ activated samples for sorption measurements.

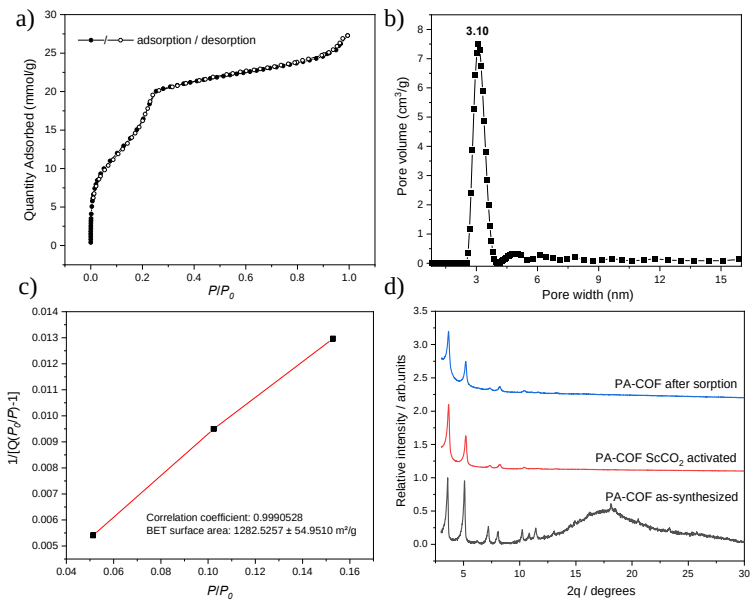

Figure 3.69. (a) Nitrogen adsorption/desorption isotherms for **PA-COF** recorded at 77 K. (b) Pore size distribution profiles of **PA-COF** calculated by NL-DFT. (c) BET surface area plot for **PA-COF**. The x axis range was selected from P/P_0 = 0.05~0.3 to satisfy both a correlation coefficient > 0.995 and a positive C value. (d) PXRD comparison of **PA-COF**, as synthesized, after $scCO_2$ activation and after sorption test. We used $scCO_2$ activated samples for sorption measurements.

3.5 Conclusion

For this work, our initial plan was to develop a second strategy for constructing 3D COFs of **nbo** topology with a neutral boronate ester linkage, aiming for larger porosity (5.5 nm *vs.* 3.7 nm) and higher BET surface area compared with the SPB-COFs based-on spiroborate linkage in the last chapter. Based on the strategy used for the preparation of the first **nbo** MOF (MOF-601),[3] we designed and synthesized two new diboronic acid linkers, named BPDA-2 and BPDA-4, by introducing two or four methyl group substitutions at the 2,2' or 2,2',6,6' position of the planar 1,4-biphenyldiboronic acid (linker BPDA). We expected to realize 3D boronate ester linked COFs of **nbo** topology from the reaction between the square $(OH)_8$PcCo and linker BPDA-2 and BPDA-4. However, the result turned out to be different from our expectations.

Under the synthesis condition we applied, the reaction between $(OH)_8$PcCo and the near planar linker BPDA afforded a 2D COF with boronate ester linkage, while reacting $(OH)_8$PcCo with linker BPDA-4 yielded 3D BPDA-4-COF of **nbo** topology but with an unexpected spiroborate linkage. The reaction between $(OH)_8$PcCo and linker BPDA-2 gave BPDA-2-COF of a mixed phase of boronate ester-linked 2D structure and spiroborate linked 3D structure. Model compounds prepared under COF synthesis conditions confirmed the formation of the spiroborate linkage in BPDA-2-COF and BPDA-4-COF. We proposed that the formation of sp^3 hybridized boron-based spiroborate linkages in BPDA-2-COF and BPDA-4-COF were related to the geometry of the linear diboronic acid linkers. We also proposed a possible reaction mechanism based on a related reported work.[9,10] Based on this mechanism, we successfully prepared a spiroborate-linked 3D COF of **nbo** topology using phenylboronic acid to replace the diboronic acid linkers for the formation of PA-COF. Moreover, the model compound single crystal structure of this reaction system confirmed its spiroborate linkage and the $[NH_2Et_2]^+$ counter cation. All COF structures were characterized by FT-IR, solid-state ^{13}C CP MAS and ^{11}B MAS NMR. The crystal structure of the 2D BPDA-COF and 3D PA-COF was confirmed by the well-resolved TEM images. The 2D BPDA-COF showed an experimental BET surface area of 1371 $m^2\ g^{-1}$, while the measured surface area for BPDA-2-COF, BPDA-4-COF and PA-COF were 1307, 1246 and 1282 $m^2\ g^{-1}$, respectively. The low BET surface area of the latter three COFs can be attributed to the not fully activated structure (FT-IR detected DEF residue in the activated COFs) and partial structure collapse during $scCO_2$ activation.

3.6 Materials and methods

All reagents were obtained from Sigma-Aldrich, Manchester Organics, or TCI Europe. Anhydrous solvents were purchased from Sigma-Aldrich, Acros Organics or Fisher Scientific. All chemicals were used without further purification. All gases for sorption analysis were supplied by BOC at a purity of ≥99.9%. Reactions were carried out under nitrogen atmosphere using standard Schlenk techniques.

3.6.1 Solution nuclear magnetic resonance

NMR spectra were recorded on a Bruker Avance 400 NMR spectrometer, operating at frequencies of 400 MHz (^{1}H) and 100 MHz (^{13}C) and referenced against the residual ^{1}H or ^{13}C signal of the solvent. ^{11}B spectra operating at 128MHz using deuterium lock for referencing.

3.6.2 Solid-state ^{13}C CP MAS and ^{11}B MAS nuclear magnetic resonance

Solid-state NMR experiments were performed on a Bruker Avance III HD spectrometer using the Durham University (UK) solid-state NMR service. Carbon-13 magic-angle spinning measurements were carried out at 100.63 MHz using a Bruker Avance III HD spectrometer and 4 mm (rotor o.d.) probe. Spectra were acquired at a spin rate of 10 kHz. Cross-polarisation (CP) spectra were recorded with TOSS spinning sideband suppression, 0.8 ms contact time and with a recycle delay of 1 s. Carbon spectral referencing is relative to neat tetramethylsilane, carried out by setting the high-frequency signal from an external sample of adamantane to 38.5 ppm. 50 Hz of line broadening was added to improve the signal to noise. Boron-11 magic-angle spinning measurements were carried out at 128.39 MHz using a Bruker Avance III HD spectrometer and 4 mm (rotor o.d.) probe. Spectra were acquired at a spin rate of 20 kHz. All direct excitation ^{11}B spectra were acquired with a 1 us 30-degree solid pulse which was determined from a 6 us solution pulse determined on BF_3/OEt_2. The spectra were acquired with a recycle delay of 1 s determined on the sample. Boron spectral referencing is relative to BF_3/OEt_2. Since the probe used has a boron background, a spectrum of an empty rotor was collected, and this was subtracted from all spectra.

3.6.3 Mass spectrometry

High resolution mass spectrometry (HR-MS) as performed on an Agilent Technologies 6530B accurate- mass QTOF mixed ESI/APCI mass spectrometer (capillary voltage 4000 V, fragmentor 225 V) in positive- ion detection mode. Matrix-assisted laser desorption ionization time-of-flight

mass (MALDI-TOF MS) spectra were recorded on an Applied Biosystems BioSpectrometry model Voyager-DE-STR spectrometer in reflector or linear mode.

3.6.4 Elemental analysis

CHN analysis was performed on a Thermo EA1112 Flash CHNS-O Analyzer using standard microanalytical procedures.

3.6.5 Inductively coupled plasma optical emission spectrometry

Inductively coupled plasma optical emission spectrometry (ICP-OES) measurements were conducted on an ICP-OES Agilent 5110. Samples were digested in concentrated nitric acid (67-69%, trace metal analysis grade) by microwave, and then diluted using distilled water.

3.6.6 Powder X-ray diffraction

Laboratory powder X-ray diffraction (PXRD) data patterns were collected in transmission mode on samples held on thin Mylar film in aluminium well plates on a Panalytical Empyrean diffractometer equipped with a high throughput screening (HTS) XYZ stage, X-ray focusing mirror, and PIXcel detector, using Cu-Kα radiation, λ = 1.54184 Å. For HT screening, PXRD patterns were measured over the 2θ range 1-56° in 0.013° steps over 30 minutes.

3.6.7 Single crystal X-ray diffraction

Single crystal X-ray data for the model compounds were measured on a Rigaku MicroMax-007 HF rotating anode diffractometer (Mo-Kα radiation, λ = 0.71073 Å, Kappa 4-circle goniometer, Rigaku Saturn724+ detector), and data reduction was performed using CrysAlisPro. Structures were solved with SHELXL[23]and refined by full-matrix least squares on $|F|^2$ by SHELXL,[24] interfaced through the programme OLEX2.[25] All non- H atoms were refined anisotropically. H atoms bonded to C atoms were fixed in geometrically estimated positions and refined using the riding model. H atoms bonded to N atoms were located in the different maps and refined isotropically. For full refinement details, see **Tables 3.1**.

3.6.8 Fourier-transform infrared spectroscopy

Attenuated total reflection (ATR)-FT-IR spectra were obtained with an ATR method on a Bruker Tensor-27 spectrometer at room temperature.

3.6.9 Thermogravimetric analysis

TGA analysis was carried out using a TA Q5000IR analyzer with an automated vertical overhead thermobalance. Samples were heated at a rate of 10 °C/min under a dry nitrogen gas flow.

3.6.10 Scanning electron microscopy

SEM images were recorded using a Hitachi S-4800 cold field emission scanning electron microscope (FE- SEM). Samples were prepared by depositing the dry powders on a silicon disk and then coating the samples with Chromium using an Emitech K550X automated sputter coater.

3.6.11 Transmission electron microscopy

TEM images were obtained using a JEOL 2100+ microscope operating at 200KV equipped with a Gatan Rio Camera. Since COF materials are electron beam sensitive, the electron beam damage to the specimen was minimized as much as possible. A single HR-TEM image was recorded with an exposure time of 2 seconds. After drift compensation, some frames can be superimposed to increase the signal-to-noise (SN) ratio.

COF crystals were dispersed in anhydrous acetone by ultrasonication and drop-cast on a holey carbon film on 200 mesh copper grids.

3.6.12 Gas sorption analysis

Surface areas were measured by nitrogen sorption at 77.3 K. Powder samples were degassed offline at room temperature, followed by degassing on the analysis port under vacuum at room temperature for 12 hours. Isotherms were measured using a Micromeritics 2020 volumetric adsorption analyzer. Surface areas were calculated from a selected range within the relative pressure (P/P_0) range from 0.05 to 0.30 of the adsorption branch, to satisfy both a correlation coefficient > 0.995 and a positive C value.

3.6.13 COFs structure modelling

As is discussed in the introduction part of this chapter, we suppose the reaction between $(OH)_8$PcCo and linker BPDA will give 2D BPDA-COF with **sql** topology, while the reaction between $(OH)_8$PcCo and linker BPDA-2 and BPDA-4 will give 3D COFs of **nbo** topology, both based-on boronate ester linkage. As the torsion angle of the linker BPDA-2 (60~90º) is between the value of

linker BPDA (0~15º) and linker BPDA-4 (85~90º) (**Figure 3.49**), we constructed 2D COF models with **sql** topology for BPDA-COF and BPDA-2-COF, and 3D COF models with **nbo** topology for BPDA-2-COF and BPDA-4-COF, based-on boronate ester linkage. Moreover, as the interpenetration issue has to be considered in 3D COFs, especially under our situation here, where the 3D COFs of boronate ester linkage has a large pore volume of 5.5 × 5.5 × 5.5 nm^3. Considering this, we constructed 3D COF models for the 3D phase BPDA-2-COF and BPDA-4-COF, with interpenetration level up to five-fold to check the interpenetration in COFs. All these COF models are constructed using zeo++ code[26] and Material Studio software, the obtained COF models were optimized using the Universal force field, implemented in the Forcite module of the BIOVIA Materials Studio software. PXRD based on these models were simulated and compared with the experimental PXRD pattern to find the best fit for COF structure determination.

However, the experimental and simulated PXRD comparison results showed that while the BPDA-COF is of 2D **sql** topology and with a borate ester linkage, BPDA-4-COF exhibited an experimental PXRD pattern can fit well with the spiroborate model in chapter 2. Experimental PXRD pattern of BPDA-2-COF showed a mixed phase of 2D (boronate ester-linked) and 3D (spiroborate-linked) (**Figure 3.36**). Moreover, the possibility of forming the interpenetrated 3D COFs (based-on boronate ester linkage) was also examined using the proposed 3D BPDA-4-COF with up to five-fold interpenetration, none of the simulated PXRD pattern based-on these interpenetrated models can fit with the experimental PXRD pattern of BPDA-4-COF (**Figure 3.38-3.39**). Later studies on the model compound system and the formation of the 3D PA-COF corroborated the formation of spiroborate linkage in BPDA-2-COF and BPDA-4-COF.

To illustrate these structures more clearly, **Figure 3.70** shows a comparison between the 2D **sql** and 3D **nbo** topology; **Figure 3.71** showed a structure comparison between the 2D BPDA-COF and the 2D phase in BPDA-2-COF; **Figure 3.72** summarized a structure comparison between the proposed 3D BPDA-4-COF with non-interpenetrated **nbo** topology, based-on boronate ester linkage (this structure is our initially expected structure but was not realized experimentally in this chapter), and the 3D spiroborate-linked COF models adopted from chapter 2.

Structure accuracy of the optimized COF models was checked by comparing the average C-C bond length in the benzene rings. Results are summarized in **Figure 3.71(e)(f)** and **Figure 3.72(e)(f)**, all in good agreement with the reported value ≈ 1.4 Å.[27]

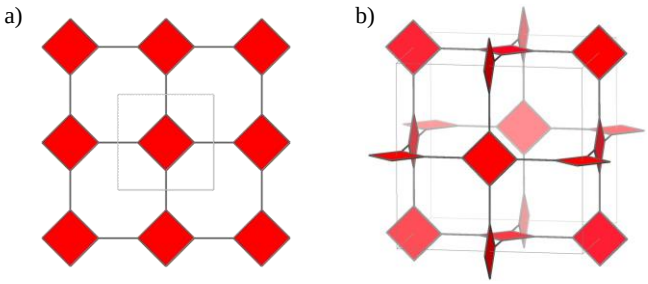

Figure 3.70. Graph representation of the (a) 2D **sql** topology; (b) 3D **nbo** topology. All topologies are shown as their corresponding augmented net. The gray lines indicate the unit cells. In the 2D **sql** topology, each two neighbouring square units are co-planar, while in the 3D **nbo** topology, each two neighbouring square units are of perpendicular orientation.

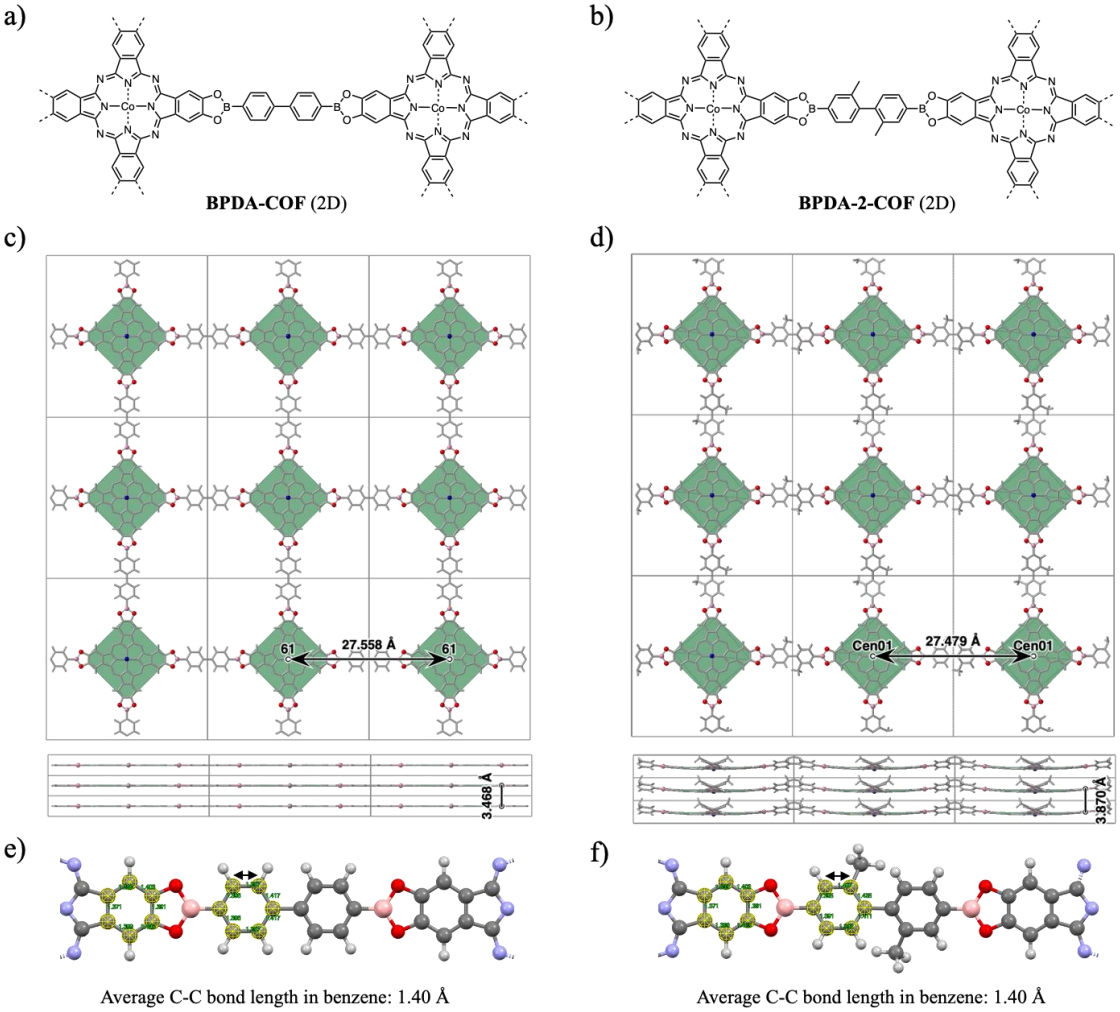

Figure 3.71. (a)(b) ChemDraw structure; (c)(d) Structure model representation from two view directions, with unit cell parameters marked, and (e)(f) COF model structure accuracy checking through the average C-C bond length in the benzene rings of the 2D **BPDA-COF** and the 2D phase **BPDA-2-COF** based-on boronate ester linkage. Pink, blue and red atoms represent boron, cobalt and oxygen, respectively; gray lines indicate the unit cell; the green square represents the PcCo unit.

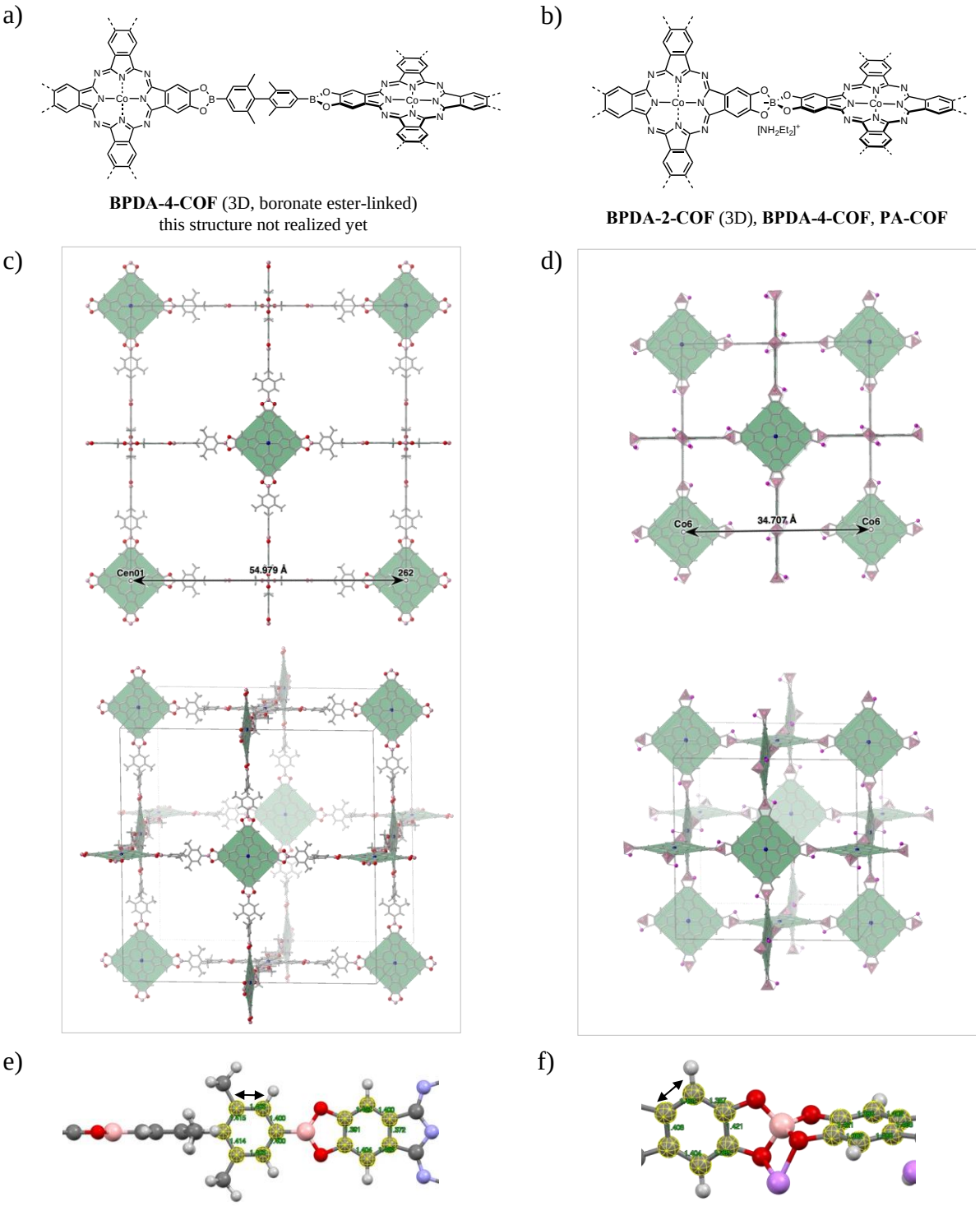

Figure 3.72. (a)(b) ChemDraw structure; (c)(d) Structure model representation from two view directions, with unit cell parameters marked, and (e)(f) COF model structure accuracy checking through the average C-C bond length in the benzene rings of the 3D phase **BPDA-4-COF** based on boronate ester linkage (this structure was not realized experimentally here) and the 3D COF based-on spiroborate linkage (including the 3D phase **BPDA-2-COF**, **BPDA-4-COF** and **PA-COF**). Pink, blue and red atoms represent boron, cobalt and oxygen, respectively; gray lines indicate the unit cell; the green square represents the PcCo unit.

3.7 Atomic coordinates of the fitted COF models

Fractional atomic coordinates and unit cell parameters of the 2D BPDA-COF model of **sql** topology, in AA stacking mode.

Name: 2D **BPDA-COF** model of **sql** topology				
Space Group: P4/MMM (No.123) a=b= 27.5581 (Å), c= 3.4684 (Å), α=β=γ= 90°				
Atom Name	**x**	**y**	**z**	**Occupancy**
H	0.69377	0.40885	0.50000	1.00
C	0.65099	0.47513	0.50000	1.00
C	0.60030	0.46078	0.50000	1.00
C	0.69395	0.44809	0.50000	1.00
C	0.73731	0.47477	0.50000	1.00
O	0.78362	0.45536	0.50000	1.00
C	0.89485	0.45630	0.50000	1.00
C	0.94554	0.45619	0.50000	1.00
H	0.87575	0.42192	0.50000	1.00
H	0.03755	0.42104	0.50000	1.00
N	0.58566	0.41434	0.50000	1.00
N	0.57047	0.50000	0.50000	1.00
B	0.81254	0.50000	0.50000	1.00
C	0.86924	0.50000	0.50000	1.00
C	0.97248	0.50000	0.50000	1.00
Co	0.50000	0.50000	0.50000	1.00

Fractional atomic coordinates and unit cell parameters of the 2D BPDA-2-COF model of **sql** topology, in AA stacking mode.

Name: 2D **BPDA-2-COF** model of **sql** topology				
Space Group: P4/MMM (No.123) a=b= 27.5581 (Å), c= 3.4684 (Å), α=β=γ= 90°				
Atom Name	**x**	**y**	**z**	**Occupancy**
H	0.69790	0.40655	0.52222	1.00
C	0.65257	0.47415	0.52222	1.00
C	0.60314	0.46109	0.52222	1.00
C	0.69682	0.44642	0.52222	1.00
C	0.73963	0.47530	0.52222	1.00
O	0.78500	0.45875	0.52222	1.00
C	0.89222	0.45491	0.59893	1.00
C	0.94613	0.45491	0.59893	1.00
H	0.87227	0.42154	0.65570	1.00
C	0.97312	0.40984	0.67560	1.00
H	0.30210	0.40655	0.52222	1.00
C	0.34743	0.47415	0.52222	1.00
C	0.39686	0.46109	0.52222	1.00
C	0.30318	0.44642	0.52222	1.00

C	0.26037	0.47530	0.52222	1.00
O	0.21500	0.45875	0.52222	1.00
C	0.10778	0.45491	0.44554	1.00
C	0.05387	0.45491	0.44554	1.00
H	0.12773	0.42154	0.38877	1.00
H	0.03389	0.42154	0.38877	1.00
N	0.58603	0.41397	0.52222	1.00
N	0.57748	0.50002	0.52222	1.00
B	0.81360	0.50002	0.52222	1.00
C	0.86530	0.50002	0.52221	1.00
C	0.97308	0.50002	0.52221	1.00
H	0.97977	1.38894	0.46383	1.00
H	0.95155	1.38782	0.83659	1.00
H	1.00798	1.41931	0.78326	1.00
Co	0.50000	0.50000	0.52222	1.00

Fractional atomic coordinates and unit cell parameters of the 3D non-interpenetrated SPB-based COF model (Li^+ as counter cation) with **nbo** topology.

Name: 3D non-interpenetrated SPB-COF model (Li^+ as counter cation) of **nbo** topology				
Space Group: R-3 (No.148) a=b=c= 34.7072 (Å), α=β=γ= 89.6530°				
Atom Name	**x**	**y**	**z**	**Occupancy**
C	-0.01979	-0.11888	0.49952	1.00
C	-0.96773	-0.07885	0.49855	1.00
C	-0.15300	-0.95743	0.50240	1.00
C	-0.18684	-0.97851	0.50203	1.00
C	-0.52064	-0.61873	-0.00133	1.00
C	-0.46820	-0.57913	-0.00074	1.00
C	-0.65297	-0.45671	-0.00134	1.00
C	-0.68678	-0.47785	-0.00186	1.00
C	-0.97923	-0.11896	0.49841	1.00
C	-0.03178	-0.07884	0.49985	1.00
C	-0.84690	-0.95869	0.50000	1.00
C	-0.81352	-0.98059	0.49951	1.00
C	-0.48008	-0.61902	-0.00120	1.00
C	-0.53225	-0.57851	-0.00088	1.00
C	-0.34696	-0.45933	0.00081	1.00
C	-0.31358	-0.48121	0.00129	1.00
C	-0.11886	-0.01995	0.50067	1.00
C	-0.07891	-0.96785	0.50154	1.00
C	-0.95721	-0.15293	0.49718	1.00
C	-0.97827	-0.18678	0.49729	1.00
C	-0.61888	-0.51921	-0.00048	1.00
C	-0.57878	-0.46722	-0.00010	1.00
C	-0.45856	-0.65341	-0.00134	1.00
C	-0.48036	-0.68658	-0.00150	1.00
C	-0.11900	-0.97941	0.50159	1.00

C	-0.07880	-0.03189	0.50049	1.00
C	-0.95888	-0.84684	0.50001	1.00
C	-0.98082	-0.81350	0.50091	1.00
C	-0.61893	-0.47865	-0.00055	1.00
C	-0.57891	-0.53127	-0.00033	1.00
C	-0.45750	-0.34746	0.00180	1.00
C	-0.47870	-0.31344	0.00192	1.00
O	-0.96764	-0.77593	0.50000	1.00
O	-0.46478	-0.27696	0.00239	1.00
O	-0.03576	-0.77664	0.50410	1.00
O	-0.53297	-0.27576	0.00094	1.00
O	-0.77596	-0.96740	0.50079	1.00
O	-0.27606	-0.46794	0.00104	1.00
O	-0.77656	-0.03550	0.49714	1.00
O	-0.27659	-0.53615	0.00285	1.00
H	-0.92750	-0.84685	0.49932	1.00
H	-0.42614	-0.34790	0.00211	1.00
H	-0.07413	-0.84729	0.50395	1.00
H	-0.57283	-0.34645	0.00162	1.00
H	-0.84698	-0.92730	0.50061	1.00
H	-0.34716	-0.42795	0.00112	1.00
H	-0.84716	-0.07392	0.49667	1.00
H	-0.34711	-0.57466	0.00158	1.00
N	-0.06849	-0.06859	0.50020	1.00
N	-0.56885	-0.56801	-0.00062	1.00
N	-0.93115	-0.06874	0.49806	1.00
N	-0.43150	-0.56932	-0.00029	1.00
N	0.00015	-0.05478	0.49941	1.00
N	-0.50016	-0.55476	-0.00060	1.00
N	-0.05479	0.00006	0.50082	1.00
N	-0.55478	-0.49944	-0.00007	1.00
B	-0.00358	-0.74997	0.50387	1.00
B	-0.74992	-0.00327	0.49714	1.00
Li	-0.24966	-0.45410	0.95663	1.00
Li	-0.45312	-0.75114	0.04308	1.00
Co	0.00000	-0.50000	0.50000	1.00
Co	-0.50000	-0.00000	-0.00000	1.00

3.8 Reference

(1) Ockwig, N. W.; Co, A. P.; Keeffe, M. O.; Matzger, A. J.; Yaghi, O. M. Porous , Crystalline , Covalent Organic Frameworks. **2005**, *310* (5751), 1166–1171.

(2) El-Kaderi, H. M.; Hunt, J. R.; José L. Mendoza-Cortés, A. P. C.; Taylor, R. E.; O'Keeffe, M.; Yaghi, O. M. Designed Synthesis of 3D Covalent Organic Frameworks. *Science.* **2007**, *316* (5822), 268–273.

(3) Furukawa, H.; Kim, J.; Ockwig, N. W.; O'Keeffe, M.; Yaghi, O. M. Control of Vertex Geometry, Structure Dimensionality, Functionality, and Pore Metrics in the Reticular Synthesis of Crystalline Metal-Organic Frameworks and Polyhedra. *J. Am. Chem. Soc.* **2008**, *130* (35), 11650–11661.

(4) Lu, W.; Wei, Z.; Gu, Z. Y.; Liu, T. F.; Park, J.; Park, J.; Tian, J.; Zhang, M.; Zhang, Q.; Gentle, T.; Bosch, M.; Zhou, H. C. Tuning the Structure and Function of Metal-Organic Frameworks via Linker Design. *Chem. Soc. Rev.* **2014**, *43* (16), 5561–5593.

(5) Neti, V. S. P. K.; Wu, X.; Hosseini, M.; Bernal, R. A.; Deng, S.; Echegoyen, L. Synthesis of a Phthalocyanine 2D Covalent Organic Framework. *CrystEngComm* **2013**, *15* (36), 7157–7160.

(6) Helms, A.; Heiler, D.; McLendon, G. Electron Transfer in Bis-Porphyrin Donor-Acceptor Compounds with Polyphenylene Spacers Shows a Weak Distance Dependence. *J. Am. Chem. Soc.* **1992**, *114* (15), 6227–6238.

(7) Mullin, W. J.; Pawle, R. H.; Sharber, S. A.; Müller, P.; Thomas, S. W. Programmed Twisting of Phenylene-Ethynylene Linkages from Aromatic Stacking Interactions. *J. Mater. Chem. C* **2019**, *7* (5), 1198–1207.

(8) Su, J. H.; Lee, G. H.; Peng, S. M.; Chiu, C. W. A Spiroborate-Based Anionic Bis-N-Heterocyclic Carbene. *Dalt. Trans.* **2014**, *43* (8), 3059–3062.

(9) Hall, D. G. Structure, Properties, and Preparation of Boronic Acid Derivatives. In *Boronic Acids*; John Wiley & Sons, Ltd, 2011; pp 1–133.

(10) Smith, B. J.; Hwang, N.; Chavez, A. D.; Novotney, J. L.; Dichtel, W. R. Growth Rates and Water Stability of 2D Boronate Ester Covalent Organic Frameworks. *Chem. Commun.* **2015**, *51* (35), 7532–7535.

(11) Lor, J. P.; Edwards, J. O. Polyol Complexes and Structure of the Benzeneboronate Ion. *J. Org. Chem.* **1959**, *24* (6), 769–774.

(12) Gaafar, M. S.; El-Aal, N. S. A.; Gerges, O. W.; El-Amir, G. Elastic Properties and Structural Studies on Some Zinc-Borate Glasses Derived from Ultrasonic, FT-IR and X-Ray Techniques. *J. Alloys Compd.* **2009**, *475* (1–2), 535–542.

(13) Hu, Y.; Teat, S. J.; Gong, W.; Zhou, Z.; Jin, Y.; Chen, H.; Wu, J.; Cui, Y.; Jiang, T.; Cheng, X.; Zhang, W. Single Crystals of Mechanically Entwined Helical Covalent Polymers. *Nat. Chem.* **2021**, *13* (7), 660–665.

(14) Niu, W.; Smith, M. D.; Lavigne, J. J. Substituent Effects on the Structure and Supramolecular Assembly of Bis(Dioxaborole)s Derived from 1,2,4,5-Tetrahydroxybenzene. *Cryst. Growth Des.* **2006**, *6* (6), 1274–1277.

(15) Han, Y. S.; An, S.; Dai, J.; Hu, J.; Xu, Q.; Song, F.; Li, M.; Peng, C.; Liu, H. Defect-Engineering of Anionic Porous Aromatic Frameworks for Ammonia Capture. *ACS Appl. Polym. Mater.* **2021**, *3* (9), 4534–4542.

(16) Seoudi, R.; El-Bahy, G. S.; El Sayed, Z. A. FTIR, TGA and DC Electrical Conductivity Studies of Phthalocyanine and Its Complexes. *J. Mol. Struct.* **2005**, *753* (1), 119–126.

(17) Kumar, P.; Kumar, A.; Sreedhar, B.; Sain, B.; Ray, S. S.; Jain, S. L. Cobalt Phthalocyanine Immobilized on Graphene Oxide: An Efficient Visible-Active Catalyst for the Photoreduction of Carbon Dioxide. *Chem. – A Eur. J.* **2014**, *20* (20), 6154–6161.

(18) Nelson, A. P.; Farha, O. K.; Mulfort, K. L.; Hupp, J. T. Supercritical Processing as a Route to High Internal Surface Areas and Permanent Microporosity in Metal−Organic Framework Materials. *J. Am. Chem. Soc.* **2009**, *131* (2), 458–460.

(19) Willems, T. F.; Rycroft, C. H.; Kazi, M.; Meza, J. C.; Haranczyk, M. Algorithms and Tools for High-Throughput Geometry-Based Analysis of Crystalline Porous Materials. *Microporous Mesoporous Mater.*

2012, *149* (1), 134–141.

(20) Wang, X.; Chen, L.; Chong, S. Y.; Little, M. A.; Wu, Y.; Zhu, W. H.; Clowes, R.; Yan, Y.; Zwijnenburg, M. A.; Sprick, R. S.; Cooper, A. I. Sulfone-Containing Covalent Organic Frameworks for Photocatalytic Hydrogen Evolution from Water. *Nat. Chem.* **2018**, *10* (12), 1180–1189.

(21) Fu, Z.; Wang, X.; Gardner, A. M.; Wang, X.; Chong, S. Y.; Neri, G.; Cowan, A. J.; Liu, L.; Li, X.; Vogel, A.; Clowes, R.; Bilton, M.; Chen, L.; Sprick, R. S.; Cooper, A. I. A Stable Covalent Organic Framework for Photocatalytic Carbon Dioxide Reduction. *Chem. Sci.* **2020**, *11* (2), 543–550.

(22) Zhang, W.; Chen, L.; Dai, S.; Zhao, C.; Ma, C.; Wei, L.; Zhu, M.; Chong, S. Y.; Yang, H.; Liu, L.; Bai, Y.; Yu, M.; Xu, Y.; Zhu, X.-W.; Zhu, Q.; An, S.; Sprick, R. S.; Little, M. A.; Wu, X.; Jiang, S.; Wu, Y.; Zhang, Y.-B.; Tian, H.; Zhu, W.-H.; Cooper, A. I. Reconstructed Covalent Organic Frameworks. *Nature* **2022**, *604* (7904), 72–79.

(23) Sheldrick, G. M. SHELXT - Integrated Space-Group and Crystal-Structure Determination. *Acta Crystallogr. Sect. A Found. Crystallogr.* **2015**, *A71* (1), 3–8.

(24) Sheldrick, G. M. Crystal Structure Refinement with SHELXL. *Acta Crystallogr. Sect. C Struct. Chem.* **2015**, *C71* (1), 3–8.

(25) Dolomanov, O. V.; Bourhis, L. J.; Gildea, R. J.; Howard, J. A. K.; Puschmann, H. OLEX2: A Complete Structure Solution, Refinement and Analysis Program. *J. Appl. Crystallogr.* **2009**, *42* (2), 339–341.

(26) Martin, R. L.; Haranczyk, M. Construction and Characterization of Structure Models of Crystalline Porous Polymers. *Cryst. Growth Des.* **2014**, *14* (5), 2431–2440.

(27) Ermer, O. Concerning the Structure of Benzene. *Angew. Chemie Int. Ed. English* **1987**, *26* (8), 782–784.

Chapter 4

Summary and outlook

In this thesis, my main aim was to design and synthesize 3D COFs with novel topologies. Generally, there are two strategies available for accessing 3D COFs. The first strategy is 3D COF structure construction from multi-linking organic polyhedral nodes. However, the synthetic complexity of such organic polyhedral nodes severely limits the structural diversity of 3D COFs compared with their MOF counterparts. In MOFs, polyhedral metal clusters of a various number of coordination sites (up to 24-c)[1] are easily accessible for 3D framework construction. A second strategy to prepare 3D COFs is by controlling the spatial alignment of the planar or near planar organic nodes. While this strategy greatly simplifies the synthesis of organic nodes, 3D COF structures reported using this method, such as COFs of **ffc**,[2] **tbo**[3] and **fjh**[4] topology, mostly rely on the unpredictable rotation of imine bonds. Here, we planned to focus on the second strategy for targeting novel 3D COF structures/topologies developing methods with improved predictability compared to the conventional reliance on imine bonds rotation.

Based on the minimal edge-transitive principle, we choose to target the **nbo** topology as it is one of the regular nets with the transitivity of [1111]. These regular nets are supposed to be the most likely products for building blocks of specific geometries and thus ideal blueprints for targeted synthesis.[5] Following the reticular chemistry principle, two elements are required to target **nbo** topology: an organic 4-c node with square geometry and a method that can realize the perpendicular orientation of the two neighbouring squares. The perpendicular orientation is the key point for the success of this project. With this in mind, we then proposed two strategies to target 3D COFs of **nbo** topology. In the first strategy, a rigid tetrahedra-shaped ionic spiroborate linkage was introduced to reticulate the two neighbouring squares into perpendicular orientation. While the second strategy follows the same principle for obtaining the first **nbo** MOF (MOF-601) by linker geometry tuning.[6] The feasibility of each strategy was supported by the conformer search results from the Cambridge Structural Database (CSD) and these two strategies were conducted in **Chapter 2** and **Chapter 3**, respectively.

In **Chapter 2**, we successfully constructed a series of 3D SPB-COFs of **nbo** topology with square planar $(OH)_8$PcCo and the tetrahedra-shaped ionic spiroborate (SPB) linkage. The perpendicular orientation induced by the tetrahedral spiroborate linkage can be evidenced by single crystal structures of model compounds. PXRD comparison between the experimental and simulated pattern confirmed all SPB-COFs showed an underlying non-interpenetrated **nbo** topology. Among all SPB-COFs, SPB-COF-DBA, with $[n\text{-}Bu_2NH_2]^+$ (DBA) as counter cations, exhibited the best crystallinity, with 11 resolved diffraction peaks can be distinguished from the experimental PXRD pattern that fit the simulated pattern. FT-IR and solid-state ^{13}C and ^{11}B NMR spectra confirmed the structure of SPB-COFs. SPB-COF-DBA showed a BET surface area of 1726 $m^2\ g^{-1}$ after super-

critical CO_2 ($scCO_2$) activation. Benefitted from the good crystallinity of SPB-COF-DBA, the crystal structure of SPB-COF-DBA can be clearly visualized from HR-TEM images, with the identified periodic lattice (3.47 nm) in good agreement with the refined unit cell parameters (3.4744(2) nm).

In **Chapter 3**, based on the design principle mentioned above, following the preparation of the first **nbo** MOF (MOF-601),[6] we designed and synthesized two new diboronic acid linkers, namely, BPDA-2 and BPDA-4, by introducing two or four methyl group substitutions at the 2,2' or 2,2',6,6' position on the biphenyl unit in the planar1,4-biphenyldiboronic acid (linker BPDA). Our initial expectation is to realize 3D COFs of **nbo** topology with boronate ester linkage from the condensation reaction between the square $(OH)_8$PcCo and linker BPDA-2 or BPDA-4. We expect this neutral linkage together with longer linkers will contribute to larger accessible porosity in these new COFs and thus endow these new COFs with some good performance in either gas adsorptions or separations, though accompanied by an increased possibility to interpenetrate. However, the experimental results turned out to be out of our expectations.

In our case, while applying *N*,*N*-diethylformamide (DEF) as the solvent, by comparing the experimental and simulated PXRD pattern, COFs yielded from the reaction between $(OH)_8$PcCo and linker BPDA showed a 2D boronate ester-linked COF of **sql** topology, while the reaction between $(OH)_8$PcCo and linker BPDA-4 yielded a 3D COF of **nbo** topology but with spiroborate linkage rather than the expected neutral boronate ester linkage. The most interesting one is when reacting $(OH)_8$PcCo with linker BPDA-2, it yielded a COF with mixed 2D and 3D phases. Model compounds synthesized under COF preparation conditions confirmed the formation of spiroborate linkage in BPDA-2-COF and BPDA-4-COF. The following mechanism study inspired us to use phenylboronic acid to replace the diboronic acid linkers and it turned out to give us the same spiroborate-based 3D COF structure of **nbo** topology. Moreover, single crystal structure of the model compound-PA from this reaction system evidenced its spiroborate structure and the $[NH_2Et_2]^+$ counter cation. The crystal structure of the 2D BPDA-COF and 3D PA-COF was confirmed by the well-resolved TEM images, while only the 3D phase can be identified from the TEM images of the mix-phased BPDA-2-COF. The obtained 2D BPDA-COF showed an experimental BET surface area of 1371 $m^2\ g^{-1}$, while the measured surface area for BPDA-2-COF, BPDA-4-COF and PA-COF were 1307, 1246 and 1282 $m^2\ g^{-1}$, respectively. The low BET surface area of the latter three COFs can be attributed to two factors: 1. COF structures were not fully activated, as FT-IR spectra shows DEF residue in the activated COFs. 2. partial structure collapse during $scCO_2$ activation, as can be evidenced by the PXRD comparison before and after activation.

As for this work, we will keep carrying on exploring of the reaction mechanism to clearly understand this unexpected spiroborate linkage formation here.

In general, for novel 3D COFs structure exploration, either the multi-linking polyhedral nodes methods or the alignment control of planar units are all good methods for 3D COFs structure construction. Theoretically, these two methods together can realize almost all the 3D topologies listed in RCSR. We can expect in the near future that various organic polyhedral nodes with multiple linking sites will be synthesised, and more 3D COFs structures will be reported by applying these two strategies, as this field is currently drawing increasing research interest. The development of this field propagates the related structure characterization techniques like 3DED, reversely, advances in 3DED will also promote the developments of 3D COFs field. Solving COF structures solution problem in the future, both by advances in characterization techniques such as 3DED, or through more reliable synthesis, will be a key to unlocking the practical potential of COFs. The work in this thesis is a further step on that journey.

Reference

(1) Guillerm, V.; Kim, D.; Eubank, J. F.; Luebke, R.; Liu, X.; Adil, K.; Lah, M. S.; Eddaoudi, M. A Supermolecular Building Approach for the Design and Construction of Metal-Organic Frameworks. *Chem. Soc. Rev.* **2014**, *43* (16), 6141–6172.

(2) Lan, Y.; Han, X.; Tong, M.; Huang, H.; Yang, Q.; Liu, D.; Zhao, X.; Zhong, C. Materials Genomics Methods for High-Throughput Construction of COFs and Targeted Synthesis. *Nat. Commun.* **2018**, *9*, 5274.

(3) Kang, X.; Han, X.; Yuan, C.; Cheng, C.; Liu, Y.; Cui, Y. Reticular Synthesis of Tbo Topology Covalent Organic Frameworks. *J. Am. Chem. Soc.* **2020**, *142* (38), 16346–16356.

(4) Nguyen, H. L.; Gropp, C.; Ma, Y.; Zhu, C.; Yaghi, O. M. 3D Covalent Organic Frameworks Selectively Crystallized through Conformational Design. *J. Am. Chem. Soc.* **2020**, *142* (48), 20335–20339.

(5) Chen, Z.; Jiang, H.; O'Keeffe, M.; Eddaoudi, M. Minimal Edge-Transitive Nets for the Design and Construction of Metal-Organic Frameworks. *Faraday Discuss.* **2017**, *201*, 127–143.

(6) Furukawa, H.; Kim, J.; Ockwig, N. W.; O'Keeffe, M.; Yaghi, O. M. Control of Vertex Geometry, Structure Dimensionality, Functionality, and Pore Metrics in the Reticular Synthesis of Crystalline Metal-Organic Frameworks and Polyhedra. *J. Am. Chem. Soc.* **2008**, *130* (35), 11650–11661.

Appendix

In addition to the core work described in Chapters 1-3, I also contributed to the structure modelling in five other studies, as follows. This is briefly outlined in this appendix: see papers for more details.

(1) Z. Fu, X. Wang, A.M. Gardner, **X. Wang**, S.Y. Chong, G. Neri, A.J. Cowan, L. Liu, X. Li, A. Vogel, R. Clowes, M. Bilton, L. Chen, R.S. Sprick, & A.I. Cooper. A stable covalent organic framework for photocatalytic carbon dioxide reduction. Chem. Sci., 2020, 11, 2, 543-550.

My contribution: COF structure modelling (2D COF with **sql** topology).

(2) X. Wang, Z. Fu, L. Zheng, C. Zhao, **X. Wang**, S.Y. Chong, F. McBride, R. Raval, M. Bilton, L. Liu, X. Wu, L. Chen, R.S. Sprick, & A.I. Cooper. Covalent Organic Framework Nanosheets Embedding Single Cobalt Sites for Photocatalytic Reduction of Carbon Dioxide. Chem. Mater., 2020, 32, 21, 9107−9114.

My contribution: COF structure modelling (2D COFs with **sql** topology).

(3) K. Wang, Z. Jia, Y. Bai, **X. Wang**, S.E. Hodgkiss, L. Chen, S.Y. Chong, X. Wang, H. Yang, Y. Xu, F. Feng, J.W. Ward, & A.I. Cooper. Synthesis of Stable Thiazole-Linked Covalent Organic Frameworks via a Multicomponent Reaction. J. Am. Chem. Soc., 2020, 142, 25, 11131−11138.

My contribution: COF structure modelling (2D COFs with **hcb** topology).

(4) Q. Zhu, **X. Wang**, R. Clowes, P. Cui, L. Chen, M.A. Little, & A.I. Cooper. 3D Cage COFs: A Dynamic Three-Dimensional Covalent Organic Framework with High-Connectivity Organic Cage Nodes. J. Am. Chem. Soc., 2020, 142, 39, 16842−16848.

My contribution: COF structure modelling (3D Cage COF with **acs** topology).

(5) H. Gao, Q. Zhu, A.R. Neale, M. Bahri, **X. Wang**, H. Yang, L. Liu, R. Clowes, N.D. Browning, R.S. Sprick, M.A. Little, L.J. Hardwick, & A.I. Cooper. Integrated Covalent Organic Framework/Carbon Nanotube Composite as Li-Ion Positive Electrode with Ultra-High Rate Performance. Adv. Energy Mater., 2021, 11, 39, 2101880.

My contribution: COF structure modelling (2D COF with **hcb** topology).

(1) Z. Fu, X. Wang, A.M. Gardner, **X. Wang**, S.Y. Chong, G. Neri, A.J. Cowan, L. Liu, X. Li, A. Vogel, R. Clowes, M. Bilton, L. Chen, R.S. Sprick, & A.I. Cooper. A stable covalent organic framework for photocatalytic carbon dioxide reduction. Chem. Sci., 2020, 11, 2, 543-550.

My contribution: COF structure modelling (2D COF with **sql** topology).

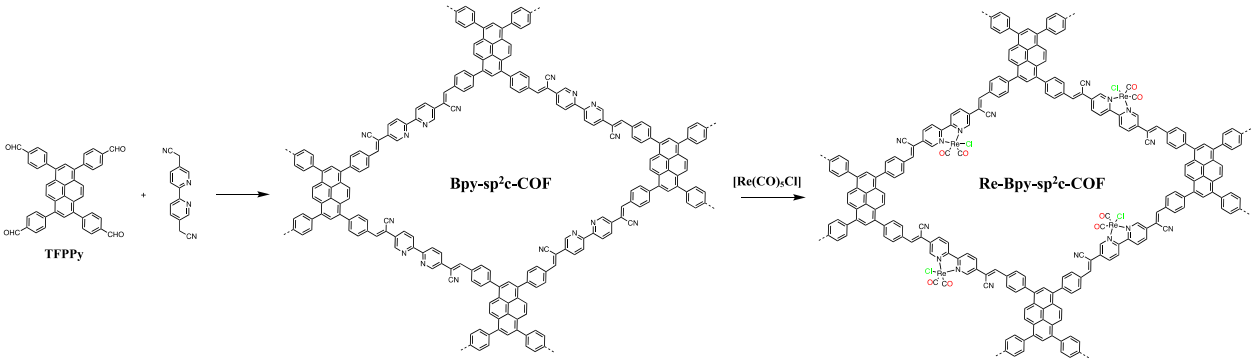

Figure 1. Scheme for the synthesis of **Bpy-sp^{2}c-COF** and **Re-Bpy-sp^{2}c-COF**.

COF structural modelling:

According to the Reticular Chemistry Structure Resource (RCSR) database,[1] there are two possible 2D topologies exist for building block pair of TFPPy and a linear linker: **sql** and **kgm** (**Figure 2**.). **Bpy-sp^{2}c-COF (Figure 1.)**models based on these topologies are constructed using zeo++ code[2] and Material Studio software, the obtained COF models were optimized with the Drieding force filed (COF structure based on AB-stacking mode of **kgm** topology) implemented in the Forcite or the DFTB+ (other COF structures) module of the BIOVIA Materials Studio software. PXRD based on these two models were simulated and compared with the experimental PXRD pattern to find the best fit for COF structure determination. The comparison results showed that **Bpy-sp^{2}c-COF** is of 2D **sql** topology with AA-stacking mode (eclipsed) (**Figure 3.**). As for the structural modelling of **Re-Bpy-sp^{2}c-COF**, which is formed after post-synthetic modification of **Bpy-sp^{2}c-COF**, the ligand $Re(CO)_5Cl$ was incorporated manually in Material Studio, by referring the single crystal structure of related organic fragments with $Re(CO)_5Cl$ ligand from the Cambridge Structural Database (CSD). Further geometry optimization of these two COFs was operated by Dr. Linjiang Chen in VASP.[3]

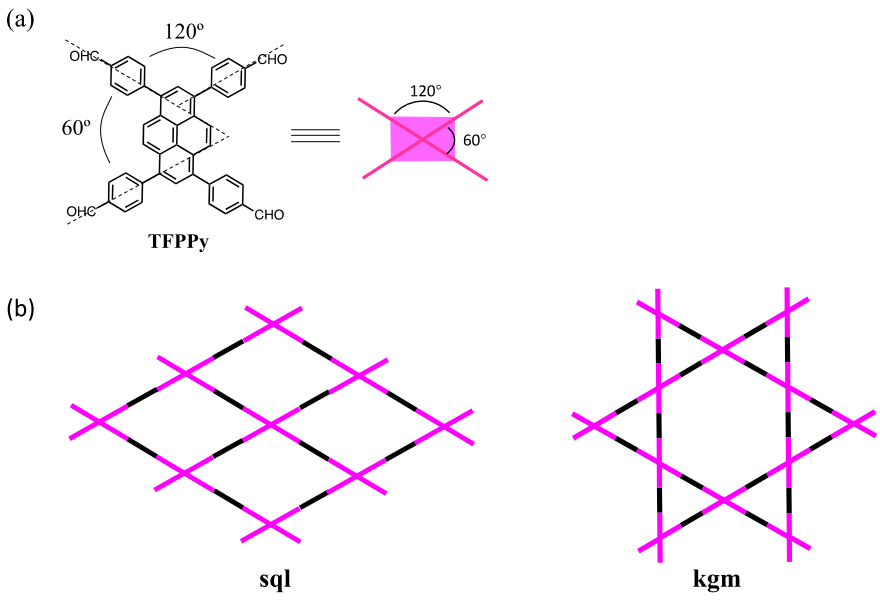

Figure 2. (a) The geometry illustration of **TFPPy** unit. (b) The two possible topologies: **sql** and **kgm**.

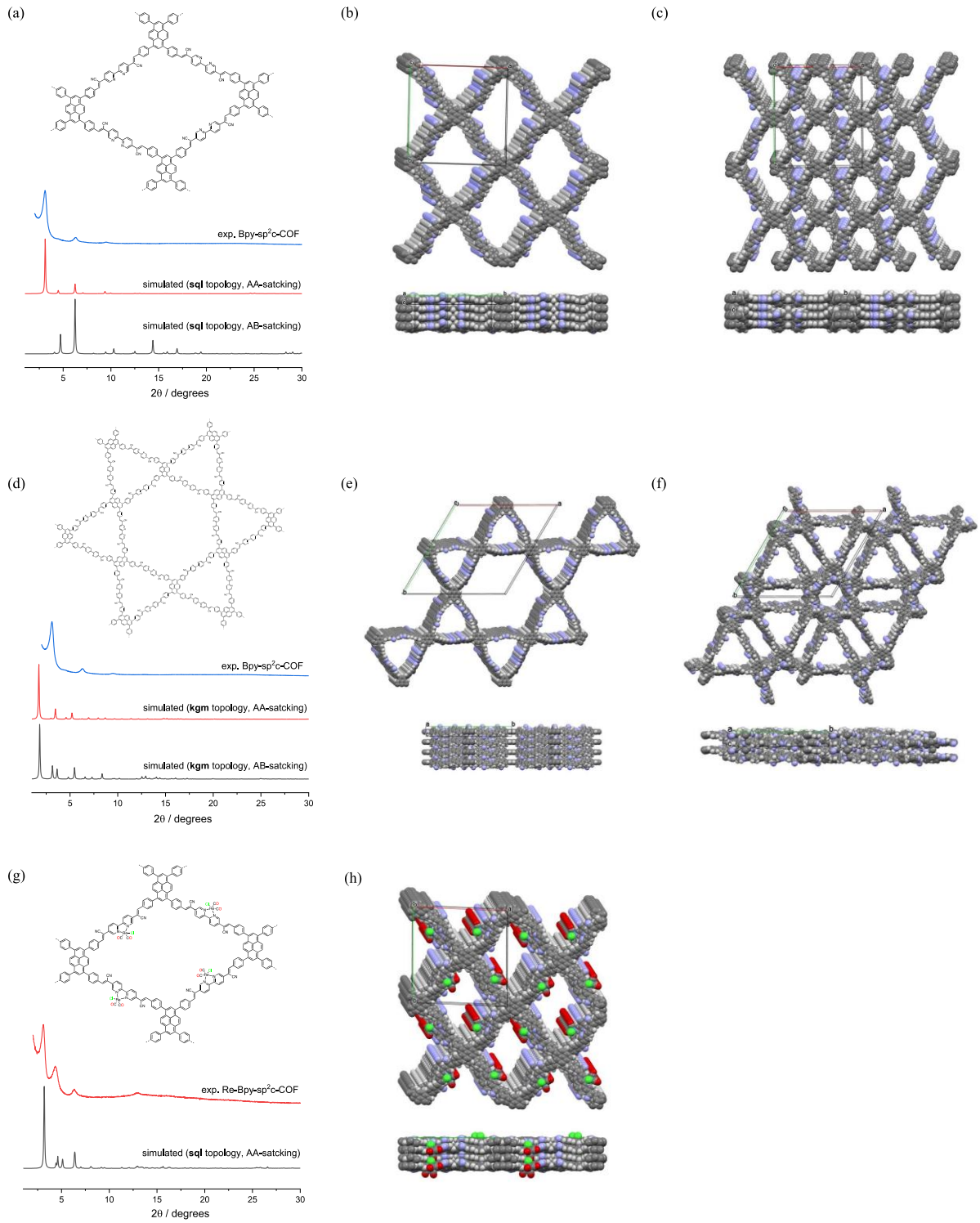

Figure 3. (a) Experimental and simulated PXRD comparison of **Bpy-sp^{2}c-COF** based-on **sql** topology and its corresponding structure based-on the (b) AA-stacking mode (c) AB-stacking mode of **sql** topology; (d) Experimental and simulated PXRD comparison of **Bpy-sp^{2}c-COF** based-on **kgm** topology and its corresponding structure based-on the (e) AA-stacking mode (f) AB-stacking mode of **kgm** topology; (g) Experimental and simulated PXRD comparison of **Re-Bpy-sp^{2}c-COF** based-on **sql** topology and its corresponding structure based-on the (h) AA-stacking mode of **sql** topology.

(2) X. Wang, Z. Fu, L. Zheng, C. Zhao, **X. Wang**, S.Y. Chong, F. McBride, R. Raval, M. Bilton, L. Liu, X. Wu, L. Chen, R.S. Sprick, & A.I. Cooper. Covalent Organic Framework Nanosheets Embedding Single Cobalt Sites for Photocatalytic Reduction of Carbon Dioxide. Chem. Mater., 2020, 32, 21, 9107−9114.

My contribution: COF structure modelling (2D COFs with **sql** topology).

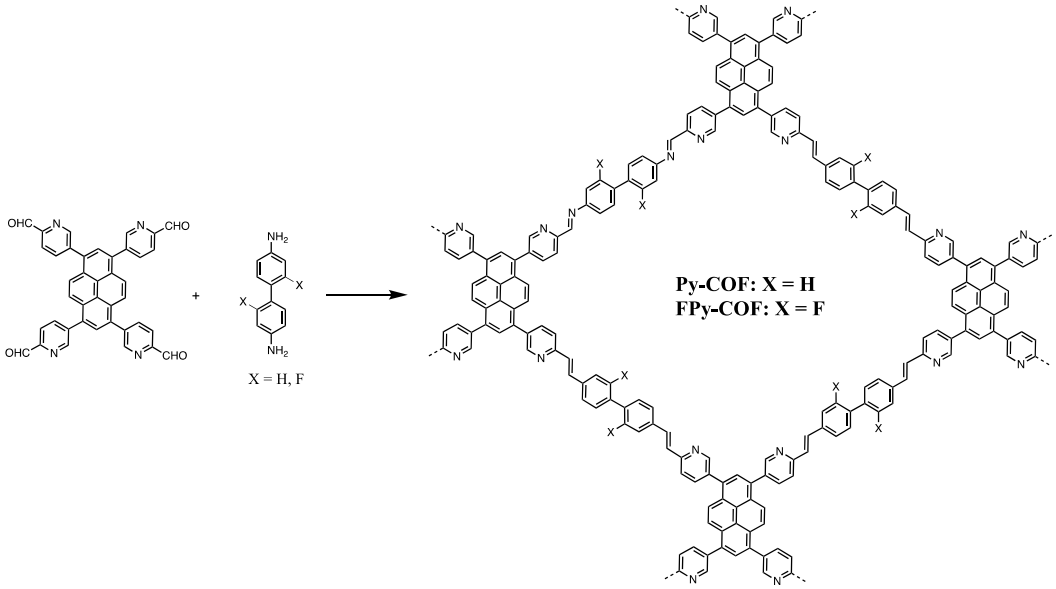

Figure 4. Scheme for the synthesis of **Py-COF** and **FPy-COF**.

COF structural modelling:

The situation here is similar to the former **Bpy-sp^2-COFs**, since the 5,5′,5″,5‴-(pyrene-1,3,6,8-tetrayl)- tetrapicolinaldehyde building unit used for COFs synthesis here (**Figure 4.**) is of the same geometry of the **TFPPy** unit for the synthesis of **Bpy-sp^2-COFs**. Thus, following the same principle, two possible 2D topologies exist for **(F)Py-COFs**: **sql** and **kgm**. **(F)Py-COFs** models based on these topologies are constructed using zeo++ code[2] and Material Studio software, the obtained COF models were optimized with the Drieding force filed implemented in the Forcite module of the BIOVIA Materials Studio software. PXRD based on these two models were simulated and compared with the experimental PXRD pattern to find the best fit for COF structure determination. The comparison results showed that **(F)Py-COFs** is of 2D sql topology with AA-stacking mode (eclipsed) (**Figure 5.**). Further geometry optimization of these two COFs was operated by Dr. Linjiang Chen in VASP.[3]

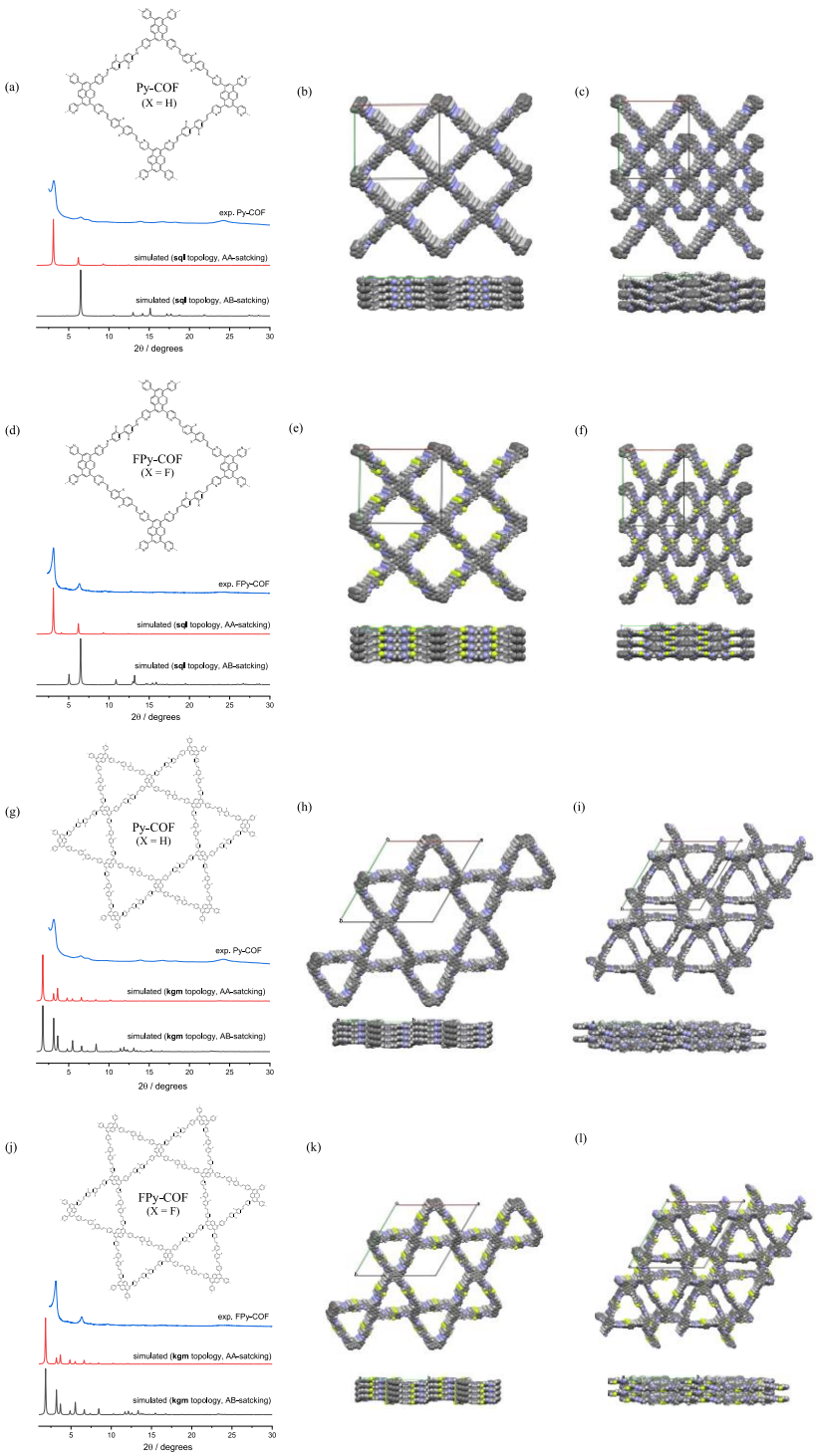

Figure 5. (a) Experimental and simulated PXRD comparison of **Py-COF** based-on **sql** topology and its corresponding structure based-on the (b) AA-stacking mode (c) AB-stacking mode of **kgm** topology; (d) Experimental and simulated PXRD comparison of **FPy-COF** based-on **sql** topology and its corresponding structure based-on the (e) AA-stacking mode (f) AB-stacking mode of **sql** topology; (g) Experimental and simulated PXRD comparison of **Py-COF** based-on **kgm** topology and its corresponding structure based-on the (h) AA-stacking mode (i) AB-stacking mode of **kgm** topology; (j) Experimental and simulated PXRD comparison of **FPy-COF** based-on **kgm** topology and its corresponding structure based-on the (k) AA-stacking mode (l) AB-stacking mode of **kgm** topology.

(3) K. Wang, Z. Jia, Y. Bai, **X. Wang**, S.E. Hodgkiss, L. Chen, S.Y. Chong, X. Wang, H. Yang, Y. Xu, F. Feng, J.W. Ward, & A.I. Cooper. Synthesis of Stable Thiazole-Linked Covalent Organic Frameworks via a Multicomponent Reaction. J. Am. Chem. Soc., 2020, 142, 25, 11131−11138.

My contribution: COF structure modelling (2D COFs with **hcb** topology).

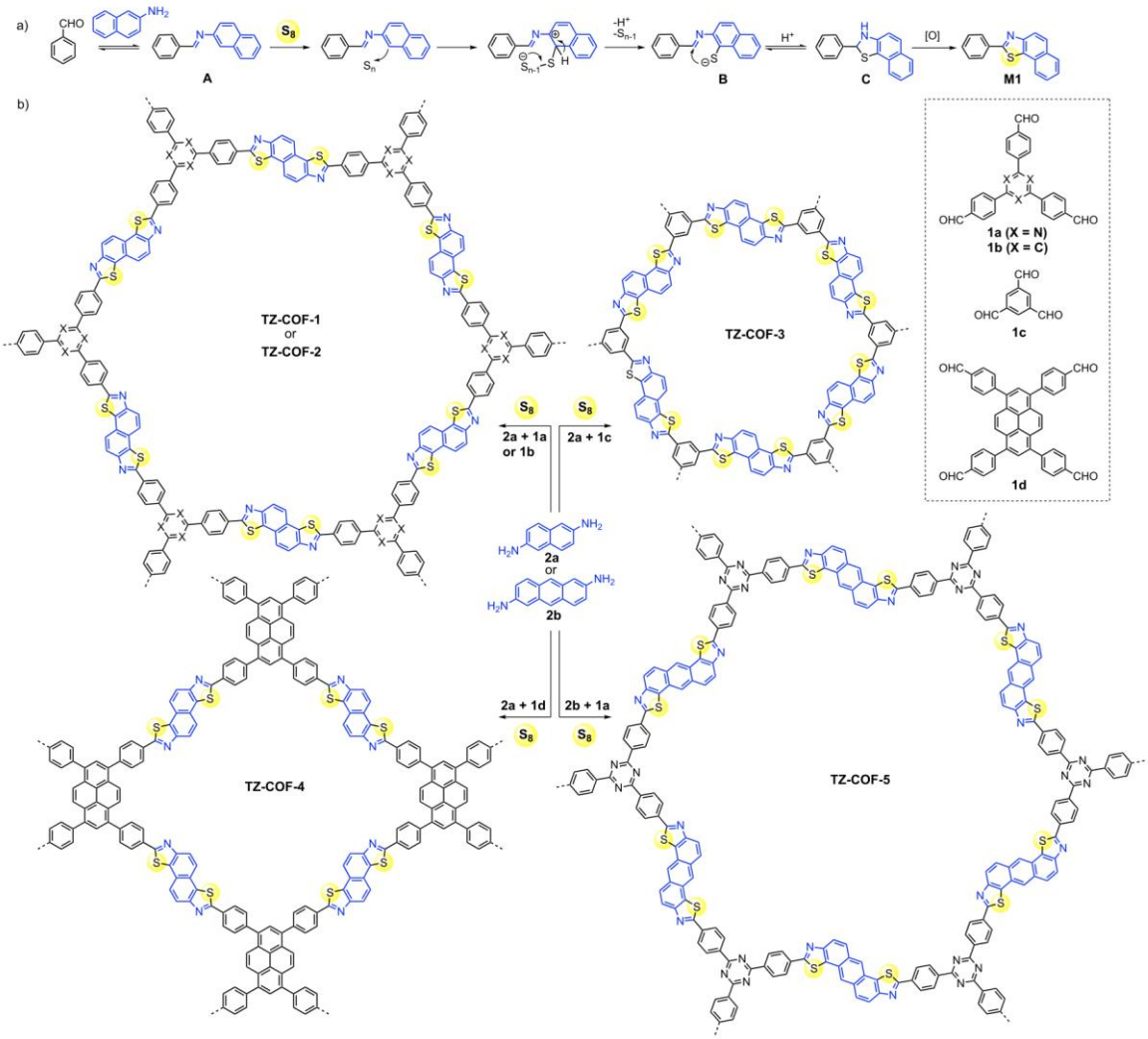

Figure 6. Synthesis of Thiazole-Linked Covalent Organic Frameworks **(TZ-COFs) 1−5**. (a) Proposed Mechanism of Thiazole Formation (b) Synthesis of Thiazole-Linked COFs by a Multicomponent Reaction.

COF structural modelling:

The scheme for the synthesis of TZ-COF-1~5 is shown in **Figure 6**. According to the Reticular Chemistry Structure Resource (RCSR) database,[1] the reaction between a regular triangle organic building unit and a linear linker gives COFs of **hcb** topology (**Figure 7.**) Following this principle, **TZ-COF-1, -2, -3** and **-5** are all supposed to have **hcb** topology. While the situation for **TZ-COF-4** is similar to the former **Bpy-sp^2-COFs**, since the same **TFPPy** unit is used here for the synthesis

of **TZ-COF-4**. Thus, following the same principle, two possible 2D topologies exist for **TZ-COF-4**: **sql** and **kgm**. **TZ-COF-4** models based on these topologies are constructed using zeo++ code[2] and Material Studio software, the obtained COF models were optimized with the Drieding force filed implemented in the Forcite module of the BIOVIA Materials Studio software. PXRD based on these two models were simulated and compared with the experimental PXRD pattern to find the best fit for COF structure determination. The comparison results showed that **TZ-COF-1, -2, -3** and **-5** are all of **hcb** topology and adopts the AA-stacking mode (eclipsed) (**Figure 8.**), while **TZ-COF-4** is of 2D **sql** topology with AA-stacking mode (eclipsed) (**Figure 9.**). Further geometry optimization of these two COFs was operated by Dr. Linjiang Chen in VASP.[3]

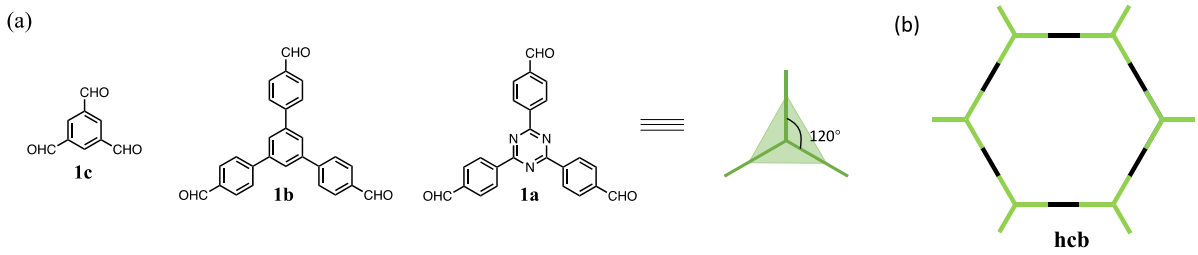

Figure 7. (a) The geometry illustration of compound **1a**, **1b** and **1c**. (b) **hcb** topology.

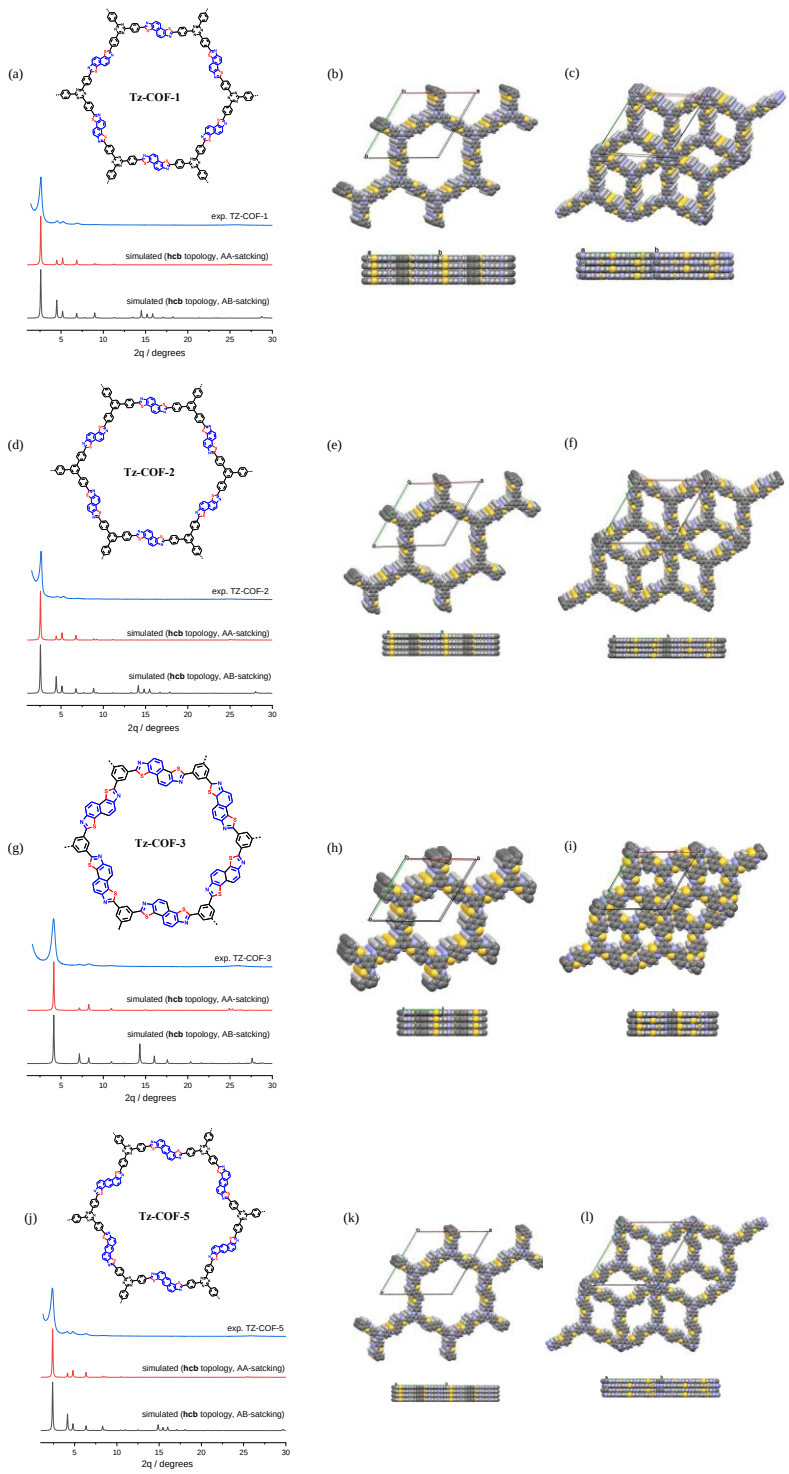

Figure 8. (a) Experimental and simulated PXRD comparison of **Tz-COF-1** based-on **hcb** topology and its corresponding structure based-on the (b) AA-stacking mode (c) AB-stacking mode of **hcb** topology; (d) Experimental and simulated PXRD comparison of **Tz-COF-2** based-on **hcb** topology and its corresponding structure based-on the (e) AA-stacking mode (f) AB-stacking mode of **hcb** topology; (g) Experimental and simulated PXRD comparison of **Tz-COF-3** based-on **hcb** topology and its corresponding structure based-on the (h) AA-stacking mode (i) AB-stacking mode of **hcb** topology; (j) Experimental and simulated PXRD comparison of **Tz-COF-5** based-on **hcb** topology and its corresponding structure based-on the (k) AA-stacking mode (l) AB-stacking mode of **hcb** topology.

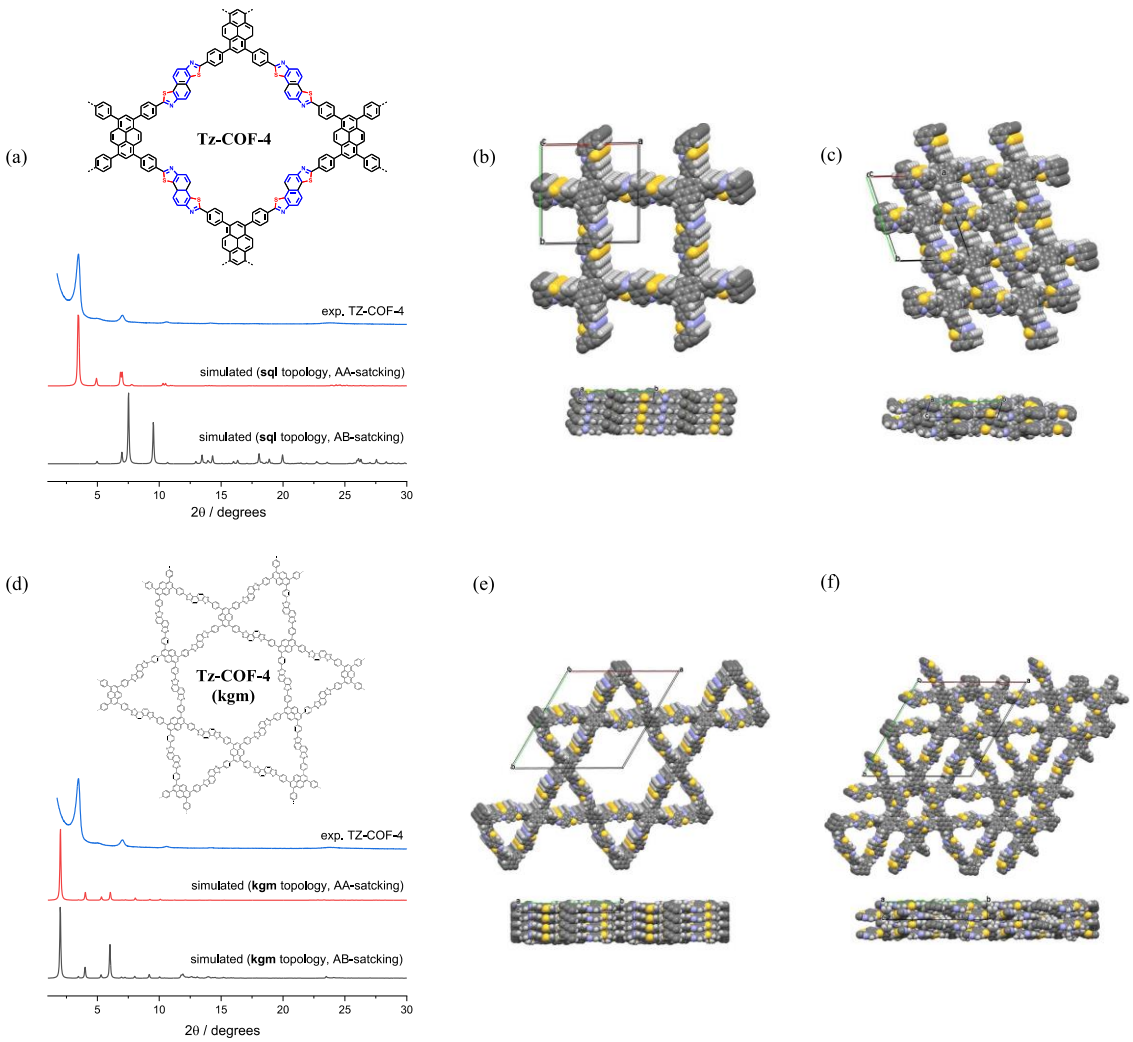

Figure 9. (a) Experimental and simulated PXRD comparison of **Tz-COF-4** based-on **sql** topology and its corresponding structure based-on the (b) AA-stacking mode (c) AB-stacking mode of **sql** topology; (d) Experimental and simulated PXRD comparison of **Tz-COF-4** based-on **kgm** topology and its corresponding structure based-on the (e) AA-stacking mode (f) AB-stacking mode of **kgm** topology.

(4) Q. Zhu, **X. Wang**, R. Clowes, P. Cui, L. Chen, M.A. Little, & A.I. Cooper. 3D Cage COFs: A Dynamic Three-Dimensional Covalent Organic Framework with High-Connectivity Organic Cage Nodes. J. Am. Chem. Soc., 2020, 142, 39, 16842−16848.

My contribution: COF structure modelling (3D Cage COF with **acs** topology).

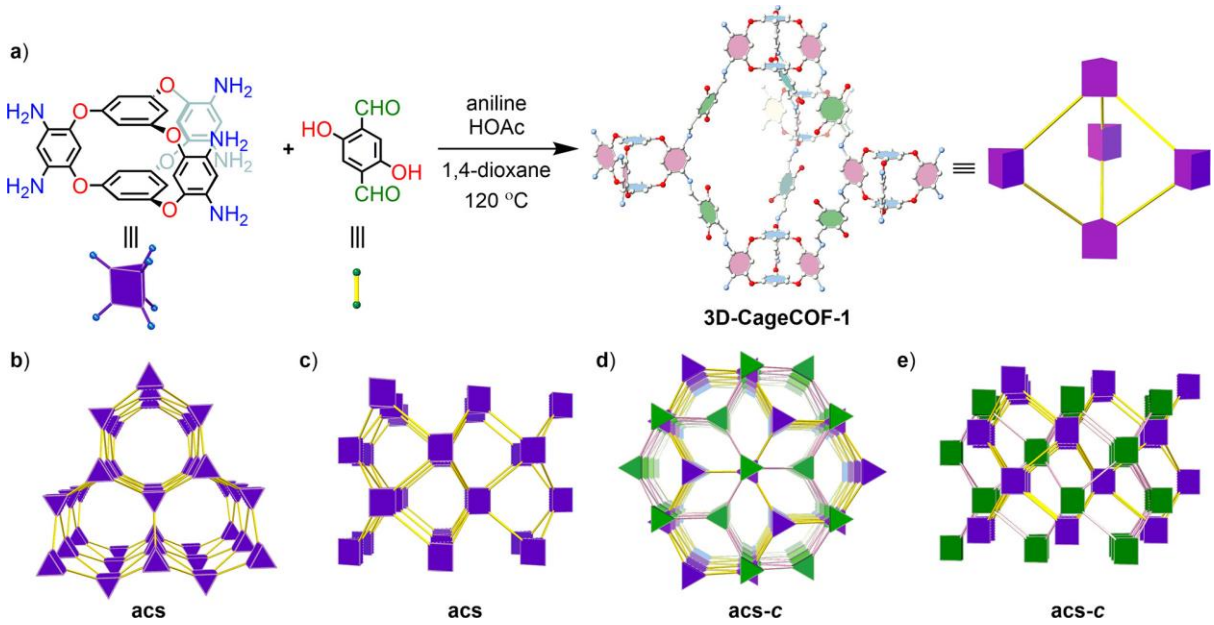

Figure 10. (a) Scheme for the synthesis of **3D-CageCOF-1** from **Cage-6-NH$_2$** and **DHTPA**, which can be topologically represented as a triangular prism and a linear strut, respectively. Model atom colors: C, white; N, blue; O, red. H atoms are omitted for clarity. (b, c) Two views of an **acs** crystal net, where the purple nodes represent the cage-based building blocks; (d, e) two comparable views of the 2-fold interpenetrated **acs-c** net (c, catenated), with the cage nodes belonging to the different nets colored in purple or green.

COF structural modelling:

The scheme for the synthesis of 3D-CageCOF-1 is shown in **Figure 10**. According to the Reticular Chemistry Structure Resource (RCSR) database,[1] the reaction between an organic trigonal prism building block and a linear linker will possibly give COFs of **acs**, **snx**, **snw** and **lcy** topologies. Based on the topological preference rule discussed in the first chapter, **acs** and **lcy** topologies are supposed to be more likely to form since these two nets are edge-transitive (number of edges = 1), while **snx** and **snw** topologies all have two edges. Besides, the mean average angle deviation (AAD) values[4] calculated for the nets: **acs**, **snx**, **snw** and **lcy**, are 0.35, 1.22, 1.58 and 4.32º, respectively, which further addressed that this cage COF is more likely to adopt **acs** topology (**Table 1.**).Besides, for a more accurate structure illustration, COFs of **acs** topology with up to three-fold interpenetration was built (**Figure 12. and 13.**). All COF models are constructed using zeo++ code[2] and Material Studio software, the obtained COF models were optimized with the Drieding force

filed implemented in the Forcite module of the BIOVIA Materials Studio software. PXRD based on these two models were simulated and compared with the experimental PXRD pattern to find the best fit for COF structures determination. The experimental and simulated PXRD comparison results for the DMF solvated sample showed this COF is potentially have a two-fold interpenetrated **acs** topology. Further geometry optimization of these two COFs was operated by Dr. Linjiang Chen in VASP.[3] Dr. Linjiang Chen prepared the DMF-loaded COF models and the small pore (sp-) COF models of the activated COF samples.

Table 1. Topological preference ranking for **3D-CageCOF-1** by mean average angle deviation (AAD)[a].

topology	**acs**	**snx**	**snw**	**lcy**
no. edge	1	2	2	1
mean AAD (º)	0.35	1.22	1.58	4.32

a. The AAD is a measure of how well the chosen building blocks fit on a target crystal net; the smaller the AAD value, the better the fit of the building blocks to the target topology. For each topology, the mean AAD value reported above corresponds to the most optimized embedding orientation of the building blocks into the net. Here, we used maximum symmetry embedded topologies as blueprints without further optimization, and the cage building block adopted a highly symmetrical, trigonal prism geometry. The AAD analyses were carried out using the weaver code developed by Schmid and co-workers.[4] According to the AAD results, **acs** is the most preferred topology for the organic cage building block.

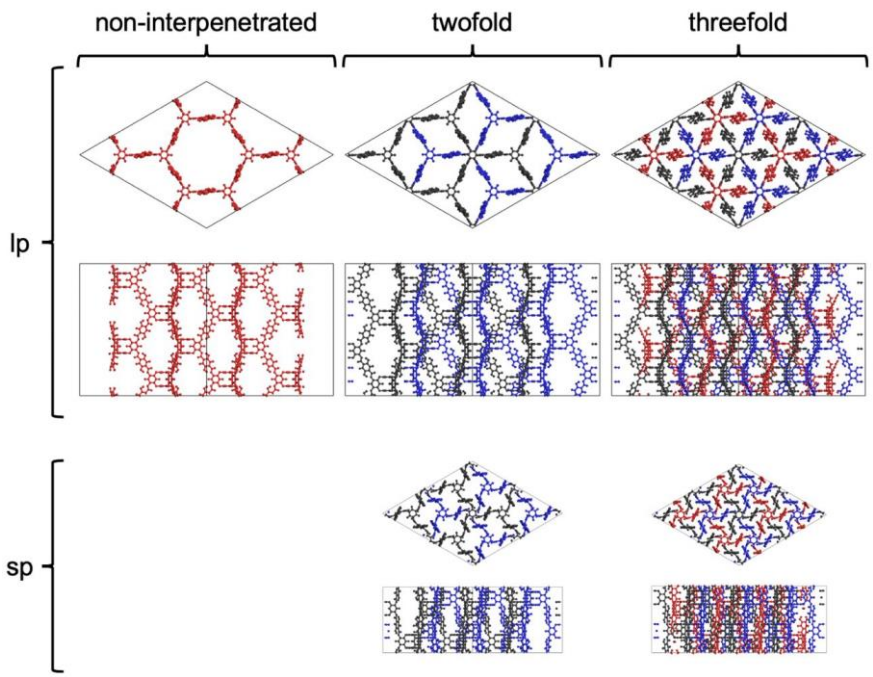

Figure 11. Structural models simulated for **3D-CageCOF-1**: **lp**, large-pore; **sp**, small-pore.

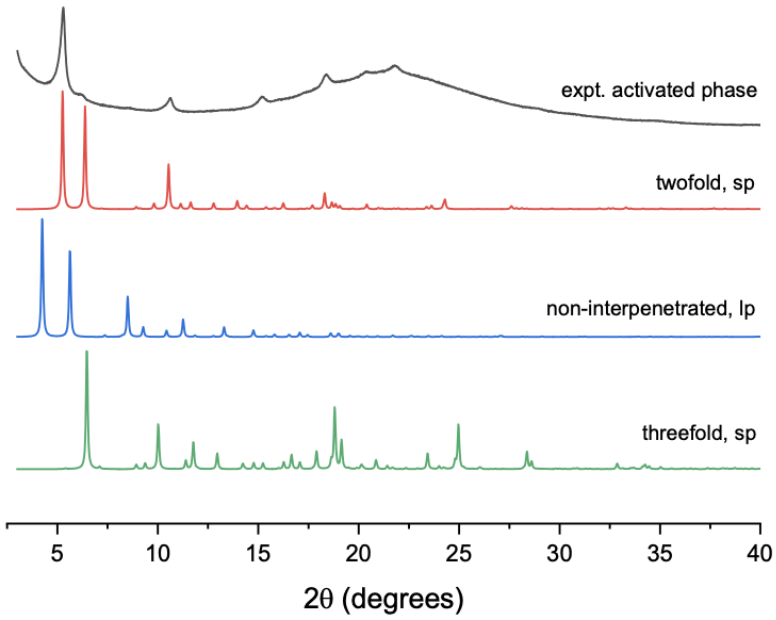

Figure 12. Comparison of PXRD patterns between the experimental activated phase and the atomistic models.

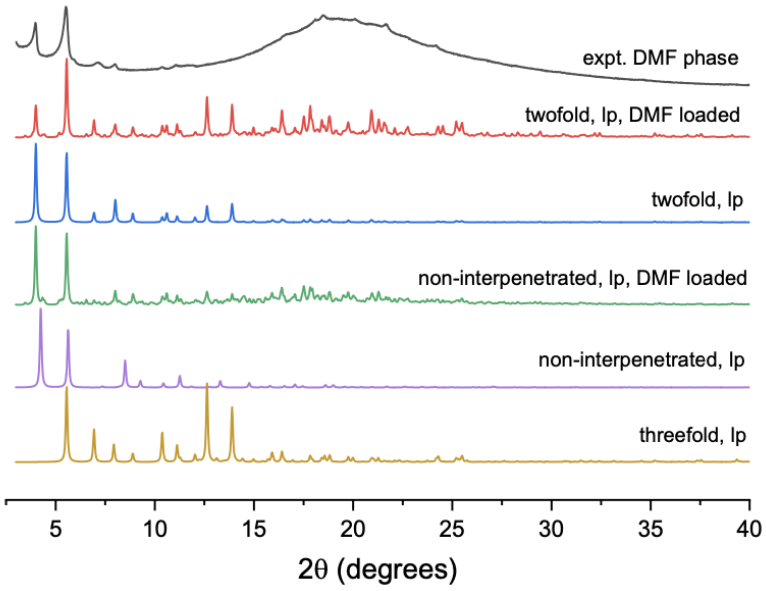

Figure 13. Comparison of PXRD patterns between the experimental DMF phase and the atomistic models.

(5) H. Gao, Q. Zhu, A.R. Neale, M. Bahri, **X. Wang**, H. Yang, L. Liu, R. Clowes, N.D. Browning, R.S. Sprick, M.A. Little, L.J. Hardwick, & A.I. Cooper. Integrated Covalent Organic Framework/Carbon Nanotube Composite as Li-Ion Positive Electrode with Ultra-High Rate Performance. Adv. Energy Mater., 2021, 11, 39, 2101880.

My contribution: COF structure modelling (2D COF with **hcb** topology).

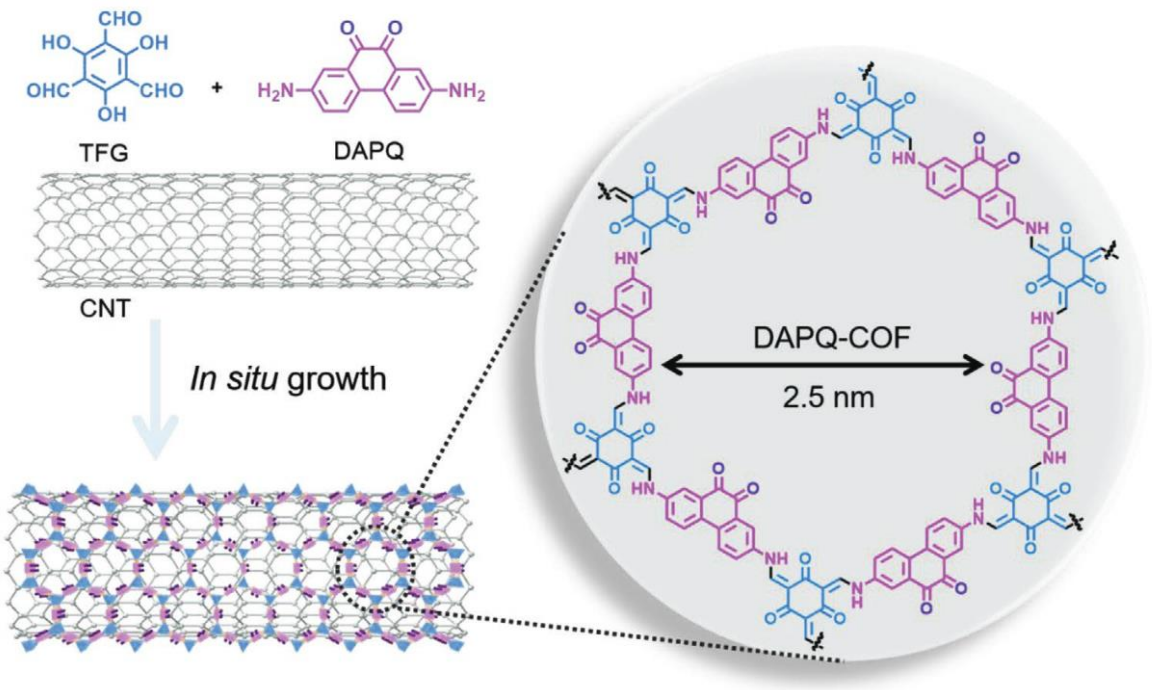

Figure 14. Scheme for the synthesis of **DAPQ-COF**.

COF structural modelling:

The scheme for the synthesis of DAPQ-COF is shown in **Figure 14**. Similar to TZ-COFs discussed before, the reaction between a regular triangle organic building unit and a linear linker is supposed to give COFs of **hcb** topology. Based-on such principle, COFs of **hcb** topology with AA, AB and ABC-stacking mode were constructed using zeo++ code[2] and Material Studio software, the obtained COF models were optimized with the Drieding force filed implemented in the Forcite module of the BIOVIA Materials Studio software. PXRD based on these three models were simulated and compared with the experimental PXRD pattern to find the best fit for COF structure determination. The comparison results showed that **DAPQ-COF** is of **hcb** topology and adopts the AA-stacking mode (eclipsed) (**Figure 15.**).

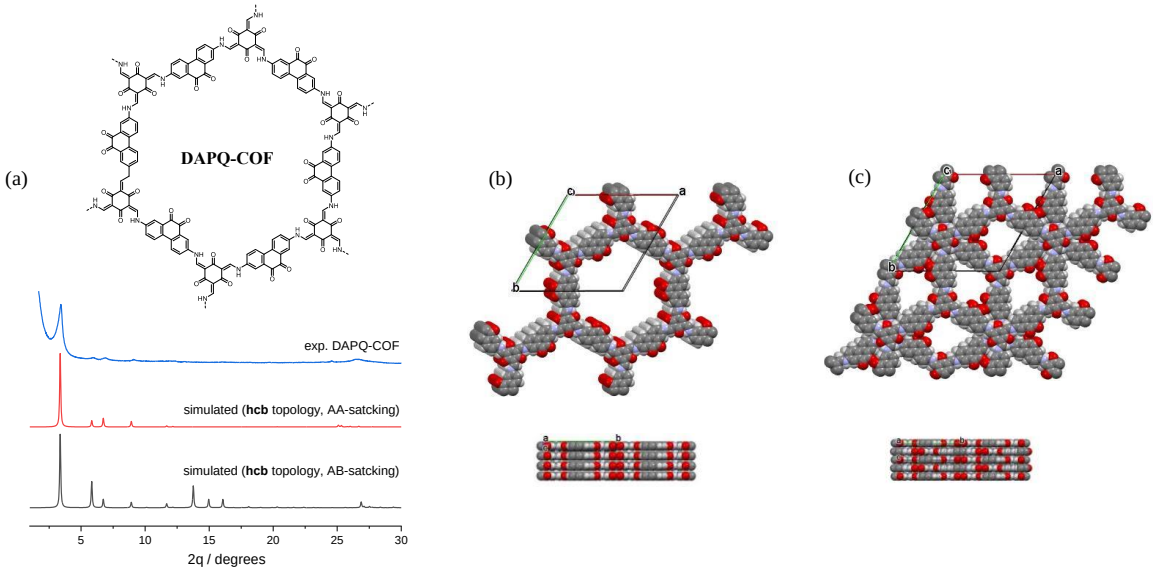

Figure 15. (a) Experimental and simulated PXRD comparison of **DAPQ-COF** based-on **hcb** topology and its corresponding structure based-on the (b) AA-stacking mode (c) AB-stacking mode of **hcb** topology.

Reference

(1) Keeffe, M. O.; Peskov, M. a; Ramsden, S. J.; Yaghi, O. M. (RCSR) Database of , and Symbols for , Crystal. *Acc. Chem. Res.* **2008**, *41* (12), 1782–1789.

(2) Willems, T. F.; Rycroft, C. H.; Kazi, M.; Meza, J. C.; Haranczyk, M. Algorithms and Tools for High-Throughput Geometry-Based Analysis of Crystalline Porous Materials. *Microporous Mesoporous Mater.* **2012**, *149* (1), 134–141.

(3) Hafner, J. Ab-Initio Simulations of Materials Using VASP: Density-Functional Theory and Beyond. *J. Comput. Chem.* **2008**, *29* (13), 2044–2078.

(4) Keupp, J.; Schmid, R. TopoFF: MOF Structure Prediction Using Specifically Optimized Blueprints. *Faraday Discuss.* **2018**, *211*, 79–101.